

**Supramolecular Assemblies of Organic/Inorganic
Guests through Macrocyclic Receptors:
Construction, Characterization and their
Prospective Applications**

By

Raman Khurana

CHEM01201504018

Bhabha Atomic Research Centre, Mumbai-400085

A thesis submitted to the

Board of Studies in Chemical Sciences

In partial fulfillment of requirements

for the Degree of

DOCTOR OF PHILOSOPHY

of

HOMI BHABHA NATIONAL INSTITUTE



August, 2019

Homi Bhabha National Institute¹

Recommendations of the Viva Voce Committee

As members of the Viva Voce Committee, we certify that we have read the dissertation prepared by **Raman Khurana** entitled “**Supramolecular Assemblies of Organic/Inorganic Guests through Macrocyclic Receptors: Construction, Characterization and their Prospective Applications**” and recommend that it may be accepted as fulfilling the thesis requirement for the award of Degree of Doctor of Philosophy.

Chairman - Prof. A. C. Bhasikuttan



Date: 25.10.2019

Guide / Convener - Prof. J. Mohanty



Date: 25.10.19

Examiner - Prof. A. L. Koner



Date: 25.01.2019

Member 1- Prof. P. K. Mohapatra



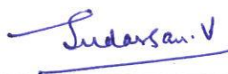
Date: 25.10.2019

Member 2- Prof. H. P. Upadhyaya



Date: 25/10/2019

Member 3- Prof. V. Sudarsan



Date: 25/10/2019

Final approval and acceptance of this thesis is contingent upon the candidate's submission of the final copies of the thesis to HBNI.

I/~~We~~ hereby certify that I/~~we~~ have read this thesis prepared under my/our direction and recommend that it may be accepted as fulfilling the thesis requirement.

Date: 25.10.19

Place: HBNI, Mumbai



Dr. J. Mohanty
(Guide)

STATEMENT BY AUTHOR

This dissertation has been submitted in partial fulfillment of requirements for an advanced degree at Homi Bhabha National Institute (HBNI) and is deposited in the Library to be made available to borrowers under rules of the HBNI.

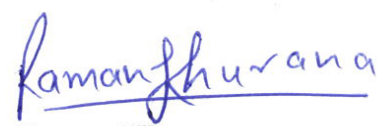
Brief quotations from this dissertation are allowable without special permission, provided that accurate acknowledgement of source is made. Requests for permission for extended quotation from or reproduction of this manuscript in whole or in part may be granted by the Competent Authority of HBNI when in his or her judgment the proposed use of the material is in the interests of scholarship. In all other instances, however, permission must be obtained from the author.



Raman Khurana

DECLARATION

I, hereby declare that the investigation presented in the thesis has been carried out by me. The work is original and has not been submitted earlier as a whole or in part for a degree / diploma at this or any other Institution / University.


Raman Khurana

List of Publications arising from the thesis

Journal

1. “Redox-mediated Negative Differential Resistance (NDR) Behavior in Perylenediimide Derivative: A Supramolecular Approach”, **Raman Khurana**, J. Mohanty, N. Padma, N. Barooah, A. C. Bhasikuttan, *Chem. Eur. J.*, **2019**, (DOI: 10.1002/chem.201902641).
2. “Supramolecularly Enhanced Emission of Thiazole Orange with Sulfobutylether β -cyclodextrin: Stimuli-Responsive Fluorescence Sensor for Tyramine”, **Raman Khurana**, N. Barooah, A. C. Bhasikuttan, J. Mohanty, *ChemPhysChem.*, **2019**, (DOI: 10.1002/cphc.201900656).
3. “Supramolecular Nanorods of (N-methylpyridyl) Porphyrin with Captisol: Effective Photosensitizer for Anti-bacterial and Anti-tumor Activities”, **Raman Khurana**, A.S. Kakatkar, S. Chatterjee, N. Barooah, A. Kunwar, A.C. Bhasikuttan, J. Mohanty, *Front. Chem. Supramolecular Chemistry*, **2019**, 7, 452.
4. “Ultra-Bright Rhodamines with Sulfobutylether- β -Cyclodextrin: A Viable Supramolecular Dye Laser in Aqueous Medium”, **Raman Khurana**, S. Agarwalla, G. Sridhar, N. Barooah, A. C. Bhasikuttan, J. Mohanty, *ChemPhysChem.*, **2018**, 19, 2349-2356.
5. “Modulation in the acidity constant of acridine dye with cucurbiturils: stimuli-responsive pKa tuning and dye relocation into live cells”, **Raman Khurana**, N. Barooah, A. C. Bhasikuttan, J. Mohanty, *Org. Biomol. Chem.*, **2017**, 15, 8448-8857.
6. “Emissive Naphthalendiimide Based Radical Anion in Supramolecular Confinement of Cucurbituril Nanaocavity” **Raman Khurana**, J. Mohanty, A. C. Bhasikuttan, N. Barooah, **2019**, (Manuscript under prepration).

Book Chapter

1. “Cucurbituril-Functionalized Supramolecular Assemblies: Gateways to Diverse Applications”, J. Mohanty, **Raman Khurana**, N. Barooah, A. C. Bhasikuttan, In **Cucurbituril-based Functional Materials**, Chapter 11, 2019, 235-257, *Royal Society of Chemistry*.

Other Publications Associated in research work

7. “Cooperative enhancement of antibacterial activity of sanguinarine drug through p-sulfonatocalix[6]arene-functionalized silver nanoparticles”, C. Mehra, R. Gala, A. Kakatkar, V. Kumar, **Raman Khurana**, S. Chatterjee, N N. Kumar, N. Barooah, A. Bhasikuttan, J. Mohanty, (Revised version submitted), *CC-COM-09-2019-007378*.
8. “Fluorescence enhancement of cationic styrylcoumarin-cucurbit [7] uril complexes: Enhanced stability and cellular membrane localization”, P. Jana, T. Mukherjee, **Raman Khurana**, N. Barooah, V. Soppina, J. Mohanty, S. Kanvah, *Journal of Photochemistry & Photobiology A: Chemistry*, **2019**, 384, 112062.
9. “Photophysical and Protolytic Properties of Neutral Red with Macrocyclic Receptors: Fluorescence Sensor and Drug Delivery Applications”, J. Mohanty, **Raman Khurana**, N. Barooah, A. C. Bhasikuttan, *J. Indian Chem. Soc.*, **2018**, 95, 533-548.
10. “DNA-Induced Novel Optical Features of Ethyl Viologen-Tethered Perylenediimide Triad”, J. H. Mondal, B. Pramanik, M. N. Shinde, **Raman Khurana**, N. Barooah, A. C. Bhasikuttan, D. Das, J. Mohanty. *J. Phys.Chem. C.*, **2018**, 122, 18061-18069
11. “pH-responsive Molecular Assemblies of Pyridylbutadiene Derivative with Cucurbit[7]uril”, K. Vasu,[#] **Raman Khurana**,[#] J. Mohanty, S. Kanvah, *RSC Adv.*, **2018**, 8, 16738-16745 (# = Equal contribution)
12. “Stimuli-responsive Supra-biomolecular Nanoassemblies of Cucurbit [7] uril with Bovine Serum Albumin: Drug Delivery and Sensor Applications”, N. Barooah, **Raman Khurana**, A. C. Bhasikuttan, J. Mohanty, *Isr. J. Chem.*, **2018**, 58 (3-4), 276-285
13. “Modulation of Protolytic Equilibrium of Bichromophoric Coumarin-30 Dye with Cucurbit [8] uril Encapsulation”, N. Barooah, **Raman Khurana**, A. C. Bhasikuttan, J. Mohanty, *Chem. Select.*, **2017**, 2, 7387-7393
14. “Sulfobutylether- β -Cyclodextrin for Inhibition and Rupture of Amyloid Fibrils”, M. N. Shinde,[#] **Raman Khurana**,[#] N. Barooah, A. C. Bhasikuttan, J. Mohanty, *J. Phys. Chem. C.*, **2017**, 121, 20057-20065.(# = Equal contribution)
15. “Metal Ion-induced Supramolecular pK_a Tuning and Fluorescence Regeneration of p-Sulfonatocalixarene Encapsulated Neutral Red Dye”, M. N. Shinde, **Raman Khurana**, N. Barooah, A. C. Bhasikuttan, J. Mohanty, *Org. Biomol. Chem.*, **2017**, 15, 3975-3985.

16. “Stimuli-responsive Cucurbit[7]uril-mediated BSA Nanoassembly for Uptake and Release of Doxorubicin”, N. Barooah, A. Kunwar, **Raman Khurana**, A. C. Bhasikuttan, J. Mohanty, *Chem. Asian J.*, **2017**, 12, 122–129.

Conferences

1. “Noncovalent interaction of acridine with cucurbiturils: Effect on photophysics and acidity constants”, **Raman Khurana**, N. Barooah, J. Mohanty TSRP-2016, BARC, Mumbai, India.

2. “Photophysical aspects of perylene diimide derivatives in preorganized and self-assembled systems in aqueous medium”, **Raman Khurana**, Shakkira E, J. Mohanty, A. C. Bhasikuttan, N. Barooah, NFCFA-2017, BITS Pilani, Goa, India.

3. “Stimuli-Responsive cucurbit[7]uril mediated BSA nanoassembly for uptake and release of doxorubicin”, **Raman Khurana**, N. Barooah, A. Kunwar, A. C. Bhasikuttan, J. Mohanty, NSRP-2017, Manipal University, Manipal, India.

4. “Metal ion-induced supramolecular pK_a tuning and fluorescence regeneration of *p*-sulfonatocalixarene encapsulated neutral red dye”, **Raman Khurana**, M. N. Shinde, N. Barooah, A. C. Bhasikuttan, J. Mohanty, CRSI NSC-21-2017, CSIR-IICT, Hyderabad, India. (**Best Poster Award**)

5. “Aggregation Induced Fluorescence of Thiazole Orange with Sulfobutylether- β -Cyclodextrin: Stimuli Responsive Modulation in the Photophysical Behavior”, **Raman Khurana**, N. Barooah, A. C. Bhasikuttan, J. Mohanty, TSRP-2018, BARC, Mumbai, India.

6. “Surpassing Hydrophobic Aggregation of Perylene Diimide Derivative through Supramolecular Host- Guest Interaction in Aqueous Medium”, **Raman Khurana**, J. Mohanty, N. Padma, A. C. Bhasikuttan, N. Barooah, TSRP-2018, BARC, Mumbai, India.

7. “Host–Guest Interaction of Rhodamine dyes with Sulfobutylether- β -Cyclodextrin: A Viable Approach for Supramolecular Aqueous Dye Laser”, **Raman Khurana**, S. Agarwalla, G. Sridhar, N. Barooah, A. C. Bhasikuttan, J. Mohanty, ISMSC-2018, **Quebec City, Canada**.

8. “Water Based Supramolecular Dye Laser: Ultra-Bright Sulfobutylether- β -Cyclodextrin Encapsulated Rhodamine Dyes”, **Raman Khurana**, S. Agarwalla, G. Sridhar, N. Barooah, A. C. Bhasikuttan, J. Mohanty, ICW-2018, Kottayam, Kerala, India.

9. "Supramolecular complexation of (N-methylpyridyl) Porphyrin with Sulfobutylether- β -cyclodextrin: Effective Photosensitizing Behavior", **Raman Khurana**, N. Barooah, A. C. Bhasikuttan, J. Mohanty, NSRP-2019, Visva-Bharati Santiniketan, West Bengal, India.

10. "Stimuli-Responsive Supramolecular Assemblies of Organic / Inorganic Guest through Macrocyclic Rceptor: Prospective Applications", **Raman Khurana**, J. Mohanty, NSRP-2019, Visva-Bharati Santiniketan, West Bengal, India (Oral Presentation)

11. "Supramolecular complexation of (N-methylpyridyl) Porphyrin with Sulfobutylether- β -cyclodextrin: Effective Photosensitizing Behavior", **Raman Khurana**, N. Barooah, A. C. Bhasikuttan, J. Mohanty, IIT Bombay Diamond Jubilee Chemistry Symposium. Mumbai, India. 2019.

12. "Supramolecular Complexation of (N-methylpyridyl) Porphyrin with Sulfobutylether- β -cyclodextrin: Effective Photosensitizing Behavior Laser", **Raman Khurana**, N. Barooah, A. C. Bhasikuttan, J. Mohanty, ISMSC-2019, Lecce, Italy.


Raman Khurana

Dedicated to.....

*my beloved
family*

ACKNOWLEDGEMENTS

Undertaking the responsibilities towards this PhD thesis has been a truly life-changing experience for me and it would not have been possible to do without the support and guidance that I received from many people.

*First and foremost, I would like to extend my sincere gratitude to my research guide **Dr. (Mrs.) Jyotirmayee Mohanty** for introducing me to this exciting field of science and for her dedicated help, advice, inspiration, encouragement and continuous support, throughout my Ph.D work. Her enthusiastic temperament, out of box thinking, integral view on research and her mission for providing high-quality work, has made a deep impression on me. The joy and enthusiasm she has for her research is contagious and motivational for me, even during tough times in the Ph.D. pursuit. I have learnt extensively from her, including how to raise new possibilities, how to regard an old question from a new perspective, how to approach a problem by systematic thinking and exploiting serendipity. Apart from excellent scientific carrier, she is also an honest and real human being. I have been inspired by her encouraging character and researcher too. Thank you very much mam for being a friend, philosopher and guide of mine.*

*I feel obliged and extend my heartfelt appreciation to **Dr. A.C. Bhasikuttan** who has been truly invaluable to me both at academic and personal level. I am indebted to him for always believing in me and sharing his excellent knowledge and scientific understanding with me. His constant guidance, cooperation, motivation and support have always encouraged me and kept me going ahead.*

*My special words of thanks should also go to **Dr. Nilotpāl Barooah** who patiently cleared all my queries and was available round the clock with his priceless suggestions. I owe a lot of gratitude to him for his technical help, fruitful scientific discussions and moral support offered to me from time to time throughout the course of the work. I thank him for guiding me not only in research but also in other facets of my life.*

*I greatly appreciate **Dr. D. B. Naik** for boosting up my confidence and for his knowledge sharing and valuable suggestions. I wish to express sincere thanks to **Dr. Sudhir Kapoor**, Director, Chemistry group and Head, RPCD and **Dr. A. K. Tyagi**, Head, Chemistry Division for constant support and all RPCD members for creating*

*such friendly, cooperative and competitive environment in the lab. I'm highly grateful to my doctoral committee **Dr. A. C. Bhasikuttan** (Chairman), **Dr. P. K. Mohapatra** (Member), **Dr. H. P. Upadhyaya** (Member), **Dr. V. Sudarsan** (Member) for their critical reviews and suggestions during the progress review and pre-synopsis seminar. I express my deep regards to my all co-authors **Dr. Amit Kunwar** for cytotoxicity and antitumor activity experiments, **Dr. N. Padma** for I-V characteristic experiments, **A. S. Kakatkar**, **Dr. S. Chatterjee** for antibacterial studies and also to **S. Agarwalla**, **G. Sridhar** for dye laser experiments. I am deeply grateful to **Dr. V. S. Tripathi**, **Pushpa**, **Dr. S. N. Achary** and **Dr. Girija** guiding me in the CV, SEM, XRD and AFM measurements.*

*I extend my sincere regards to **Dr. S. Dutta Choudhary**, **Dr. Apurav Guleria**, **Dr. Arunakumar Mora** and my senior **Dr. Meenakshi Shinde** for valuable suggestions and helping me during the initial days of my Ph.D work. A special thanks to my friends **Shaukat**, **Utpal**, **Tapas**, **Marinal**, **Rupali**, **Prachi**, **Vishwa**, **Avinash**, **Jayanta**, **Poojan**, **Santosh**, **Sarita**, **Harjeet**, **Navneet** and **Chanpreet** for sharing various cheerful moments. Life would have been extremely dull and monotonous without the pleasant and refreshing company of them.*

I owe my heartfelt gratitude and indebtedness to my parents, my brother and bhabhi and my sister. Their infallible love and support has always been my strength. Their patience and sacrifice will remain my inspiration throughout my life.

*Finally, I would like to thank my fiancée, **Rishu**, who has been my closest companion on this journey. Words fail me to express my appreciation for her whose love, care and persistent confidence in me has taken the load off my shoulder.*

CONTENTS

	Page No.
Synopsis	1-12
Abbreviations	13-14
List of Figures	15-26
List of Tables	27
CHAPTER 1: Introduction	28-56
1.1 Supramolecular Chemistry	29
1.2 Host-Guest Chemistry	32
1.3 Pre-Organized Macrocyclic Hosts	34
1.3.1 Cucurbit[n]urils	35
1.3.2 Cyclodextrins	37
1.4 Chromophoric Guest Molecules	39
1.5 Mechanistic Aspects of Host– Guest Binding	41
1.5.1 Molecular recognition properties	41
1.5.2 Hydrophobic effect and binding sites	43
1.6 Validation of the Host-Guest Interactions	44
1.6.1 Absorption and Fluorescence Studies	45
1.6.1.1 Lambert-Beer’s Law	45
1.6.1.2 Types of electronic transitions through exciting and deexciting pathways	46
1.6.2 Time-resolved Fluorescence Measurement	49
1.6.3 Isothermal Titration Calorimetry	49
1.6.4 ¹ H-NMR Measurement	50
1.7 Applications based on Host-Guest Chemistry	51
1.7.1 Water-based Supramolecular Dye Laser	51
1.7.2 Cucurbit[8]uril-Based Supramolecular Approach to Fabricate Tunable Luminescent Materials	52
1.7.3 Enhanced Supramolecular Photosensitizing Behavior	52
1.7.4 Enhanced Antibacterial Activity of Fluoroquinolone Drugs	53
1.7.5 Fluorescence Sensor for Metal Ions	53
1.7.6 Drug Delivery with Specific Target	54
1.8 Motivation and Objective of the Present Work	55

CHAPTER 2: Materials and Experimental Methods	57-78
2.1 Introduction	58
2.2 Ultraviolet-Visible (UV-vis) Absorption Spectroscopy	58
2.3 Steady State Fluorescence Spectroscopy	60
2.4 Time Resolved Fluorescence Spectroscopy	62
2.4.1 Basic Principles of TCSPC Technique	63
2.5 Circular Dichroism (CD) measurements	65
2.6 Isothermal Titration Calorimetric (ITC) Measurements	66
2.7 ¹ H-NMR Spectroscopic Measurements	68
2.8 Scanning Electron Microscopy (SEM)	68
2.9 Fluorescence Microscopy (FM)	69
2.10 Atomic Force Microscopy (AFM)	69
2.11 Dynamic Light Scattering (DLS)	69
2.12 Synthesis of N,N'-bis-(L/D)-phenylalanyl perylenebisimide (L/D-Phe-PDI)	69
2.13 Synthesis of N, N'-bis-2-(2-aminoethyl)benzimidazolyl naphthalene dimide (NDI-BzIm)	70
2.14 Experimental Method	72
2.14.1 Evaluation of binding constant for 1:1 complex	72
2.14.2 Evaluation of binding constant for 1:2 complex	73
2.14.3 Hydrodynamic volume calculation from anisotropy measurements	74
2.14.4 Cellular uptake studies	74
2.14.5 Thin film deposition and I-V measurements	75
2.14.6 Broad-band dye laser experiments	75
2.14.7 Narrow-band dye laser experiments	75
2.14.8 Photostability measurement of Rhodamine dyes	76
2.14.9 Photostability measurements of TMPyP dye	76
2.14.10 Singlet oxygen (¹ O ₂) generation measurements	77
2.14.11 Antibacterial activity measurements	77
2.13.12 Photosensitization activity in tumor cells	78
CHAPTER 3: Host–Guest Interaction of Acridine dye with Cucurbiturils: Stimuli Responsive pK_a Tuning and Guest Relocation into Live Cells	79-104

3.1 Introduction	80
3.2 Materials and Methods	82
3.3 Results and Discussion	83
3.3.1 Absorption Spectral Characteristics of Acridine Dye in the Presence of Cucurbiturils	83
3.3.2 Steady-state Fluorescence Characteristics of Acridine Dye in the Presence of Cucurbiturils	86
3.3.3 ¹ H NMR Studies of the Complexes	93
3.3.4 Effect of Inclusion Complex Formation on the Acidity Constant of Acridine Dye	94
3.3.5 Geometry Optimization of the Complexes	96
3.3.6 Stimuli-Responsive Fluorescence Regeneration and pK _a tuning of the Cucurbituril-Acridine Complexes	97
3.4 Conclusions	103
CHAPTER 4: Supramolecular Interaction of Aromatic Diimides with Macrocyclic Hosts: Applications in Organic Electronics	105-148
4.1 Introduction	106
Part-1: Generation of Stable and Emissive Radical Anion from Naphthalenediimide Derivative in the Presence of Cucurbiturils	107-124
4.1.1 Introduction	108
4.1.2 Materials and Methods	109
4.1.3 Results and Discussion	109
4.1.3.1 ¹ H-NMR Measurements	110
4.1.3.2 Absorption and Steady-State Fluorescence Measurements	111
4.1.3.3 Isothermal Titration Calorimetric Measurements	115
4.1.3.4 SEM and FM Measurements	116
4.1.3.5 Absorption Behavior of NDI-BzIm Radical	117
4.1.3.6 Fluorescence Emission and Lifetime Measurements	120
4.1.4. Conclusions	123
Part-2: Deaggregation of Perylenediimide Derivative through Supramolecular Host-Guest Approach: Negative differential resistance (NDR) behavior	125-148
4.2.1 Introduction	126
4.2.2 Materials and Methods	128

4.2.3 Results and Discussion	128
4.2.3.1 Ground-State Absorption and Emission Measurements	129
4.2.3.2 Circular Dichroism (CD) Measurements	132
4.2.3.3 Fluorescence Lifetime and Anisotropy Measurements	135
4.2.3.4 ¹ H-NMR Measurements	137
4.2.3.5 SEM, AFM and FM Measurements	138
4.2.3.6 I-V Characteristics and Negative Differential Resistance (NDR) Behavior	141
4.2.4 Conclusions	147
CHAPTER 5: Supramolecular Interaction of Rhodamines and Thiazole Orange with Sulfobutylether-β-cyclodextrin: Applications in Aqueous Dye Laser and Fluorescence Sensor	149-190
Part-1: Host–Guest Interaction of Rhodamine Dyes with Sulfobutylether-β-cyclodextrin: A Viable Approach for Supramolecular Aqueous Dye Laser	150-168
5.1.1 Introduction	151
5.1.2 Materials and Methods	152
5.1.3 Results and Discussion	153
5.1.3.1 Absorption and Fluorescence Properties of Rhodamine dyes with SBE ₇ β CD	153
5.1.3.2 Isothermal Titration Calorimetric (ITC) Study	158
5.1.3.3 Deaggregation of Rhodamine Dyes with SBE ₇ β CD	160
5.1.3.4. Broad-band and Narrow-band Lasing Behaviour of Rhodamine Dyes in presence of SBE ₇ β CD	162
5.1.3.5 Photostability of Rhodamine Dyes with SBE ₇ β CD	166
5.1.4. Conclusions	167
Part-2: Supramolecularly Enhanced Emission of Thiazole Orange with Sulfobutylether-β-cyclodextrin: On/Off fluorescence Sensor for Tyramine neurotransmitter	169-190
5.2.1 Introduction	170
5.2.2 Materials and Methods	172
5.2.3 Results and Discussion	173
5.2.3.1 Absorption Spectral Characteristics of Thiazole Orange with SBE ₇ β CD	173
5.2.3.2 Fluorescence Spectral Characteristics of Thiazole	175

Orange with SBE ₇ βCD	
5.2.3.3 Time-Resolved Fluorescence and Anisotropy studies of Thiazole Orange with SBE ₇ βCD	176
5.2.3.4 ¹ H NMR Studies of Thiazole Orange with SBE ₇ βCD	178
5.2.3.5 Isothermal Titration Calorimetric (ITC) Measurements of Thiazole Orange with SBE ₇ βCD	180
5.2.3.6 Circular Dichroism (CD) Studies of Thiazole Orange with SBE ₇ βCD	181
5.2.3.7 Stimuli-Responsive Fluorescence on-off Mechanism of SBE ₇ βCD:TO Assembly	182
5.2.4 Conclusions	189
CHAPTER 6: Supramolecular Photosensitizer of (N-methyl pyridyl) Porphyrin with Captisol: Enhanced Antibacterial and Antitumor Activities	191-213
6.1 Introduction	192
6.2 Material and Methods	194
6.3 Results and Discussion	195
6.3.1 Absorption and Emission Behavior of TMPyP with Captisol	195
6.3.2 ¹ H NMR Measurements	198
6.3.3 Isothermal Titration Calorimetric Measurement	199
6.3.4 Dynamic Light Scattering (DLS) Measurements	200
6.3.5 SEM and FM Measurements	201
6.3.6 Photostability and Singlet Oxygen Generation Measurements	203
6.3.7 Photosensitized Antibacterial and Antitumor Activities	207
6.4 Conclusions	212
CHAPTER 7: Conclusions and Future Perspectives	214-220
7.1 Summary	215
7.2 Future perspective	219
REFERENCES	221-231

SYNOPSIS

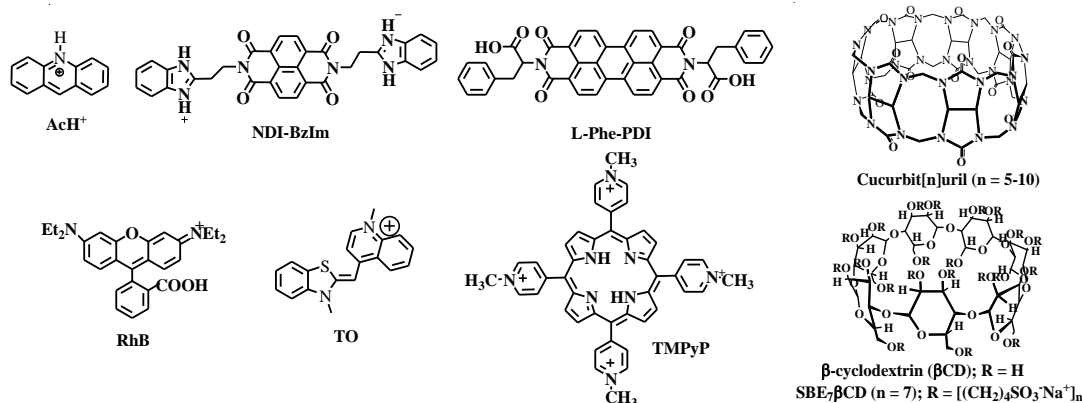
In the past decades, scientists have made enormous advances in creating nanoscale assemblies and structures with the aim to achieve applications ranging from targeted drug delivery to the development of functional materials.¹ One of the many different strategies for making synthetic functional materials takes advantage of self-assembly, the method by which well-ordered structural patterns are formed spontaneously from self-directed organization of the individual components through noncovalent interactions.² In conceiving the same, chemists have often relied upon molecular recognition-guided supramolecular interactions, which allow rational control of the ensuing non-covalent interactions and their cooperativity, as a very powerful construction principle for novel hierarchically ordered molecular assemblies with unprecedented physicochemical properties.³ Many attempts have been made over the last few decades to realize such non-covalently linked host–guest complexes using classical synthetic macrocyclic host molecules like cyclodextrins, calixarenes, cucurbiturils etc. The noncovalent interactions, which encompasses electrostatic interactions like dipole–dipole, ion–dipole, hydrogen bonding interactions and hydrophobic interactions like van der Waals, π – π interactions, dispersion interactions, stabilizes the host-guest complex in its optimum stoichiometric composition and structural geometry, which in turn brings out novel features apart from their individual molecular properties. Such host-guest complexes/assemblies have attracted immense research interest due to their tremendous potential in many applied areas, especially in constructing functional materials, fluorescence sensors, on-off switches, controlled cellular uptake and release for drug delivery, etc.^{4–6} Since the binding interactions are non-covalent in nature, different external stimuli like competitive binders, pH,

temperature, light, etc. are used to obtain stimuli responsive control/tuning of the molecular properties of the complex.

This thesis describes the construction of few such supramolecular assemblies between the selective chromophoric dyes as guest molecules with specific macrocyclic hosts and its characterization by different spectroscopic methods such as UV-visible and fluorescence spectroscopy, isothermal titration calorimetry (ITC), circular dichroism (CD), atomic force microscopy (AFM), scanning electron microscopy (SEM) and ^1H NMR spectroscopy. Different types of chromophoric guest molecules such as acridine, rhodamines, thiazole orange, porphyrin and aromatic diimides have been employed against suitable macrocyclic hosts in realizing their tunable/stimuli responsive applications. The thesis also presents their promising applications in drug delivery, photodynamic therapy, organic electronics, aqueous dye laser, protein fibril inhibitor and fluorescence sensor, etc.^{5, 6}

Two classes of macrocyclic hosts have been used. One, the Cucurbit[*n*]uril (CBn), a relatively new class of macrocycles, comprises of glycoluril monomers joined by pairs of methylene bridges and depending upon the number of glycoluril units of these host molecules, homologues of different cavity sizes and portal dimensions are known.⁷ The pumpkin-shaped CBn is having highly symmetrical structure with two identical carbonyl portals and a hydrophobic cavity which can accommodate the organic guest molecules partly or completely to form stable inclusion complexes. The hydrophobic interior offers a credible inclusion site for nonpolar molecules, the portals containing polar carbonyl groups allow the binding of cations and molecules through ion-dipole, charge-dipole and H-bonding interactions and the peripheral electron deficient carbon centers show interaction towards poly

anions. In this research work, cucurbit[7]uril (CB7) and cucurbit[8]uril (CB8) are used to study their interaction with naphthalenediimide derivatives, which stabilized the anion radical generated on light irradiation.



Chemical structures of guest dyes and macrocyclic hosts

The other macrocyclic host, β -cyclodextrin (β CD) and its derivative sulfobutylether- β -cyclodextrin (SBE₇ β CD, commercially known as captisol) are used to investigate their interactions with perylenediimide derivative, rhodamines, thiazole orange and porphyrins. CDs are composed of cyclic oligomers composed of 6, 7 and 8 α -D-glucose units respectively for α , β or γ and represents one of the most extensively studied macromolecular host system for binding of organic fluorophores. CDs possess a hydrophobic inner cavity as well as a primary and secondary hydroxyl group rim, which provides additional hydrogen bonding motifs for the binding of organic guests. Structurally, SBE₇ β CD, a chemically modified β -CD macrocycle, i.e. a cyclic hydrophilic oligosaccharide, where four secondary alcoholic groups in the wider rim and three alternate primary alcoholic groups in the narrow rim of β -CD have been

substituted by sulfobutylether chains and have been used to enhance and stability of drugs through encapsulation.

Chapter 1: Introduction

This chapter describes the fundamentals of supramolecular chemistry of host-guest interactions, the types of noncovalent interactions, binding mechanism between the host and guest to form supramolecular assemblies, stoichiometry and their applications in different areas. Since the chromophoric dyes are used as guest molecules, the modulation in the photophysical properties such as absorption, emission behavior upon complexation with macrocyclic hosts and their characterization have been explained in this chapter. Since the supramolecular assemblies are held together by comparatively weak non-covalent interactions, the preferential affinity of these forces and the stoichiometric arrangements of the complexes bring out significant modulation in the physico-chemical properties of the guests. The stimuli-responsive tuning in the photophysical properties of the supramolecular assemblies and their promising applications in drug delivery and optical sensor have been briefly explained in this chapter. The chapter also gives a glimpse of the projected application of the demonstrated complexes in the field of lasing behavior of rhodamines in aqueous medium, negative differential resistance behavior of perylenediimide derivatives, enhanced photosensitizing behavior of porphyrins, anion radical emission from naphthalenediimide derivative and aggregation induced emission of thiazole orange complex etc.

Chapter 2: Materials and Experimental Methods

Apart from the details of the materials used in the reported studies, this chapter also describes the details of experimental techniques and methods, used for the

characterization of the host-guest complexes are described. The details of UV-vis absorption and steady-state fluorescence spectrophotometers, time-resolved fluorescence spectrometer which works on the principle of time-correlated single photon counting, circular dichroism (CD) and ^1H - nuclear magnetic resonance (^1H -NMR) used for primary characterization of host-guest complexes have been discussed. A brief description of isothermal titration calorimetry (ITC) technique used to find the thermodynamic parameters and stoichiometry of the host-guest complexes has been discussed. Further the basic principles of operation along with outline of all the instruments like fluorescence microscope (FM), Scanning electron microscope (SEM) and dynamic light scattering (DLS) used to find out the pattern and size of supramolecular assemblies have been elaborated. Synthetic procedure of the N, N'-bis-(L/D)-phenylalanyl-PDI derivative and N, N'-bis-2-(2-aminoethyl)benzimidazolyl naphthalenedimide and different methods such as photo-cytotoxicity assay for cell viability study, anti-bacterial activity under white light irradiation and aqueous dye laser experiments have been explained in this chapter.

Chapter 3: Host–Guest Interaction of Acridine dye with Cucurbiturils: Stimuli Responsive pK_a Tuning and Guest Relocation into Live Cells

Chapter 3 deals with the investigation of the noncovalent host-guest interactions of the cationic (AcH^+) and neutral (Ac) forms of the acridine dye with the macrocyclic hosts such as cucurbit[7]uril (CB7) and cucurbit[8]uril (CB8) and the effect of cavity size on the photophysical properties and the protolytic equilibrium of acridine dye. The cationic form undergoes significant complexation with CB7 ($K_{\text{eq}} = 10^6 \text{ M}^{-1}$), causing a sharp decrease in the fluorescence intensity, whereas, the neutral Ac form of the dye undergoes weak complexation with CB7 ($K_{\text{eq}} = 10^3 \text{ M}^{-1}$). On the other hand, AcH^+

form shows strong emission quenching on interaction with CB8. Both the forms form 1:1 complex with CB7 and the cationic form undergoes 1:2 CB8:AcH⁺ complex formation and has been confirmed from Job plot. The strong affinity of CB7 and CB8 to the protonated form resulted in a large upward pK_a shift ($\Delta pK_a \sim 3.6$ units for CB7 and ~ 1.3 units for CB8) in the dye. Taking advantage of the above modulations in the fluorescence and pK_a values, adamantylamine-induced fluorescence regeneration, controlled pK_a tuning and dye relocation from the CB7 cavity to live cell lines have been established in this research work, which find potential applications in fluorescence *off-on* sensor and drug delivery.

Chapter 4: Supramolecular Interaction of Aromatic Diimides with Macrocyclic Hosts: Applications in Organic Electronics

Organic radical anions are important intermediates in various natural and artificial electron transfer processes. Radical anions derived from aromatic diimides play an important role due to their stability and ease of generation. Extensive studies in the line of host-guest interaction have been carried out and the Chapter 4 has been organized to include the detailed characterization of host-guest interaction of two diimide derivatives and are discussed as Part 1 and Part 2.

Part-1: Generation of stable and emissive radical anion from naphthalenediimide derivative in the presence of cucurbiturils

Among various aromatic diimides the 1,4,5,8- Naphthalenetetracarboxylic acid diimide (NDI)-derivatives have been extensively explored as a building block for the generation of various supramolecularly assembled systems, both in organic and aqueous media due to their propensity for π -stacking, electron-accepting nature and easy structural manipulations. In this study, the synthesis of N, N'-bis-2-(2-aminoethyl)benzimidazolyl naphthalenediimide (NDI-BzIm) compound has been

established. The formation of stable and emissive NDI radical anion of ethyl benzimidazole appended NDI derivative (NDI-BzIm) through contrasting encapsulation behavior of CB7 and CB8 under light irradiation in aqueous environment at ambient condition has been described in this chapter. The generation of emissive radical anion will broaden the scope of NDI radical anion chemistry for potential application in fluorescence spectroscopy and optoelectronic applications.

Part-2: Deaggregation of perylenediimide derivative through supramolecular host-guest approach: Negative differential resistance (NDR) behavior

Deaggregated perylenediimide (PDI) derivatives exhibit exceptionally high emission quantum yield, high photostability and appropriate molecular features required for organic electronics and photovoltaic devices. In this study, a metal-dye-metal constructed large and stable negative differential resistance (NDR) behavior at ambient conditions using a facile supramolecular strategy by surpassing the strong hydrophobic association of N, N'-bis-(L/D)-phenylalanyl-PDI derivatives, ((L/D)-Phe-PDI) and allowing them in their deaggregated form have been discussed. The host-guest interaction of (L/D)-Phe-PDI dyes by the β -CD macrocyclic host resulted in a dramatic enhancement in the emission yield of the PDI derivative in aqueous medium (from 0.28 to 0.90). In the thin film deposits, the monomeric β -CD/(L/D)-Phe-PDI complex displayed well connected sheet like morphology, whereas the uncomplexed (L/D)-Phe-PDI dye remained as scattered lumps. The large and reversible *I-V* characteristics displaying strong NDR behavior is attributed to the oxidation/reduction processes involving the rigid π rich monomeric PDI core and is established stable at least for about six months when stored at ambient conditions, a promising system for organic electronics and photovoltaic applications.

Chapter 5: Supramolecular Interaction of Rhodamines and Thiazole Orange with Sulfobutylether- β -cyclodextrin: Applications in Aqueous Dye Laser and Fluorescence Sensor

Part-1: Host–guest interaction of rhodamine dyes with sulfobutylether- β -cyclodextrin: A viable approach for supramolecular aqueous dye laser

Aqueous dye lasers, though much sought after, could not be of practical use as the laser dyes, in general, tend to strongly aggregate in water thereby severely diminishing the optical output. The supramolecular strategy of stabilizing the dyes in their fluorescent monomeric form and bringing out dramatic enhancement of emission yield in aqueous medium has been applied in this study. The noncovalent interactions of two prominent laser dyes, namely, rhodamine 6G (Rh6G) and rhodamine B (RhB) with a water soluble macrocyclic host, sulfobutylether- β -cyclodextrin (SBE $_7\beta$ CD) have been discussed. Changes in the absorption and fluorescence behaviour of the dye in presence of SBE $_7\beta$ CD host clearly indicated adequate complex formation between the dye and the host molecule ($K \sim 10^4 \text{ M}^{-1}$). Job plot, fluorescence lifetime/anisotropy measurements and the thermodynamic parameters from ITC measurements adjudicated a 1:1 stoichiometric complex formation as the major mode of interaction between dye and the SBE $_7\beta$ CD host. Consequently, SBE $_7\beta$ CD prevents the dye aggregation/adsorption and present the rhodamine dyes in their monomeric forms with enhanced fluorescence yield and brightness. These vital parameters are utilized to optimize and demonstrate a cost-effective supramolecular broad-band as well as narrow-band aqueous dye laser systems with improved lasing efficiencies, better beam profile and enhanced durability as compared to the presently available non-aqueous dye lasers and have been discussed in this chapter.

Part-2: Supramolecularly Enhanced Emission of thiazole orange with sulfobutylether- β -cyclodextrin: On/off fluorescence sensor for tyramine neurotransmitter

In this chapter, the investigation of noncovalent supramolecular interactions of thiazole orange (TO) with sulfobutylether- β -cyclodextrin (SBE₇ β CD) macrocycle and the effect of concentration of SBE₇ β CD on the assembly formation of TO and its photophysical properties have been described. At 1:1 equivalent concentration, four molecules of TO get assembled at the portals of SBE₇ β CD and further addition of SBE₇ β CD leads to the formation of 1:1 SBE₇ β CD:TO complex and are characterized by absorption, fluorescence and circular dichroism measurements. The observation of aggregation induced emission (AIE) from 1:4 SBE₇ β CD:TO assembly and the tuning of AIE behavior by applying external stimuli to construct *on-off* fluorescence sensor to detect tyramine, a blood pressure regulating neurotransmitter, with LOD 575 nM and to design optical supramolecular thermometer in the ambient temperature range have been discussed.

Chapter 6: Supramolecular Photosensitizer of (N-methylpyridyl) Porphyrin with Captisol: Enhanced Antibacterial and Antitumor Activities

Porphyrins, especially the 5,10,15,20-tetrakis(4-*N*-methylpyridyl) porphyrin (TMPyP), are well accepted as photosensitizers due to strong absorption from visible to near-infrared region, good singlet oxygen quantum yields as well as chemical versatility,⁴ all of which can be further modulated through planned supramolecular strategies. In this chapter, the construction of supramolecular nanorods of TMPyP dye/drug with captisol (sulfobutylether- β -cyclodextrin, (SBE₇ β CD)) macrocycle through host-guest interaction has been explained. The availability of four cationic *N*-methylpyridyl groups favors multiple binding interactions with the captisol host, building an

extended supramolecular assembly of captisol and TMPyP. In addition to the spectroscopic characterizations for the assembly formation, the same has been pictured in SEM and FM images as nanorods of $\sim 10\ \mu\text{m}$ in length or more. Complexation of TMPyP has brought out beneficial features over the uncomplexed TMPyP dye; enhanced singlet oxygen yield, improved photostability and better photosensitizing effect, all supportive of efficient photodynamic therapy activity and have been discussed in this chapter. The Captisol:TMPyP complex displayed enhanced antibacterial activity towards *E. coli* under white light irradiation as compared to TMPyP alone. Cell viability studies performed in lung carcinoma A549 cells with light irradiation documented increased cytotoxicity of the complex towards the cancer cells whereas reduced dark toxicity is observed towards normal CHO cells. All these synergistic effects of supramolecular nanorods of Captisol-TMPyP complex make the system an effective photosensitizer and a superior antibacterial and antitumor agent.

Chapter 7: Conclusions and Future Perspectives

This concluding chapter describes the overall summary of this thesis work with future perspectives to utilize this work on practical applications. The present thesis work reveals that stimuli-responsive supramolecular assemblies constructed by host-guest approach and its use in wide range of practical applications. Supramolecular tuning in the pK_a value using macrocyclic hosts and our studies with CHO cell lines rightly established a controlled relocation of acridine (the neutral form) into the cell lines by AD as the stimulant. In future, it would be appropriate to work on the complexes of active drug molecules of similar structural features incorporated in relevant cell lines to enhance the desired effect. In chapter 4, for the first time, we demonstrate a *metal-*

dye-metal constructed intense and stable negative differential resistance (NDR) behavior at ambient conditions and generation and stabilization of emissive NDI radical anion in presence of CB7 and CB8 hosts in aqueous medium. The long fluorescence lifetime of these NDI radical anions stabilized by macrocyclic hosts may be useful in lifetime imaging studies which employ NDI based compounds for photodynamic therapy. This fascinating chemistry of encapsulated radical ions of the diimide derivative may fetch utility in developing controlled NDR effect in organic electronics and hence the more studies on varied derivatization in improving the NDR feature may be taken up and the same may be studied for their photovoltaic activity as well. We also presented a methodology for achieving ultra-bright Rhodamines in water and its applicability has been proven in a practical laser system and several such laser dyes of different tuning region need to be examined in future, with different hosts as well. The claim of selective *on-off* fluorescence sensor for the detection of tyramine against other neurotransmitters with LOD ~575 nM (79 ppb) is quite promising and expect its continued study for improving the LOD in a varied mixture of other amines and real biological samples. On the otherhand supramolecular assembly of TMPyP dye/drug with captisol macrocycle increased singlet state yield and lifetime, enhanced singlet oxygen yield, improved photostability and overall, much better photosensitizing effect. Utilizing the improved features of TMPyP-captisol complex in its biological stride of A549 cells and *E. coli*, more studies are pending to ascertain its utility in a selective manner towards other pathogens and selective malignant cells.

References:

1. J.-M. Lehn, *Science*, **1985**, 227, 849–856.
2. M. J. Frampson, H. L. Anderson, *Angew. Chem., Int. Ed.*, **2007**, 46, 1028–1064.
3. Y. H. Ko, E. Kim, I. Hwang, K. Kim, *Chem. Commun.*, 2007, 1305–1315.
4. P. Cosma, L. Catucci, P. Fini, P. L. Dentuto, A. Agostiano, N. Angelini, L. M. Scolaro, *Photochem. Photobiol.* **2006**, 82, 563–569.
5. R. Khurana, S. Agarwalla, G. Sridhar, N. Barooah, A. C. Bhasikuttan, J. Mohanty, *ChemPhysChem*, 19, **2018**, 2349–2356
6. M. N. Shinde, R. Khurana, N. Barooah, A. C. Bhasikuttan, J. Mohanty, *J. Phys. Chem. C*, **2017**, 121, 20057–20065.
7. J. W. Lee, S. Samal, N. Salvapalam, H.-J. Kim, K. Kim, *Acc. Chem. Res.*, **2003**, 36, 621–630.
8. R. N. Dsouza, U. Pischel, W. M. Nau, *Chem. Rev.*, **2011**, 111, 7941–7980.

LIST OF ABBREVIATIONS

CDs	Cyclodextrins
BSA:	Bovine serum albumin
CBn (n = 5-14)	Cucurbit[n]uril
CXs	Calixarenes
SBE ₇ βCD	Sulfobutylether-β-cyclodextrin
ArOH	Phenol
PAHs	Polycyclic aromatic hydrocarbons
UV-vis	Ultraviolet–visible
ITC	Isothermal titration calorimetry
CD	Circular Dichroism
¹ H-NMR	Proton nuclear magnetic resonance
SEM	Scanning electron microscopy
FM	Fluorescence microscopy
KR	Kiton red
Rh-B	Rhodamine-B
Rh-6G	Rhodamine-6G
Por	Porphyrin
tQ[14]	twisted cucurbit[14]uril
TO	Thiazole orange
DOX	Doxorubicin
DOFL	Danofloxacin
NRFL	Norfloxacin
OFL	Ofloxacin
MIC	Minimum inhibitory concentration
CPC	Cetylpyridinium chloride
DLS	Dynamic light scattering
TCSPC	Time-correlated-single-photon-counting
CFD	Constant Fraction Discriminator
TAC	Time to Amplitude Converter
MCA	Multichannel Analyzer

IRF	Instrument response function
AFM	Atomic Force Microscopy
NDI-BzIm	N, N'-bis[2-(2-aminoethyl)benzimidazolyl] naphthalene dimide
L/D-Phe-PDI	N,N'-bis-(L/D)-phenylalanyl perylenebisimide
DMF	Dimethylformamide
CHO	Chinese hamster ovary
PBS	Phosphate buffered saline
Ac	Acridine
AD	Adamantylamine
EPR	Electron paramagnetic resonance
XRD	X-Ray Diffraction
NDR	Negative Differential Resistance
PVR	Peak to valley ratio
CV	Cyclic Voltammetry
FCS	Fluorescence correlation spectroscopy
OD	Optical Density
AIE	Aggregation induced emission
Tyr	Tyramine
ICD	Induced circular dichroism
LOD	Limit of detection
PDT	Photodynamic therapy
TMPyP	5,10,15,20-tetrakis(4- <i>N</i> -methylpyridyl)porphyrin
DPBF	1,3-diphenylisobenzofuran
E. coli	Escherichia coli

List of Figures

Figure 1.1: Schematic representation of conversion from molecule to supramolecular chemistry, molecule to supramolecule and supramolecular devices.

Figure 1.2: Different types of applications of supramolecular host-guest chemistry

Figure 1.3: Typical shapes of the cucurbituril host are shown for easy visualization and molecular structures of CB7 and CB8 hosts.

Figure 1.4: Chemical structures of α -CD, β -CD and γ -CD hosts.

Figure 1.5: Chemical structure of cyclodextrin and typical shapes of the β -CD and SBE₇ β CD host are shown for easy visualization.

Figure 1.6: Chemical structures of the selective guest molecules used in the research work.

Figure 1.7: Specific interaction sites of cucurbituril and cyclodextrin hosts which participate in host-guest interaction.

Figure 1.8: Schematic representation of the different photoprocesses that an excited molecule can participate.

Figure 1.9: The Jablonski diagram, showing different photophysical processes undergo by an electronically excited molecule. Straight arrows and dash arrows represent the radiative and non-radiative processes, respectively. Abbreviations are: IC-Internal Conversion; ISC-Intersystem Crossing; RISC-Reverse ISC; VR-Vibrational Relaxation; Fl-Fluorescence; Ph-Phosphoresence; S_i-ith singlet state and T_i-ith triplet state.

Figure 2.1: Schematic diagram of a double beam UV-vis Absorption spectrophotometer

Figure 2.2: Schematic diagram of a steady-state fluorescence spectrometer.

Figure 2.3: Schematic diagram of a time-correlated-single-photon-counting (TCSPC) spectrometer.

Figure 2.4: Schematic diagram of a circular dichroism spectrophotometer.

Figure 2.5: Schematic diagram of a Isothermal Titration Calorimetric (ITC) microcalorimeter

Figure 2.6: Synthetic route of L/D-Phe-PDI dye

Figure 2.7: Synthetic route of NDI-BzIm dye

Figure 3.1: Chemical structures of protonated (AcH^+) and neutral (Ac) forms of acridine dye.

Figure 3.2: Absorption spectra of acridine ($2.45 \times 10^{-6} \text{ M}$) in water at different pHs: (1) 2.6, (2) 4.0, (3) 4.5, (4) 5.0, (5) 5.6, (6) 6.1, (7) 7.0, (8) 8.1 and (9) 9.1. Inset: variation in absorbance with pH at 354 nm.

Figure 3.3: Absorption spectra of AcH^+ ($5.7 \times 10^{-6} \text{ M}$) in aqueous solution at different concentrations of CB7 (A) and CB8 (B) at pH 3.5. $[\text{CB7}]/\mu\text{M}$: (1) 0, (2) 2, (3) 4, (4) 6, (5) 10, (6) 20, (7) 80 and (8) 150. $[\text{CB8}]/\mu\text{M}$: (1) 0.0, (2) 0.9, (3) 2.2, (4) 4.4, (5) 6.6, (6) 8.8, (7) 13.2, (8) 26.4 and (9) 53.0. Insets show the Job plots for the respective systems, OD changes monitored at 353 nm.

Figure 3.4: Concentration dependent normalized absorption spectra of acridine dye at pH ~ 3.5 .

Figure 3.5: Absorption spectra of Ac ($4.5 \times 10^{-6} \text{ M}$) in aqueous solution at different CB7 concentrations at pH 11. $[\text{CB7}]/\mu\text{M}$: (1) 0, (2) 5, (3) 20, (4) 77, (5) 113, (6) 157 and (7) 206.

Figure 3.6: (A) Fluorescence spectra of AcH^+ ($5.7 \times 10^{-6} \text{ M}$) in aqueous solution at different concentrations of CB7 at pH 3.5. $[\text{CB7}]/\mu\text{M}$: (1) 0, (2) 2, (3) 4, (4) 6, (5) 10, (6) 20, (7) 80 and (8) 150. Insets show the changes in the fluorescence intensity (ΔI_f) versus $[\text{CB7}]$ of the respective complex systems. (B) Fluorescence spectra of Ac ($4.5 \times 10^{-6} \text{ M}$) in aqueous solution at different CB7 concentrations at pH 11. $[\text{CB7}]/\text{mM}$: (1) 0.0, (2) 0.02, (3) 0.04, (4) 0.11, (5) 0.16, (6) 0.21, (7) 0.46, (8) 0.90 and (9) 1.35.

Figure 3.7: Fluorescence spectra of AcH^+ ($5.7 \times 10^{-6} \text{ M}$) in aqueous solution at different concentrations of CB8 at pH 3.5. $[\text{CB8}]/\mu\text{M}$: (1) 0.0, (2) 0.9, (3) 2.2, (4) 4.4, (5) 6.6, (6) 8.8, (7) 11.0, (8) 20, (9) 53.0 and (10) 66.0. Insets show the changes in the fluorescence intensity (ΔI_f) versus $[\text{CB8}]$ of the respective complex systems.

Figure 3.8: (A) ITC isotherm for titration of AcH^+ with CB7 in water at 25°C . (B) ITC isotherm for titration of CB8 with AcH^+ in water at 25°C .

Figure 3.9: Decay traces of AcH^+ in solutions at pH ~ 3.5 in the absence (1) and presence (2) of $250 \mu\text{M}$ CB7 (A) and $70 \mu\text{M}$ CB8 (B). 'L' represents excitation lamp profile. $\lambda_{\text{ex}} = 374 \text{ nm}$.

Figure 3.10: ^1H NMR spectra (500 MHz) of $\sim 100 \mu\text{M}$ acridine dye in the absence (a) and in the presence (b) of 1 mM CB7 and (c) $80 \mu\text{M}$ CB8 in D_2O at pD 4.5. Inset: Pictorial representation of ACH^+ .

Figure 3.11: (A) Absorption spectra of acridine (5.1×10^{-6} M) in water containing ~ 200 μ M CB7 at different pHs: (1) 4.3, (2) 6.2, (3) 7.6, (4) 8.0, (5) 8.4, (6) 8.9, (7) 9.5, (8) 9.9, (9) 10.3 and (10) 11.3. (B) Absorption spectra of acridine (5.0×10^{-6} M) in water containing ~ 22 μ M CB8 at different pHs: (1) 4.2, (2) 5.0, (3) 5.5, (4) 6.0, (5) 6.6, (6) 7.1, (7) 7.7 and (8) 8.5.

Figure 3.12: The variation in the absorbance of acridine at 353 nm with pH in the absence (a) and in the presence of 22 μ M CB8 (b) and 200 μ M CB7 (c).

Figure 3.13: Front view of the optimized geometry of the 1:1 CB7:AcH⁺ (a) and 1:2 CB8:AcH⁺ (b) complexes.

Figure 3.14: (A) Fluorescence spectra of AcH⁺ (~ 6.1 μ M) (1) in the absence of CB7 and (2-7) in the presence of CB7 (30 μ M) with [AD] / μ M: (2) 0.0, (3) 3.5, (4) 11.0, (5) 12.5, (6) 15.0, and (7) 20.0. (B) Fluorescence spectra of AcH⁺ (~ 6.9 μ M): (1) in the absence of CB8 and (2-7) in the presence of CB8 (22 μ M) with [AD] / μ M: (2) 0.0, (3) 5.0, (4) 6.5, (5) 7.5, (6) 8.0, and (7) 9.0. Insets show the corresponding absorption spectra.

Figure 3.15: Fluorescence spectra of CB7:AcH⁺ complex (A) and CB8:AcH⁺ complex (B) with increasing temperature. T/ °C: (1) 20, (2) 30, (3) 40, (4) 50, (5) 60, (6) 70 and (8) 80.

Figure 3.16: (A) pH Titration of the absorbance ($\lambda_{mon} = 400$ nm) of acridine (~ 6.5 μ M), (1) in the absence of CB7 and AD and (2-5) in the presence of CB7 (200 μ M) with [AD] / μ M: (2) 100, (3) 70, (4) 42 and (5) 0.0 (B) pH Titration of the absorbance ($\lambda_{mon} = 400$ nm) of acridine (~ 6.3 μ M), (1) in the absence of CB8 and AD and (2-3) in the presence of CB8 (22 μ M) with [AD]/ μ M: (2) 13 and (3) 0.0

Figure 3.17: Fluorescence spectra of acridine in different environments at pH 7.4: (1) acridine dye, (2) CB7, (3) CB7-AD in CHO cell lines. Inset shows the fluorescence spectra of the treated cell lines after washing with PBS buffer in the respective conditions.

Figure 3.18: Fluorescence microscopic images recorded from CHO cell lines at pH 7.4 after treating them with uncomplexed acridine dye (10 μ M) (a); acridine dye (10 μ M)-CB7 (1 mM) (b); and acridine dye-CB7 (1 mM)-AD (100 μ M) (c).

Figure 3.19: Schematic representation of the adamantylamine-induced dye relocation from the CB7 cavity to the live cells.

Figure 4.1: Chemical structures of protonated form of N, N'-bis-2-(2-aminoethyl)benzimidazolyl naphthalene dimide (NDI-BzIm) dye.

Figure 4.2: ^1H -NMR spectra NDI-BzIm (50 μM , in D_2O at pD -3.5) free (A), with 2.5eq. of CB7 (B) and 2 eq. of CB8 (C).

Figure 4.3: Absorption (A and C) and Emission (B and D) spectra of NDI-BzIm (9 μM , in H_2O at pH -3.5) with CB7 and CB8. (A and B) $[\text{CB7}]/\mu\text{M}$: (1) 0, (2) 1, (3) 4, (4) 8, (5) 14, (6) 24, (7) 40, (8) 98, (9) 154, (10) 226. (C and D) $[\text{CB8}]/\mu\text{M}$: (1) 0, (2) 1, (3) 2, (4) 5, (5) 7, (6) 8.5, (7) 10.6, (8) 12.4, (9) 15.8, (10) 22.7, (11) 32.5, (12) 50. $\lambda_{\text{exc}} = 355\text{nm}$

Figure 4.4: Job plots for the CB7:NDI-BzIm (A) and CB8:NDI-BzIm (B) complexes. Total concentration of the two components was (A) 16.0 μM and (B) 25 μM . $\lambda_{\text{mon}} = 382\text{ nm}$ (A) and $\lambda_{\text{mon}} = 350\text{ nm}$ (B).

Figure 4.5: Raw data for the titration of 100 μM NDI-BzIm with CB[7] and CB[8] at pH 2.5 in water and 25 $^\circ\text{C}$, (A) showing the calorimetric response as successive injections of the CB7 are added to NDI-BzIm filled the sample cell and (B) NDI-BzIm are added to the filled CB8 sample cell. Integrated heat profile of the calorimetric titration shown in panel (1). In panel (2) solid line represents the best nonlinear least-squares fit to a one set of binding site model for 4.5A and sequential binding-site model for 4.5B.

Figure 4.6: SEM and FM images obtained from samples deposited on respective substrate surface; (a,b,c) NDI-BzIm alone, (d, e, f) NDI-BzIm/CB7 complex and (g, h, i) NDI-BzIm/CB8 complex.

Figure 4.7: Photo Irradiation (355 nm) for 30 minutes, (A) Absorption and (B) Electron paramagnetic resonance spectra of 50 μM NDI-BzIm (1) with 100 μM CB7 (2) and 50 μM CB8 in H_2O (pH 3.5).

Figure 4.8: Absorption spectra after 30 minutes white light irradiation, (A) CB7 (200 μM):NDI-BzIm (100 μM) spectra recorded every 15 minutes time interval and (B) CB8 (50 μM):NDI-BzIm (50 μM) every 5 minutes time interval.

Figure 4.9: Emission spectra (A) and decay trace (B) after photoirradiation (355 nm for 30 minutes) of 50 μM NDI-BzIm (1) with 100 μM CB7 (2), 50 μM CB8 (3) and 50 μM CB8 (4) without irradiation in H_2O (pH 3.5, $\lambda_{\text{ex}} = 355\text{ nm}$). Inset: Recovery of fluorescence decay with time of (CB8:NDI-BzIm $^{+2}$) 2:2 after irradiation (0-60 mins).

Figure 4.10: Fluorescence spectra after white light 30 minutes irradiation, (A) for the CB7 (100 μM): (50 μM) NDI-BzIm were recorded within 15 minutes time interval and (B) for the

CB8 (50 μM):(50 μM) NDI-BzIm were recorded different time interval, $\lambda_{\text{ex}} = 355 \text{ nm}$ for both complex.

Figure 4.11: (A) Fluorescence spectra after white light 30 minutes irradiation for the CB7 (100 μM):NDI-BzIm (50 μM), $\lambda_{\text{ex}} = 440 \text{ nm}$ (1) and CB8 (50 μM):NDI-BzIm (50 μM) $\lambda_{\text{ex}} = 470 \text{ nm}$ (2) complexes. (B) Excitation and absorption spectra of CB7:NDI-BzIm radical $\lambda_{\text{em}} = 550$.

Figure 4.12: Chemical structures of protonated forms of N,N'-bis-phenylalanyl perylenediimide (L-Phe-PDI or D-Phe-PDI) dye.

Figure 4.13: Absorption (A) and emission (B, $\lambda_{\text{ex}}=490 \text{ nm}$) spectra of L-Phe-PDI (2.4 μM , Tris buffer) in presence of β -CD host/mM, 0 (1); 0.08 (2); 0.24 (3); 0.46 (4); 0.76 (5); 1.12 (6); 1.45 (7); 2.06 (8); 3.19 (9); 4.91 (10), Jobs plot (Inset 4.2.1A) and binding curve (inset 4.2.1B) for interaction of L-Phe-PDI with β -CD host.

Figure 4.14: Absorption (A) and emission spectra of D-Phe-PDI (3.4 μM) dye at different concentration of β -CD in Tris-HCl buffer at pH7.5; β -CD / mM: 1) 0.0, 2) 0.1, 3) 0.24, 4) 0.5, 5) 0.8, 6) 1.1, 7) 1.45, 8) 2.1, and 9) 3.19. $\lambda_{\text{ex}} = 490 \text{ nm}$. Inset of (B) shows the binding isotherm (fl. intensity v/s concentration of β -CD), $K=(K_1.K_2) = 3.3 \times 10^6 \text{ M}^{-2}$

Figure 4.15: Absorption spectra (a) and excitation spectra (b) of L-Phe-PDI. Spectrum (c) is the absorption and excitation spectra (d) obtained for the β CD/L-Phe-PDI complex.

Figure 4.16: (A) CD spectra of L-Phe-PDI (30 μM , pH 7.5, tris buffer) recorded in presence of $[\beta\text{-CD}]/\text{mM}$, 0 (1); 1.16 (2); 3.1 (3); 6.3 (4); 15.0 (5). (B) CD spectra of D-Phe-PDI (20 μM) dye (1) and in presence of β -CD (10 mM, 2) in Tris-HCl buffer, pH 7.5

Figure 4.17: ITC isotherm for titration of L-Phe-PDI with β -CD host in Tris-HCl buffer pH 7.5 at 25 $^{\circ}\text{C}$.

Figure 4.18: Geometry optimized structures of free Phe-PDI and 1:1 and 2:1 host-guest complexes with β -CD host.

Figure 4.19: (A) Decay traces of L-Phe-PDI (2.4 μM in tris buffer, pH 7.5) in absence (1) and in presence (2) of 5.0 mM β -CD host and IRF (L). Inset: Anisotropy decay of free L-Phe-PDI (a) and in presence of β -CD host (b). $\lambda_{\text{ex}} = 445 \text{ nm}$, $\lambda_{\text{em}} = 580 \text{ nm}$. (B) Fluorescence decay traces of L-Phe-PDI (1.85 μM) dye at different concentration of β -CD in water at pH-2.5. β -CD / mM: 1) 0.0, 2) 1.4, 3) 2.4, 4) 4.3, 5) 13.26, 'L' represents the lamp profile. $\lambda_{\text{ex}} = 490 \text{ nm}$

Figure 4.20: (A) Fluorescence spectra of L-Phe-PDI ($1.85 \mu\text{M}$) dye at different concentration of β -CD in water pH-2.5 β -CD / mM: 1) 0.0, 2) 0.15, 3) 0.5, 4) 0.9, 5) 1.4, 6) 2.42, 7) 4.35, 8) 7.56, $\lambda_{\text{ex}} = 490 \text{ nm}$. (B) Decay trace of L-Phe-PDI ($35 \mu\text{M}$) in water with different pH: 1) 2.5, 2) 4.0, 3) 7.5, 'L' represents the lamp profile. $\lambda_{\text{ex}} = 490 \text{ nm}$.

Figure 4.21: ^1H -NMR spectra recorded for uncomplexed L-Phe-PDI (A); and in presence of β -CD host (B); s, solvent, asterisks indicate β -CD protons.

Figure 4.22: SEM (a-c, d-f); FM (g-i, j-l); and AFM (m, n) images obtained from samples deposited on respective substrate surface; L-Phe-PDI (a-c, g-i, m) and β -CD/L-Phe-PDI complex (d-f, j-l, n).

Figure 4.23: The powder XRD patterns recorded for L-Phe-PDI, β -CD and the β -CD/L-Phe-PDI complex.

Figure 4.24: I-V characteristics recorded for the film of β -CD/L-Phe-PDI complex (a), for the control L-Phe-PDI dye (b) and the β -CD (c) under ambient condition (A) and under Vacuum (B).

Figure 4.25: (A) I-V characteristics recorded for the film of β -CD/L-Phe-PDI complex at ambient conditions and at different concentrations than the traces presented in Fig.4.2.12. (B) Several scans of the I-V characteristics recorded for the film of β -CD/L-Phe-PDI complex under vacuum.

Figure 4.26: Enlarged scale display of Fig. 4.2.12 showing the I-V characteristics recorded for the film of β -CD/L-Phe-PDI complex (a), for the control L-Phe-PDI dye (b) and the β -CD (c) under ambient condition (A) and under Vacuum (B)

Figure 4.27: I-V curve recorded with multiple scans only in one direction; only in the positive (0 to +15V) (A) and only in the negative (0 to -15V) (B) directions.

Figure 4.28: Cyclic Voltammetry traces (scan rate 100 mV/sec, Ag/AgCl reference) obtained from PDI ($100 \mu\text{M}$) in the presence (a) and absence (b) of β -CD (16 mM).

Figure 4.29: Solid state fluorescence spectra of L-Phe-PDI ($10 \mu\text{M}$) dye (a) and that of β -CD/L-Phe-PDI complex (b) deposited as thin films.

Figure 4.30: Chemical structure of L-Phe-PDI and β -CD host (a); schematic representation of host induced deaggregation process (b); photograph of solution of L-Phe-PDI (c) and β -CD/L-Phe-PDI complex under UV light (d); I-V scan setup (e), I-V curve (f) and the FM images of β -CD/L-Phe-PDI complex (g).

Figure 5.1.1: Chemical structures of Rhodamine B, Rhodamine 6G and Sulfobutylether- β -cyclodextrin (SBE $_7\beta$ CD)

Figure 5.1.2: Absorption spectra of (A) RhB ($\sim 1.4 \mu\text{M}$) and (B) Rh6G ($\sim 1.5 \mu\text{M}$) at different concentrations of SBE $_7\beta$ -CD. (A) [SBE $_7\beta$ CD] / μM : (1) 0.0, (2) 2.5, (3) 5.0, (4) 10.0, (5) 25.0, (6) 49.7, (7) 99.0, (8) 196.0, (9) 384.0, (10) 610.0 and (11) 909. (B) [SBE $_7\beta$ CD] / μM : (1) 0.0, (2) 5.0, (3) 10.0, (4) 25.0, (5) 49.7, (6) 99.0, (7) 196.0, (8) 384.0, (9) 610.0, (10) 740.7 and (11) 909. Insets show the binding isotherms. $\lambda_{\text{mon}} = 567 \text{ nm}$ for RhB and 525 nm for Rh6G.

Figure 5.1.3: Job plots for the SBE $_7\beta$ CD:RhB (A) and SBE $_7\beta$ CD:Rh6G (B) complexes. Total concentration of the two components was $10 \mu\text{M}$. $\lambda_{\text{mon}} = 570 \text{ nm}$ (A) and $\lambda_{\text{mon}} = 540 \text{ nm}$ (B).

Figure 5.1.4: Fluorescence spectra of (A) RhB ($\sim 1.4 \mu\text{M}$) and (B) Rh6G ($\sim 1.5 \mu\text{M}$) at different concentrations of SBE $_7\beta$ -CD. (A) [SBE $_7\beta$ CD] / μM : (1) 0.0, (2) 5.0, (3) 10.0, (4) 25.0, (5) 49.7, (6) 99.0, (7) 196.0, (8) 384.0, (9) 610.0 and (10) 909. (B) [SBE $_7\beta$ CD] / μM : (1) 0.0, (2) 2.5, (3) 5.0, (4) 10.0, (5) 99.0, (6) 196.0, (7) 384, (8) 610.0 and (9) 909. $\lambda_{\text{ex}} = 520 \text{ nm}$ for RhB and 490 nm for Rh6G.

Figures 5.1.5: (A) Fluorescence decay traces of RhB ($\sim 1.4 \mu\text{M}$) at different concentrations of SBE $_7\beta$ CD. (A) [SBE $_7\beta$ CD] / μM : (1) 0, (2) 64, (3) 160, (4) 302, (5) 484 and (6) 909. (B) Fluorescence decay traces of Rh6G ($\sim 1.4 \mu\text{M}$) in the absence and presence of $909 \mu\text{M}$ of SBE $_7\beta$ CD. $\lambda_{\text{ex}} = 490 \text{ nm}$, $\lambda_{\text{mon}} = 580 \text{ nm}$ and L represents the lamp profile. Insets show the anisotropy decay traces of the corresponding dyes in the absence (1) and presence of 0.9 mM of SBE $_7\beta$ CD (2). $\lambda_{\text{ex}} = 445 \text{ nm}$ and $\lambda_{\text{mon}} = 580 \text{ nm}$.

Figure 5.1.6: (A) Raw data for the titration of $50 \mu\text{M}$ Rhodamine B and Rhodamine 6G with 5 mM SBE $_7\beta$ CD at pH 7.4 in tris-buffer (10 mM) and 25°C , showing the calorimetric response as successive injections of the host are added to the sample cell. (B) Integrated heat profile of the calorimetric titration shown in panel A. The solid line represents the best nonlinear least-squares fit to a sequential binding- site model.

Figures 5.1.7: Absorption spectra (in 1 mm cuvette) of (A) RhB ($\sim 220 \mu\text{M}$) and (B) Rh6G ($\sim 285 \mu\text{M}$) at different concentrations of SBE $_7\beta$ CD. (A) [SBE $_7\beta$ CD] / mM : (1) 0.0, (2) 0.03, (3) 0.1, (4) 0.2, (5) 0.38, (6) 0.65, (7) 0.91, (8) 1.75 and (9) 3.85. (B) [SBE $_7\beta$ CD] / mM : (1) 0.0, (2) 0.03, (3) 0.08, (4) 0.15, (5) 0.29, (6) 0.48, (7) 0.65, (8) 0.91, (9) 1.75 and (10) 3.00.

Figure 5.1.8: Fluorescence spectra (in 1 mm cuvette, front face geometry) of (A) RhB ($\sim 220 \mu\text{M}$) and (B) Rh6G ($\sim 285 \mu\text{M}$) in the absence (1) and presence (2) of SBE $_7\beta$ CD (3.85 mM for

RhB and 3 mM for Rh6G) in water. Insets in (A) & (B) show the photographs of the respective dyes in water in the absence (i) and presence (ii) SBE₇βCD under UV-light.

Figure 5.1.9: Fluorescence decay traces (in 1 mm cuvette, front face geometry) of (A) RhB (~220 μM) and (B) Rh6G (~285 μM) in the absence (1) and presence (3) of SBE₇βCD (3.85 mM for RhB and 3 mM for Rh6G) in water and in EtOH (2). L represents the lamp profile. $\lambda_{ex} = 490$ nm.

Figure 5.1.10: Lasing efficiency of plot of (A) RhB (~300 μM) and (B) Rh6G (~300 μM) in aqueous solution at different concentrations of SBE₇βCD using a broad-band dye laser setup. The dotted line represents the lasing efficiency of (A) RhB and (B) Rh6G in optically matched ethanol solutions.

Figure 5.1.11: (A) Narrow band dye laser setup. The laser beam profiles for RhB in water with 4 mM SBE₇βCD (B) and in ethanol (C), obtained at identical gain depth (similar OD at pump wavelength i.e. 532 nm) using a digital camera.

Figure 5.1.12: Tuning curves of RhB (A) and Rh6G (B) in EtOH (1) and in the presence of 4 mM SBE₇βCD (2) at a pump energy of ~5 mJ. Variation of output energy of RhB (C) and Rh6G (D) in EtOH (1) and in the presence of ~4 mM SBE₇βCD (2).

Figure 5.1.13: Absorption spectra of RhB in EtOH (A) and in the presence of SBE₇β-CD in water (B) and Rh6G in EtOH (C) and in the presence of SBE₇β-CD in water (D) at different times of laser irradiation. $\lambda_{irrdn} = 532$ nm. Time of irrdn/min: 1) 0, 2) 15, 3) 45, 4) 105, 5) 180 and 240.

Figure 5.2.1: Chemical structures of thiazole orange (TO) Tyramine (Tyr) and the macrocyclic host, sulfobutyl ether β-cyclodextrin sodium salt.

Figure 5.2.2: Absorption spectra of TO (3 μM) in aqueous solution at different concentrations of SBE₇βCD. [SBE₇βCD]/μM: (1) 0.0, (2) 0.25, (3) 0.5, (4) 1.5, (5) 3.0, (6) 6.0, (7) 20.0, (8) 40.0, (9) 80 and (10) 130.0. Inset shows the Job plot evaluated by the absorbance changes at 500 nm for the SBE₇β-CD:TO complex. n_{Dye} represents the mole fraction of TO. The trace has been analysed for multiple distribution; 1 and 2.

Figure 5.2.3: Fluorescence spectra of TO (3 μM) in aqueous solution at different concentrations of SBE₇βCD. [SBE₇βCD]/μM: (1) 0.0, (2) 0.25, (3) 0.5, (4) 1.5, (5) 3.0, (6) 6.0, (7) 20.0, (8) 40.0, (9) 80, (10) 230 and (11) 760. Inset shows the variation in the

fluorescence intensity at 660 nm (1) and 520 nm (2) with increase in the concentration of SBE₇βCD.

Figure 5.2.4: Fluorescence decay traces of SBE₇βCD (6 μM):TO (3 μM) (trace 1) and SBE₇βCD (400 μM):TO (3 μM) at 640 nm (trace 2) and 520 nm (trace 3). *L* is the lamp profile. Inset shows the anisotropy decay traces of the respective complexes. $\lambda_{\text{ex}} = 445$ nm, $\lambda_{\text{mon}} = 640$ nm.

Figure 5.2.5: Upper layer shows the chemical structure of TO. (B) ¹H NMR signals of the aromatic rings of TO (100 μM) in the absence (a) and presence of 200 μM (b) and 4 mM (c) of SBE₇βCD in D₂O.

Figure 5.2.6: ITC isotherms for titration of TO (200 μM) with SBE₇βCD (400 μM) at 25 °C in aqueous solution. The upper panel shows the instrumental power function versus time (injected aliquots) plot. The lower panel shows the plot for heat of reaction obtained from the integration of the calorimetric traces, plotted against the host/guest molar ratio. The solid line represents the best nonlinear least-squares fit to a sequential binding-site model.

Figure 5.2.7: Circular dichroism spectra of TO (30 μM) at different concentrations of SBE₇βCD. [SBE₇βCD] / mM: (1) 0.0, (2) 0.06, (3) 1.06, (4) 2.7 and (5) 7.7.

Figure 5.2.8: (A) Fluorescence spectra of 1:4 (SBE₇βCD:TO) assembly at different temperatures, Temp (°C): 10 (1), 20 (2), 30 (3), 40 (4), 50 (5), 60 (6), 70 (7), 80 (8) and 90 (9). Inset shows the emission intensities at 660 nm monitored at different temperatures with heating and cooling cycles in the range 10°C to 90°C. (B) Lifetime decay traces of (1:4) SBE₇βCD:TO assembly at different temperatures. Temp/°C: 20 (1), 30 (2), 40 (3), 50 (4), 60 (5), 70 (6), 80 (7) and 90 (8). Inset of Fig.5.2.7 B shows the anisotropy decay traces at 20 °C (1) and 90 °C (2). $\lambda_{\text{ex}} = 465$ nm (for fluorescence spectra measurements), $\lambda_{\text{ex}} = 445$ nm and $\lambda_{\text{mon}} = 650$ nm. (C) CD spectrum recorded for SBE₇βCD:TO assembly at different temperatures. Temp/°C: 10 (1), 30 (2), 50 (3), 70 (4) and 90 (5). Dotted line in Fig. C indicates the CD spectrum of TO free dye at higher concentration (30 μM).

Figure 5.2.9: The percentage of fluorescence quenching of SBE₇βCD:TO (1:4) assembly in the presence of 12 μM concentration of neurotransmitters. **Inset:** Fluorescence quenching at 660 nm for the SBE₇βCD:TO (1:4) assembly for (a) Tyramine and (b) other neurotransmitter amines.

Figure 5.2.10: (A) The fluorescence titration of 1:4 SBE₇βCD:TO assembly with tyramine. [Tyramine]/μM: 0 (1), 1 (2), 3 (3), 5 (4), 8 (5), 12 (6), 20 (7), 25 (8), 35 (9), 50 (10) and 100 (11). (B) Fluorescence quenching of 1:4 SBE₇βCD:TO assembly at different concentrations of tyramine. $\lambda_{ex} = 465$ nm and $\lambda_{mon} = 660$ nm.

Figure 6.1: Chemical structures of TMPyP, captisol and the representation of the Captisol:TMPyP complex

Figure 6.2: Absorption (A) and fluorescence (B) spectra of TMPyP (2.1 μM) in aqueous solution at different concentrations of captisol. [Captisol] / μM: (1) 0, (2) 0.25, (3) 0.5, (4) 0.75, (5) 1.0, (6) 3.5, (8) 7.0, (8) 14.8 and (9) 22 at pH ~7.4. In (A), Inset I and Inset II show the changes in the sorot band and Q band (500-700 nm) region, respectively, in the presence of 22 μM captisol. In (B), Inset shows Jobs plot using the fluorescence intensity ratio (I_{717}/I_{653}) with mole fraction of TMPyP, n_{TMPyP} , for the Captisol:TMPyP complex (a) and only TMPyP solution (b) under identical concentration conditions.

Figure 6.2: Fluorescence decay traces ($\lambda_{ex} = 445$ nm, $\lambda_{mon} = 650$ nm) of ~2 μM TMPyP solution at different concentration of captisol. [Captisol] / μM: 0.0 (1), 0.25 (2), 0.5 (3), 1.0 (4) and 22.0 (5). L represents the instrument response function. The inset displays the fluorescence anisotropy traces under the conditions for the fluorescence decay traces 1 and 5.

Figure 6.4: ¹H NMR spectra of (a) TMPyP, (b) TMPyP and captisol (1.0 equiv.) and (c) TMPyP and captisol (2.0 equiv.) in D₂O. Inset: N-methyl pyridyl moiety with a part of the central porphyrin moiety and the pictorial representation of the host interaction.

Figure 6.5: Upper panel shows the raw data for the titration of 100 μM TMPyP with 600 μM captisol at pH 7.4 in phosphate buffer (10 mM) and 25 °C, showing the calorimetric response as successive injections of the host are added to the sample cell. Lower panel shows the integrated heat profile of the calorimetric titration given in the upper panel. The solid line represents the best nonlinear least-squares fit to a sequential binding- site model.

Figure 6.6: Size distribution curve obtained during addition of captisol to TMPyP(500 μM) solution with Captisol (A) 0.25 mM, (B) 0.5 mM, (C) 1 mM, (D) 2 mM indicating the formation of extended assemblies/moieties.

Figure 6.7: SEM (a-f) and FM (g-j) images of TMPyP alone (a-c, g, h) and TMPyP (2 μM) with captisol (25 μM) (d-f, i, j) using green light excitation.

Figure 6.8: AFM images of (B1) TMPyP and (B2) TMPyP (2 μM) with captisol (25 μM).

Figure 6.9: Photodegradation of TMPyP (2 μM) in aerated water in the absence (A) and presence (B) of 25 μM of captisol followed through the decrease of the visible absorption with increasing time of irradiation at 422 nm using a 150 W xenon lamp from a steady state fluorimeter. (C) Changes in the absorbance of TMPyP monitored at 422 nm on irradiation at 422 ± 2.5 nm using 150W Xenon lamp from the steady state fluorimeter; TMPyP alone (1) and Captisol:TMPyP complex (2).

Figure 6.10: Plot of the changes in the fluorescence intensity (I_f) with increasing concentration of Captisol at 660 nm in aqueous solution (A) and in DMF (B).

Figure 6.11: The consumption of DPBF as a function of irradiation time in the air-equilibrated DMF solution of DPBF and TMPyP (~ 2 μM) in the absence (1), presence of 20 μM captisol (2). Trace (3) represent the singlet oxygen yield evaluated for $[\text{Ru}(\text{bpy})_3]^{2+}$ as standard ($\Phi(^1\text{O}_2^*) = 0.81$) in air equilibrated CH_3OH) under similar irradiation conditions.

Figure 6.12: Images of plates showing bacterial growth of *E. coli* in terms of colonies in the absence of any additive (a) and presence of TMPyP (5 μM) (b) and with TMPyP (5 μM):captisol (20 μM) (c) at pH 7.5 after white light irradiation for 5 minutes. (d) is the bar chart representation of the percentage of inhibition in bacterial growth by TMPyP (5 μM) in the absence (black bar) and presence (red bar) of captisol (20 μM) with irradiation time 0 min (i); 1 min (ii); 5 min (iii) against *E. Coli* (Gram -ve) bacteria.

Figure 6.13: Plates showing growth of Gram positive *Staphylococcus aureus* in colonies with TMPyP (A) and Captisol:TMPyP complex (B) on light irradiation.

Figure 6.14: Pictorial representation of the singlet oxygen generation from the TMPyP complex and killing of *E.coli* bacteria and A549 cancerous cell lines.

Figure 6.15: (A) Cell viability studies carried out in lung carcinoma A549 cell lines using MTT assay with the addition of respective TMPyP, Captisol:TMPyP and Control systems under white light irradiation (red bars, a, c, e) and in dark conditions (green bars b, d, f). The circled portion indicates the enhanced toxicity of Captisol:TMPyP complex in the A549 cancer cell lines under white light irradiation. (B-D) The phase contrast images of living lung carcinoma A549 cells in DMEM medium in the absence of any additive treated as control (B), in the presence of TMPyP (5 μM) (C) and in the presence of Captisol (75 μM):TMPyP (5 μM) complex (D), after 30 minutes white light irradiation during MTT assay.

Figure 6.16: Cell viability studies carried out in lung carcinoma A549 cell lines (red and green bars) using MTT assay with the addition of respective TMPyP, Captisol:TMPyP and

Control systems under white light irradiation (red bars, a, c, e) and in dark conditions (green bars b, d, f). The black bars (i, ii, iii) represent similar studies carried out in normal CHO cells under dark condition.

Figure 7.1: *Chemical structures of guest dyes and macrocyclic hosts*

List of Tables

Table 1.1: Molecular dimensions and solubility in water for important CB homologues.

Table 1.2: Molecular dimensions and solubility in water for important CD hosts.

Table 4.1: Excited state lifetime values evaluated from the fluorescence decays of NDI-BzIm (50 μ M) in water at pH 2-3 in the presence of (50 μ M) CB8 with different time interval.

Table 4.2: Excited state lifetime values evaluated from the fluorescence decays of NDI-BzIm (50 μ M) in water at pH 2-3 in the presence of (100 μ M) CB7 with different time interval.

Table 5.1.1: Lasing parameters of RhB and Rh6G dyes in EtOH and SBE₇ β CD/water systems using 532nm laser irradiation (10 Hz, 5 mJ).

Table-5.2.1: Fluorescence decay parameters for TO (~3 μ M) at different concentrations of SBE₇ β CD.

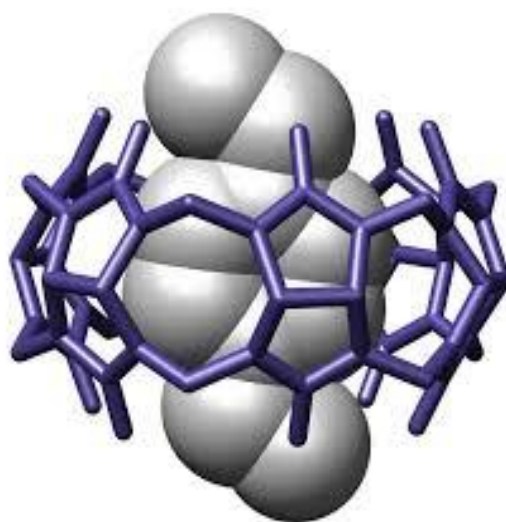
Table-5.2.2: Thermodynamic parameters of SBE₇ β CD:TO system obtained from the ITC data

Table-5.2.3: Fluorescence decay parameters for TO (~8.8 μ M):SBE₇ β CD (~15 μ M) systems at different temperatures

Table 6.1: DLS measurements carried out in solutions of 500 μ M TMPyP with the addition of varying concentrations of Captisol

Chapter 1

Introduction



1.1 Supramolecular Chemistry

Supramolecular chemistry refers to an area of chemistry that specializes in the study of noncovalent interactions within and between molecules, covering the structures and functions of the entities formed by the association of two or more chemical species.^{1, 2} Traditionally, chemists have focused on studying how atoms and ions are held together by covalent bonds and ionic bonds, and how these bonds are formed and broken during chemical reactions.² By contrast, researchers in supramolecular chemistry examine the weaker and reversible noncovalent interactions, such as electrostatic interactions like dipole–dipole, ion–dipole, hydrogen bonding interactions and hydrophobic interactions like van der Waals, π – π interactions, dispersion interactions etc.¹⁻⁴ One may be tempted to believe that the structures and properties of these assemblies or materials can be directly related to those of the individual molecules that comprise them. However, the novel properties and functions of the new entities, in general, cannot be deduced by a simple summation of the properties of the individual molecules and are particularly true with biological molecular systems, such as DNAs, that are derived from the spatial and sequential organization of component molecules through weak non-covalent interactions.⁴ Often tailor-made organization and a well-selected combination of supramolecular elements leads to systems with incredible performance and are effectively exploited into several technological applications.

Thus, the power of supramolecular chemistry lies in the role of various weak noncovalent interactions mentioned above.⁵ The existence of intermolecular interaction was first axiom by Johannes Diderik van der Waals in 1873.⁶ Hermann Emil Fischer, Nobel laureate, introduced the philosophical roots of supramolecular chemistry by proposing "lock and key" mechanism for enzyme-substrate interactions

in 1894,⁶ which is the fundamental principle of molecular recognition and host-guest chemistry.^{6, 7} Moreover other basic concepts of supramolecular chemistry which was developed during last decades like molecular self-assembly, molecular recognition, molecular imprinting techniques, concepts of molecular machines, complexation, mechanically interlocked molecular architectures/devices and biomimetics.⁶⁻⁹ These concepts have potential applications in the field of materials technology, efficient catalysis, controlled drug delivery, data storage, processing devices, green chemistry and high-tech devices.^{6, 7, 10-12}

Supramolecular chemistry came to centre stage of chemical science when Jean-Marie Lehn, Donald J Cram, and Charles J Pedersen bagged the Nobel Prize in 1987 for supramolecular chemistry involving the chemical, physical, and biological features of molecular assemblies having a greater potential in many applied areas, especially in constructing functional materials, fluorescence sensors, on-off switches, controlled cellular uptake and release for drug delivery, etc.^{8, 9, 13, 14} They also stabilized the molecular machine with multi-component systems in which the reversible movement of the components can be controlled by an external stimulus. Nondegenerate rotaxanes, nondegenerate catenanes and pseudorotaxanes are the well know examples of the molecular machines.¹⁵ In the past decades, scientists have made enormous advances in creating nanoscale assemblies and structures with the aim to achieve applications ranging from targeted drug delivery to the development of functional materials.¹⁶ More recently in 2016 the supramolecular chemistry once again come to research limelight with another set of Nobel Prize awarded to Jean-Pierre Sauvage, J. Fraser Stoddart and Ben. L. Feringa for their work in the area of molecular machines with the development of the control of the motions of the

components in those systems, which results in a change in properties which produce a signal that allows the operation of the machine to be monitored.^{17, 18}

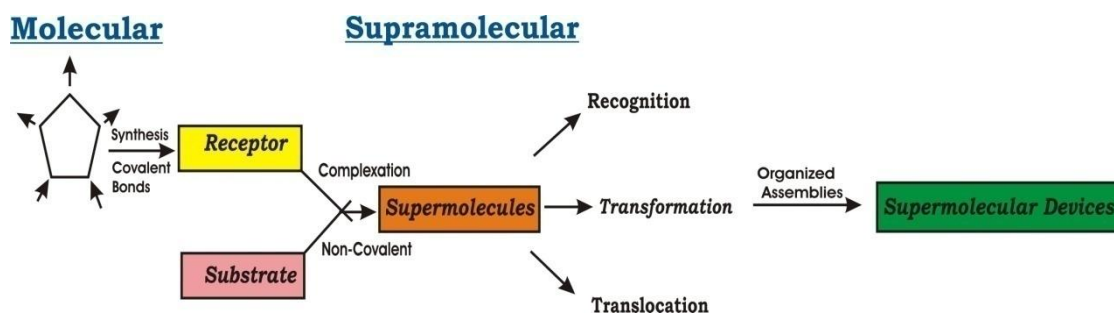


Figure 1.1: Schematic representation of conversion from molecule to supramolecular chemistry, molecule to supramolecule and supramolecular devices.¹⁹

One of the many other different strategies for making synthetic functional materials takes advantage of self-assembly, the method by which well-ordered structural patterns are formed spontaneously from self-directed organization of the individual components through only noncovalent interactions.^{4, 5}

Within the field of supramolecular chemistry there is an increasing interest towards host-guest chemistry which is mainly focussed on the potential applications of macrocycles including crown ethers, cyclodextrins, calixarenes, pillararenes and cucurbiturils. In this chapter, some representative contributions in the construction of controllable macrocyclic supramolecular assemblies in aqueous solution are presented with prominence on the stimuli-responsive control manner and wide applications of their properties. Along these years, electrochemical and photochemical motifs became integrated into supramolecular systems to increase functional applications. In addition, the research activities on supramolecular chemistry has seen an upsurge in the areas of synthetic self-replicating systems and molecular information processing devices. The emerging science of nanotechnology also had a strong influence on the subject, with building blocks such as fullerenes, nanoparticles, and dendrimers becoming involved

in synthetic systems.^{1, 4, 14} On a broad view, supramolecular chemistry has proved useful for the development of new materials, pharmaceuticals, drug delivery systems, high-tech sensors, and contrast agents for diagnostic scans. It is also useful for the design of catalysts, solid-state reactions, and treatments of radioactive wastes.^{3, 7, 14} In addition, the study of noncovalent interactions is crucial to understanding many biological activities and processes, including cell structure and vision, which has far-fetched goal of mimicking and exploiting natural events at human will.

1.2 Host-Guest Chemistry

Molecular recognition forms the basis for supramolecular chemistry, because the construction of any supramolecular systems involves selective molecular combination. Host–guest chemistry has been in the forefront of supramolecular chemistry where the host-macromolecules recognize and encapsulate specific molecules, atoms, or ions (guests) to form complexes.⁷ Guest molecules that assure the essential steric and charge characteristics can be encapsulated by the host by weak and reversible noncovalent interactions, such as electrostatic interaction, dispersion interaction, hydrogen bonding, etc. Through such host–guest inclusion complexation, two or more chemical moieties can be interacting together by noncovalent interactions with reversible manner, providing huge possibilities for the construction of novel supramolecularly assembled structure. The preferential involvement of these interactions and the ensuing stoichiometric arrangements of the complexes bring out substantial modulation in the molecular properties of the guests and are conveniently controlled by external stimuli such as competitive binders, pH, temperature, light, etc.²⁰⁻²²

However, specific control in response to a variety of triggers/stimulators remains challenging as such noncovalent interactions very much act as a part of several substrate specific/enzymatic interactions in the biological systems. Such host-guest complexes/assemblies have attracted past few decades, immense research interest due to their tremendous potential in many applied areas, especially in constructing functional materials, fluorescence sensors, on-off switches, controlled cellular uptake and release for drug delivery, etc.^{8, 14, 23-25} A series of macrocyclic molecules and their derivatives have been developed, including cyclodextrins (CDs), calixarenes (CXs), cucurbit[n]urils (CBs), crown ethers, cyclophanes, pillar[n]arenes, and so on. These pre-organized macrocyclic molecules are treated as the hosts having cavities to encapsulate the guests.

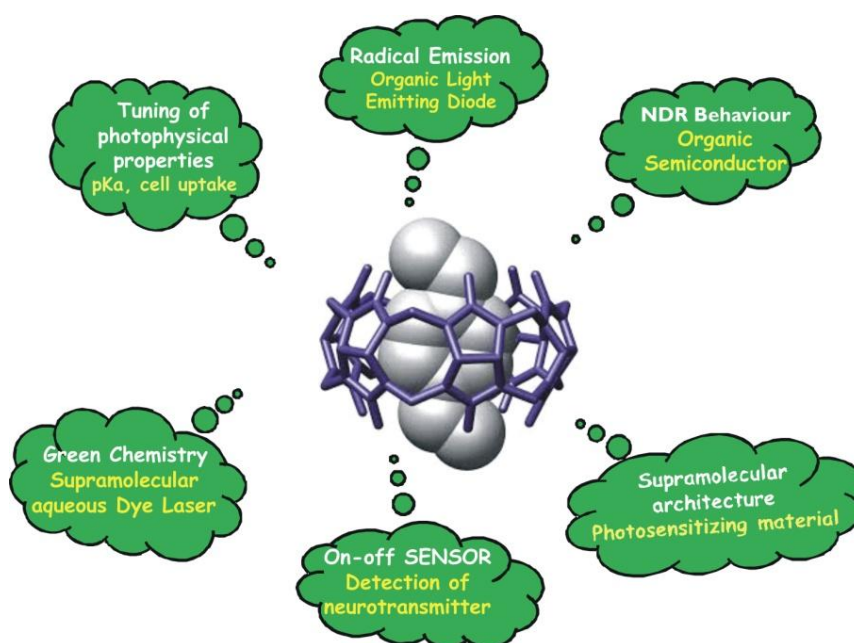


Figure 1.2: Different types of applications of supramolecular host-guest chemistry

In the present Ph.D. program our aim is to construct few such supramolecular assemblies based on host-guest complexes between the selective chromophoric dyes as guest molecules with specific pre-organized macrocyclic host molecules and thus to

find their possible applications in different areas like drug delivery, photodynamic therapy, organic electronics, aqueous dye laser, protein fibril inhibitor and fluorescence sensor, etc (see in Fig. 1.2).^{7, 26-32}

1.3 Pre-Organized Macrocyclic Hosts

The facile and reversible process in the host-guest inclusion complex formation provides opportunities to construct smart supramolecular systems that have the adaptive capability to respond to different external environments. Practically, the controlled release of guest molecules are attempted in response to various external stimuli such as temperature, pH, light, salt, enzymes, etc.^{33, 34} A number of synthetic pre-organized macrocyclic host molecules including cyclodextrins (CDs), cucurbit[n]urils (CBn), calixarenes (CXs), etc. have been employed to encapsulate the various guest molecules as these macrocycles have been established to be biocompatible.^{35, 36} The development of such biocompatible and stimuli-responsive supramolecular assemblies have become a prime focus in biomedical fields, organic electronics and also in sensor applications.³⁷ The highly selective and specific non-covalent interactions among the guests and the cavitands under the preset solution conditions allow a rational design to control the sizes and morphologies of the resultant nanoassemblies. Thus, a combination of control of size/ morphologies with stimuli responsive uptake/release would recommend such nanoassemblies as the potential candidate for controlled drug delivery modules. They have also been used to formulate, protect, and deliver drugs, as reversal agents to mitigate adverse drug side effects, and for various sensitive sensing applications.^{8, 25, 37, 38} In this thesis, we have used two classes of pre-organized macrocyclic host molecules. One is the

Cucurbit[*n*]uril (CB_{*n*}), a relatively new class of macrocycle and other one β -cyclodextrin (β CD) and its derivative sulfobutylether- β -cyclodextrin (SBE₇ β CD).

1.3.1 Cucurbit[*n*]urils

Cucurbit[*n*]urils (CB_{*n*}) is a relatively new class of cavitand macrocycles that originally revealed by Behrend in 1905 but completely characterized in 1981. They are composed of methylene-bridged glycoluril monomers having highly symmetrical hydrophobic cavities accessible through two identical partially negatively charged carbonyl-fringed portals.³⁹⁻⁴³ Synthetically the cucurbituril homologues are prepared by acid-catalyzed condensation of glycoluril with formaldehyde under optimized conditions.^{41, 44-46}

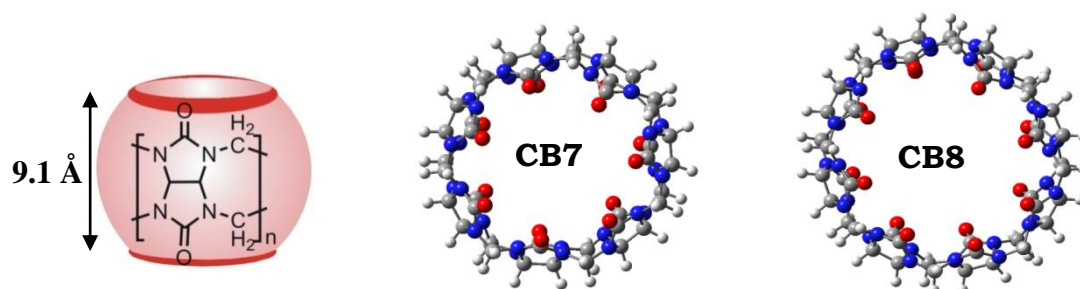


Figure 1.3: Typical shapes of the cucurbituril host are shown for easy visualization and molecular structures of CB7 and CB8 hosts.

Table 1.1: Molecular dimensions and solubility in water for important CB homologues.

Parameters	CB5	CB6	CB7	CB8
Portal diameter (Å)	2.4	3.9	5.4	6.9
Cavity diameter (Å)	4.4	5.8	7.3	8.8
Height (Å)	9.1	9.1	9.1	9.1
Solubility (mM) ^{*41, 43}	20-30	0.02-0.03	20-30	0.075

**solubility is some extent dependent on solution conditions, like pH, salt content, etc. and accordingly values reported in different literatures are somewhat different. All these solubility values measured in water with 3mM HCl*

Different homologues of cucurbit[n]urils (commonly abbreviated as CBn; $n = 5-14$, represents number of glycoluril units in the macrocycle, Fig. 1.3) with varying cavity sizes and portal dimensions with a constant height (9.1 Å) are known.^{38, 39, 41, 43} The portal rims of the CBs are a bit narrower than the internal cavity diameter of the hosts. On the other hand inverted CB also has been synthesis and isolated by Kim's group.⁴⁵ In which a single glycoluril unit directed into the CB cavity and two methine protons within the cavity, which reduced the cavity dimension of the Inverted CBn (iCBn).⁴⁵ Dimensions and solubility (in water) of the important CB homologues are given in Table 1.1. The pumpkin-shaped CBn have received considerable research interest over the past decade because their unique aqueous host-guest chemistry provides a means to generate a wide variety of supramolecular functional systems through hydrophobic, ion/charge-dipole and hydrogen bonding interactions.^{36, 40, 42, 47-49} Recently, cucurbit[14]uril (remained in the twisted form and abbreviated as tQ[14]) has been synthesized which has two kinds of cavities and adopts a folded, figure-of-eight confirmation.⁵⁰ The CB homologues display varying degree of water solubility and can be enhanced in the presence of salts, low pH, or in the presence of charged guests (Table 1.1).^{41, 43} Redox-active polyoxovanadate, polyoxomolybdate and polyoxotungstate anion clusters interact strongly with the equatorial periphery of CB6, CB7 and CB8.^{51, 52} Conversely, the cavity of CB8 is large enough to accommodate more than one guest molecules to form multiple/higher order host-guest complexes.⁵³⁻⁵⁶ In recent years, the CB-complexes has been shown to exhibit low *in vitro* as well as *in vivo* toxicity, thereby facilitating biologically relevant applications of these macrocycles.^{35, 39, 57, 58} Aptly their usages are attempted in energy storage, photonic devices, drug delivery vehicles, sensors as well as in therapeutics, etc.⁷

1.3.2 Cyclodextrins

Naturally occurring macrocyclic receptors such as cyclodextrins (CDs) are one of the most important members of the supramolecular family. The Villiers and Hebd in 1891 purposed CDs are naturally occurring compounds that can be produced by bacterial fermentation in large scales.^{11, 59} Cyclodextrin units have truncated cone like shape due to the chair conformation of the glucopyranose units. CDs (α , β and γ CDs) are cyclic oligomers composed of 6, 7, and 8 α -D-glucose units respectively and contain a significantly hydrophobic central cavity and a hydrophilic outer surface (Fig. 1.4).^{7, 60-64} The central cavity is lined by the skeletal carbons and ethereal oxygens of the glucose residues provide hydrophobic character to CDs for binding nonpolar alkyl and aryl residues. The hydroxyl groups are orientated to the cone exterior with the primary hydroxyl groups of the sugar residues at the narrow edge of the cone and the secondary hydroxyl groups at the wider edge. This hydroxyl group arrangement provides additional hydrogen bonding sites for the binding of organic/inorganic guests, particularly anionic guest molecules. CDs represent one of the most widely studied host molecular systems for binding of fluorescent dyes.^{40, 65}

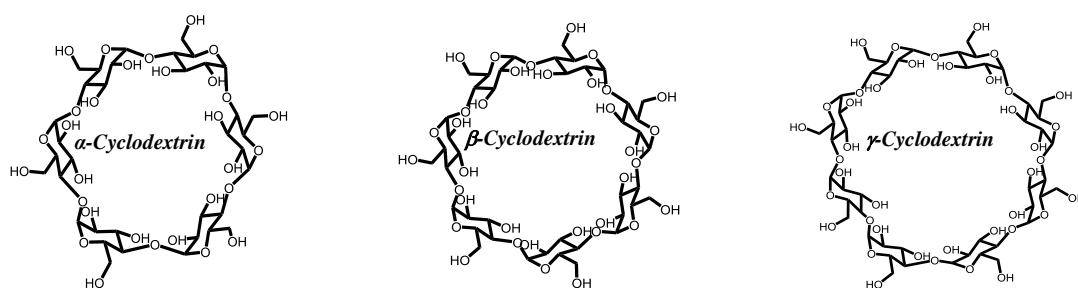


Figure 1.4: Chemical structures of α -CD, β -CD and γ -CD hosts.

In the family of CDs, the cavity size depends upon the number of glucopyranose monomer units involved, which increases with increase in the numbers.

The diameter of the wider rim of cyclodextrin increases from 5.3 Å for α -CD to around 8.3 Å for γ -CD and narrow rim increases from 4.7 Å for α -CD to around 7.5 Å for γ -CD with their constant cavity height of about 7.9 Å (Table 1.2).^{5, 61, 65}

Table 1.2: Molecular dimensions and solubility in water for important CD hosts.

Parameters	α CD	β CD	γ CD
Narrow rim diameter (Å)	4.7	6.0	7.5
Wider rim diameter (Å)	5.3	6.5	8.3
Height (Å)	7.9	7.9	7.9
Solubility (mM) ^{43, 66}	120-150	16	175

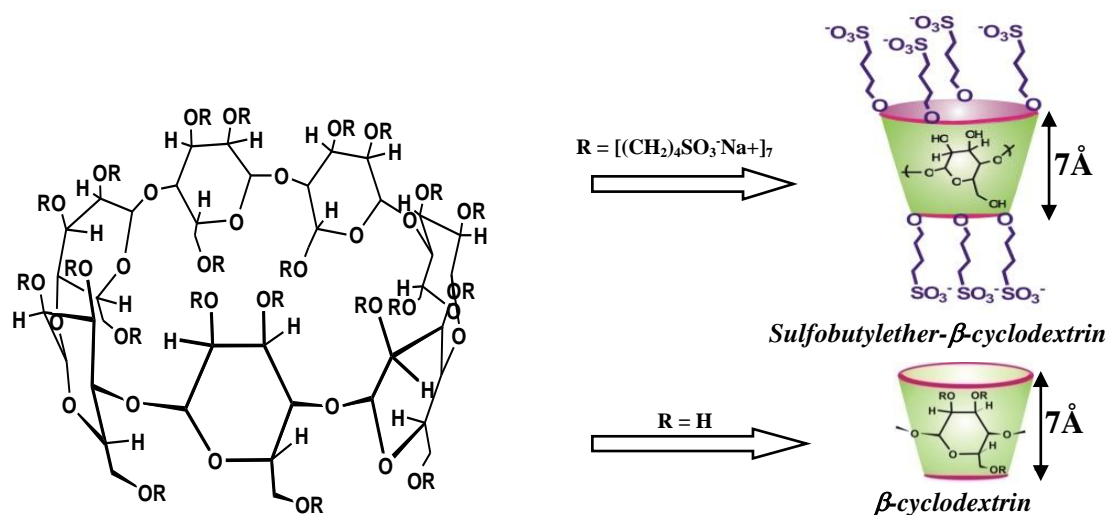


Figure 1.5: Chemical structure of cyclodextrin and typical shapes of the β -CD and SBE₇ β CD host are shown for easy visualization.

The CDs show their preference for the neutral guest molecules with participation of the weaker hydrophobic and hydrogen bonding interaction to form inclusion complexes thereby, reducing the binding constant value. In this regard, various chemically modified CD derivatives have also been developed which have the potential to show electrostatic as well as hydrophobic interaction toward cationic as

well as neutral guest molecules.⁶⁰ One of them is sulfobutylether- β -cyclodextrin (commercially known as Captisol, SBE₇ β CD, Fig. 1.5), a chemically modified cyclodextrin moiety with a structure designed to optimize the solubility and stability of drugs, has received much attention. Structurally, captisol is a cyclic hydrophilic oligosaccharide, where four secondary alcoholic groups in the wider rim and three alternate primary alcoholic groups in the narrow rim of β -CD have been substituted by sulfobutylether chains (Fig. 1.5).⁶⁷

1.4 Chromophoric Guest Molecules

Presently, complexation between macrocyclic hosts with chromophoric guests has proved its utility in wide range of applications like, in chemosensing,⁶⁸ optoelectronics, optical sensor,⁵⁴ on-off switches,^{53, 69} logic gates,⁷⁰ photostabilization,^{22, 71} supramolecular catalysis,⁷² drug delivery vehicles,^{38, 73} enzymatic assay,⁷⁴ nanocapsules,⁷⁵ supramolecular architectures^{23, 28} and other stimulus responsive functional devices.⁷⁶ Especially, encapsulation of chromophore guest dyes by macrocyclic hosts often leads to dramatic modulation of their photophysical properties due to the change of microenvironment of dye as compared to the microenvironment of the free dye in aqueous solution.⁴² Thus the confinement of the dye molecules by the host cavities introduces the restriction of rotational and vibrational motions of the dyes which lead to large reduction in the nonradiative decay for the excited dye molecules inside the host cavities. In this regard, the inclusive review written by Nau and co-workers assimilated a huge quantity of information on modulation of photophysical properties and various applications for a large number of dye-CD, dye-CBn and dye-calix[n]arene systems.⁴⁰ Apart from the photochemical properties, other chemical and physicochemical properties of the organic chromophoric dyes can also

be modulated on their encapsulation into the host cavities. One such phenomenon is the deaggregation of fluorophores in aqueous medium by supramolecular encapsulation.

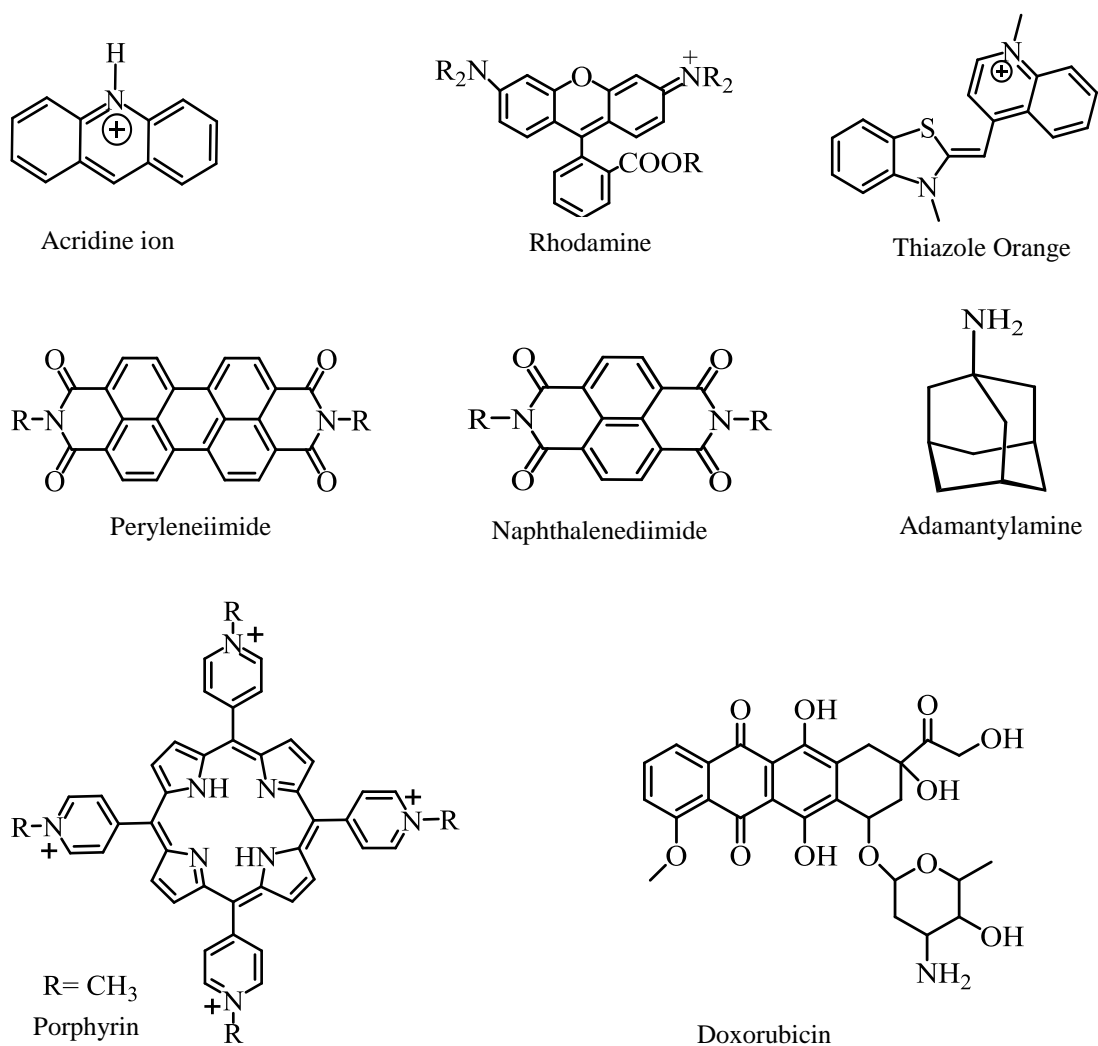


Figure 1.6: Chemical structures of the selective guest molecules used in the research work.

Organic fluorophores often tend to form aggregates with diminishing optical output in aqueous medium,³² which effect the properties of various guest molecules such as reduced the singlet oxygen yield,²⁸ fluorescence intensity, lasing efficiency³² and photostability. Although, the hydrophobic aggregation of organic fluorophores in

aqueous medium can be avoided by their supramolecular host-guest complex formation with appropriate water soluble macrocyclic hosts.⁴⁰ Such supramolecular deaggregation yields dramatic enhancement of fluorophore emission as well as photostability in aqueous medium.^{30, 77} Specifically, this approach has tremendous potential when applied to the aqueous dye laser, photosensitizing behavior and organic electronics.

The main objective of the present study involves the construction of supramolecular assemblies between the selective chromophoric dyes as guest molecules with specific macrocyclic hosts so as to exploit the deaggregation and large shift in the protolytic equilibrium on host-guest complexation for enhanced fluorescence and controlled guest relocation. Different types of chromophoric guest molecules such as acridine, rhodamines, thiazole orange, porphyrin and aromatic diimides (see in Fig. 1.6) have been employed against suitable macrocyclic hosts in realizing their tunable/stimuli responsive applications.

1.5 Mechanistic Aspects of Host– Guest Binding

Cucurbit[*n*]uril and cyclodextrin are two kinds of most popular pre-organized host molecules which are able to form complex with various types of guest molecules like cationic, anionic and neutral guests due to noncovalent interactions. For a mechanistic purpose, understanding the nature of their sensitivity and selectivity towards guests is of great importance.

1.5.1 Molecular recognition properties

Based on the number of d-glucopyranose and glycoluril units involved in the homologues of both host molecules (CBs, CDs), cavity dimensions with varying sizes are obtained, which have been responsible for their useful recognition features

towards guest molecules and the binding stoichiometry of the complex totally depends upon the cavity dimension of the host molecules.^{41, 43} All cucurbituril homologues, except the smallest CB5, can form much stronger host/guest inclusion complexes with a variety of guests including organic and inorganic compounds and their binding constants ranging from 10^4 to 10^{15} M^{-1} .^{8, 43, 78} Smallest cavity size of the CB5 shows binding towards small gas molecules like N_2 , O_2 , Xe within the cavity and cations like NH_4^+ and Pb^{2+} at the portals. CB6 and CB7 forms stable inclusion complexes with guest molecules like diamino alkanes, benzyl amines, adamantyl amine, methyl viologen cations, fluorescent dyes, surfactants, metal ions, metal nanoparticles, etc. through complete or partial encapsulation of the guest molecules.^{39, 42, 43, 79, 80} Whereas the higher homologue of CB, cucurbit[8]uril (CB8), forms stable fluorescent or nonfluorescent ternary complexes with multiple homo/hetero-guests which lead to support both the contrasting phenomena of emission quenching as well as strong excimer emission.⁵³⁻⁵⁵ On the other hand, CD molecules are however hydrophobic in nature and this property help them to encapsulate and recognizes a variety of guest molecules, especially the organic chromophoric dyes, through hydrophobic as well as hydrogen bonding interactions which lead to the formation of well-defined host–guest complexes.^{11, 61, 66} Native α -CD forms stable inclusion complexes with small size guest molecules like barbiturates, ArOH, tensides, terpenes, β -CD with barbiturates, amino acids, PAHs, ArOH, aflatoxins, hydantoins, antiepileptic drugs and γ -CD with steroidal drugs and also weak complexation with amino acids.^{40, 61, 66, 81}

1.5.2 Hydrophobic effect and binding sites

The hydrophobic effect in the course of supramolecular host–guest complexation is a combination of three effects, (i) differential dispersion interactions, (ii) desolvation of the guest and (iii) desolvation of the host in which high energy water molecules are released.

In both CBs and CDs, the inner region of the cavity is hydrophobic in nature, which favours the high affinity toward nonpolar organic residues. However, most of the chromophoric organic dyes are nonpolar in its neutral form. Therefore, the strong H-bonding between water molecules is disturbed by the presence of nonpolar dye molecules which lead to form less hydrogen bond between water molecules. The water can interact with the hydrophobic solute through van der Waals forces, but these interactions are weaker than H-bonding. On the other side pre-organized host have hydrophobic cavity which encapsulated the high energy hydration water molecules. During encapsulation of the guest by host, high energy water molecules have ejected and formed the hydrogen bond with other core water molecules which lead to increase the solvation entropies. This process is energetically favorable due to increase in the solvation entropies as well as enthalpy of the system. Therefore, ion-dipole interactions in water are not the main driving force between the interacting host-guest molecules. However, CBs in particular act preferentially as the cation receptor hosts, forming very strong inclusion complexes with cationic guest molecules due to the participation of the strong ion-dipole interaction involving the cationic charge of the guest and the negatively polarized portal of the host, besides the usual hydrophobic interaction. Unlike CBs, the CDs show their preference for the neutral molecules to

form inclusion complexes, albeit with much reduced binding constants than CBs, mainly due to the participation of the weaker hydrophobic interaction, though hydrogen bonding interaction involving the portal hydroxyl groups of the host and specific interaction site of the guest may play some role to stabilize the host-guest complex.^{10, 24, 43, 61, 65, 66, 82, 83} Some of the major interaction sites for the two class of the host molecules are shown in Fig. 1.7.

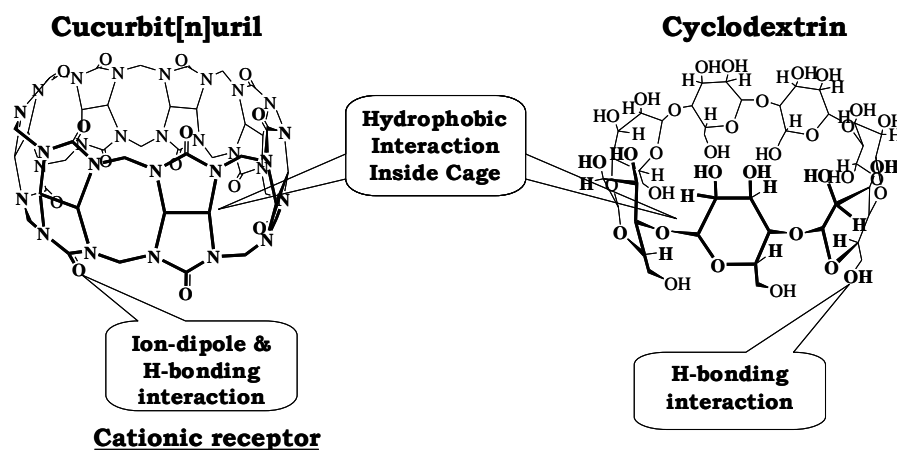


Figure 1.7: Specific interaction sites of cucurbituril and cyclodextrin hosts which participate in host-guest interaction.

1.6 Validation of the Host-Guest Interactions

The effect of host-guest interaction on the photochemical properties of the encapsulated chromophoric organic guests such as fluorescence properties, excited state lifetime and acid base properties, etc. has been studied by UV-vis absorption and steady-state and time-resolved fluorescence techniques. Other techniques like isothermal titration calorimetry (ITC), ¹H-NMR, circular dichroism (CD) have also been used in some selective cases to supplement the results obtained from absorption and fluorescence studies. In some cases, we have also used the SEM and FM to obtain supportive evidences for the structural morphology of the host-guest complexes.

1.6.1 Absorption and Fluorescence Studies

Chromophoric dyes formed the inclusion complex with the macrocyclic hosts can lead to large modulations in their photophysical and other properties.⁸⁴ The first step to study the photophysical properties of chromophoric dye molecules needs to discuss about all important aspects governing photochemical processes.

1.6.1.1 Lambert-Beer's Law

The rate of absorption of electromagnetic radiation by a chemical system is governed by Lambert-Beer's law. This law states that "The fraction of electromagnetic radiation absorbed by a medium is independent of the intensity of the incident radiation but proportional to the thickness of the absorbing medium and the concentration of the absorbing molecules in the optical path."⁸⁵⁻⁸⁷

Mathematically the Lambert-Beer's law can be expressed as,

$$-\frac{dI}{I} = \alpha_v C dl \quad (1.1)$$

where, α_v is the proportionality constant, dl is the thickness of the medium, and C is the concentration of the absorbing molecules. On integration we get,

$$\ln \frac{I_0}{I} = \alpha_v Cl \quad (1.2)$$

or, $\log \frac{I_0}{I} = \varepsilon_v Cl \quad (1.3)$

Where I_0 is the intensity of the incident light on the whole sample, I is the intensity of the transmitted light from the sample and $\varepsilon_v = \alpha_v / 2.303$, is the molar extinction coefficient of the sample. To be mentioned here that ε_v is a function of the frequency

(ν) of the absorbing light and it is the measure of the efficiency of the absorption of a particular frequency of light by the sample molecules. The quantity $\log(I_0/I) = \epsilon_\nu Cl = OD = A$ is commonly known as the absorbance (abbreviated as A) or the optical density (abbreviated as OD) of the sample.^{86, 87}

1.6.1.2 Types of electronic transitions through exciting and deexciting pathways

Light absorbed by the molecule can cause different types of electronic transition, which depends upon the nature of molecular orbitals (MOs) involved. Prof. M. Kasha has developed a convenient system of notation to express various electronic transitions in organic molecules based on the nature of the initial and the final orbitals involved in the electronic transition.^{87, 88}

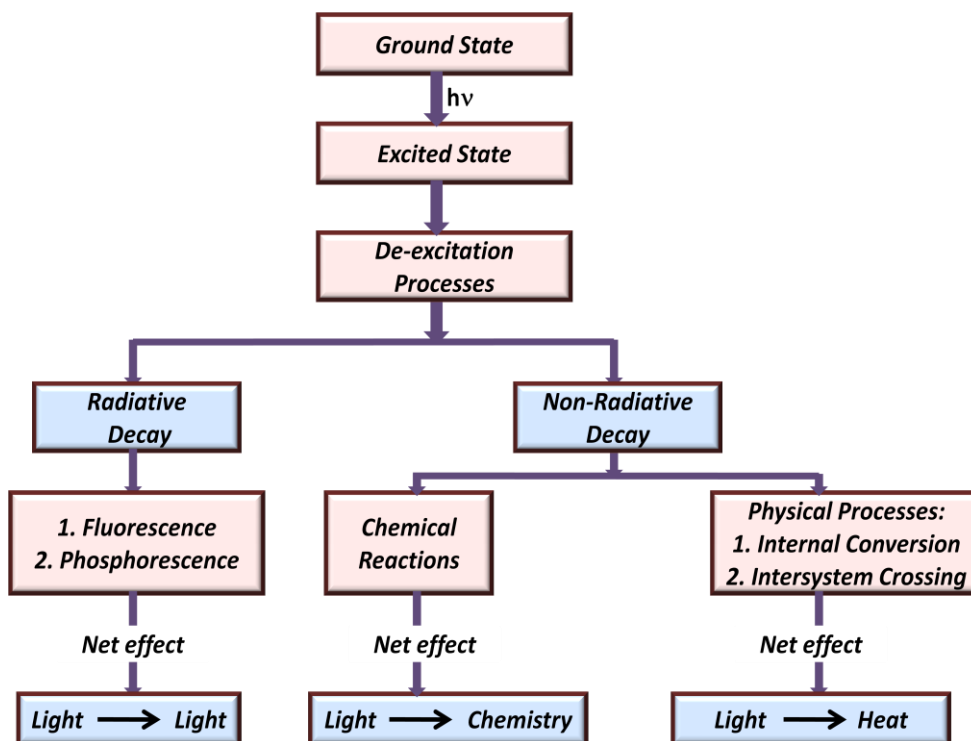


Figure 1.8: Schematic representation of the different photoprocesses that an excited molecule can participate.

In general, there are two types of molecular orbitals, Highest occupied molecular orbital (HOMO) and Lowest unoccupied molecular orbital (LUMO). On absorption of

a photon of appropriate wavelength, electron from HOMO (bonding or nonbonding orbitals) can be promoted to LUMO, which is usually an antibonding orbital. Depending upon the wavelength of the light absorbed, several electronic transitions can be observed for a chromophoric molecule.

Therefore after excitation of chromophoric molecule through light absorption, the excited molecule (M^*) can dissipate its excitation energy through several photophysical and photochemical pathways. These deexcitation pathways can be divided into two classes: (1) radiative processes, that involve the emission of light from the excited molecules and (2) non-radiative processes, in which the excited states depopulate nonradiatively without emitting any light. Fig. 1.8 represents an overview of the different photophysical processes that a molecule can undergo following light absorption. Different radiative and nonradiative photophysical processes that an excited molecule can undergo are represented by the well known Jablonsky diagram as shown in Fig. 1.9. The absorption spectrum of chromophoric dyes arises due to the wavelength dependent changes in the absorption of light photons by the ground state molecules. Similarly, the emission spectrum arises for the wavelength dependent changes in the number of emitted light photons from the excited chromophoric molecules via radiative transition. Therefore, the microenvironment of the chromophoric dyes changes during inclusion complex formation with host cavities in comparison to the microenvironment of the free dye in aqueous solution.

Moreover, this complexation leads to the restriction in the rotation and vibrational motions of the chromophoric dyes and this in turn causes the change in the absorption and fluorescence spectra. One of the reasons for this change is that encapsulated chromophoric dye experiences a less polar microenvironment⁸⁹ which

modulates the energy difference between the electronic states and also reduces the nonradiative deexcitation pathways of the excited dyes. For example aggregate form of the dyes shows broad absorption spectra; deaggregation by host-guest inclusion complex formation lead to resolve the absorption profile as well as enhance the emission intensity.

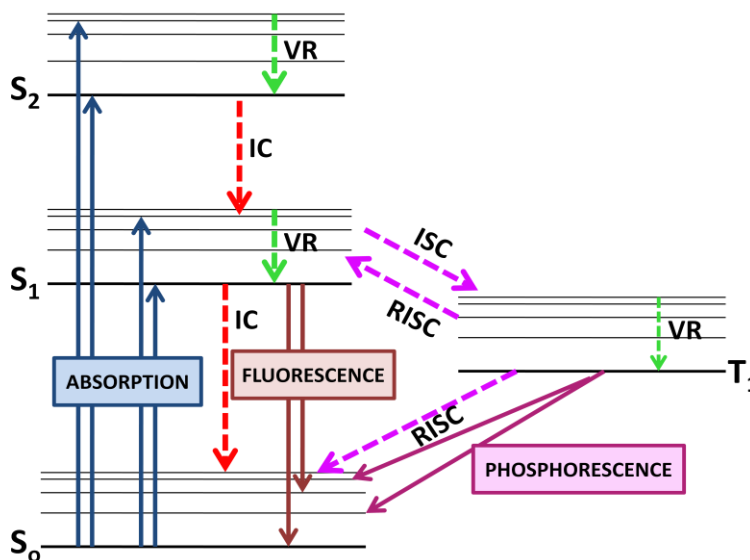


Figure 1.9: The Jablonski diagram, showing different photophysical processes undergo by an electronically excited molecule. Straight arrows and dash arrows represent the radiative and non-radiative processes, respectively. Abbreviations are: IC-Internal Conversion; ISC-Intersystem Crossing; RISC-Reverse ISC; VR-Vibrational Relaxation; S_i -ith singlet state and T_i -ith triplet state.

On the other hand, large cavity size host molecule shows ternary complex formation which causes the quenched fluorescence intensity due to excimer formation and usually excimer forms of the dyes are nonfluorescent or very weakly fluorescent in nature. Absorption and emission titration of dyes with host also gives the details of binding constant and stoichiometry of the complex.^{5, 89}

1.6.2 Time-resolved Fluorescence Measurement

As per the earlier discussion, the encapsulation of dyes by host molecule reduces the nonradiative deexcitation pathways of the excited dyes which also affects the lifetime of excited state of dyes. The lifetime (τ) of an excited state is defined as the average time that the molecules of a chemical system can spend in the excited state.⁸⁶ The deactivation of the molecules from an excited state usually follows a simple first order rate equation.

$$[M^*] = [M^*]_0 \exp(-\Sigma k_i t) \quad (1.4)$$

where $[M^*]$ and $[M^*]_0$ are the concentrations of the excited molecules at time 't' and at zero time, respectively, and Σk_i is the summation of the first order rate constants of all the possible deactivation processes.^{86, 90} Following eq. 1.4 the average time that the molecules spend in the excited state can be obtained as,

$$\tau = 1 / \Sigma k_i \quad (1.5)$$

Mathematically, the lifetime τ is that time by which the numbers of the excited molecules are reduced to $1/e^{\text{th}}$ of their initial concentration.

1.6.3 Isothermal Titration Calorimetry

In supramolecular host-guest chemistry, isothermal titration calorimetry (ITC) is an important and useful technique for evaluating the host-guest binding interactions.⁸⁹ For example, ITC can be employed to measure the enthalpic and entropic contributions to the binding interactions between the hosts and guests molecules.⁹¹ The ITC titration is performed at constant pressure and temperature, meaning that a single ITC experiment offers data on the binding enthalpy, the equilibrium association constant and the stoichiometry of the host-guest complexation. Hence, a single ITC

experiment offers direct access to the key of thermodynamic parameters like Gibbs energy, enthalpy and entropy of the host-guest interactions. ITC determines directly the heat evolved in a reaction process (Q_T) when host molecule binds with guest at constant pressure is proportional to the molar enthalpy change (ΔH) associated with that process and the amount of host-guest complex formed:

$$Q_T = V_o [ML]\Delta H \quad (1.6)$$

Where V_o is the volume of the calorimetric cell, and $[M]_T$ is the total concentration of macromolecule (Host) in the cell. The first condition implies that the enthalpy of interaction (i.e. enthalpy for complex formation) is different from zero. The second condition is fulfilled from the first condition, as Q_T is proportional to advance of the binding process:

$$\frac{[ML]}{[M]_T} = \frac{Q_T}{V_o[M]_T\Delta H} \quad (1.7)$$

It is possible to use Equations 1 and 2 in a model-free manner for estimation of the binding enthalpy if the complete saturation of the macromolecule (Host) is achieved.

1.6.4 ¹H-NMR Measurement

¹H-NMR is one of the most useful and common methods to study the interaction between a macrocyclic host and any chromophoric dye molecules. The changes observed in the NMR parameters such as chemical shifts, spin-spin coupling, and relaxation times are useful to find out the binding/stability constant, type of interaction, binding sites, and the structure of the host-guest complexes. In the ¹H-NMR measurement the observed chemical shift of a proton is the average of the chemical shifts in the complex and uncomplex environments. Equation 1 describes the formation of a host-guest complexation to observe average chemical shift for 1:1

stoichiometry and the NMR result obtained only when the observed proton is located on the host molecule.⁵

$$\delta_{obs} = X_H\delta_H + X_{HG}\delta_{HG} \quad (1.8)$$

The δ_{obs} value observed as ^1H chemical shift, X_H and X_{HG} are the mole fractions of free host and complex, respectively δ_H and δ_{HG} the chemical shifts of the host and host-guest complex.

1.7 Applications based on Host-Guest Chemistry

Construction of smart materials based on supramolecular interactions has received considerable research interest owing to their potential applications in energy storage, photonic devices, drug delivery vehicles, sensors as well as in therapeutics. In this context studies on supramolecular assemblies of organic guests using various macrocyclic receptors as they provide a unique way to control the tailor-made nanoarchitectures in creating pre-designed functional materials. This section will cover some of the recent works, on the spectacular molecular properties of macrocyclic host-based supramolecular functional assemblies of few organic dyes having technological and biological importance. The following sections discuss about the various applications of the host-guest complexes such as aqueous dye laser, light emitting devices, metal ions sensor, antibacterial agents and drug delivery vehicles.

1.7.1 Water-based Supramolecular Dye Laser

Increased water solubility, enhanced stability, and prevention of aggregation/adsorption of organic dyes in aqueous solution are the crucial parameters for a dye laser system and is nicely demonstrated by the operation of a supramolecularly-assisted aqueous dye laser system of rhodamine dyes with CB7 as the macrocyclic host additive.^{92, 93}

The effect of CB7 on the performance of aqueous dyes solution of kiton red, rhodamine-B and rhodamine-6G has been investigated by both broad-band and narrow-band dye laser set-ups with respect to the practically relevant parameters like lasing efficiency, lasing stability and beam quality. Large increase in lasing efficiency is observed with addition of micromolar concentration of CB7 to the aqueous solution of dye, predominantly due to the deaggregating action of CB7 on the rhodamine dyes.⁹⁴

1.7.2 Cucurbit[8]uril-Based Supramolecular Approach to Fabricate Tunable Luminescent Materials

Light-emitting materials with tunable properties may offer fascinating applications in optoelectronic devices, fluorescent sensors, and imaging agents. A facile cucurbit[8]uril (CB8)-based supramolecular approach that greatly decreases the number of required synthetic steps and produces smart luminescent materials in aqueous solution with tunable and dynamical photophysical properties.⁴⁸ Because of the peculiar electronic distributions of the chromophoric guest 4,4'-(1E,1'E)-1,4-phenylenebis(ethene-2,1-yl)-bis(1-carboxyethylpyridinium) bromide, within the rigid hydrophobic cavity of the cucurbit[8]uril host, color tuning of emissions such as cyan, yellow, green, and white light achieved with better efficiency.⁴⁴ Furthermore, the host–guest interaction, which triggers ratiometric fluorescence responses between blue and yellow emissions, provides evidence that may be used for obtaining pure white-light emission by control of supramolecular assemblies in a cost effective approach.

1.7.3 Enhanced Supramolecular Photosensitizing Behavior

Recently, Zhang et al. fabricated a series of supramolecular photosensitizers from porphyrin derivatives (Por) containing quaternary ammonium groups with

cucurbit[7]uril (CB7) based on host–guest interactions.⁹⁵ The antibacterial activity of Por in the dark could be turned *off* upon binding with CB7, whereas the antibacterial activity under white-light illumination could be turned *on*.⁹⁵

Furthermore, Zhang et al. reported the construction of a supramolecular complex of a water-soluble bifunctional monomer bearing perylenediimide with cucurbit[7]uril on the basis of host–guest complexation, which could be reduced to forming radical anions in the presence of *E. coli*. It was found that this supramolecular complex could display different ability of generating radical anions by facultative anaerobic and aerobic bacteria in terms of their various reductive abilities.

1.7.4 Enhanced Antibacterial Activity of Fluoroquinolone Drugs

Contributing to this, Mohanty et al. demonstrated the significant enhancement in the antibacterial activity of second- and third-generation fluoroquinolone drugs, namely, danofloxacin (DOFL), norfloxacin (NRFL), ofloxacin (OFL), in the presence of CB7, against four pathogenic bacteria at different pH conditions.⁹⁶ In the case of all drugs, the minimum inhibitory concentration (MIC) was reduced to three-five fold in the presence of CB7. The extended shelf-life (antibacterial activity over a period of time) of the fluoroquinolone drugs in the presence of CB7, irrespective of the four types of bacteria, can be attributed to the enhanced photostability of their CB7 complexes.⁹⁶ All these studies are highly encouraging for the use of CB7 for the design and development of new long acting antibiotic formulations.

1.7.5 Fluorescence Sensor for Metal Ions

Organic fluorescence sensor for metal ions is a new technique which has attracted tremendous attention due to its advantages in terms of high emission efficiency and admirable selectivity. In this context, Tao et al. have developed the water based

fluorescence sensor for different metals ions based on the interaction of twisted cucurbit[14]uril (tQ[14]) and thiazole orange (TO) in aqueous medium.²⁵ In this method tQ[14] formed the complex with TO and enhanced the strong fluorescence intensity of TO in both neutral and acidic solutions as compared to free TO. Therefore, they monitor the interaction of the tQ[14]/TO complex with nineteen selected common metal ions. Only Hg^{+2} can lead to increase and Ba^{+2} can lead to reduce the fluorescence intensity of a 2:1 tQ[14]/TO complex in neutral and acidic aqueous solutions.²⁵ On the other side Ba^{2+} or Pb^{2+} can reduce fluorescence intensity of the tQ[14]/TO (15 :1) complex in aqueous HCl solution (pH-2). Therefore, the tQ[14]/TO complex could be act as a supramolecular fluorescence-based sensor for the detection of Hg^{2+} , Ba^{2+} , and Pb^{2+} ions.²⁵

1.7.6 Drug Delivery with Specific Target

In a recent report, Mohanty et al. have established the construction of a non-toxic nanoassembly of bovine serum albumin (BSA) protein and the cucurbit[7]uril macrocycle as well as its stimuli-responsive breakage with adamantylamine or change in pH, which restores the protein structure and recognition properties.³⁸ The assembly showed efficient loading and controlled release of a standard anticancer drug, doxorubicin (DOX), and the same was validated in live cells (Fig. 1.15A).³⁸ The cell viability studies documented that the DOX loaded assembly mask the cytotoxicity of DOX and the toxicity can be revived at the target on demand, triggering its therapeutic activation and is more effective in the cancer cells.³⁸ In addition, they are highly promising for stabilizing/protecting the native protein structure, a viable approach to prevent/inhibit protein misfolding and aggregation, responsible for several neurodegenerative diseases.

1.8 Motivation and Objective of the Present Work

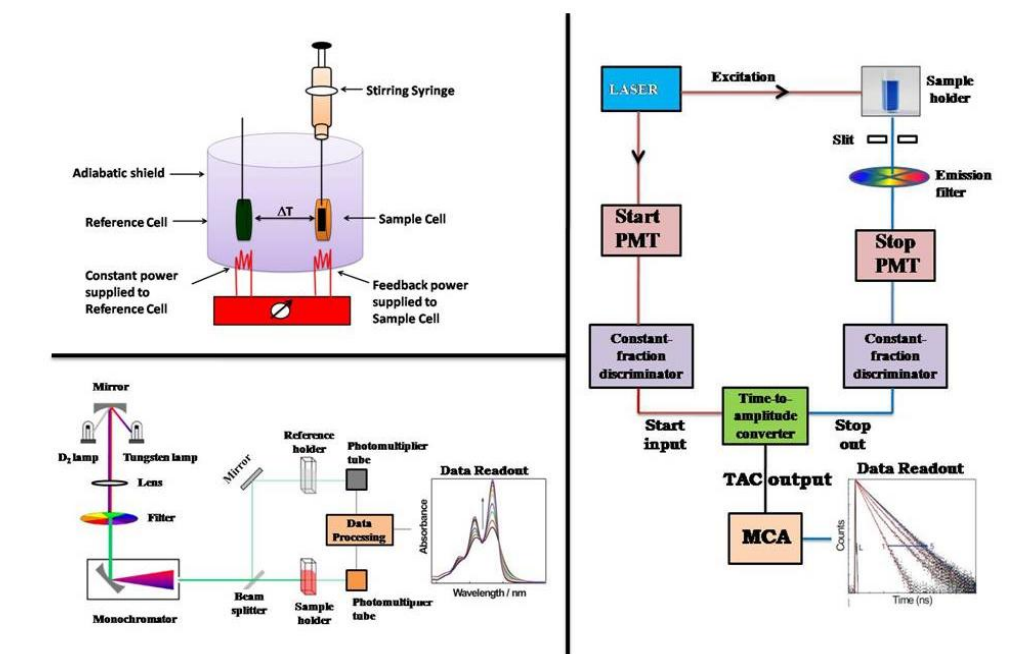
In the past decades, scientists have made enormous advances in creating supramolecular assemblies and molecules with the aim to achieve applications ranging from targeted drug delivery to the development of functional materials.⁴ One of the many different strategies for making supramolecular assembly, disassembly and the adaptive rearrangement of their molecular components have attracted very significant interest in supramolecule host-guest chemistry, the strategy by which well-ordered structural patterns are formed spontaneously from self-directed organization of the individual components through noncovalent interactions.^{5,10,12} Many attempts have been made over the last few decades to realize such non-covalently linked host-guest complexes using classical synthetic macrocyclic host molecules like cyclodextrins, calixarenes, cucurbiturils etc. Stabilize the host-guest complex with optimum stoichiometric composition and structural geometry, which in turn brings out novel features apart from their individual molecular properties. Such host-guest complexes/assemblies have attracted immense research interest due to their tremendous potential in many applied areas, especially in constructing functional materials, fluorescence sensors, on-off switches, controlled cellular uptake and release for drug delivery, etc.²⁶⁻³⁰

In this context, the present thesis aims to construct few such supramolecular assemblies between the selective chromophoric dyes as guest molecules with specific pre-organized macrocyclic host molecules for practical applications with better properties and to characterize them by different spectroscopic methods such as UV-visible and fluorescence spectroscopy, isothermal titration calorimetry (ITC), circular

dichroism (CD), atomic force microscopy (AFM), scanning electron microscopy (SEM) and ^1H NMR spectroscopy. Different types of chromophoric guest molecules such as acridine, rhodamines, thiazole orange, porphyrin and aromatic diimides have been used with suitable macrocyclic hosts to demonstrate their possible applications in different areas like drug delivery, photodynamic therapy, organic electronics, aqueous dye laser, protein fibril inhibitor and fluorescence sensor.²⁸⁻³¹

Chapter 2

Materials and Experimental Methods



2.1 Introduction

To understand the modulation in the photophysical properties of the chromophoric guest dyes upon complexation with the preorganized host molecules, it is necessary to investigate the ground state as well as the excited state properties of the complexes. In this chapter, the details of experimental techniques and methods used for the characterization of the host-guest complexes have been explained. The details of UV-vis absorption and steady-state fluorescence spectrophotometers, time-resolved fluorescence spectrometer which works on the principle of time-correlated single photon counting and circular dichroism spectrometer (CD) used for the photophysical studies of host-guest complexes have been discussed. A brief description of isothermal titration calorimetry (ITC) technique used to find the thermodynamic parameters and stoichiometry of the host-guest complexes has also been provided. Furthermore, the details of other instruments like ^1H - nuclear magnetic resonance (^1H -NMR), fluorescence microscope (FM), scanning electron microscope (SEM) and dynamic light scattering (DLS) which have been used to find out the binding interaction, pattern and size of supramolecular assemblies, have been briefly discussed. Synthetic procedure of the N, N'-bis-(L/D)-phenylalanyl-PDI derivative and N, N'-bis-2-(2-aminoethyl)benzimidazolyl naphthalenediimide and different methods such as photocytotoxicity assay for cell viability study, anti-bacterial activity under white light irradiation and aqueous dye laser experiments have been explained in this chapter.

2.2 Ultraviolet-Visible (UV-vis) Absorption Spectroscopy

To understand the effect of absorption of light by the chromophores, it is important to know the optical absorption characteristics of the complexed and uncomplexed dyes under study. In this study we collect information about the ground-state absorption

characteristics of the chemical compounds in terms of the wavelengths of the absorption bands and the molar extinction coefficients at different wavelengths. UV-vis absorption mainly depends upon the electronic structure and the surrounding environment of the absorbing chromophore which allow the characterization and identification of several chromophoric systems. Change in the surrounding environment like solvent polarity, hydrogen binding ability and polarizability^{85-87, 97} often induce significant change in absorption spectra. Therefore, small change provides us wealth of information regarding the type of ground-state interactions between the chromophoric guests and pre-organized macrocyclic hosts. Measurement of ground state absorption spectra are always very essential to adjust the concentration of the absorbing species in the solution for the purpose of their investigation using different other characterization techniques.

The working principle of the absorption spectrometer is based on the Beer-Lambert's law in which absorbance (A) of an absorbing species in a solution is directly proportional to the concentration (C) of the species and its molar extinction coefficient (ϵ_λ) at the monitoring wavelength λ and is given by the equation 2.1

$$A = \log \left(\frac{I_0}{I} \right) = \epsilon_\lambda Cl \quad (2.1)$$

Where the I_0 and I are the intensities of the incident and transmitted light, respectively, and l is the path length for the light beam passing through the sample cuvette. For spectral measurements the sample is usually taken in the quartz cuvette of 1 cm path length.

Ground state absorption spectra of the chromophoric dyes were recorded using the double beam UV-vis spectrophotometer, from Jasco, Tokyo, Japan (model V-650), available in the department. The wavelength range covered in the spectrophotometer

is 200-800 nm. The light sources used in the spectrophotometer are tungsten (W) lamp for the 800 to 350 nm region and a D₂ lamp for the 350-200 nm region. In the spectrophotometer, Si-photodiodes are used as the light detectors with minimum wavelength resolution is 0.2 nm and lowest absorbance measurable is ~0.005. The schematic of a double beam UV-vis spectrophotometer is shown in Figure 2.1.

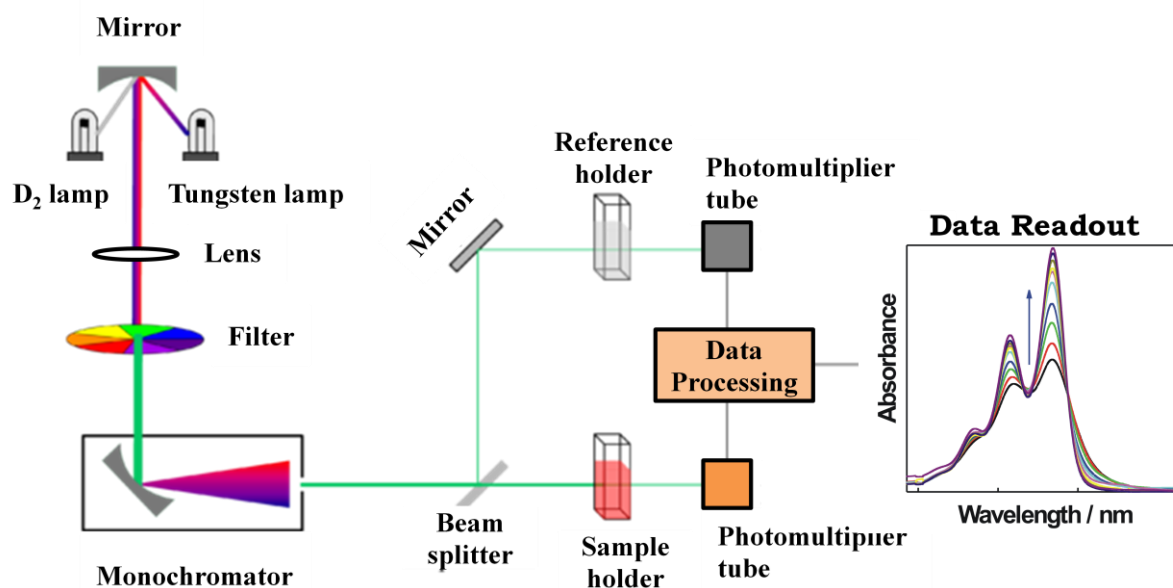


Figure 2.1: Schematic diagram of a double beam UV-vis Absorption spectrophotometer.

2.3 Steady State Fluorescence Spectroscopy

Fluorescence spectroscopy is the simple and sensitive technique to study the photophysical and photochemical processes that occur at excited state of the chromophoric dye molecules. Fluorescence technique directly measures the emission intensity distribution as a function of energy level of photoexcited molecules. The fluorescence emission intensity, emission peak position as well as spectral shape are very sensitive to the surrounding environment and nature of interaction with macrocyclic host molecules.^{85, 86, 97} In this research work, steady-state fluorescence

measurements (either emission spectra or excitation spectra) were carried out by using a FS-5 spectrofluorometer (Edinburgh Instruments, UK). The instrument uses a 450 Watt continuous powered high pressure xenon lamp as the excitation source. Sample is excited in a 1 cm x 1 cm quartz cuvette and the fluorescence is recorded in corrected mode and measured in a perpendicular direction with respect to the direction of the excitation beam source. The wavelength range covered in the present instrument is 200 to 850 nm. The schematic diagram of steady-state fluorescence spectrometer is shown in Fig. 2.2.

Quantitatively calculation of the probability of emission from the photoexcited molecules is measured by fluorescence quantum yield ($\phi_{\text{fluorescence}}$). The fluorescence quantum yield of the photoexcited molecules (ϕ_{sample}) can be expressed with respect to the quantum yield of the reference sample by using the equation 2.2.^{85, 86}

$$\phi_{\text{sample}} = \frac{A_{\text{reference}}}{F_{\text{reference}}} \times \frac{F_{\text{sample}}}{A_{\text{sample}}} \times \frac{\eta_{\text{sample}}^2}{\eta_{\text{reference}}^2} \times \phi_{\text{reference}} \quad (2.2)$$

Where $A_{\text{reference}}$ and A_{sample} are the absorbances at the excitation wavelength, $F_{\text{reference}}$ and F_{sample} are the integrated fluorescence intensities and $\eta_{\text{reference}}$ and η_{sample} are the refractive indices for the reference and the sample solutions, respectively. The measurement of quantum yield of chromophoric molecules with different macrocyclic host system provides important information regarding the aggregation and deaggregation behavior and excited state deactivation mechanism.³² Low quantum yield value leads to enhanced probability of several nonradiative relaxation pathways as compared to that of radiative relaxation.⁹⁸

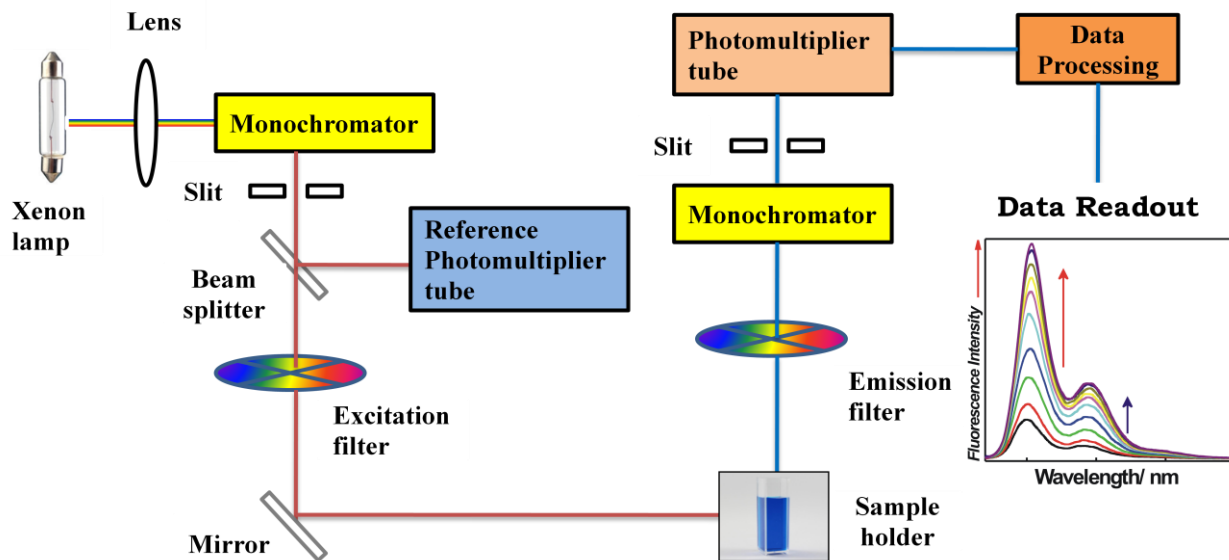


Figure 2.2: Schematic diagram of a steady-state fluorescence spectrometer.

2.4 Time Resolved Fluorescence Spectroscopy

Time-resolved fluorescence measurements were carried out using a time-correlated-single-photon-counting (TCSPC) spectrometer (IBH, UK). In this thesis work 374 nm, 406 nm and 445 nm (~100 ps, 1 MHz repetition rate) diode lasers were used for excitation of the probe molecules and a photomultiplier tube (PMT) was used for fluorescence detection. A re-convolution procedure was used to analyze the observed decays using a proper instrument response function (IRF) obtained by substituting the sample cell with a light scattered (suspension of TiO_2 in water). With the present setup, the instrument time resolution is adjudged to be better than 50 ps following re-convolution analysis. The fluorescence decays were analyzed as a sum of exponentials as,^{86, 90, 97, 99-101}

$$I(t) = \sum B_i \exp(-t / \tau_i) \quad (2.3)$$

Where, $I(t)$ is the time dependent fluorescence intensity and B_i and τ_i are the pre-exponential factor and the fluorescence lifetime for the i^{th} component of the

fluorescence decay. The quality of the fits and consequently the mono or bi-exponential nature of the decays were judged by the reduced chi-square (χ^2) values and the distribution of the weighted residuals among the data channels. For an acceptable fit, the χ^2 value was close to unity and the weighted residuals were distributed randomly among the data channels.

For anisotropy measurements, samples were excited with a vertically polarized excitation beam, and the vertically and horizontally polarized fluorescence decays were collected with a large spectral bandwidth of ~ 32 nm. Using these polarized fluorescence decays, the anisotropy decay function, $r(t)$, was constructed as follows^{85,}

86, 90, 100, 102

$$r(t) = \frac{I_V(t) - GI_H(t)}{I_V(t) + 2GI_H(t)} \quad (2.4)$$

$I_V(t)$ and $I_H(t)$ are the vertically and horizontally polarized decays, respectively, and G is the correction factor for the polarization bias of the detection setup. The G factor was determined independently by using a horizontally polarized excitation beam and measuring the two perpendicularly polarized fluorescence decays. All lifetime measurements were repeated three times. The schematic diagram of a time-correlated-single-photon-counting (TCSPC) spectrometer is shown in Fig. 2.3.

2.4.1 Basic Principles of TCSPC Technique

The principle of TCSPC measurement relies on the fact that the time-dependent probability distribution of the single photon emission from an excited molecule following its excitation is equivalent to the changes in the fluorescence intensity of the sample with time following its δ -pulse excitation.

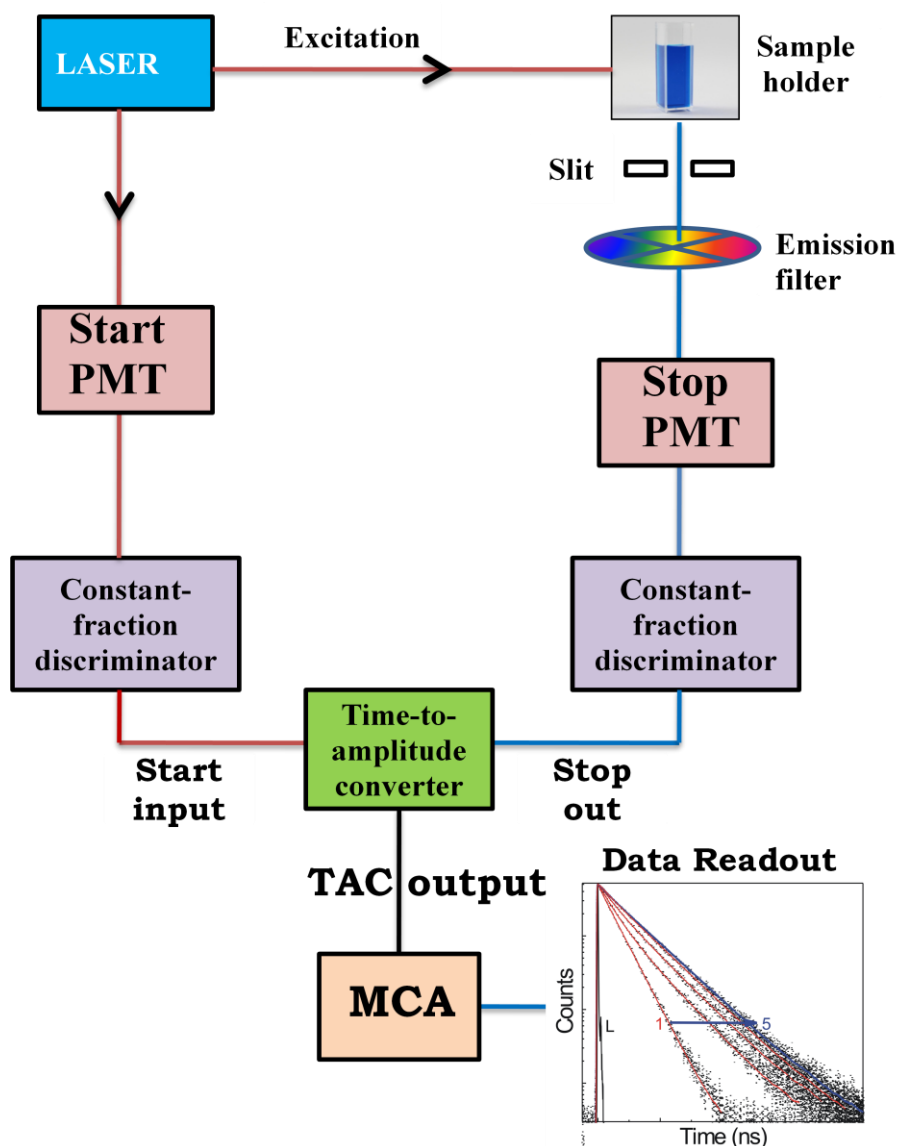


Figure 2.3: Schematic diagram of a time-correlated-single-photon-counting (TCSPC) spectrometer.

The schematic representation of a typical TCSPC set up is shown in figure 2.3, an excitation source signal that is optical pulse is split into two directions, one use for excite the sample kept in the sample holder and other light pulse is directed to a start PMT. The start PMT generates an electrical START signal, which is passing through a Constant Fraction Discriminator (CFD) to the START input of Time to Amplitude Converter (TAC) unit to initiate its charging operation. On receiving the start pulse

TAC continuously undergoes charging linearly with time. On the other side second pulse excites the sample, effectively gives rise to the emission photons. These photons are detected one by one by a stop PMT to generate electrical STOP pulse for each individual photon. The STOP pulses thus generated in the stop PMT are also routed through by another CFD and then variable delay line to the STOP input of the same TAC unit. The TAC stops its charging operation and generates an electrical output signal, which having amplitude directly proportional to time difference (Δt) between the START and the STOP pulses reaching the TAC unit. The TAC output pulse is then fed to the input of a Multichannel Analyzer (MCA) through an Analog to Digital Converter (ADC). The ADC generates a numerical value proportional to the amplitude of the TAC output pulse and thus selects the corresponding memory channel in the MCA, where a single count is added in the MCA is repeated for a large number of times and thus a histogram of counts is collected in the MCA channels. The distribution of counts against the channel number in the MCA represents the fluorescence decay curve of the sample. The fluorescence lifetimes of the samples are estimated following a suitable analysis procedure and introducing a proper time calibration for the MCA channels.^{90, 99, 100, 103, 104}

2.5 Circular Dichroism (CD) measurements

Circular dichroism spectroscopy is the primary techniques to study the stereochemical chiral compounds. In the CD spectral measurement linear polarized light (combination of two circularly polarized light) used as an excitation source. Chiral molecules have different molar extinction coefficients values for left and right circularly polarized light. Therefore, in CD spectroscopy we monitor the differences between absorption of chiral molecule for left and right circularly polarized light.¹⁰⁵ It's similar as

absorption spectroscopy in which absorbance are replaced by differences between the absorbed left and right circularly polarized light. However, linearly polarized light is converted into elliptically polarized light after absorption. The corresponding quantity of ellipticity (θ) = $\arctan(b/a)$, where b and a are the lengths of the semi-minor and semi-major ellipse axes, respectively.⁸⁹ In present research work the CD-spectroscopic measurements were carried out at room temperature and variable temperatures with MOS-500 CD spectrometer from BioLogic, France with Peltier temperature controlled cell holder assembly. Spectra were recorded with 1 mm or 10 mm path length cuvette made of Quartz suprasil from Hellma Analytics, Germany within appropriate concentration range to have reliable CD-signals.

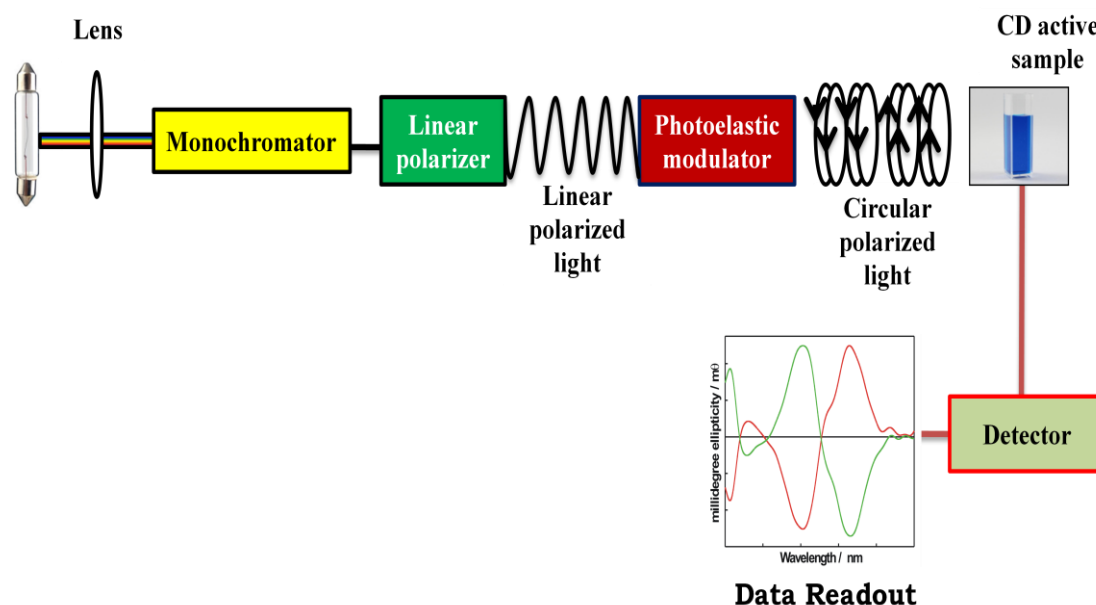


Figure 2.4: Schematic diagram of a circular dichroism spectrophotometer.

2.6 Isothermal Titration Calorimetric (ITC) Measurements

Isothermal titration calorimetry (ITC) is an important and useful physical technique to measure the thermodynamic parameters of interacting species in solution phase. ITC is a titrimetric method which performed at constant pressure and temperature and

offers data on the binding enthalpy, the equilibrium association constant between host-guest and the stoichiometry of the complex. A single ITC experiment directly offers the thermodynamic parameters for a particular system, are related to the interaction process like Gibbs energy, enthalpy and entropy.^{89, 91}

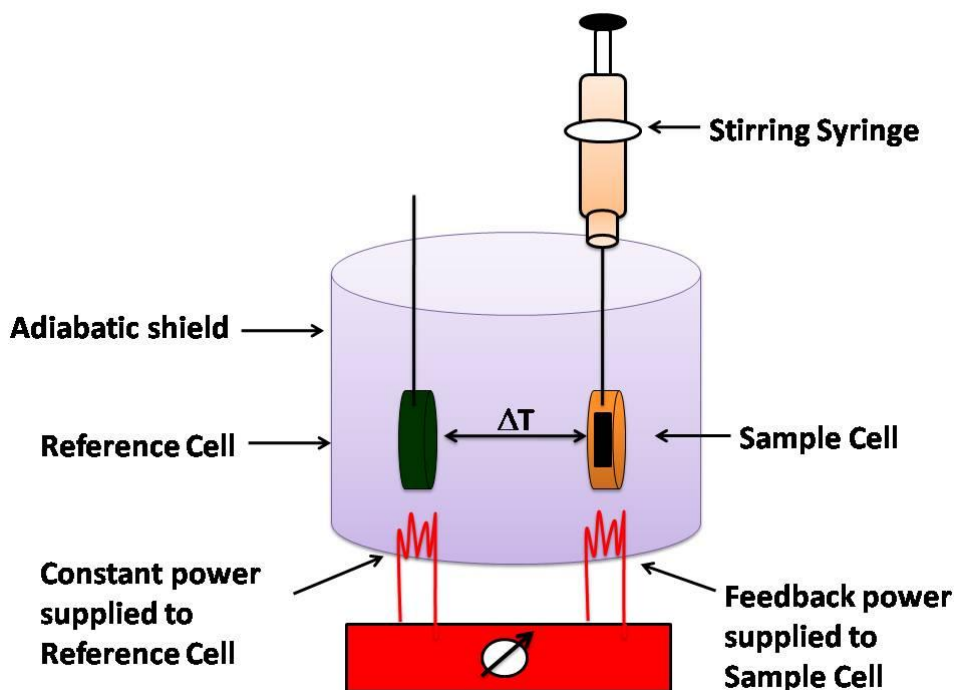


Figure 2.5: Schematic diagram of a Isothermal Titration Calorimetric (ITC) microcalorimeter.

In this instrument, there are two cells, one of which contains reference solution (water, buffer) and is used as a reference cell and the other cell contains the titrate sample.¹⁰⁶ The ligand is loaded into a syringe which sits in a very accurate injection device. The microcalorimeter needs to keep these two cells at exactly the same temperature. The heat sensing detector measured the temperature difference between the cells after every injection and gives feedback to the heater, which reduced this difference by applying voltage and return the cells to equal temperature. In my research work, the ITC experiments were carried out using a Microcal ITC 200 from

Malvern, UK. The guest solution in the sample cell was titrated by adding consecutively 19 injections of 2 μ l of Host at 25 $^{\circ}$ C and both solutions was prepared in same conditions. The first data point was removed from the data set prior to curve fitting with Origin 7.0 software. Thermodynamic parameters of the complex formation were also evaluated using the estimated binding constant value and molar reaction enthalpy (ΔH). The schematic presentation of the ITC microcalorimeter showing in figure 2.4

2.7 ^1H -NMR Spectroscopic Measurements

Over the last fifty years' nuclear magnetic resonance become a primary characterization technique to find out the structure and conformation of chemical compounds. In my research work, the ^1H -NMR experiments were performed in D_2O (99.8%) using Bruker Avance 500 MHz spectrophotometer at National NMR Facility, TIFR, Mumbai, India. Because of the very low solubility of the organic dyes in D_2O at neutral pH, ^1H -NMR experiments could be carried out only at low concentration ($\sim 200\text{-}300\text{ }\mu\text{M}$) of the dye with minimum 1000 scans per spectra. For ^1H -NMR titrations the pD values of the solutions were adjusted by addition of DCl (32% in D_2O) or NaOD (20% in D_2O). The recorded pD values were converted to pH units (+0.4) and final concentrations were determined by UV-Vis absorption spectroscopy.

2.8 Scanning Electron Microscopy (SEM)

SEM analysis was carried out using field emission SEM (Zeiss Sigma FESEM 300). For this purpose, a drop of sample ($\sim 10^{-5}$ M solution) was deposited on a Si-wafer mounted on an Aluminium stub with the help of a double-sided adhesive tape. The samples were dried at room temperature and vacuum dried for 30 min to ensure complete removal of any residual water and coated with gold before being analysed.

2.9 Fluorescence Microscopy (FM)

Fluorescence images were recorded from drop casted samples on a pre-cleaned glass plate/ cover slip using Olympus fluorescence microscope (Model – BX53, Japan) attached to Progres® digital camera.

2.10 Atomic Force Microscopy (AFM)

Images were recorded in semi-contact mode using a NT-MDT solver model P47 instrument. The sample for AFM measurement was prepared by drop casting a dilute solution on a mica sheet, followed by drying.

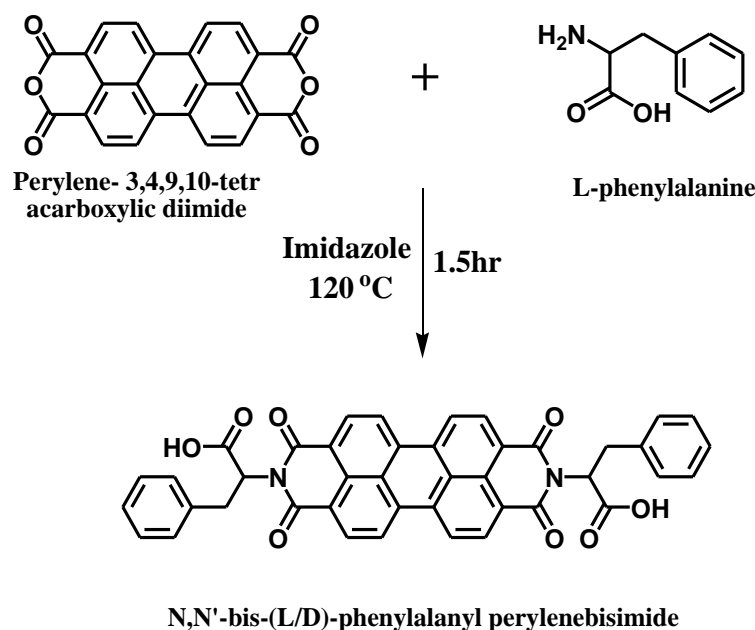
2.11 Dynamic Light Scattering (DLS)

DLS estimates the hydrodynamic diameter of colloidal particle by utilizing their intrinsic properties i.e., Brownian motion and ability to scatter the incident light. Due to the Brownian motion, the position of the particle changes with time and results in fluctuation in the intensity pattern of the scattered light. These intensity fluctuations in scattered light are directly proportional to the movement of the particles. The dynamic light scattering (DLS) measurements were carried out using Malvern 4800 Autosizer employing an Ar ion laser ($\lambda=514.5$ nm) and digital correlator. The scattered light intensity was monitored at a scattering angle of 90° and the intensity correlation function over a time range of 10^{-6} to 1s was computed.

2.12 Synthesis of N,N'-bis-(L/D)-phenylalanyl perylenebisimide (L/D-Phe-PDI)

The PDI derivatives were synthesized through condensation of perylenetetracarboxylic acid dianhydride with L(+)-phenyl alanine and D(-)-phenyl alanine in molten imidazole.¹⁰⁷ Perylene-3,4,9,10-tetracarboxylic acid dianhydride

(0.196g, 0.5mmol, 1eq.) and L/D –phenyl alanine (0.198g, 1.2mmol, 1.4eq.) was mixed thoroughly in powdered imidazole (10g) in a 100ml round bottom flask.



dihydrochloride in DMF solvent in the presence of triethylamine at 120°C. 1,4,5,8-Naphthalene tetracarboxylic-acid dianhydride (0.134g, 0.5mmol, 0.5eq.), triethylamine (4eq.) and 2-(2-aminoethyl)benzimidazole dihydrochloride (0.240g, 1.0mmol, 2eq.) was mixed thoroughly in 20ml DMF in round bottom flask. Then the mixture was stirred at 120°C for 5h in an oil bath and cooled to room temperature. The resulting precipitate was filtered and washed with distilled water until the filtrate is neutral to pH paper. ¹H-NMR (500MHz, DMSO-d₆): δ 8.62 (s, 4H), 7.71 (qd, J₁₂=5Hz, J₁₃=15Hz, 4H), 7.47 (q, J₁₂=5Hz, J₁₃=15Hz, 4H), 4.57 (m, 4H), 2.85 (m, 2H), 2.17 (m, 2H). IR-Data: 2679(b), 2604(b), 1697(s), 1657(s), 1581(s), 1456(s), 1330(s), 1246(s), 1030(s), 870(s), 744(s).

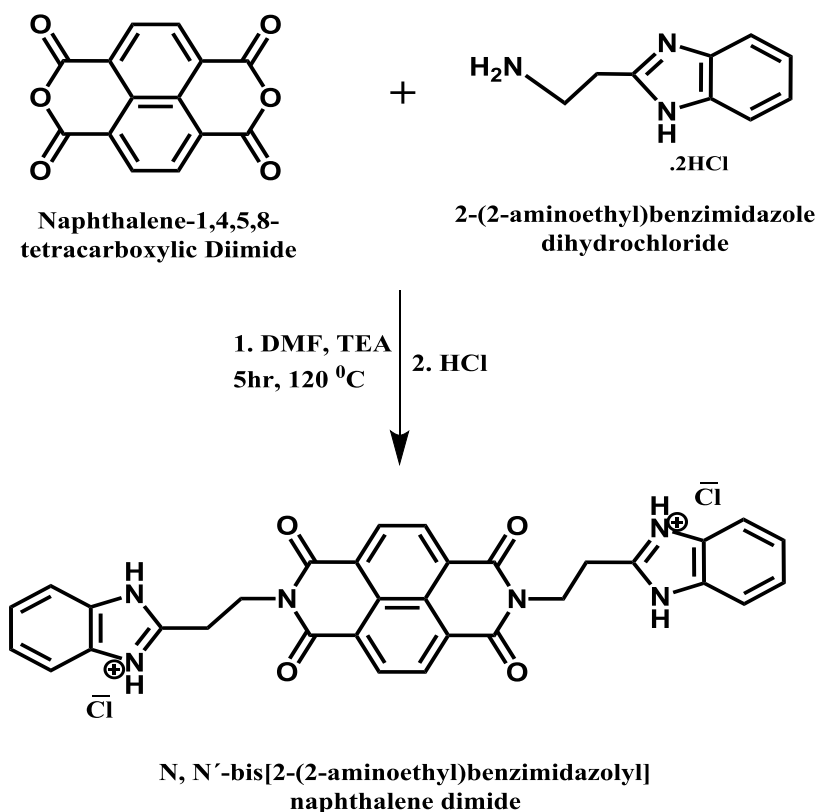


Figure 2.7: Synthetic route of NDI-BzIm dye

2.14 Experimental Method

2.14.1 Evaluation of binding constant for 1:1 complex⁵

The binding constants (K) for the different dyes with the selective host were estimated at suitable pH conditions by the fluorescence titration method assuming 1:1 complexation stoichiometry (eq. 2.5) according to eq. 2.6, which afforded satisfactory fitting results.¹⁰⁸⁻¹¹⁰



$$I_f = I_{\text{Dye}}^0 \frac{[\text{Dye}]_{eq}}{[\text{Dye}]_0} + I_{\text{Host:Dye}}^\infty \frac{[\text{Host : Dye}]_{eq}}{[\text{Dye}]_0} \quad (2.6)$$

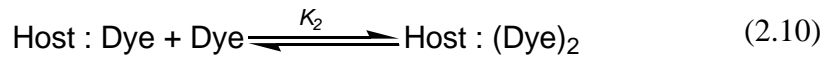
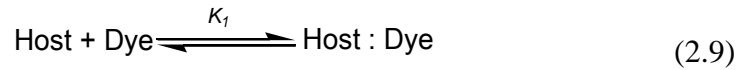
Where, I_{Dye}^0 and $I_{\text{CB7:Dye}}^\infty$ are the extrapolated fluorescence intensities of the uncomplexed and complexed form of the dye, respectively, $[\text{Dye}]_0$ and $[\text{Host}]_0$ are the respective total concentrations of dye and host, and $[\text{Dye}]_{eq}$ is the concentration of uncomplexed dye in the solution. Exchange of the dye during its excited-state lifetime, i.e. the conversion of the uncomplexed dye to the complexed one or vice versa, can be excluded since the corresponding rate constants are very small for macrocyclic host molecules.^{2,3} For fitting, the change in the fluorescence intensity (ΔI_f^λ) was plotted against the total host concentration and the obtained titration curve was fitted according to the rearranged eq. 2.7^{108, 110}

$$\Delta I_f^\lambda = \left(1 - \frac{[\text{Dye}]_{eq}}{[\text{Dye}]_0} \right) (I_{\text{CB7:Dye}}^\infty - I_{\text{Dye}}^0) \quad (2.7)$$

where, $[\text{Dye}]_{eq}$ is expressed as

$$[\text{Dye}]_{eq} = \{ K_{eq}[\text{Dye}]_0 - K_{eq}[\text{SCX6}]_0 - 1 + \sqrt{(K_{eq}[\text{Dye}]_0 + K_{eq}[\text{CB7}]_0 + 1)^2 - 4K_{eq}^2[\text{Dye}]_0[\text{CB7}]_0} \} / 2K_{eq} \quad (2.8)$$

2.14.2 Evaluation of binding constant for 1:2 complex⁵⁴



$$K_{(\text{ternary complex})} = K_1 \times K_2$$

The fluorescence intensity of the system, I , is a function of the intensities of the free guest (I_g) and the 1:1 and 1:2 host-guest complexes (I_{gh} and I_{ggh} , respectively):

$$I = x_g I_g + x_{gh} I_{gh} + 2 x_{ggh} I_{ggh} \quad (2.11)$$

x_g , x_{gh} and x_{ggh} are the mole fractions of the free guest and the 1:1 and 1:2 host-guest complexes.

The mole fractions are further defined as follows:

$$x_g = \frac{[G]}{[G]_0} \quad (2.12)$$

$$x_{gh} = \frac{[HG]}{[G]_0} \Rightarrow x_{gh} = \frac{K_1 [H]_0}{1 + K_1 [G] + K_1 K_2 [G]^2} \cdot \frac{[G]}{[G]_0} \quad (2.13)$$

$$x_{ggh} = \frac{[HG_2]}{[G]_0} \Rightarrow x_{ggh} = \frac{K_1 K_2 [H]_0}{1 + K_1 [G] + K_1 K_2 [G]^2} \cdot \frac{[G]^2}{[G]_0} \quad (2.14)$$

Thus, the fluorescence intensity of the system is obtained through substitution of eq. (2.12-2.14) into eq. (2.11).

$$I = \frac{[G]}{[G]_0} \cdot \frac{(1 + K_1 [G] + K_1 K_2 [G]^2) I_g + K_1 [H]_0 I_{gh} + 2 K_1 K_2 [H]_0 [G] I_{ggh}}{1 + K_1 [G] + K_1 K_2 [G]^2} \quad (2.15)$$

2.14.3 Hydrodynamic volume calculation from anisotropy measurements

Theoretically, the rotational correlation time (τ_r) obtained from the time-resolved anisotropy measurements, for the emitting species can be correlated to the viscosity (η) of the medium and its rotational diffusion coefficient (D_r) and is provided by the Stokes–Einstein relationship (eq. 2.16):^{86, 100}

$$\tau_r = \frac{1}{6D_r} \quad \text{where} \quad D_r = \frac{RT}{6V\eta} \quad (2.16)$$

Here, V is the hydrodynamic molecular volume of the complex, η is the viscosity of the medium and T is the absolute temperature.

2.14.4 Cellular uptake studies

Chinese hamster ovary (CHO) cells obtained from National Centre for Cell Sciences (Pune, India) were cultured in DMEM medium supplemented with 10% fetal calf serum, 100 $\mu\text{g ml}^{-1}$ streptomycin and 100 U ml^{-1} penicillin and maintained at 37 °C under 5% CO_2 and humidified air. Then, cell lines were dispersed in PBS buffer (pH 7.4) and treated separately with acridine in the absence and presence of CB7 and the complex with adamantylamine for 2h. The fluorescence spectra of these solutions were recorded. Furthermore, the treated cell lines were centrifuged and washed twice with PBS buffer before re-dispersing in the same buffer. Emission spectra were recorded with re-dispersed solution with total volume of 1mL with excitation at 358nm. For fluorescence imaging, cells were grown on cover slips, treated separately with the above solutions for 2 h, washed twice with ice cold PBS and recorded the images using an Olympus fluorescence microscope (Model-BX53, Japan) attached to a ProgResS digital camera.

2.14.5 Thin film deposition and I-V measurements

Thin films of the uncomplexed and complexed dyes were deposited on pre-cleaned quartz substrate by drop cast method. For this purpose, 500 μM solution of respective, dye, complex, host were used. Above this film, gold electrodes of thickness about 30 nm and with a channel length of 25 μm were thermally evaporated using a shadow mask, under a vacuum of about 2×10^{-5} mbar. The thickness was monitored using a quartz crystal monitor. The electrical characteristics were measured using Keithley voltage source current meter, (model 6487) in air at room temperature.

2.14.6 Broad-band Dye Laser Experiments

A broad band dye laser cavity of plane–plane resonator configuration was built around dye cell with gain cross section of 10×0.5 mm using one high reflecting (HR) mirror ($R_{\text{av}} \geq 99\%$ over 550 to 650nm) and an output coupler ($R=4\%$ with AR coating at one of the surfaces) with the cavity length of 100mm. The pump beam (Nd:YAG laser from Quantel: 532 nm, 5mJ, 10ns, 10Hz) was focused onto the dye cell (1cm path length cuvette) using 100mm cylindrical lens. All the opto-mechanical component used for holding the HR mirror, output coupler & cuvette holder had fine control over their θ , ϕ movement. The cylindrical lens was mounted on a rotational stage fitted over a translational stage for fine control. The average output power from the dye laser was measured using a M/s Ophir make power meter (Head 3A-P-V1).

2.14.7 Narrow-band Dye Laser Experiments

The lasing performance was studied in a narrow-band dye laser cavity of Littrow grating-configuration. Here the HR mirror of the broad band cavity is replaced by a reflective type holographic grating. The grating chosen was having 2400 lines/mm and fitted on a rotational stage for wavelength tuning. The cavity length was kept 240mm.

The dye solution (~100 ml) as gain medium was flown across 20×1 mm, M/s Lambda Physik dye cell to avoid thermal effects and distortion in dye laser output caused by generation of refractive index gradient in the excited hot zone induced by the pump beam. Similarly, the pump beam (Nd:YAG laser from Quantel: 532 nm, 5mJ, 10ns, 10Hz) was focused on to the flow cell using 100 mm cylindrical lens. Optically matched dye solutions at the pump wavelength (532 nm) were used for the straight comparison of the dye laser performances in ethanol and water solutions. The dye laser output power was measured across a fixed 3mm aperture using a M/s Ophir make power meter (Head 3A-P-V1). The pump power was measured using M/s Ophir make power meter (Head 50(150)A). A small fraction of dye laser output was routed through an optical fibre to a spectrometer (Avantes make spectrometer: Model AvaSpec-2048XL) to measure the wavelength of the laser light. The ensuing tuning curves for each system were constructed by measuring the average dye laser power at each scanned wavelength.

2.14.8 Photostability Measurements of Rhodamine dyes

The optically matched rhodamine dye solutions at pump wavelength (532 nm) in ethanol, and in the presence of SBE₇βCD in water were irradiated with 532 nm laser pulse (Nd:YAG laser (Quantel), 5 mJ, 10 ns, 10 Hz). At different time intervals of laser irradiation, the absorption spectra of each dye solution in a 1mm path length quartz cuvette were recorded using an UV-Vis absorption spectrometer.

2.14.9 Photostability Measurements of TMPyP dye

TMPyP and Captisol:TMPyP systems were irradiated with low irradiance light from a 150 W Xenon lamp (fluence rate $\sim 80 \mu\text{W cm}^{-2}$ for 1 hr at 422 ± 2.5 nm). The

photodegradation of these systems was monitored by measuring the absorbance at different times at 422 nm.

2.14.10 Singlet Oxygen (1O_2) Generation Measurements

We have adopted the reaction of 1O_2 , generated from TMPyP or Captisol:TMPyP system on light irradiation, with 1,3-diphenylisobenzofuran (DPBF) to evaluate the quantum yield of 1O_2 from these systems.¹¹¹ 2 mL of air-saturated DPBF solution containing TMPyP or Captisol:TMPyP in DMF in a quartz cuvette was irradiated at 510 nm (to avoid the direct excitation of DPBF). The depletion of DPBF were followed by monitoring the decrease in optical density at 417 nm. Since TMPyP is having sufficient absorbance at ~417 nm, control experiments without DPBF were carried out to determine the actual decrease in the absorbance of DPBF. $[Ru(bpy)_3]^{2+}$ was used as standard and its $^1O_2^*$ generation yield is considered as ~0.81 in air-saturated methanol.¹¹²

2.14.11 Antibacterial Activity Measurements

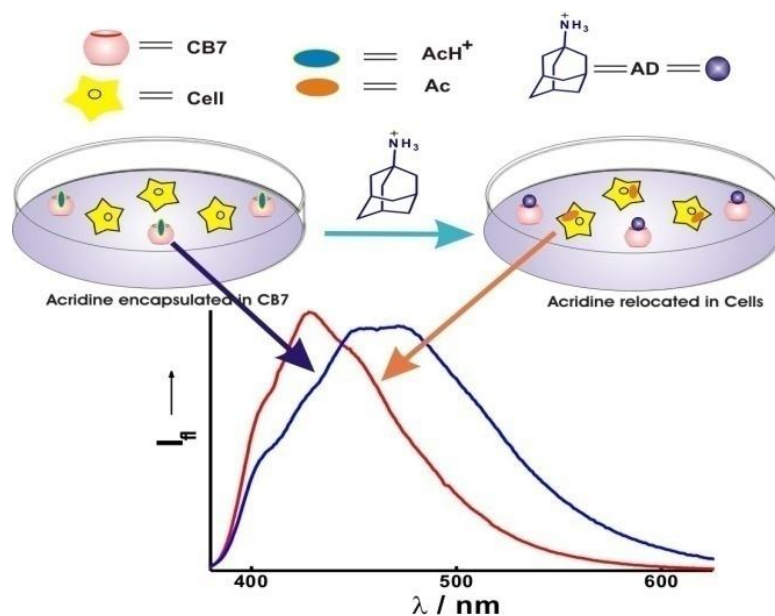
A single isolated colony of *Escherichia coli* from the Luria agar plate was transferred to 5.0 ml of Luria broth and incubated at 35 ± 2 °C for 18-20 hrs. 5 µl of the culture was then transferred to fresh medium (5.0 ml LB) and incubated at 35 ± 2 °C for 18-20 hrs. The culture was diluted to obtain 10^7 cfu/ml using 0.85% saline. The cells were incubated in dark with TMPyP or Captisol:TMPyP systems for 15 min. (15.0 ml culture containing 100 µl of dye or complexed dye) and then exposed to white light (LED, fluence rate ~50 mW cm⁻²) at different time durations. Appropriate dilutions (10^4 , 10^3) were spread plated (100 µl) on previously prepared Luria agar plates. The plates were incubated at 35 ± 2 °C for 18-20 hrs and the colonies were counted. The plates unexposed to light served as control.

2.13.12 Photosensitization Activity in Tumor Cells

MTT assay was carried out for the evaluation of cytotoxicity for TMPyP and Captisol:TMPyP systems in normal Chinese Hamster Ovary (CHO) cell line without white light irradiation and in human lung carcinoma A549 cell line with and without white light irradiation (LED, fluence rate $\sim 50 \text{ mW cm}^{-2}$). Both cell types were cultured as monolayers in phenol red free DMEM medium supplemented with 10% FBS, $100 \mu\text{g mL}^{-1}$ streptomycin and 100 U mL^{-1} penicillin at 37°C under 5% CO_2 and humidified air. In brief $\sim 2 \times 10^4$ cells in $200 \mu\text{L}$ of phenol free DMEM medium in ninety-six well plate were treated with the desired concentrations of samples and incubated at 37°C for 2 hrs. Following this, cells were exposed to white light for 30 min, cultured for 48 hrs in the humidified incubator and processed for MTT assay as described previously.²¹ The bright field images of the cells were captured using Olympus fluorescence microscope (Model-CKX41, Japan) attached to a ProgRes® digital camera. For determining the dark toxicity, cells treated with TMPyP and Captisol:TMPyP systems were cultured for 48 hrs without exposing to white light and processed for MTT assay. The control group represents cells grown in DMEM medium without any treatment. The percentage of cell viability was calculated from the decrease in absorbance at 570 nm of treated groups as compared to that of control group.

Chapter-3

Host–Guest Interaction of Acridine dye with Cucurbiturils: Stimuli Responsive pK_a Tuning and Guest Relocation into Live Cells



Org. Biomol. Chem. 15, 2017, 8448-8857

3.1 Introduction

Molecular properties of organic chromophoric guest molecules can often be modulated favourably by the formation of noncovalent host-guest complexes and such host-guest complexes are currently being used in various activities like drug delivery, aqueous dye laser, photodynamic therapy, chemosensing,¹¹³ supramolecular architectures,^{23, 114} optoelectronics like optical sensor,¹¹⁵ enzymatic assay,¹¹⁶ on-off switches^{53, 69} and logic gates,⁷⁰ photostabilization,^{22, 71} supramolecular catalysis,⁷² nanocapsules,⁷⁵ and other stimulus responsive functional devices.¹¹⁷ Especially, encapsulation of organic aromatic drug molecules by macrocyclic hosts often leads to reduce the side effects and increase the fraction of drugs that reaches its target. This supramolecular host-guest approach has expanded last few years in the pharmaceutical or biopharmaceutical field like drug solubility, protect drug from unkind environment and enhance drug localization. In accomplishing this, a large number of molecules have been studied to explore and establish the structure-property relationships with the different types of macrocyclic receptors such as cyclodextrins, calixarenes, cucurbiturils, etc.^{42, 118, 119} This macrocyclic carriers facilitated increased drug accumulation at the tumor site, enhanced cell permeability, and reduced cardio toxicity.¹²⁰ Cucurbit[n]urils (CBn), a relatively young class of macrocycles, comprise of glycoluril monomers joined by pairs of methylene bridges and depending upon the number of glycoluril units of these host molecules, homologues of different cavity sizes and portal dimensions are known (see Chapter-1, Table 1.1).^{39, 41-43, 47} The pumpkin-shaped CB is having highly symmetrical structure with two identical carbonyl portals and a hydrophobic cavity which can accommodate the organic guest molecules partly

or completely to form stable inclusion complexes, already explained in chapter-1 (1.4.1). In an earlier work, a stimuli-responsive, reversible and non-toxic supramolecular nanoassembly has been constructed based on host–guest interaction involving bovine serum albumin (BSA) and a CB7 macrocycle.³⁸ The assembly successfully uptakes the anticancer drug, Doxorubicin and efficiently releases it on interaction with an external stimulant.

In this study, we report controlled relocation of the acridine dye from the host cavity to the live cells. Acridine dye, one of the N-heterocyclic aromatic compounds, which has a planar rigid structure and shows good fluorescence quantum yield, has been largely used in fluorescent labelling of biomolecules such as DNA and RNA¹²¹ and in the manufacturing of valuable drugs showing antimicrobial/ antiseptic properties.¹²¹ Acridines are effective DNA-intercalating anticancer agents^{122, 123} and in an earlier study, Sedlacek, *et al.* have reported the pH-controlled release of polymer conjugates of acridine-based anticancer drugs in cancerous cell lines.¹²³ Acridine exists in two prototropic forms ($pK_a \sim 5.3$) in aqueous solution,^{110, 121} namely, neutral (Ac) and protonated (AcH^+ , see in Fig. 3.1) forms and shows characteristic fluorescence spectra for both the forms and therefore, acridine derivatives are also used as pH probes.¹²⁴

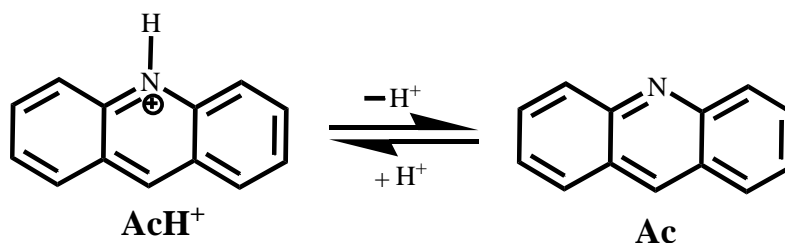


Figure 3.1: Chemical structures of protonated (AcH^+) and neutral (Ac) forms of acridine dye.

This has led to related applications in investigations of micro-heterogeneous and confined media such as micelles,¹²⁵ cyclodextrins and calixarene.¹²⁶ In the case of β - and γ -cyclodextrin macrocycles, only the neutral form of the dye gets encapsulated in their cavity, whereas the protonated form prefers to remain in the aqueous bulk.¹²⁶ However, in the case of *p*-sulfonatocalix[6]arene (SCX6), the protonated form shows strong interaction towards SCX6 than the neutral form, which leads to a large upward pK_a shift (~ 2 units) in the dye.¹¹⁰ Exploring the details of such macrocycle induced changes in the protolytic equilibrium, in this study we investigate the effect of two cucurbituril hosts i.e. cucurbit[7]uril (CB7) and cucurbit[8]uril (CB8) with acridine dye. Along with the dramatic modulation of the excited state properties of acridine due to different stoichiometric arrangement of the CB-acridine complexes, the study revealed a tunable upward pK_a shift of ~ 3.4 units, which can be readily applied for controlled relocation of the dye from the host to the live cells.

3.2 Materials and Methods

Acridine and cucurbit[8]uril were obtained from Sigma-Aldrich, and used as received. Cucurbit[7]uril (CB7) was synthesized according to the reported procedure and was characterized by $^1\text{H-NMR}$.⁴⁴⁻⁴⁶ Nanopure water (Millipore Gradient A10 System; conductivity of $0.06 \mu\text{S cm}^{-1}$) was used to prepare the sample solutions. HCl/HClO_4 as well as NaOH used for pH adjustment were obtained from Merck India. Solution pHs were measured by a pH meter model PC 2700 from EUTECH instruments, India. Before measurements, the pH meter was calibrated at two pHs, namely, at pH 7 and pH 4, by using standard pH buffer solutions from Merck (India). The details of absorption and fluorescence (steady state and time resolved) measurements and Cellular uptake studies which are used in this chapter were provided in the chapter-2.

3.3 Results and Discussion

3.3.1 Absorption Spectral Characteristics of Acridine Dye in the Presence of Cucurbiturils

Since the ground state pK_a value of the acridine dye is about 5.3,¹¹⁰ in acidic solution ($pH < 4$), the protonated AcH^+ form of the dye exists and displays a strong and sharp absorption peak at ~ 354 nm and another broad and weaker absorption band centered at ~ 400 nm along with a shoulder at ~ 340 nm (Fig. 3.2).^{127, 128} In alkaline condition ($pH > 7$), the neutral Ac form prevails, retaining the strong absorption peak at ~ 355 nm and shoulder at 340 nm but with a reduced absorption band at around 380 nm (Fig. 3.2).^{127, 128} The pH-dependent absorbance changes at 355 nm (inset of Fig. 3.2) were fitted according to the following relation (eq. 3.1),¹¹⁰

$$A_{obs} = \frac{A_{AcH^+}^{\infty}}{\{1 + 10^{pH - pK_a}\}} + \frac{A_{Ac}^{\infty}}{\{1 + 10^{pK_a - pH}\}} \quad (3.1)$$

Where A_{obs} is the observed absorbance at any pH, and $A_{AcH^+}^{\infty}$ and A_{Ac}^{∞} are the extrapolated absorbances of the AcH^+ and Ac forms, respectively. From this analysis, the pK_a value of the dye in its ground state was found to be 5.4 ± 0.1 , which matches well with the reported value.^{110, 121}

On the addition of CB7 to the aqueous solution of acridine at $pH \sim 3.5$, the absorbance of the AcH^+ at 354 nm decreases marginally with a slight hypsochromic shift of ~ 2 nm. These changes in the absorption characteristics of AcH^+ in the presence of varying CB7 concentrations are shown in Fig. 3.3A.

Interesting to note that the absorbance of AcH^+ attains a limiting value even with a very low CB7 concentration (i.e. $\sim 50 \mu M$); suggesting very strong binding of the cationic form of the dye with CB7 host. The stoichiometric evaluation was carried out

by monitoring the absorbance changes for the complex at 355 nm by continuous variation method. The Job plot method displayed maxima at 0.5 mole fraction of dye indicating a 1:1 inclusion complex formation between CB7 and the dye at pH ~3.5 (inset of Fig. 3.3A).

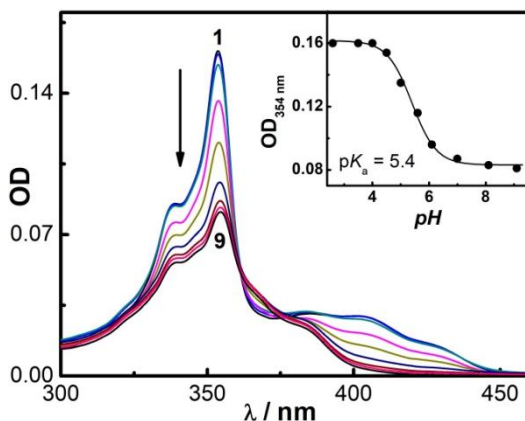


Figure 3.2: Absorption spectra of acridine (2.45×10^{-6} M) in water at different pHs. (1) 2.6, (2) 4.0, (3) 4.5, (4) 5.0, (5) 5.6, (6) 6.1, (7) 7.0, (8) 8.1 and (9) 9.1. Inset: variation in absorbance with pH at 354 nm.

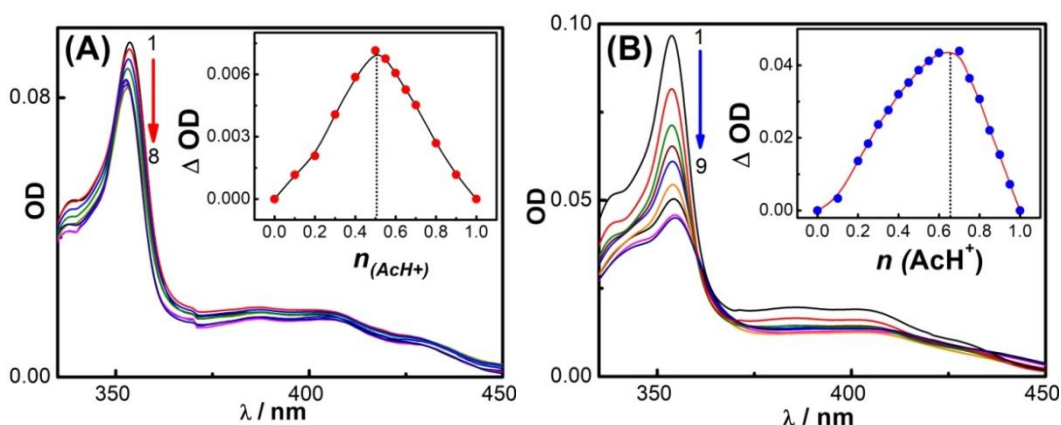


Figure 3.3: Absorption spectra of AcH^+ (5.7×10^{-6} M) in aqueous solution at different concentrations of CB7 (A) and CB8 (B) at pH 3.5. [CB7]/ μM : (1) 0, (2) 2, (3) 4, (4) 6, (5) 10, (6) 20, (7) 80 and (8) 150. [CB8]/ μM : (1) 0.0, (2) 0.9, (3) 2.2, (4) 4.4, (5) 6.6, (6) 8.8, (7) 13.2, (8) 26.4 and (9) 53.0. Insets show the Job plots for the respective systems, OD changes monitored at 353 nm.

On the other hand, upon addition of CB8 to the AcH^+ dye solution, the absorbance at the 354 nm centered band decreases significantly without any change in the peak position at 354 nm (Fig. 3.3B). Also the ratio between the peak position and the shoulder at ~340 nm, which corresponds to dimer/aggregated form decreases (see in Fig. 3.4) In this case, the absorbance of the dye attains saturation within ~20 μM concentration of CB8 indicating the strong complex formation between CB8 and AcH^+ . Comparison among the above two cases of CB7 and CB8 with AcH^+ , it is seen that the nature and extent of changes on the AcH^+ absorption characteristics are indicative of a possible difference in the interaction mode of AcH^+ with CB7 and CB8. The stoichiometric analysis by the Job plot method showed a maximum at ~0.67 mole fraction of AcH^+ (inset of Fig. 3.3B), indicating two AcH^+ dyes are encapsulated in the CB8 cavity in a 1:2 ($\text{CB8}:(\text{AcH}^+)_2$) stoichiometry. The stoichiometry is further confirmed from the isothermal titration calorimetry (ITC) experiments and energy optimization studies, discussed later.

The binding affinity of the Ac form of the dye with CB7 and CB8 was studied at pH ~11. The selection of this higher pH was necessary, as it is anticipated that the interaction of acridine with cucurbiturils may bring out a shift in the pK_a values in the upward direction (>2 units reported for several of such related dyes with CB7 and CB8)^{42, 108, 109, 129} and is also validated for acridine in the current measurements (discussed later).

The absorption spectra of the dye do not show any change even in the presence of reasonably high concentration of CB7 (Fig. 3.5) and CB8 (100 μM , maximum solubility of CB8), suggesting that Ac form does not undergo any

significant complexation with CB7 and CB8 and hence the binding of the Ac form (at pH ~ 11) must be much lower than that of the AcH^+ (at pH ~ 3.5). Due to this weak interaction and small changes in the absorption spectra, Job plot measurements could not be done at pH 11.

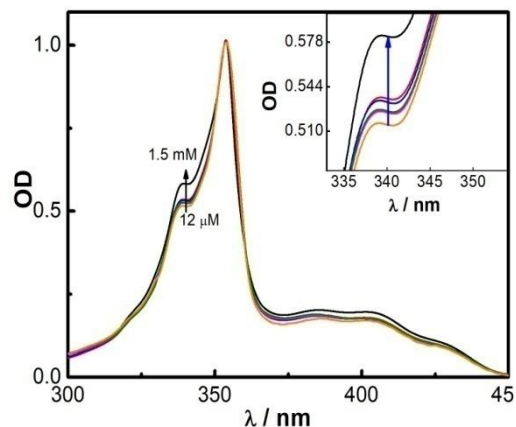


Figure 3.4: Concentration dependent normalized absorption spectra of acridine dye at pH ~ 3.5 .

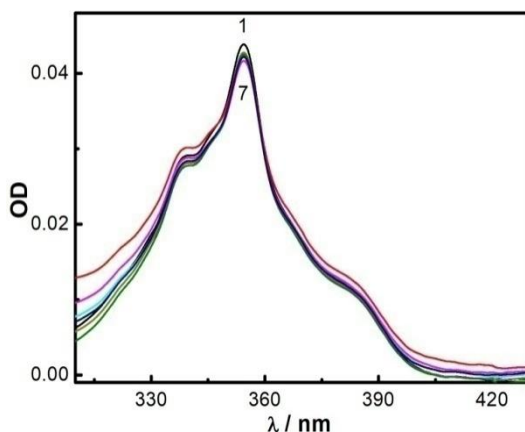


Figure 3.5: Absorption spectra of Ac (4.5×10^{-6} M) in aqueous solution at different CB7 concentrations at pH 11. $[\text{CB7}]/\mu\text{M}$: (1) 0, (2) 5, (3) 20, (4) 77, (5) 113, (6) 157 and (7) 206.

3.3.2 Steady-state Fluorescence Characteristics of Acridine Dye in the Presence of Cucurbiturils

Albeit there are very small changes in the absorbance of the AcH^+ and Ac forms of the dye in the presence of CB7, the steady-state fluorescence characteristics of AcH^+ form display considerable changes upon addition of CB7, specifically,

a large reduction in its fluorescence intensity at 479 nm (see in Fig. 3.6A), indicating strong interaction between AcH^+ form and CB7. Ac form (at pH 11) displayed gradual decrease in the fluorescence intensity with the addition of CB7, without any change in its maximum at 430 nm (Fig. 3.6B). This is in contrast to the fluorescence enhancement generally observed with other dyes such as neutral red, acridine orange (dimethylamine derivative of acridine), coumarins, thioflavin T etc. with CB7.^{108, 130, 131} In this regard, the strong fluorescence quenching observed in case of acridine in the presence of CB7 is very interesting as these changes represent an inclusion complex formation between them. Nevertheless, the possibility of a small percentage of exclusion complex formation between CB7 and the dye cannot be totally ruled out completely. It is known that the fluorescence behavior of acridine depends on the nature of solvents; dye is fluorescent in protic solvents and nonfluorescent in aprotic solvents and has been interpreted as the hydrogen bond interaction causes an interchange of the electronic character in the lowest excited singlet state i.e. $\pi-\pi^*$ in protic solvents such as in water and methanol and $n-\pi^*$ in aprotic solvents such as hydrocarbons.¹³²

It may happen that the encapsulation of dye inside the hydrophobic cavity of cucurbituril changes the electronic character from $\pi-\pi^*$ to $n-\pi^*$. As a result, the CB7-dye complex is nonemissive in nature and the fluorescence intensity decreases on increasing the concentration of CB7 due to the increase in the concentration of the complex. The decrease in the fluorescence intensity of both AcH^+ and Ac on complexation with CB7 can also be attributed to the

charge transfer type or hydrogen bonding interactions of the encapsulated dye with the carbonyl rim of CB7.

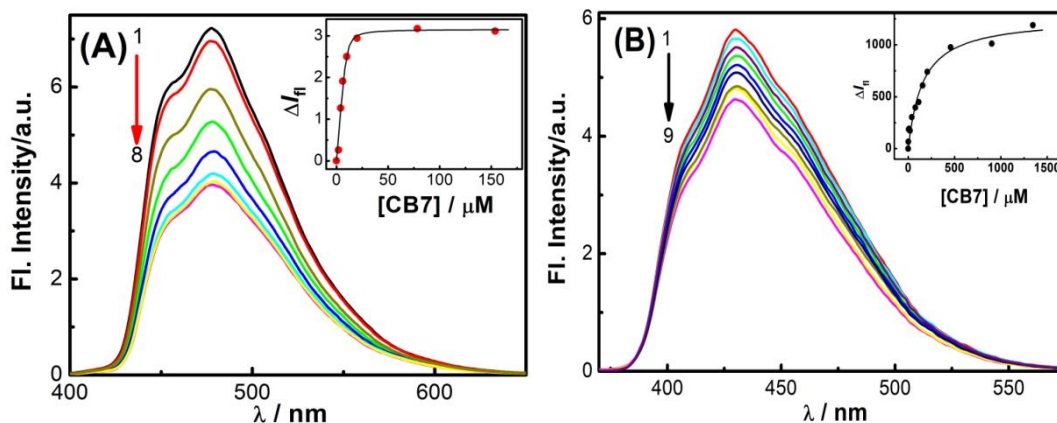


Figure 3.6: (A) Fluorescence spectra of AcH^+ ($5.7 \times 10^{-6} \text{ M}$) in aqueous solution at different concentrations of CB7 at pH 3.5. [CB7]/ μM : (1) 0, (2) 2, (3) 4, (4) 6, (5) 10, (6) 20, (7) 80 and (8) 150. Insets show the changes in the fluorescence intensity (ΔI_f) versus [CB7] of the respective complex systems. (B) Fluorescence spectra of Ac ($4.5 \times 10^{-6} \text{ M}$) in aqueous solution at different CB7 concentrations at pH 11. [CB7]/mM: (1) 0.0, (2) 0.02, (3) 0.04, (4) 0.11, (5) 0.16, (6) 0.21, (7) 0.46, (8) 0.90 and (9) 1.35.

However, in the case of CB8 as presented in Fig. 3.7, the fluorescence intensity monitored at 477 nm displayed a dramatic decrease i.e. ~ 5 fold with $\sim 50 \mu\text{M}$ CB8 concentration. The extent of fluorescence intensity decrease observed in CB8 is distinctly different from changes observed in the CB7 case. These notable differences in the fluorescence behavior of AcH^+ , independently introduced by CB7 and CB8 would, indicate different structural environments experienced by the dye due to the variation in the cavity dimensions of the two macrocyclic homologues.

The severe fluorescence quenching observed with CB8 host as compared to CB7, is also in line with the dimer formation contented from the Job plot (1:2 stoichiometry of $\text{CB8}:\text{AcH}^+$ system) as one would expect fluorescence

quenching due to the non-fluorescent excimer type of interaction within the cavity¹³³ along with the possible changes in the electronic character from $\pi-\pi^*$ to $n-\pi^*$ in the CB8 cavity.²⁹

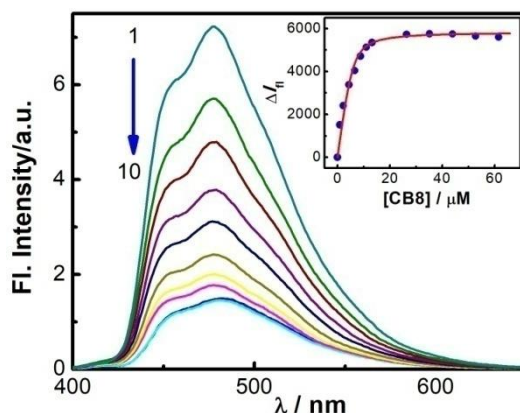


Figure 3.7: Fluorescence spectra of AcH^+ (5.7×10^{-6} M) in aqueous solution at different concentrations of CB8 at pH 3.5. $[\text{CB8}]/\mu\text{M}$: (1) 0.0, (2) 0.9, (3) 2.2, (4) 4.4, (5) 6.6, (6) 8.8, (7) 11.0, (8) 20, (9) 53.0 and (10) 66.0. Insets show the changes in the fluorescence intensity (ΔI_f) versus $[\text{CB8}]$ of the respective complex systems.

The details of the binding interactions of the dye with the CBs were further analyzed by following the fluorescence quenching with the increasing concentration of the hosts. The binding constants (K) for the AcH^+ and Ac forms of acridine dye with CB7 host were evaluated by the fluorescence titration method, assuming 1:1 complexation stoichiometry (see details in chapter 2, 2.14.1).¹⁰⁸ Concentration of the dye was maintained constant at a particular pH (3.5 for AcH^+ or 11 for Ac) while the concentration of CB7 was varied till the fluorescence changes reached saturation. From the plot of emission intensity (at 477 for AcH^+ and 430 nm for Ac) with CB7 (insets of Fig. 3.6A and Fig. 3.6B), the binding constants were estimated in agreement to 1:1 model (see details in chapter 2, 2.14.1) and are found to be $(1.8 \pm 0.4) \times 10^6$

M^{-1} for the $\text{CB7}:\text{AcH}^+$ complex and $(6.5 \pm 0.3) \times 10^3 \text{ M}^{-1}$ for the $\text{CB7}:\text{Ac}$ complex. According to these values, the protonated form of acridine binds more than two orders of magnitude stronger to CB7, compared to the neutral form. In the presence of CB8, the net binding constant ($K_{\text{ternary}} = K_1 \times K_2$) of the ternary complex $\text{CB8} \cdot (\text{AcH}^+)_2$, estimated from the fluorescence titration curve (Insets of Fig. 3.7), was found to be $(5.2 \pm 0.8) \times 10^9 \text{ M}^{-2}$ by using a 1:2 complexation model, (see details in chapter 2, 2.14.2). However, due to the solubility limitation of CB8, similar titration on Ac with CB8 (at pH ~11) could not be carried out, and the binding constant for the neutral form with CB8 could not be estimated reliably.

Furthermore, the binding stoichiometry of both the $\text{CB7}:\text{AcH}^+$ and $\text{CB8}:\text{AcH}^+$ systems was corroborated by the ITC measurements. The data obtained from ITC measurement is consistent with the 1:1 complex formation between CB7 and AcH^+ (see in Fig. 3.8A). ITC afforded 50 times lower binding constant ($K = (3.8 \pm 0.2) \times 10^4 \text{ M}^{-1}$) as obtained from the fluorescence titration since the ITC experiments were carried out in 10mM acetate buffer (pH 3.8). On the other hand, ITC titrations of CB8 with AcH^+ led to sequential binding isotherms (Fig. 3.8B), which are also diagnostic of 1:2 stoichiometry for the $\text{CB8}:\text{AcH}^+$ system. For the ITC titrations, a sequential 1:2 binding model gave a satisfactory fit, from which a net ternary binding constant of $K_{\text{ternary}} = K_1 \times K_2 = 1.7 \times 10^9 \text{ M}^{-2}$ has been evaluated. In fact, this value may be associated with a larger error limit due to the higher-order complexation pattern and low absolute heats, limited by the solubility of CB8. The π -stacking between two AcH^+ dyes

in the CB8 cavity and the ion-dipole interaction between the dye and host overcome the repulsion between two similar charges AcH^+ molecules.

The strong binding of the protonated form with CB7 and CB8 can be readily rationalized by recollecting that along with the hydrophobic interaction inside the CB cages, the host is also having cation receptor property, since their carbonyl rims can stabilize the positive charges of the guest through ion-dipole interaction. The decrease in the fluorescence intensity of both AcH^+ and Ac on binding with CB7 can be attributed to the hydrogen bonding or charge transfer type of interactions of the encaged dye with carbonyl rim of CB7, whereas the large decrease in the fluorescence intensity of AcH^+ with CB8 can be attributed to the formation of nonemissive excimer of the dye in the CB8 cavity along with the hydrogen bonding and charge transfer interactions.^{55, 69, 133}

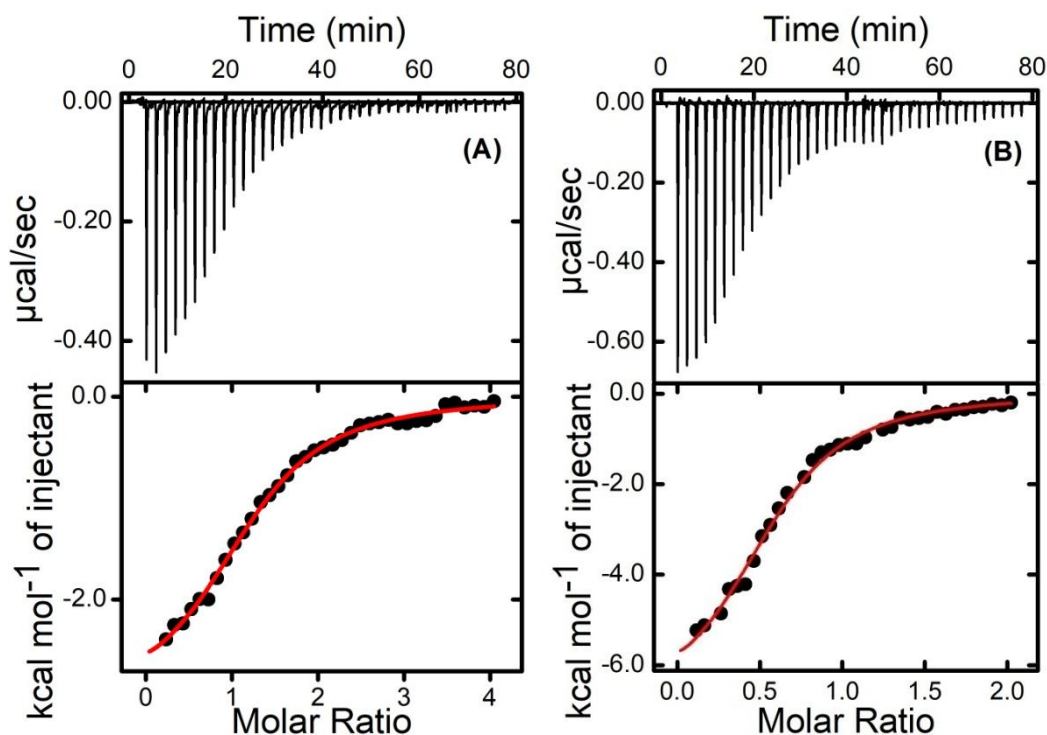


Figure 3.8: (A) ITC isotherm for titration of AcH^+ with CB7 in water at 25 °C. (B) ITC isotherm for titration of CB8 with AcH^+ in water at 25 °C.

The fluorescence decays of both AcH^+ and Ac forms in aqueous solution (at pH 3.5 and 11, respectively) in the absence and presence of CB7 and CB8 have been measured. The fluorescence decays of both AcH^+ and Ac forms are effectively mono-exponential in the absence of CB and the fluorescence lifetimes (τ_f) are 31.5 ns and 9.1 ns, respectively.¹¹⁰ The typical decay traces of AcH^+ forms in the absence and presence of CB are shown in Figures. 3.9. However, to our surprise, there is no change in the fluorescence lifetime of both the forms in the presence of CB7 (Fig. 3.9A).

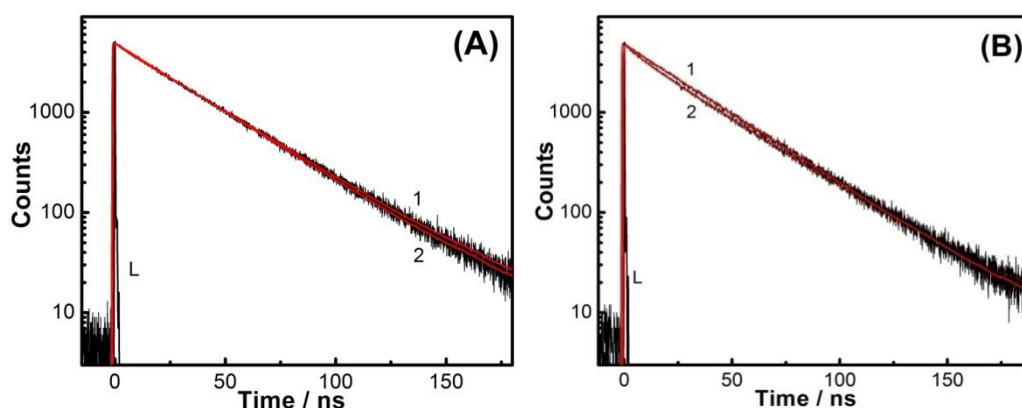


Figure 3.9: Decay traces of AcH^+ in solutions at pH ~ 3.5 in the absence (1) and presence (2) of 250 μM CB7 (A) and 70 μM CB8 (B). 'L' represents excitation lamp profile. $\lambda_{\text{ex}} = 374 \text{ nm}$.

As we see that the fluorescence quenching is observed at very low concentration of CB7, it indicates that the interaction between CB7 and AcH^+ is diffusionless and follows static quenching leading to a nonemissive ground state complex. Since the free AcH^+ form shows a very good fluorescence quantum yield ($\Phi_f \sim 0.56$), a small percentage of its existence will display the emission from the free dye and its corresponding decay trace recorded in the nanosecond time region. Explicitly, a simple estimate of this at the highest concentration of

the host concentration reveals that $\sim 0.6\%$ of the free dye would remain in the solution. Whereas, upon addition of CB8 to the AcH^+ solution (at pH 3.5), a minor component (4%) having a lifetime of approximately ~ 5 ns appeared without affecting the major component of lifetime (31.5 ns). The minor component could be attributed to the lifetime of the CB8 induced dimer (see in Fig. 3.9B).

3.3.3 ^1H NMR Studies of the Complexes

^1H NMR measurements are carried out to get insight about the positioning of the acridine dye and CB in the complex from the changes in the chemical shifts. We have looked at the ^1H NMR chemical shifts of the aryl protons (H_a to H_e) of acridine dye in the absence and presence of CB at pD ~ 4.5 in Fig. 3.10.

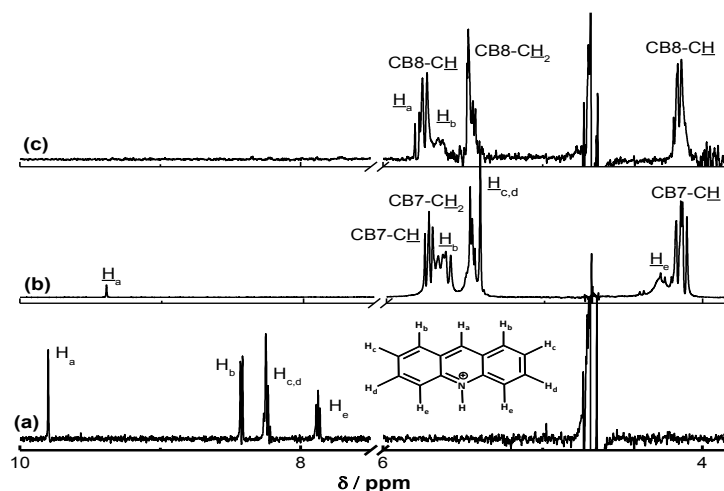


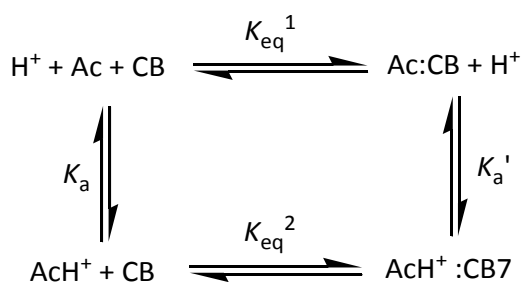
Figure 3.10: ^1H NMR spectra (500 MHz) of ~ 100 μM acridine dye in the absence (a) and in the presence (b) of 1mM CB7 and (c) 80 μM CB8 in D_2O at pD 4.5. Inset: Pictorial representation of ACH^+ .

The NMR spectrum shows four signals at δ 9.8, 8.4, 8.2 and 7.9 ppm corresponding to four different aryl protons (H_a , H_b , $\text{H}_{c,d}$ and H_e).¹¹⁰ Large upfield shifts (more than 2.7 ppm) were observed in all the aryl proton signals

in the presence of CB and merged with the CB signals. The upfield shift indicates the inclusion of acridine in the hydrophobic cavity of cucurbiturils.

3.3.4 Effect of Inclusion Complex Formation on the Acidity Constant of Acridine Dye

Taking into account that both the AcH^+ and Ac forms of acridine dye go through considerable complexation with CB7 and CB8 hosts, the prototropic equilibria for the dye·CB7/CB8 systems can be represented by the four-state thermodynamic model in Scheme 3.1,^{55, 108, 109, 129, 134-136} where K_a and K_a' represent the acid dissociation constants for the free and the complexed dye, respectively, and K_{eq}^1 and K_{eq}^2 represent the binding constants for the Ac and AcH^+ forms of the dye with CB7/CB8. The effect of CB7/CB8 on the acid–base characteristics of the acridine dye was investigated by following the changes in the absorption spectra of the dye with varying pH in the presence of $\sim 200 \mu\text{M}$ CB7 (Fig. 3.11A) and $\sim 22 \mu\text{M}$ CB8 (Fig. 3.11B).



Scheme 3.1. Four-state equilibrium model

$$K_a' = K_a K_{\text{eq}}^1 (\text{Ac}) / K_{\text{eq}}^2 (\text{AcH}^+) \quad (3.2)$$

According to Scheme 3.1, the absorbance as a function of pH of the dye solution at any particular wavelength can be expressed as:¹¹⁰

$$\begin{aligned}
 OD = & \frac{OD_{AcH^+}^\infty}{(1 + 10^{pH-pK_a} + 10^{pH-pK_a'} K_{eq}^1 [CB]_0 + K_{eq}^2 [CB]_0)} + \frac{OD_{Ac}^\infty}{(1 + 10^{pK_a-pH} + 10^{pK_a-pH} K_{eq}^2 [CB]_0 + K_{eq}^1 [CB]_0)} \\
 & + \frac{OD_{CB:AcH^+}^\infty}{(1 + 10^{pH-pK_a'} + 10^{pH-pK_a'} \frac{1}{K_{eq}^1 [CB]_0} + \frac{1}{K_{eq}^2 [CB]_0})} + \frac{OD_{CB:Ac}^\infty}{(1 + 10^{pK_a'-pH} + 10^{pK_a'-pH} \frac{1}{K_{eq}^2 [CB]_0} + \frac{1}{K_{eq}^1 [CB]_0})}
 \end{aligned} \quad (3.3)$$

where, $OD_{AcH^+}^\infty$, OD_{Ac}^∞ , $OD_{CB:AcH^+}^\infty$ and $OD_{CB:Ac}^\infty$ are the extra polated absorbance of the respective AcH^+ , Ac , $CB:AcH^+$ or $CB:Ac$ forms.

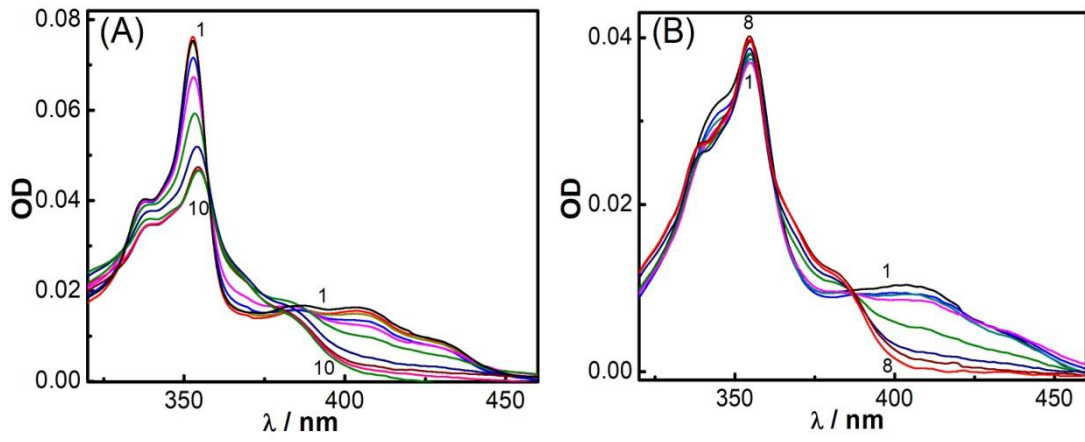


Figure 3.11: (A) Absorption spectra of acridine ($5.1 \times 10^{-6} M$) in water containing $\sim 200 \mu M$ CB7 at different pHs: (1) 4.3, (2) 6.2, (3) 7.6, (4) 8.0, (5) 8.4, (6) 8.9, (7) 9.5, (8) 9.9, (9) 10.3 and (10) 11.3. (B) Absorption spectra of acridine ($5.0 \times 10^{-6} M$) in water containing $\sim 22 \mu M$ CB8 at different pHs: (1) 4.2, (2) 5.0, (3) 5.5, (4) 6.0, (5) 6.6, (6) 7.1, (7) 7.7 and (8) 8.5.

Fig. 3.11 shows the changes in the absorbance at 353 nm of both the dye·CB7/CB8 systems as a function of pH of the solution. Fitting of the data in Fig. 3.12 (c) according to eq. 3.3 and substituting $pK_a = 5.4$ (obtained from the inset of Fig. 3.2), $K_{eq}^1 = 6.5 \times 10^3 M^{-1}$ and $K_{eq}^2 = 1.8 \times 10^6 M^{-1}$, the pK_a' value thus evaluated for the complexed dye with CB7 is 8.8 ± 0.1 . This pK_a' value is substantially higher (upward shift by ~ 3.4 units) than the pK_a value of the free dye in aqueous solution. This is in

reasonably good agreement with the value (8.0) projected from the four state model using relative binding constants (using eq. 3.2). Due to the solubility limitation of CB8, the binding constant for the neutral form with CB8 could not be estimated reliably. However, from the curve obtained in the presence of $\sim 22 \mu\text{M}$ CB8 (Fig. 3.12 (b)), the $\text{p}K_a'$ value for the CB8:dye complex is evaluated as 6.7 (using eq. 3.1). The upward $\text{p}K_a$ shift observed in the case of CB can be rationalized as all the negatively charged carbonyl groups are now involved, which allow stronger ion-dipole interactions to stabilize the protonated over the neutral form of the guest.

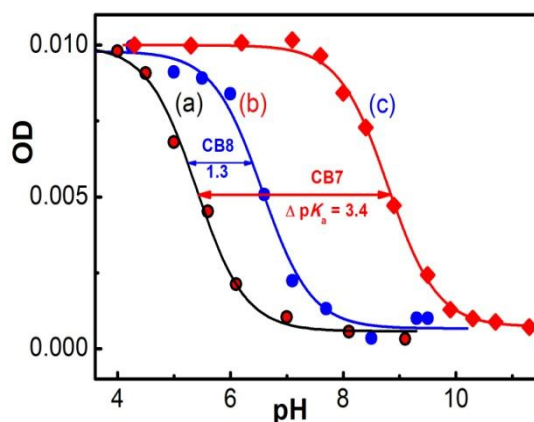


Figure 3.12: The variation in the absorbance of acridine at 353 nm with pH in the absence (a) and in the presence of 22 μM CB8 (b) and 200 μM CB7 (c).

3.3.5 Geometry Optimization of the Complexes

To get more insight about the stability of the complexes, we have optimized the ground-state geometries of CB7:AcH^+ , $\text{CB8:(AcH}^+)_2$ complexes at PM3 level, incorporating molecular mechanics (MM) correction, using the Gaussian package.¹³⁷ In all the cases, the geometry optimization was carried out without any symmetry constraint. Care was taken to avoid any false minima, by using

several input geometries, corresponding to the different anticipated conformations. The front view of optimized structures of the CB7:AcH⁺, CB8:(AcH⁺)₂ complexes are shown in Fig. 3.13. In this arrangement, the AcH⁺ is situated vertically along the centre of the CB7 cavity. This brings the positive charge carrying –NH groups in the middle of AcH⁺ in close vicinity of the negatively charged carbonyl portals of the CB7. In this geometry, the carbonyl oxygen atoms of CB7 and CB8 are involved in strong hydrogen bonding interaction with the –NH hydrogen of AcH⁺ and are placed as close as 1.8Å to 2.4Å (Fig.3.13). In case of CB8:(AcH⁺)₂ complex, the two AcH⁺ molecules are placed in the π -stacking distance within the CB8 cavity. From the optimized parameters, the ΔH_f value is estimated to be -38.4 kcal/mol for the 1:1 CB7:AcH⁺ complex and -22.8 kcal/mol for the 1:2 CB8:(AcH⁺)₂ complex. The positioning of AcH⁺ in the CB cavity rationalizes the observed pK_a shifts and the fluorescence changes for the encapsulated dye.

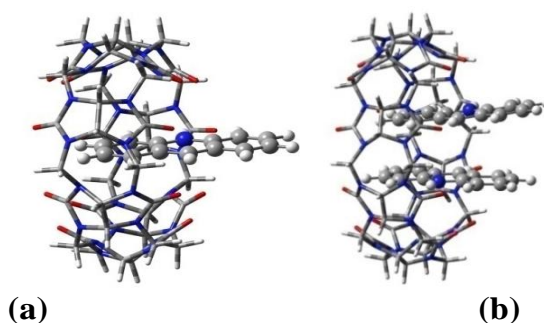


Figure 3.13: Front view of the optimized geometry of the 1:1 CB7:AcH⁺ (a) and 1:2 CB8:AcH⁺ (b) complexes.

3.3.6 Stimuli-Responsive Fluorescence Regeneration and pK_a tuning of the Cucurbituril-Acridine Complexes

Subsequent to the demonstration of fluorescence quenching and supramolecular pK_a shifts of the acridine dye in the presence of cucurbiturils, we have

attempted stimuli-responsive tuning, especially in the fluorescence behavior and pK_a shift by using a competitive binder, i.e. adamantylamine (AD). AD was selected as competitive binder due to its strong binding interaction with cucurbiturils,^{75, 138} which effectively lowers the CB-acridine binding interaction thereby altering spectral features.

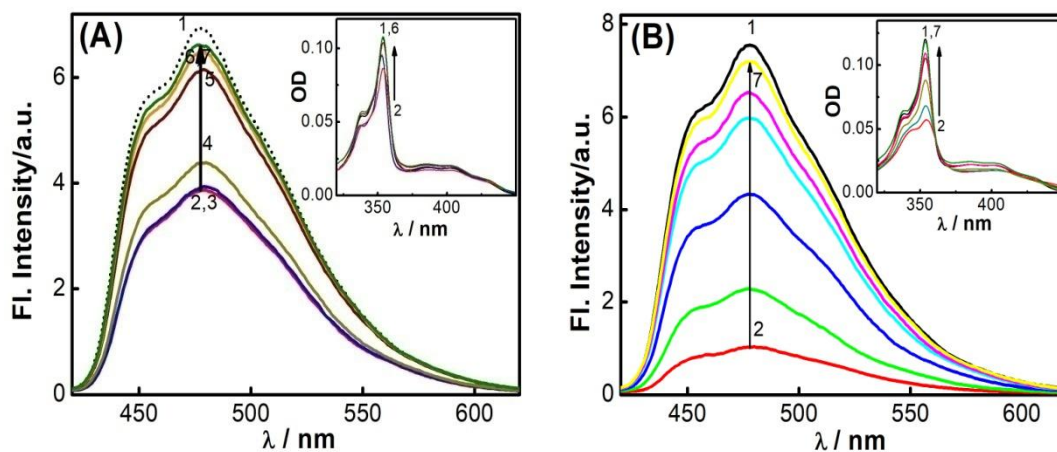


Figure 3.14: (A) Fluorescence spectra of AcH^+ (~6.1 μM) (1) in the absence of CB7 and (2-7) in the presence of CB7 (30 μM) with $[AD] / \mu M$: (2) 0.0, (3) 3.5, (4) 11.0, (5) 12.5, (6) 15.0, and (7) 20.0. (B) Fluorescence spectra of AcH^+ (~6.9 μM) (1) in the absence of CB8 and (2-7) in the presence of CB8 (22 μM) with $[AD] / \mu M$: (2) 0.0, (3) 5.0, (4) 6.5, (5) 7.5, (6) 8.0, and (7) 9.0. Insets show the corresponding absorption spectra.

Alternatively, temperature dependence studies have been carried out to weaken the noncovalent interactions between CB and the dye. It is observed that either by adding AD or by increasing the temperature of the cucurbituril-complexed acridine dye solution, the absorption spectra retracted to the features of AcH^+ alone, and the fluorescence intensity also regained to that of AcH^+ thus turning the fluorescence *off* system to fluorescence *on* (see in Fig. 3.14 and Fig. 3.15). Note that the complete regeneration of fluorescence intensity of the CB7/8 complexed acridine is achieved

with 10-20 μM concentration of AD (Fig. 3.14), rather than the increasing temperature to 90 $^{\circ}\text{C}$ (see in Fig.3.15).

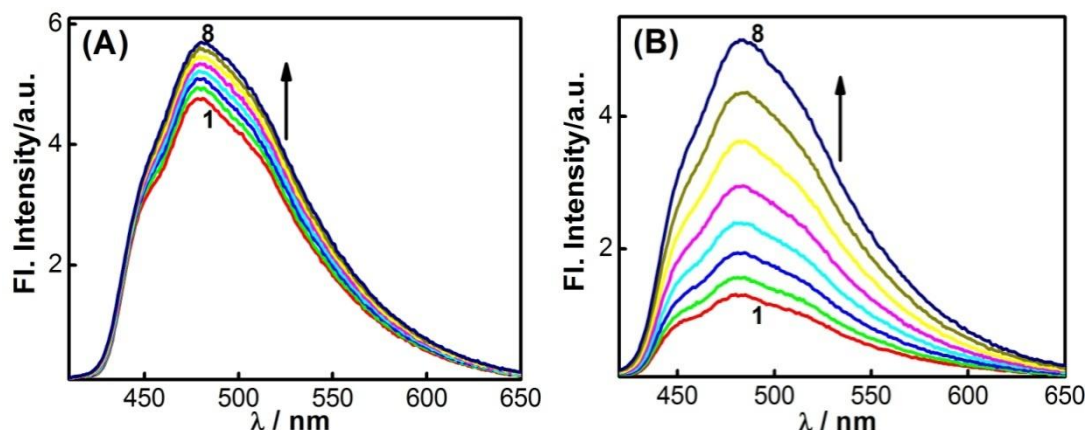


Figure 3.15: Fluorescence spectra of CB7:AcH⁺ complex (A) and CB8:AcH⁺ complex (B) with increasing temperature. $T/^{\circ}\text{C}$: (1) 20, (2) 30, (3) 40, (4) 50, (5) 60, (6) 70 and (8) 80.

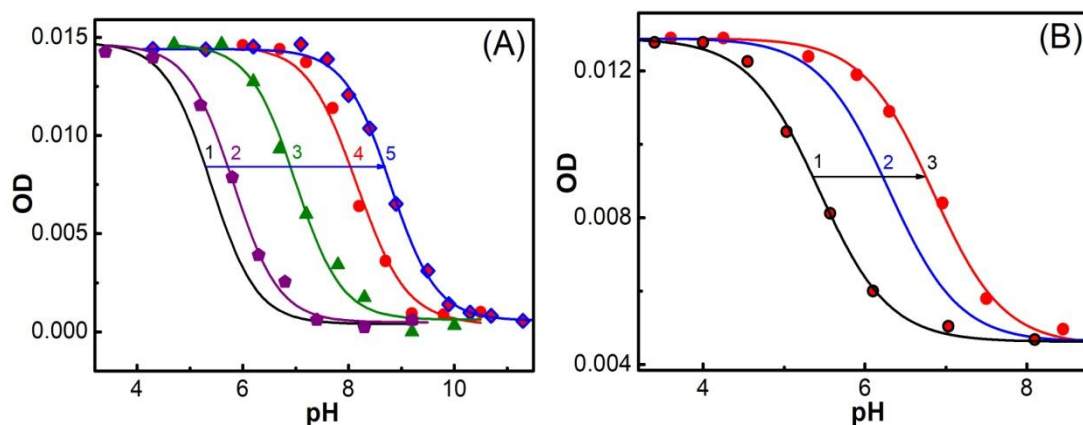


Figure 3.16: (A) pH Titration of the absorbance ($\lambda_{\text{mon}} = 400 \text{ nm}$) of acridine ($\sim 6.5 \mu\text{M}$), (1) in the absence of CB7 and AD and (2-5) in the presence of CB7 (200 μM) with $[\text{AD}]/\mu\text{M}$: (2) 100, (3) 70, (4) 42 and (5) 0.0 (B) pH Titration of the absorbance ($\lambda_{\text{mon}} = 400 \text{ nm}$) of acridine ($\sim 6.3 \mu\text{M}$), (1) in the absence of CB8 and AD and (2-3) in the presence of CB8 (22 μM) with $[\text{AD}]/\mu\text{M}$: (2) 13 and (3) 0.0

Further, to tune the pK_a shift desirably, we have carried out spectrophotometric pH titration of acridine in the presence of CB7 (200 μM) or CB8 (22 μM) and appropriate concentration of AD. The pH titration curves for

the CB:Ac system gradually shifted towards that of the free dye on increasing the AD concentration due to the competitive binding of AD at the carbonyl portals of CB. As evident from the pH dependent titration of CB:Ac in the presence of 41 μM AD shifted the pK_a value from 8.8 to 8.1, while 70 μM and 100 μM of AD tuned the pK_a value to 7.0 and 5.9 (see in Fig. 3.16A) . Similarly, 13 μM AD shifted the pK_a value of CB8:Ac from 6.7 to 6.2 (see in Fig, 6.2B).

The gradual decrease in the pK'_a value for the CB:Ac complexes (Fig. 3.16) on addition of AD therefore provides an easy and convenient method for the controlled release of a potential drug. It is to be noted that the highest concentration of adamantylamine ($\sim 100\ \mu\text{M}$) used for this pK_a tuning is much less (100-5000 times) as compared to the concentration of metal ions (10-500 mM Na^+ or 10-50 mM Ca^{2+}) used in the reported host-guest complexes.^{129, 139} In a recent study, we have reported the stimulus responsive uptake and release of an anticancer drug doxorubicin from the supra-biomolecular assembly of CB7 and bovine serum albumin.³⁸

The utility of the admantylamine (AD)-responsive pK_a tuning of acridine dye in the presence of cucurbit[7]uril host has been tested in cell lines to evaluate the controlled uptake of acridine by the live cells. In this work we have selected Chinese Hamster Ovary (CHO) normal cell lines and the uptake of acridine is directly monitored by the changes in the fluorescence characteristics. The cell lines are dispersed in PBS buffer (pH 7.4) and the CB7 complexed acridine dye in the absence and presence of AD are separately added to the cell lines along with a control sample of acridine alone in three different vials and

kept for 2 hours. As the pH of the medium is more than the pK_a value (5.4) of the dye, the uncomplexed dye remains in the neutral form in CHO cell lines and shows emission maxima at ~428 nm. However, the complexed dye, being in the AcH^+ form, shows a broad emission spectrum with peak maxima at ~473 nm in the cellular medium. Upon addition of AD to the cell line containing CB7 complex solution, the emission maxima shifted from 473 nm (characteristic of the AcH^+ form included in CB7) to 428 nm (characteristic of the Ac form in the cell lines) as shown in the inset of Fig. 3.17 demonstrating the relocation of acridine in to the CHO cell lines. Further to verify the uptake of the acridine dye by the cells, we have washed the cells with PBS buffer to remove the excess dye in the medium. The fluorescence spectra of the cells after wash displayed emission maxima at ~428 nm corresponding to the neutral form of the dye. This clearly acknowledges that the protonated form of the dye (in the form of CB7- AcH^+ complex) at pH 7.4 remains in the medium and only gets transferred to the cells when AD is introduced to the cellular medium. Mechanistically, the dye released from the CB7 cavity due to the presence of AD as the competitive binder, gets converted into the neutral (Ac) form in the medium at pH 7.4, which preferentially moves to the cell lines, demonstrating a controlled release and cellular uptake as depicted in Fig 3.19. The relocation of acridine dye is further verified from the fluorescence images of the treated cell lines (Fig. 3.18). The fluorescence images for the CHO cells treated with uncomplexed acridine (Fig. 3.18(a)) or complexed dye with AD (Fig. 3.18(c)) could only be captured in spite of fast bleaching of the acridine dye, confirming the uptake of Ac form of acridine by the cell, which is released through the action of AD. It

may be pointed out here that due to the existence of equilibria among various components ($\text{CB7}:\text{AcH}^+$, AcH^+ and $\text{CB7}:\text{AD}$), the availability of free AcH^+/Ac will be relatively less than that of only acridine system and is expected to get reflected as less number of fluorescent spots in the image recorded (Fig. 3.18(c)). Similar cell experiments using $\text{CB8}\cdot(\text{AcH}^+)_2$ could not be carried out due to the small pK_a shift (~ 1.3 units) and the dye will remain in neutral Ac form even in the presence of CB8 at pH 7.4.

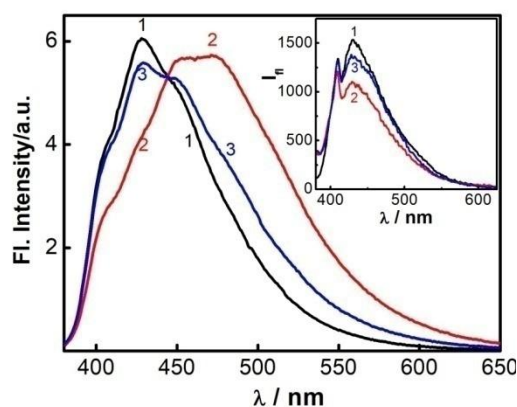
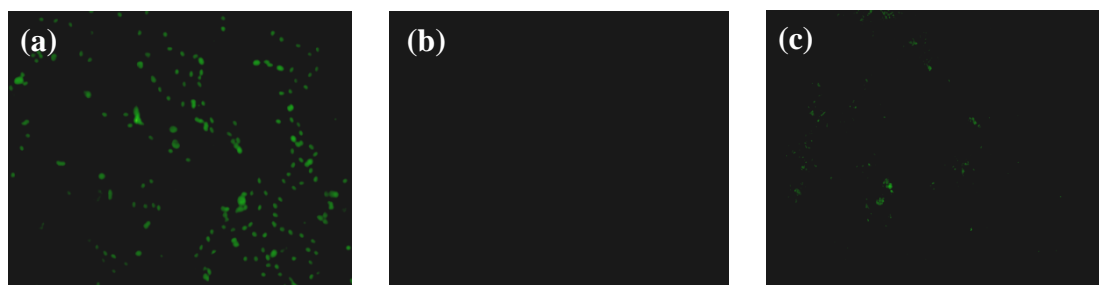


Figure 3.17: Fluorescence spectra of acridine in different environments at pH 7.4: (1) acridine dye, (2) CB7 , (3) CB7-AD in CHO cell lines. Inset shows the fluorescence spectra of the treated cell lines after washing with PBS buffer in the respective conditions.



Ac (Ac form)

Ac- CB7 (AcH^+ form)

Ac- CB7-AD (Ac form)

Figure 3.18: Fluorescence microscopic images recorded from CHO cell lines at pH 7.4 after treating them with uncomplexed acridine dye ($10\ \mu\text{M}$) (a); acridine dye ($10\ \mu\text{M}$)- CB7 ($1\ \text{mM}$) (b); and acridine dye- CB7 ($1\ \text{mM}$)- AD ($100\ \mu\text{M}$) (c).

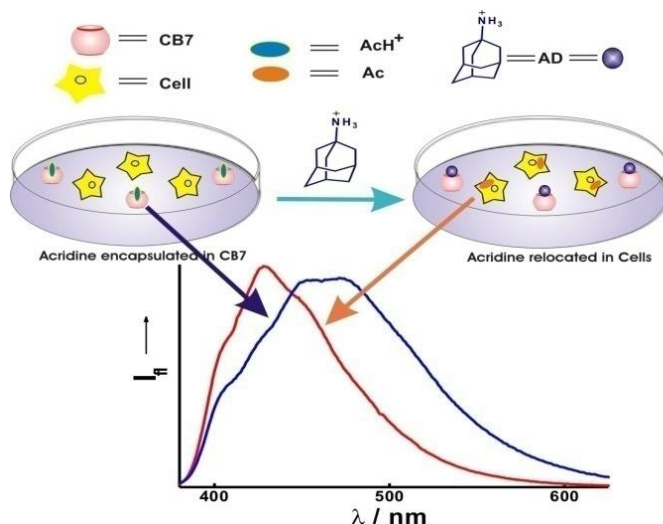


Figure 3.19: Schematic representation of the adamantylamine-induced dye relocation from the CB7 cavity to the live cells.

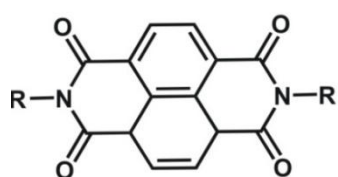
3.4 Conclusions

Host–guest interactions of two cucurbituril hosts and a biologically relevant dye, acridine, have been investigated by ground-state optical absorption and steady-state and time-resolved fluorescence studies. Compared with the neutral form of the dye (Ac), the protonated form (AcH^+) extended stronger noncovalent interactions with the CB hosts, leading to significant changes in the protolytic equilibrium of the dye and resulted in dramatic changes in the excited-state properties. The differences in the cavity dimensions and the portal features of CB7/CB8 hosts bring out notable differences in the stoichiometry, a 1:1 complex is formed with the CB7 while a 1:2 host–guest stoichiometry is preferred with the CB8 host. As a result, acridine displayed an upward $\text{p}K_{\text{a}}$ shifts by more than 3.4 and 1.3 units, respectively with CB7 and CB8. In other words, it makes the guest more basic, because both the CB hosts stabilize the protonated form of the dye by ion–dipole interactions in the ground state.

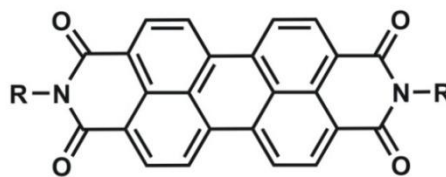
Consequently, acridine displayed severe fluorescence quenching, which were regenerated with adamantylamine as the additive. This also supported the gradual tuning in the pK_a of acridine between 5.4 and 8.8. Such supramolecular tuning in the pK_a using macrocyclic hosts are of immense current interest, as they find applications in drug delivery, catalysis, and sensor applications. In this direction our studies with CHO cell lines rightly established a controlled relocation of acridine (the neutral form) into the cell lines by AD as the stimulant.

Chapter 4

Supramolecular Interaction of Aromatic Diimides with Macrocyclic Hosts: Applications in Organic Electronics

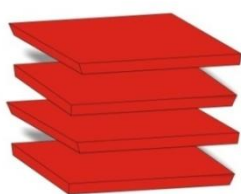


Naphthalene diimide

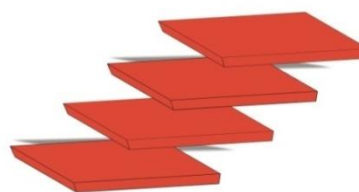


Perylene diimide

Aggregation Behavior



Plane to plane stacking



End to End stacking

4.1 Introduction

The Naphthalenediimide (NDI) and Perylenediimide (PDI) dyes are most explored aromatic diimide fluorescent materials due to their high luminescence efficiency. Which have often used as pigments, colorants and represent a unique class of fluorophore due to their excellent photochemical and thermal stability along with unmatched optical properties.^{140, 141} NDI and PDI dyes have remarkable photophysical properties and found applications in various supramolecular systems such as supramolecular photosystems, synthetic ion channels, organic electronic,³⁰ photovoltaic devices,^{142, 143} fluorescence spectroscopy,¹⁴⁴ and metallo-supramolecular architectures.¹⁴⁵⁻¹⁴⁷ Moreover, the strong π -acidity of aromatic diimide derivatives has been discussed in conjunction with anion- π interactions as well as donor-acceptor complexes. Due to the rigid aromatic perylene and naphthalene core, aromatic diimide derivatives are strongly hydrophobic in nature and because of which, most of these studies are confined to the organic medium. In aqueous medium, mostly aromatic diimide dyes form nonfluorescent aggregates through strong π - π stacking interactions.¹⁴⁸ The emission quantum yield of the synthetic water soluble PDIs remained low for most of the cases. On the other side, NDI dyes are less stable and weakly fluorescent due to the charge transfer fluorescence quenching in aqueous medium.

This chapter, we present the host-guest complexation of two synthesized diimide dyes i.e. N, N'-bis-2-(2-aminoethyl)benzimidazolyl naphthalene diimide (NDI-BzIm) and N,N'-bis-phenylalanyl perylenediimide (Phe-PDI) derivatives in two different parts. The interaction of NDI derivative with cucurbiturils and the stabilization and emission of radical anion through complexation are discussed in Part-1. Whereas, the interaction of PDI dye with β -cyclodextrin (β CD) and the negative differential resistance behavior of the complex are explained in Part-2

Part-1

Generation of Stable and Emissive Radical Anion from Naphthalenediimide Derivative in the Presence of Cucurbiturils



To be communicated

4.1.1 Introduction

Organic radical anions are important intermediates in various natural and artificial electron transfer processes and also used in organic light emitting diode¹⁴⁹⁻¹⁵¹ and photovoltaic devices.^{149, 152-154} Radical anions derived from aromatic diimides play an important role due to their stability and ease of generation. NDI dyes form radical anions under photoirradiation due to the low value of one-electron reduction potential (NDI: $E_{\text{red}}^1 = -1.10 \text{ V vs. Fc/Fc}^+$).^{155, 156} NDI radical anions may also be generated by chemical,¹⁵⁶ electrochemical^{153, 157} and photochemical^{158, 159} methods. However, despite of the application of NDI derivatives in designing various supramolecular structures utilizing the unmatched features of NDI core,^{160, 161} the study on the NDI radicals in supramolecular environment remained underexplored. Apart from the design of NDI based cyclophane by Lehn^{15, 153, 162} and others to utilize the charge transfer interactions for novel host-guest assemblies,^{158, 159, 163} the interaction of NDI derivatives with various preorganized synthetic hosts is a relatively unexplored area. Among various aromatic diimides the 1,4,5,8-naphthalene-tetracarboxylic-acid-diimide (NDI)-derivatives have been extensively explored as a building block for the generation of various supramolecularly assembled systems,^{153, 157} both in organic and aqueous media due to their propensity for π -stacking, electron-accepting nature and easy structural manipulations.^{157, 164} Thus in this study, we have used the synthetic receptor cucurbit[n]uril ($n = 7, 8$) to make emissive NDI radical anion with extraordinary stability at ambient condition. Recently Zhang et. al. have demonstrated that the encapsulation of cationic naphthalene diimide (NDI) derivative by CB7/CB8 leads to the formation of stable¹⁶⁵ but non fluorescent NDI radical anion under photoirradiation through the efficient manipulation of HOMO and LUMO energy

levels of NDI derivatives.^{165, 166} In this work, the host-guest interaction of NDI derivative and generation of stable and emissive radical anion from this derivative in the presence of cucurbiturils have been discussed. We anticipate that the demonstration of emissive radical anion will broaden the scope of NDI radical anion chemistry for potential application in fluorescence spectroscopy^{153, 157} and optoelectronic applications.¹⁶⁷⁻¹⁶⁹

4.1.2 Materials and Methods

1,4,5,8-Naphthalene-tetracarboxylic acid dianhydride, 2-(2-aminoethyl)benzimidazole dihydrochloride, dimethyl formamide (DMF, dry) and triethamine were purchased from Sigma-Aldrich and were used without further purification. Cucurbit[7]uril (CB7) and Cucurbit[8]uril (CB8) were synthesized and characterized by using ¹H NMR. Commercially available CB7 or CB8 from Sigma-Aldrich was also used for some of the experiments. Nanopure water (Millipore conductivity of 0.06 μScm^{-1}) was used to prepare the sample solutions. Hydrochloric acid used for pH adjustment was obtained from Merck, India. pH measurements were carried out with Eutech Instruments P2700 pH meter at room temperature. Before measurements, pH meter was calibrated at pH 4, 7 and 10 with pH standard buffers provided by Eutech Instruments Ltd. All experiments were carried out at ~pH 3.5. The details of absorption and fluorescence (steady state and time resolved) measurements which are used in this study were provided in the chapter-2.

4.1.3 Results and Discussion

In this study, we employed a new approach, for the first time, to demonstrate the formation of emissive stable NDI radical anion of ethyl benzimidazole appended NDI

derivative (NDI-BzIm, Fig. 4.1) through contrasting encapsulation behavior of CB7 and CB8 in aqueous environment.

The compound N, N'-bis-2-(2-aminoethyl)benzimidazolyl naphthalene dimide (NDI-BzIm) was synthesized by condensation of 2-(2-aminoethyl)benzimidazole dihydrochloride with 1,4,5,8-Naphthalene tetracarboxylic-acid dianhydride in DMF solvent in the presence of triethylamine at 120°C (see chapter-2, 2.13). NDI-BzIm was dissolved in aqueous solution at pH~2.5-3 and interaction of NDI-BzIm as hydrochloride salt with CB7/CB8 was studied and the results are discussed in the following sections.

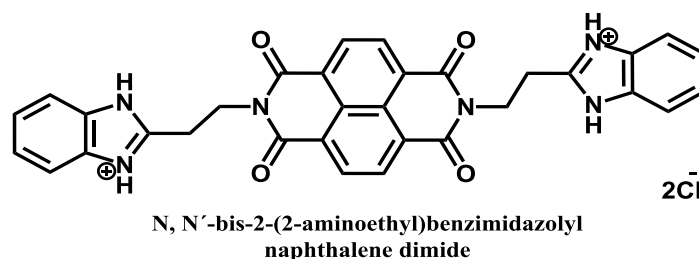


Figure 4.1: Chemical structure of protonated form of N, N'-bis-2-(2-aminoethyl)benzimidazolyl naphthalenediimide (NDI-BzIm) dye.

4.1.3.1 ¹H-NMR Measurements

As shown in the Fig. 4.1. ¹H-NMR spectroscopic studies revealed upfield shifts of the cationic benzimidazole protons of NDI-BzIm in the presence of CB7 indicating the inclusion of the dye inside the hydrophobic cavity of CB7. Whereas, the NDI core protons displayed a downfield shift experiencing the deshielding effect of the negatively polarized carbonyl portals of the CB7 host. On the other hand, in the presence of CB8 two separate signals were obtained for symmetric NDI protons indicating the different spatial arrangement of the bound NDI-BzIm molecules to CB8. The benzimidazole protons displayed an upfield shift of 1ppm from their

original position at $\delta 7.61$ in the presence of CB8 indicating their inclusion in the hydrophobic cavity of CB8 host. The methylene protons appeared as two sets showed downfield shift with respect to its original position in case of CB7 and remained unaltered as in case of CB8. With these features and keeping in mind the symmetrical molecular structure of the NDI-BzIm, it is anticipated that CB7/CB8 might interact with cationic NDI-BzIm from both the protonated benzimidazolyl ends leading to higher order stoichiometric complexes. Further insight on the supramolecular features originating from the interaction of NDI-BzIm with CB7/CB8 host was obtained from detail optical spectroscopic measurements.

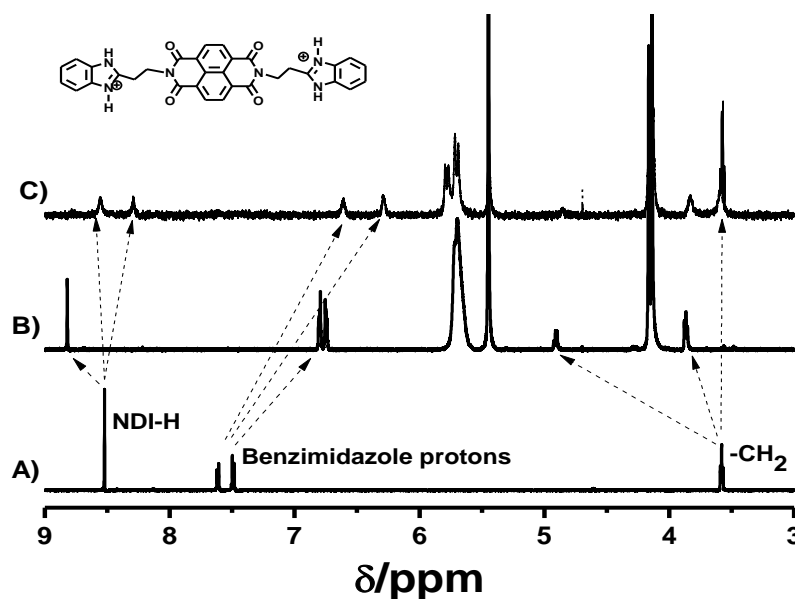


Figure 4.2: ^1H -NMR spectra NDI-BzIm (50 μM , in D_2O at pD -3.5) free (A), with 2.5 eq. of CB7 (B) and 2 eq. of CB8 (C).

4.1.3.2 Absorption and Steady-State Fluorescence Measurements

As shown in the Fig. 4.3A, ground-state absorption spectroscopic studies demonstrated that the gradual addition of CB7 to aqueous solution of NDI-BzIm (8.3 μM , pH 2.5) leads to the hypochromic shift of the vibrational progressions of $\text{S}_0\text{-S}_1$ in

the electronic transitions of NDI core at 382 nm (0-0), 363 nm (0-1) and 343 nm (0-2) along with bathochromic shifts in the absorption spectra of benzimidazole unit at higher wavelength region (inset of Fig. 4.3A). On the other hand, the mirror image emission spectra of NDI-BzIm demonstrated a gradual emission enhancement with increase in CB7 concentration leading to saturation at ~40 μ M of CB7 (Fig. 4.3B). These characteristic optical features clearly indicate the complexation of NDI-BzIm with CB7 host encapsulating the protonated benzimidazole units in its cavity from both sides in 2:1 host-guest ratio. Further, the ternary complex formed, places the NDI core in a more hydrophobic environment resulting in the emission enhancement of NDI-BzIm. Gradual addition of CB8 to the NDI-BzIm solution leads to hyperchromic shift of the absorption profile leading to the decrease ratio between the well resolved vibronic structure of S_0 - S_1 band at 382 nm (0-0) and 363 nm (0-1) with clear isosbestic points at 385 nm and 374 nm. A close look at the absorption profile reveals that the peak ratio of these vibronic transitions in the absorption spectra of NDI-BzIm approaches unity which is typical for the dimerization of NDI-derivative (Fig. 4.3C). In the emission front, quite contrasting to the behavior of NDI-BzIm with CB7, gradual addition of CB8 host leads to a new emission band centred at 525 nm (Fig. 4.3D). It was observed that the intensity of this red shifted emission band increases with increasing the concentration of CB8 in dye solution, whereas, the original emission in the blue region at 385 nm and 410 nm gradually decreases. The appearance of this new band may be well correlated to the various studies demonstrating the NDI derivatives in toluene solvent medium demonstrating¹⁷⁰ the same band at around 525 nm due to the excimer emission. In fact, as shown in the Fig. 4.3D, with gradual addition of CB8 host the emission profile also showed remarkable

excimer emission band in water at pH 2.5 demonstrating efficient non-covalent dimerization of NDI-BzIm derivative through supramolecular host-guest interaction with CB8 with 2:2 stoichiometry in aqueous medium. In time correlated single photon counting experiments NDI-BzIm demonstrates an ultrafast excited state lifetime of ~60 ps typical for the bay substituted NDI derivatives.¹⁷¹

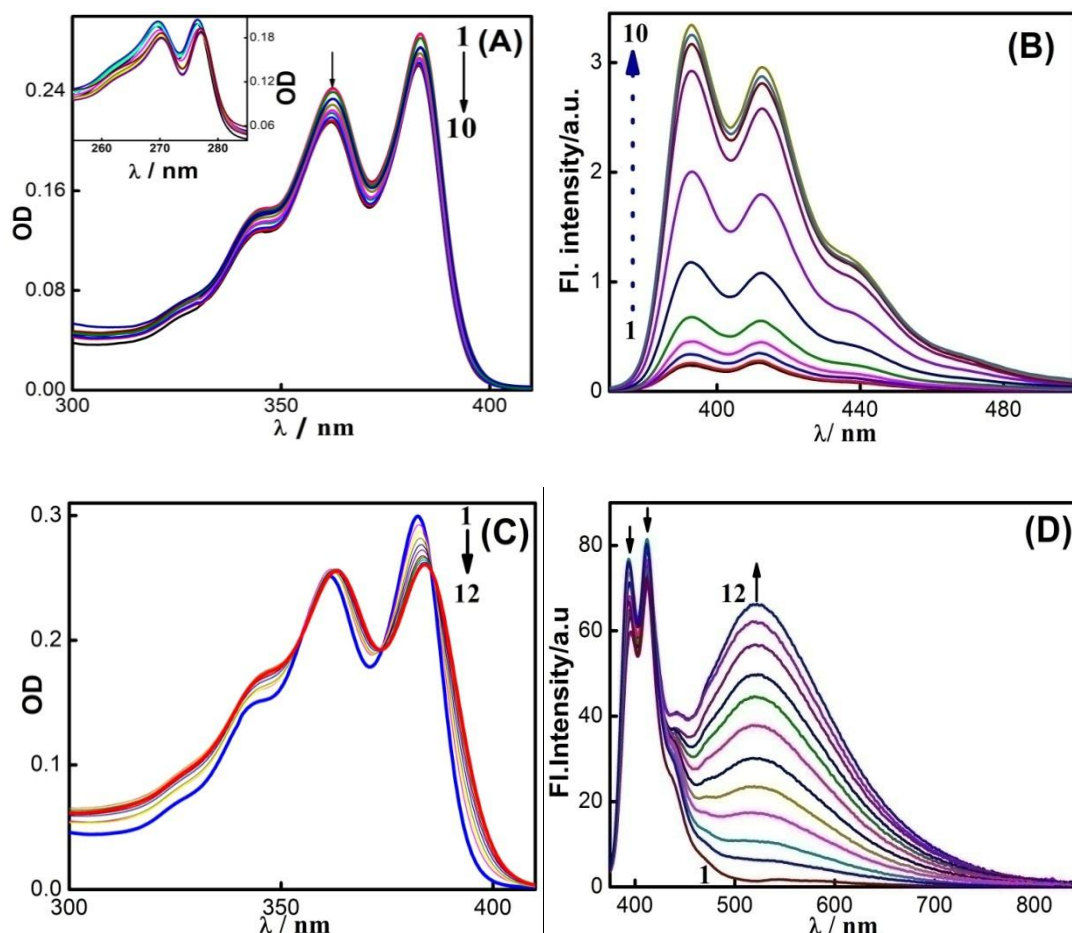


Figure 4.3: Absorption (A and C) and Emission (B and D) spectra of NDI-BzIm (9 μ M, in H_2O at pH-3.5) with CB7 and CB8. (A and B) [CB7]/ μ M: (1) 0, (2) 1, (3) 4, (4) 8, (5) 14, (6) 24, (7) 40, (8) 98, (9) 154, (10) 226. (C and D)[CB8]/ μ M: (1) 0, (2) 1, (3) 2, (4) 5, (5) 7, (6) 8.5, (7) 10.6, (8) 12.4, (9) 15.8, (10) 22.7, (11) 32.5, (12) 50. λ_{exc} = 355 nm

However, the lifetime of free NDI-BzIm and in the presence of CB7 could not be measured reliably by our present TCSPC experimental setup. On the other hand, in the presence of CB8 host, NDI-BzIm demonstrates unusually slower decay kinetics

with life time of 0.5 ns. We believe that the long lifetime of NDI-BzIm in presence of CB8 is originating from the dimer of NDI-BzIm facilitated by the complexation of CB8 host from both ends of NDI-BzIm in a 2:2 stoichiometry. Keeping in mind the relatively small cavity size of CB7 it is anticipated that the cationic NDI-BzIm interacts with CB7 host through the encapsulation of protonated benzimidazole units of two ends leading to 2:1 host guest stoichiometry. The higher homologue CB8 can effectively encapsulate two protonated benzimidazole units of two NDI-BzIm molecules from both ends forming a supramolecular complex with 2:2 stoichiometry. In such case the formation of dimer of NDI-BzIm is evident with CB8 which is further supported by the observed optical features of the guest in presence of CB8 host. As shown in Fig. 4.4 Job's continuous variation method employed to evaluate the stoichiometry of NDI-BzIm-CB7 or NDI-BzIm-CB8 complex which further verified the 2:1 and 2:2 stoichiometry of NDI-BzIm with CB7 and CB8, respectively.

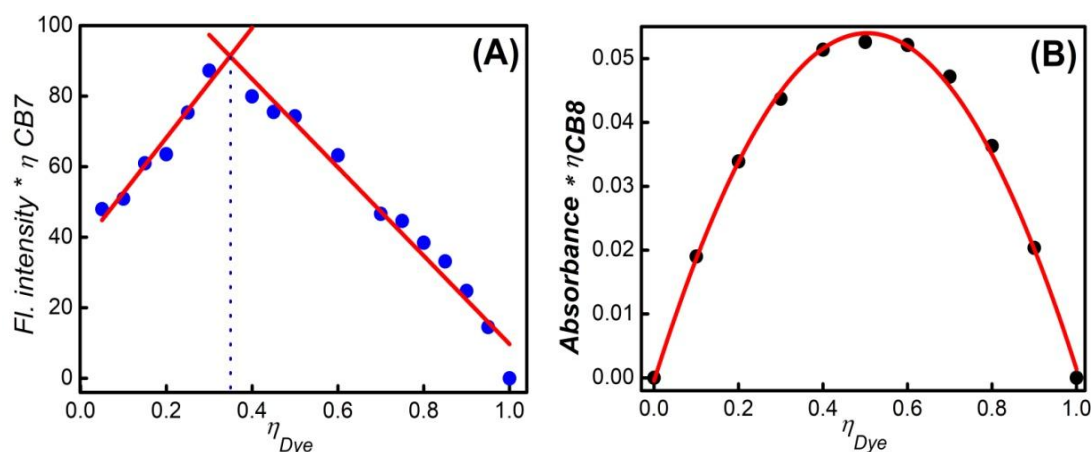


Figure 4.4: Job plots for the CB7:NDI-BzIm (A) and CB8:NDI-BzIm (B) complexes. Total concentration of the two components was (A) 16.0 μM and (B) 25 μM . $\lambda_{mon} = 382$ nm (A) and $\lambda_{mon} = 350$ nm (B).

4.1.3.3 Isothermal Titration Calorimetric Measurements

ITC data analysis indicated that interaction of NDI-BzIm induced a significant change in the titration curve when CB7 and CB8 were added into the solution of NDI-BzIm in a molar ratio of 2 : 1 and 2 : 2 (see Fig.4.5). In case of CB7 one set of binding site model was utilized to analyse the data which yields a binding constant of $(1.09 \pm 0.039) \times 10^6 \text{ M}^{-1}$ typically well within the range of moderately strong association constants observed in case of CB7 complexes. In case of CB8, from the fitting of the ITC data two binding constants were evaluated as $(5.67 \pm 1.9) \times 10^6 \text{ M}^{-1}$ and $(1.24 \pm 0.16) \times 10^5 \text{ M}^{-1}$.

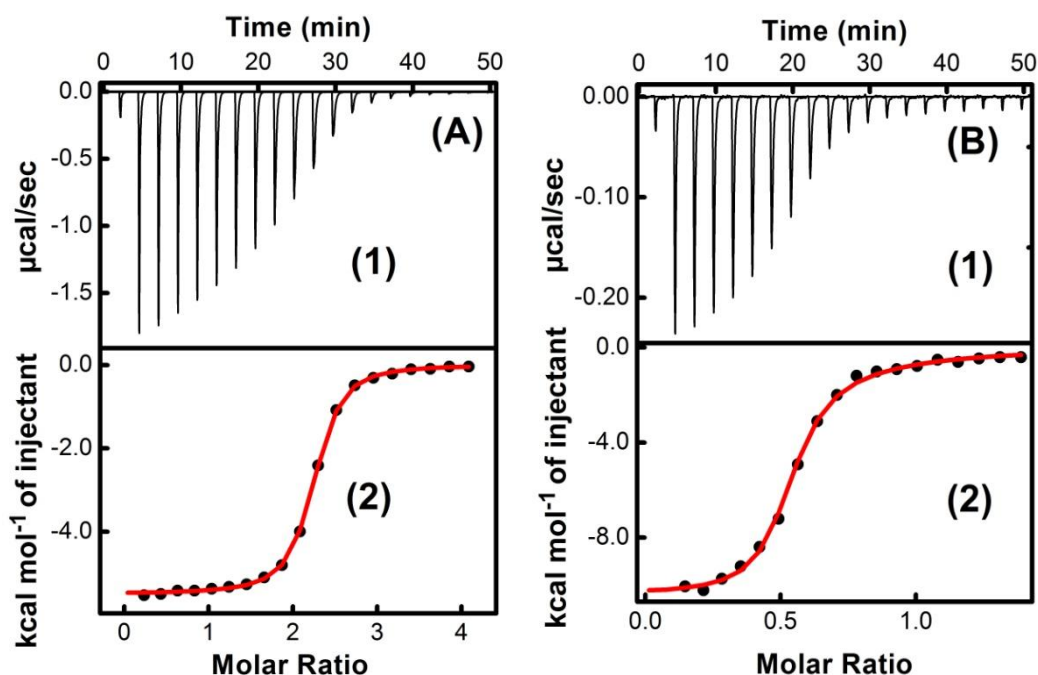


Figure 4.5: Raw data for the titration of 100 μM NDI-BzIm with CB[7] and CB[8] at pH 2.5 in water and 25 $^{\circ}\text{C}$, (A) showing the calorimetric response as successive injections of the CB7 are added to NDI-BzIm filled the sample cell and (B) NDI-BzIm are added to the filled CB8 sample cell. Integrated heat profile of the calorimetric titration shown in panel (1). In panel (2) solid line represents the best nonlinear least-squares fit to a one set of binding site model for 4.5A and sequential binding-site model for 4.5B.

From the ITC measurements the enthalpy, entropy and free energy changes for the complexation processes for the NDI-BzIm systems with both CB7 and CB8 were evaluated and the values are:

(A) $\Delta H = -5.5 \pm 0.012 \text{ kcal mol}^{-1}$, $-T\Delta S = 2.5 \text{ kcal mol}^{-1}$, $\Delta G = -2.6 \text{ kcal mol}^{-1}$ for NDI-BzIm with CB7 complex.

(B) $\Delta H_1 = -6.16 \pm 0.13 \text{ kcal mol}^{-1}$, $-T\Delta S_1 = 2.8 \text{ kcal mol}^{-1}$, $\Delta G_1 = -3.36 \text{ kcal mol}^{-1}$ and $\Delta H_2 = 4.0 \pm 0.18 \text{ kcal mol}^{-1}$, $-T\Delta S_2 = 3.95 \text{ kcal mol}^{-1}$, $\Delta G_2 = -0.05 \text{ kcal mol}^{-1}$ for NDI-BzIm with CB8 complex.

4.1.3.4 SEM and FM Measurements

To explore the advantages of the strong binding interaction and excimer formation of NDI-BzIm with CB7 and CB8, we attempted to study the morphological changes introduced in NDI-BzIm due to complexation with CB7 and CB8. The morphological analyses were carried out on the NDI-BzIm/CB(7/8) samples deposited on respective substrate surface by SEM and FM methods and the comparative images are given in Fig.4.6. As mentioned in the experimental section in chapter 2, 2.8 images were accepted only after verifying its reproducibility from several regions of the sample film. As shown in the Fig.4.6 (a,b), the SEM images of NDI-BzIm dye alone displayed randomly distributed crystalline form of the free dye, due to the self-aggregation of NDI-BzIm units. However, the SEM image obtained for NDI-BzIm in presence of CB8 and CB7 presented well-defined morphology. In the presence of CB7, highly self-assembled type morphology was observed in Fig. 4.6 (d-f). Whereas, in the presence of CB8, ellipsoidal shaped (Fig. 4.6 (g-i)) images were observed which indicate the contrasting binding behavior of both host molecules with NDI-BzIm. More convincingly, fluorescence microscopic images (Fig.4.6) captured by using the blue excitation ($\lambda_{\text{ex}}=400 \text{ nm}$) displayed bright green crystalline form of the free NDI-

BzIm dye (Fig.4.6c), whereas the NDI-BzIm/CB7 complex (Fig. 4.6f) is highly ordered self-assembled pattern. In NDI-BzIm/CB8 system, similar ellipsoidal shaped structures are observed.

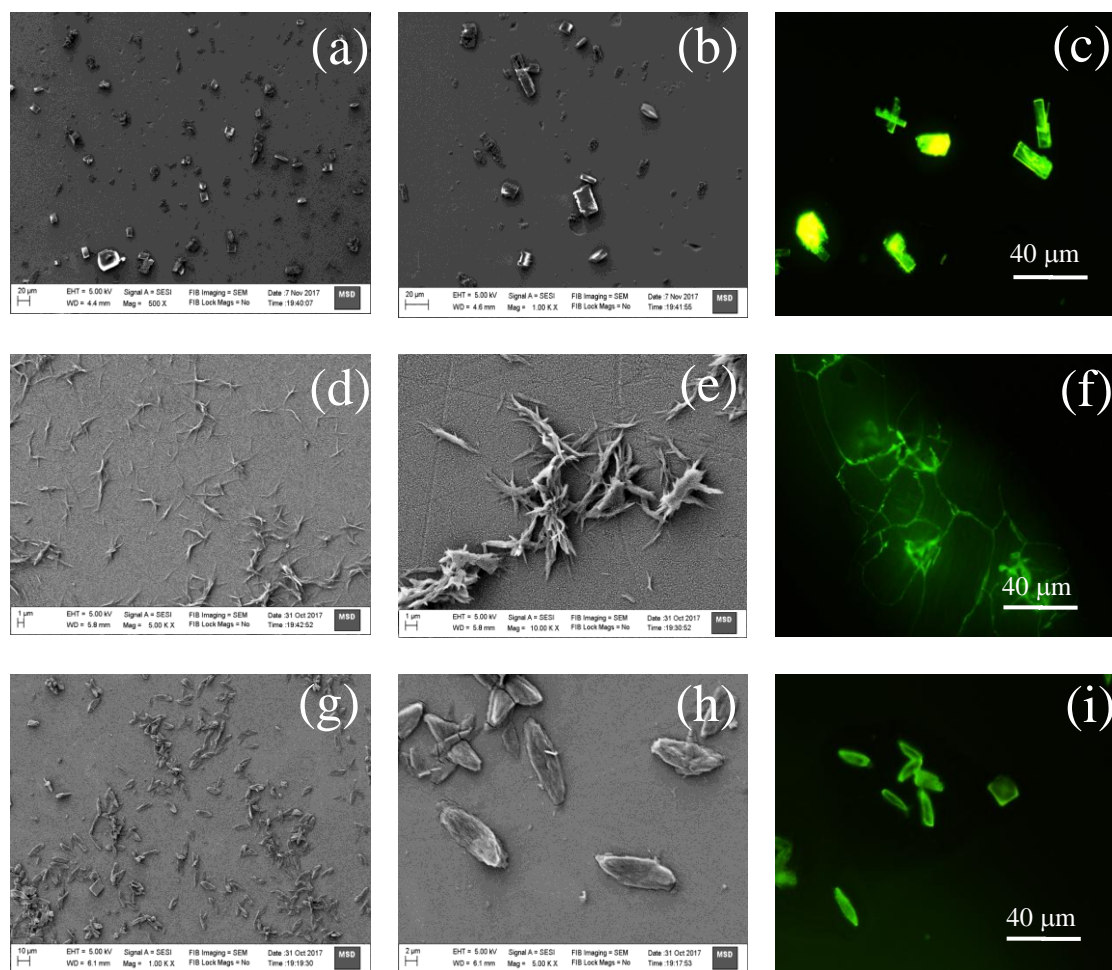


Figure 4.6: SEM and FM images obtained from samples deposited on respective substrate surface; (a,b,c) NDI-BzIm alone, (d, e, f) NDI-BzIm/CB7 complex and (g, h, i) NDI-BzIm/CB8 complex.

4.1.3.5 Absorption Behavior of NDI-BzIm Radical

Having verified the interaction of NDI-BzIm with the synthetic receptors CB7 and CB8 we focused our attention to study the behavior of the corresponding NDI radical anion in supramolecular environment. Stabilization of organic radicals at ambient condition through supramolecular interactions is currently gaining considerable

interest for their diverse applications.¹⁷² Especially NDI radical anion bears unique significance in the various areas of self-assembly,^{156, 163} anion-driven electron transfer reactions,^{153, 156} DNA binding¹⁷³ and organic electronics.¹⁶⁷ Despite of significant progress in the field of NDI radicals/radical anions, the studies on optical emission behavior of these species are still unexplored. Organic radicals are usually less emissive due to enhanced/accelerated intersystem crossing. Moreover, the stability of these species in solution is a prerequisite for optical spectroscopic studies. The following part presents our results on the emission behavior of NDI-BzIm radical anion within supramolecular confinement of CB7 and CB8 in aqueous medium.

To generate the radical anion species, NDI-BzIm in the absence and presence of the host CB7 and CB8 in aqueous solution was irradiated at 375 nm for 30 mins. It was anticipated that the photoinduced electron transfer (PET) from the chloride anion to NDI core would result in the formation of the corresponding NDI radical anions.¹⁶⁵ As shown in the trace 1, Fig. 4.7, free NDI-BzIm did not show any change in the absorption spectra after 30 mins of irradiation. Under similar conditions, in the presence of CB7, the absorbance of NDI-BzIm at 360 nm and 382 nm is significantly decreased along with the appearance of broad absorption ranging from 400-600 nm (trace 2, Fig. 4.7). Whereas, in the presence of CB8, the appearance of new absorption band centered at 440 nm with a shoulder band at 550 nm characteristic of NDI radical anion species was observed in the absorption spectra of NDI-BzIm (trace 3, Fig. 4.7). The stability of NDI radical anion under ambient conditions has been followed by UV-vis absorption spectroscopy. It was observed that in presence of visible light the radical anions formed in the presence of CB7 or CB8 quickly and disappeared within 10 minutes and the corresponding absorption spectra almost reverts back with its

original features see in Fig. 4.7. Although the exact reason for this behavior is not clear at this point it may be anticipated that the photo-induced back electron transfer from the NDI core results in the reversible behavior. In absence of visible light the NDI radical anion formed in presence of CB7 and CB8 are slowly converted to the original form within 2-3 hour of irradiation (see Fig. 4.8). During this reversible transformation we exclude the photochemical degradation of ethyl benzimidazole side chain of NDI-BzIm based on the emission features of radical anions discussed in the later part. The formation of NDI-BzIm radical anion is further verified by electron paramagnetic resonance (EPR) spectroscopy by detecting the EPR signal after UV irradiation of the sample. Within the irradiation time no EPR signals were detected for the free NDI-BzIm solution (trace 1, Fig. 4.7B). However, as shown in the trace 2, Fig.4.7B, in presence of CB7 host, weak EPR signal was observed indicating the formation of NDI radical anion. On the other hand, in the presence of CB8, intense EPR signal was observed characteristics to the NDI radical anion.

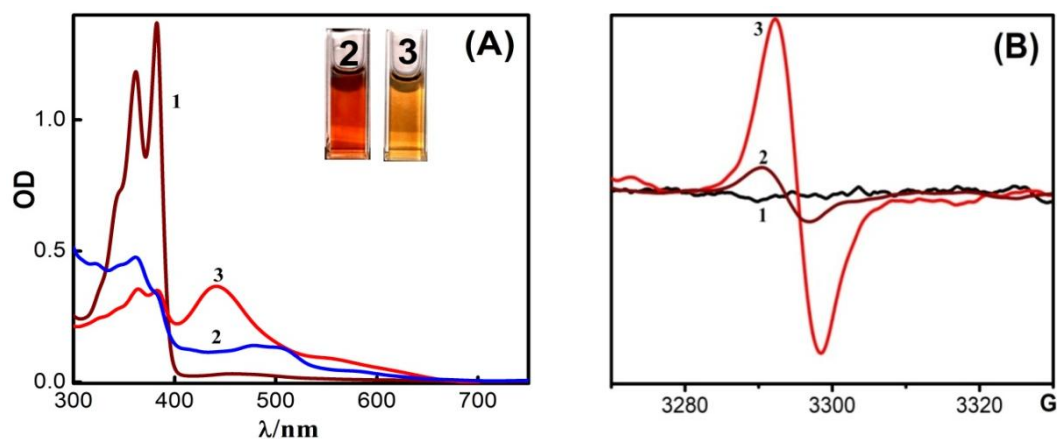


Figure 4.7: Photo Irradiation (355nm) for 30 minutes, (A) Absorption and (B) Electron paramagnetic resonance spectra of 50 μM NDI-BzIm (1) with 100 μM CB7 (2) and 50 μM CB8 in H_2O (pH 3.5).

The EPR signal is better in the later case which may be due to the high yield of NDI-BzIm radical anion in presence of CB8 as the host assists the formation of

sandwich type NDI dimer assembly with the chloride anions in the tetracation CB8-2NDI²⁺ complex in solution. Similar observation was made earlier for other cationic NDI derivative encapsulated in the cavity of the higher cucurbituril homologue namely, CB10.¹⁶⁶

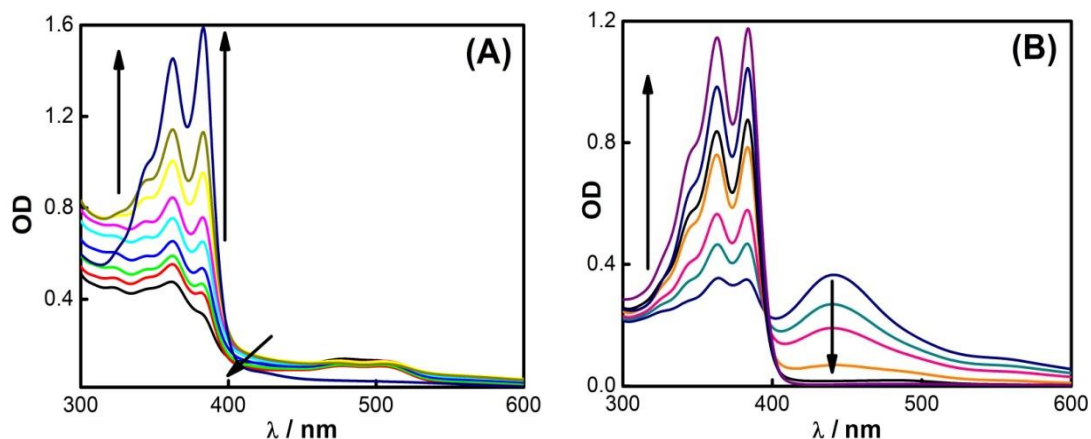


Figure 4.8: Absorption spectra after 30 minutes white light irradiation, (A) CB7 (200 μM):NDI-BzIm (100 μM) spectra recorded every 15 minutes time interval and (B) CB8 (50 μM):NDI-BzIm(50 μM) every 5 minutes time interval.

4.1.3.6 Fluorescence Emission and Lifetime Measurements

In the present case we observed that the NDI-BzIm radical anions formed in presence of macrocyclic host CB7 and CB8 has enough stability to perform emission spectroscopic studies in solution. The emission behavior of NDI-BzIm radical anions were studied by using steady state and time resolved emission spectroscopic measurements. As shown in the Fig. 4.9A with excitation at 355 nm, NDI-BzIm in the presence of CB7 displays a strong emission centered at 580 nm after irradiation of 30 mins which is completely different from characteristics shown before irradiation (Fig. 4.9A, trace 1).

Therefore, it is evident from the long wavelength emission profile of NDI-BzIm-CB7 complex that the new emission is originating from the corresponding

radical anion formed after photoirradiation. Moreover it is further confirmed from the excitation spectra of the CB7-NDI-BzIm complex after photoirradiation (see Fig. 4.11A).

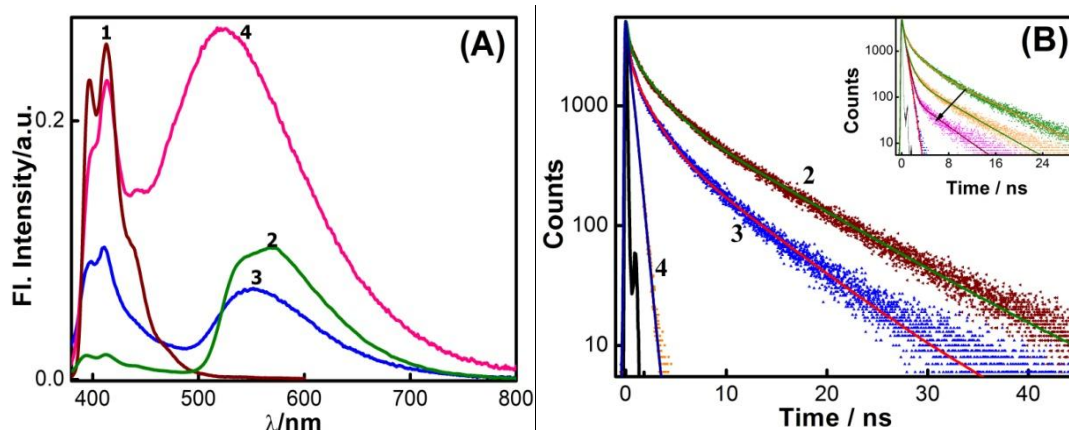


Figure 4.9: Emission spectra (A) and decay trace (B) after photoirradiation (355 nm for 30 minutes) of 50 μM NDI-BzIm (1) with 100 μM CB7 (2), 50 μM CB8 (3) and 50 μM CB8 (4) without irradiation in H_2O (pH 3.5, $\lambda_{\text{ex}} = 355 \text{ nm}$). Inset: Recovery of fluorescence decay with time of (CB8:NDIBzIm⁺²) 2:2 after irradiation (0-60 mins).

Table 4.1: Excited state lifetime values evaluated from the fluorescence decays of NDI-BzIm (50 μM) in water at pH 2-3 in the presence of (50 μM) CB8 with different time interval.

NDI-IM-CB8	τ_1/ns	τ_2/ns
0 minute	0.57 (30%)	5.30 (70 %)
10 minutes	0.53 (38%)	5.18 (62%)
20 minutes	0.47 (75%)	4.63 (25%)
22 minutes	0.46 (79%)	4.49 (21%)
25 minutes	0.46 (82%)	4.31 (18%)
40 minutes	0.46 (84%)	4.14 (16%)
Without irr	0.49 (100%)	

Table 4.2: Excited state lifetime values evaluated from the fluorescence decays of NDI-BzIm (50 μM) in water at pH 2-3 in the presence of (100 μM) CB7 with different time interval.

NDI-BzIm-CB7	τ_1/ns	τ_2/ns	τ_3/ns
0 minute	2.18 (28%)	8.99 (65%)	0.22 (7%)
20 minutes	2.06 (28%)	9.15 (63%)	0.20 (9%)
40 minutes	1.67 (28%)	8.58 (61%)	0.14 (11%)
50 minutes	1.48 (30%)	7.94 (55%)	0.12 (15%)
80 minutes	1.43 (34%)	6.60 (48%)	0.13 (18%)
150 minutes	0.59 (27%)	3.86 (28%)	0.07 (45%)
Without irr	0.06 (52%)	4.03 (48%)	

On the other hand, after photoirradiation of CB8-NDI-BzIm complex, the emission intensity is reduced with a slight red shift of the emission maxima at long wavelength region. Under similar conditions, in the presence of CB8 host, the NDI-BzIm displays slightly blue shifted emission profile as shown in Fig.4.10B. We further observed that in absence of CB7/CB8 hosts there is no change in the emission behavior of NDI-BzIm before and after irradiation of the sample (Fig. 4.9 trace 1).

Therefore, it may be concluded that no radical anion is generated with NDI-BzIm in the absence of CB7/CB8 after photoirradiation within the stipulated time. The emission from the NDI-BzIm radical anion was further confirmed by the emission spectra recorded after exciting the samples in the sole radical absorption region (see in Fig. 4.11A).

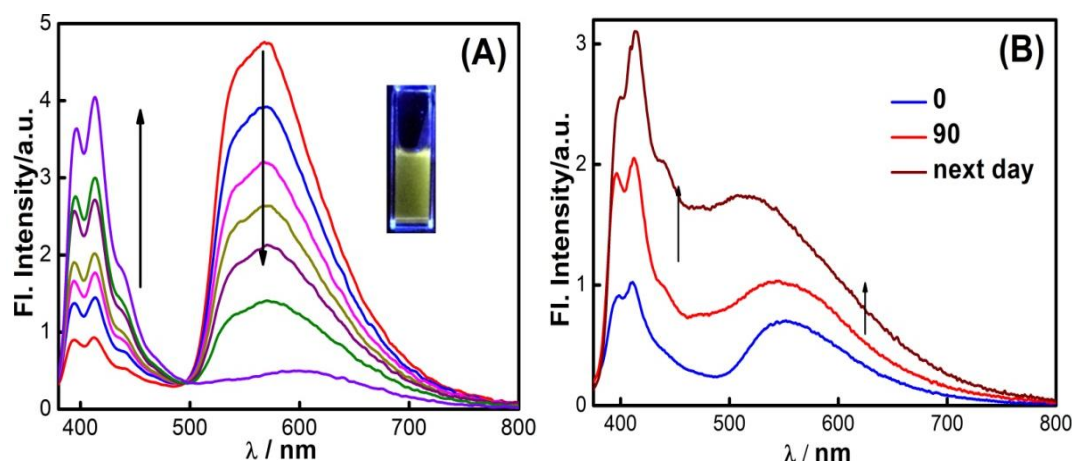


Figure 4.10: Fluorescence spectra after white light 30 minutes irradiation, (A) for the CB7 (100 μ M):(50 μ M) NDI-BzIm were recorded within 15 minutes time interval and (B) for the CB8 (50 μ M):(50 μ M) NDI-BzIm were recorded different time interval, $\lambda_{ex} = 355$ nm for both complex.

The NDI radical cation generated in presence of CB7 displays multi exponential decay kinetics with an average lifetime of 9 ns (see in Fig. 4.9B, Table 4.1). The decay kinetics of NDI radical in presence of CB8 is relatively simpler

displaying a biexponential decay with major contribution of 5.3ns component from the NDI radical along with a 0.5ns component attributed to the CB8-2NDI²⁺ complex without radical generation. It was observed that in absence of visible light the NDI radicals are sufficiently stable to measure the decay profiles in different time intervals which demonstrate their reversible behavior (see in inset Fig. 4.9B, Table 4.2).

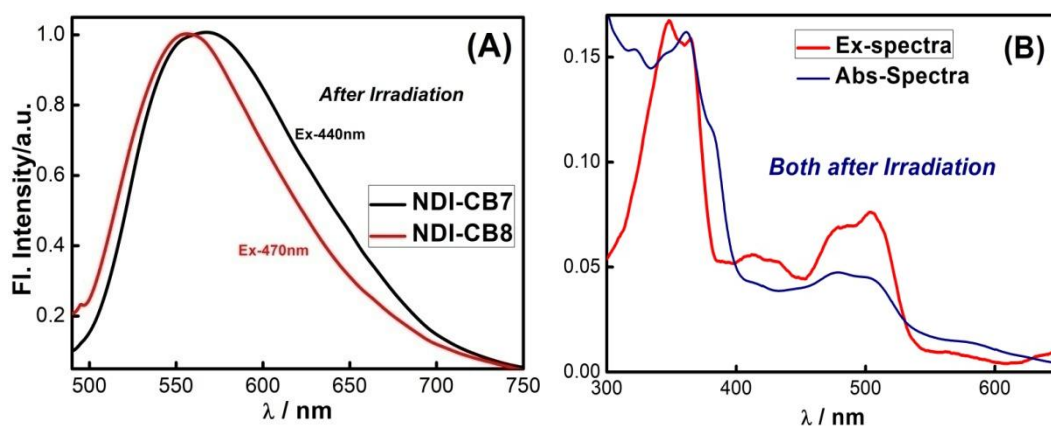


Figure 4.11: (A) Fluorescence spectra after white light 30 minutes irradiation for the CB7 (100 μ M):NDI-BzIm (50 μ M), λ_{ex} = 440 nm (1) and CB8 (50 μ M):NDI-BzIm (50 μ M) λ_{ex} = 470 nm (2) complexes. (B) Excitation and absorption spectra of CB7:NDI-BzIm radical λ_{em} = 550 nm

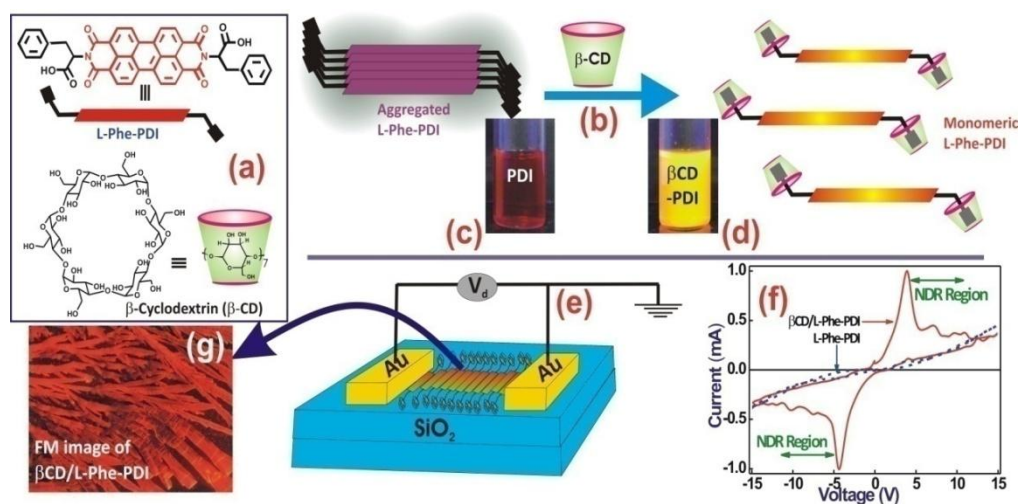
4.1.4. Conclusions

In this study the host–guest interactions of two cucurbituril hosts and imidazol derivative of NDI dye have been investigated by ground-state optical absorption and steady-state and Isothermal Titration Calorimetric studies. The differences between the cavity dimensions of CB7/CB8 hosts bring out notable differences in the stoichiometry, a 1:2 NDI dye complex is formed with the CB7 while a 2:2 host–guest stoichiometry is preferred with the CB8 host. In other words, NDI dye excimer emission band demonstrating efficient non-covalent dimerization of NDI-BzIm derivative with CB8. We also demonstrate by host-guest interaction NDI dye

promotes the radical formation in presence of CB hosts due to reduced the LUMO and HOMO energy of NDI dye. On the other side we also stabilized the emissive NDI radical anion in the presence of CB7 and CB8 hosts in aqueous medium on light irradiation. The long fluorescence lifetime of these NDI radical anions stabilized by macrocyclic hosts may be useful in lifetime imaging studies which employ NDI based compounds for photodynamic therapy. Further this study may add insight into the photoinduced electron transfer processes in NDI based supramolecular assemblies.

Part-2

Deaggregation of Perylenediimide Derivative through Supramolecular Host-Guest Approach: Negative differential resistance (NDR) behavior



Chem. Eur. J., 2019,
(DOI: 10.1002/chem.201902641).

4.2.1 Introduction

Perylene diimides (PDIs) are typical *n*-type semiconducting materials and extensively used in organic electronics.¹⁷⁴⁻¹⁷⁹ PDIs have been utilized in various electronic and optical applications, such as organic field-effect transistors (OFETs),^{143, 180, 181} fluorescent solar collectors,¹⁸² electro-photographic devices,¹⁸³ sensors,^{184, 185} dye lasers,¹⁸⁶ organic photovoltaic cells (OPVs),¹⁸⁷⁻¹⁸⁹ and optical power limiters¹⁹⁰ due to their specific physical, optical, and/or electronic properties. Higher electron mobility and better stability in ambient atmosphere have been observed by introducing electron withdrawing cyano groups at the 6 and 12 positions of PDI which maintains a good planar structure and extended aromatic π -system.¹⁹¹ In aqueous medium, PDI dyes form nonfluorescent aggregates through strong π - π stacking interactions.¹⁴⁸ Although deaggregating strategies like introduction of steric crowding at the perylene core, addition of hydrophilic side chains or bulky dendritic substitution in imide position were successfully applied,¹⁹²⁻¹⁹⁴ the emission quantum yield of the synthetic water soluble PDIs remained low for most of the cases. An interesting alternative of supramolecular approach towards suppressing strong aggregation of PDIs in water was demonstrated by Scherman *et. al.* through the host guest interaction of cationic amine substituted PDI derivative with synthetic macrocyclic receptor cucurbit[8]uril in aqueous medium.¹⁹⁵

On the other hand, there is a growing interest in molecular electronics, especially, pertaining to the electron transport through *metal-molecule-metal* junctions, relevant in building molecular-scale electronic components such as electronic switches, low power memory and logic devices, etc.^{13, 196} One of the transport phenomena in such devices is the negative differential resistance (NDR: *increased resistance with*

increasing voltage over a particular range), which is typically observed in conventional semiconductor materials and has been recently realized from various organic molecules, such as conjugated oligomers, redox-active/self-assembled monolayers and hybrid materials.^{197, 198} In practice, the NDR behavior depends not only on the temperature, device geometry and molecule-electrode interfaces, but also, on the chemical structure and properties of the organic molecules including substitution, redox properties, molecular length, conjugation and stability at room temperature.^{13, 199} In other words, NDR behavior can be improved/tuned either by covalent or noncovalent modification of the concerned molecule or by altering the composition and the physical configuration of the device.¹⁹⁸

Having realized the distinct features of non-aggregated PDIs and their immense potential in molecular-scale electronics, we synthesised water soluble PDI derivatives through condensation of perylenetetracarboxylic acid dianhydride with L(+)-phenyl alanine and D(-)-phenyl alanine in molten imidazole. Applying a supramolecular approach to address disadvantageous aggregation in PDI chemistry in water we introduced some of the naturally occurring and water soluble macrocyclic receptors, such as β -cyclodextrin (β -CD).^{98, 200} CDs possess a hydrophobic inner cavity as well as a primary and secondary hydroxyl group rim, which provides additional hydrogen bonding motifs for the binding of organic guests. In this perspective, we considered N,N'-bis-phenylalanyl derivatized perylenediimide (Phe-PDI), a water soluble dye, for a detailed study. This strong hydrophobic amino acid derivative was found to be soluble in a range of organic solvents and water (pH >6, through the deprotonation of carboxylic acid groups). The (L/D)-Phe-PDI derivatives have been also applied in designing the DNA/RNA groove binder.¹⁰⁷ A large and stable NDR behavior at

ambient conditions through surpassing the hydrophobic aggregation of perylenediimide derivatives, (L/D)-Phe-PDI, using versatile β -cyclodextrin (β -CD) macrocyclic host have been described in this chapter.³⁰ The complex material demonstrated its potential for the development of semiconductor materials, other optoelectronic devices and find its application in photovoltaics as well.

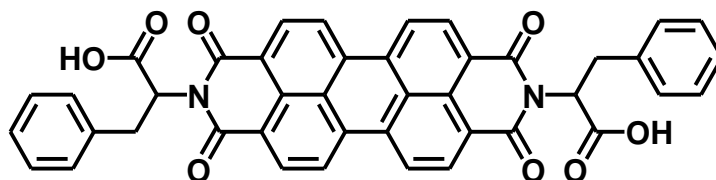
4.2.2 Materials and Methods

β -cyclodextrin (β -CD) used in the experiments was purchased from Alfa Aesar, India. Nanopure water (Millipore Gradient A10 System; conductivity of $0.06 \mu\text{S cm}^{-1}$) was used to prepare the sample solutions. Tris-HCl and sodium bicarbonate buffers were obtained from Merck, India. pH measurements were carried out with Eutech Instruments P2700 pH meter at room temperature. PDI-stock solutions were prepared in tris-HCl buffer at pH 7.5. For measurements in acidic medium (pH 3), small aliquots of PDI stock in tris-HCl buffer were added to water (50 ml) with pre-adjusted pH at room temperature and final pH were also adjusted by addition of hydrochloric acid. Fluorescence quantum yields of the free PDI and β -CD encapsulated PDI were measured by comparing the area under the curve with that of diglycyl imide derivative of PDI (PDG) in ethanol:water (1:1) mixture at pH 10.5 ($\Phi_f = 0.96$).²⁰¹ The details of absorption and fluorescence (steady state and time resolved) measurements and thin film deposition and I-V measurements which are used in this study were provided in the chapter-2.

4.2.3 Results and Discussion

The phenyl moiety of the enantiomerically pure phenylalanine substituted PDI derivative N,N'-bis-phenylalanyl perylenediimide (L-Phe-PDI or D-Phe-PDI, see in Fig. 4.12) was synthesized by following the reported procedure through condensation

of perylenetetracarboxylic acid dianhydride with L(+)-phenyl alanine and D(-)-phenyl alanine in molten imidazole in excellent yield and purity (see in chapter 2).¹⁰⁷ Interaction of both the L and D-phenyl alanine appended PDI-derivative with β -CD was studied and the results with L/D-Phe-PDI are discussed in the following sections.



N,N'-bis-(L/D)-phenylalanyl perylenebisimide

Figure 4.12: Chemical structure of protonated forms of N,N'-bis-phenylalanyl perylenediimide (L-Phe-PDI or D-Phe-PDI) dye.

4.2.3.1 Ground-State Absorption and Emission Measurements

As shown in Figure 4.13A, the absorption profile of deprotonated L/D-Phe-PDI (2.4 μ M in tris-HCl buffer) at pH 7.5 displays moderately resolved vibronic structures of S_0 - S_1 electronic transitions in the 400-650 nm region with absorption bands at 537 nm (0-0) and 500 nm (0-1), typical of PDI derivatives. However, the ratio of the intensities of these vibronic transitions (~ 1.2) conveys considerable aggregation of L/D-Phe-PDI in aqueous medium at very low concentration, which may be anticipated from the unusually strong association constants ($>10^8 \text{M}^{-1}$) of several other PDI derivatives reported in water.²⁰² Gradual addition of β -CD to the above L/D-Phe-PDI solution displayed strong hyperchromic increase in the absorption bands leading to well resolved vibronic structure of S_0 - S_1 transitions at 537 nm (0-0), 500 nm (0-1) and 470 nm (0-2) with clear isosbestic points at 552 nm and 513 nm (Figs. 4.13A and 4.14A). The ratio of these vibronic transitions in the absorption profile of L/D-Phe-

PDI approaches 1.6 which is characteristic for complete deaggregation of PDI-derivatives, in general.^{202, 203} As indicated, most water soluble PDI derivatives are practically non-fluorescent or weakly fluorescent in aqueous medium due to their strong aggregation behaviour. However, L-Phe-PDI, at low concentration ($<5 \mu\text{M}$), shows moderate emission ($\Phi_f = 0.28$) in its deprotonated form in tris-HCl buffer at pH 7.5. Resembling the structured absorption profile, the emission profile of L-Phe-PDI also displayed vibrationally resolved emission bands with maximum at 550 nm and shoulder bands centered at 590 nm and 645 nm. Strikingly, the excitation spectra recorded corresponding to the emission at 600 nm (Fig. 4.15) did not match with the absorption spectra of the same dye solution. Instead, it matched well with the absorption and excitation spectral profile of the dye in de-aggregated state prepared through β -CD interaction (Fig. 4.15).

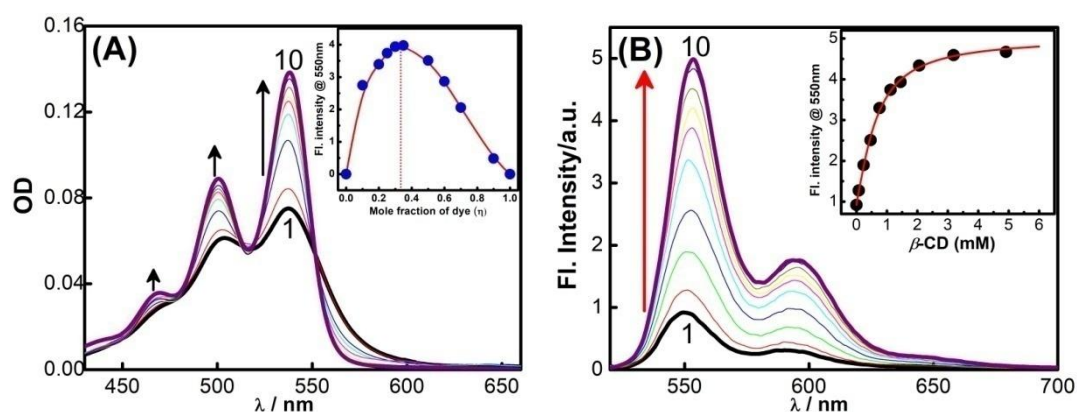


Figure 4.13: Absorption (A) and emission (B, $\lambda_{ex}=490 \text{ nm}$) spectra of L-Phe-PDI ($2.4 \mu\text{M}$, Tris buffer) in presence of β -CD host/mM, 0 (1); 0.08 (2); 0.24 (3); 0.46 (4); 0.76 (5); 1.12 (6); 1.45 (7); 2.06 (8); 3.19 (9); 4.91 (10), Jobs plot (Inset 4.2.1A) and binding curve (inset 4.2.1B) for interaction of L-Phe-PDI with β -CD host.

This concedes that the emission originates from the monomeric L-Phe-PDI dye present in the solution, whereas the dimer or higher aggregates remain non-fluorescent in the wavelength region monitored. Based on this observation, we consider that the

complexation of L/D-Phe-PDI with β -CD host would pose severe steric hindrance to the aggregation of the dyes and therefore retain them in their de-aggregated state, which, in turn, will enhance the emission intensity of the PDI dye. In fact, as shown in Figs. 4.13B, with gradual addition of β -CD host the emission profile exhibited remarkable enhancement of the L-Phe-PDI emission (in tris buffer at pH 7.5) demonstrating an efficient de-aggregation of the PDI derivative via supramolecular host-guest interaction with β -CD.

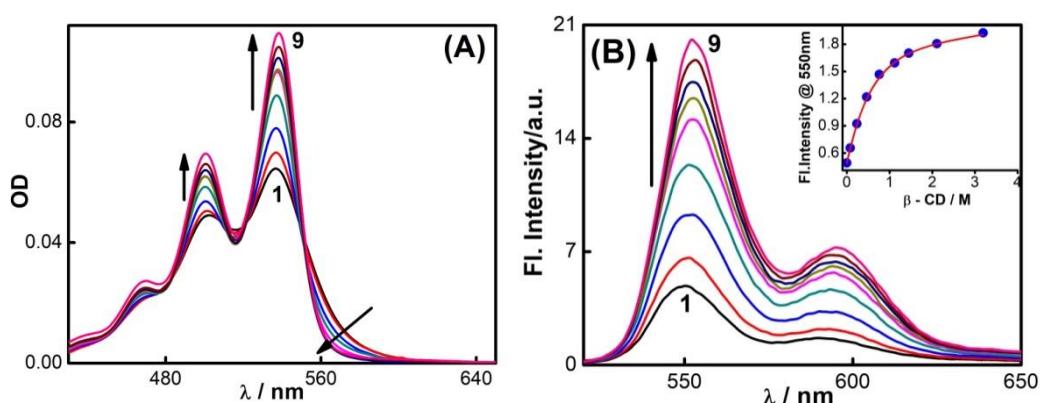


Figure 4.14: Absorption (A) and emission spectra of D-Phe-PDI (3.4 μ M) dye at different concentration of β -CD in Tris-HCl buffer at pH7.5; β -CD/mM: 1) 0.0, 2) 0.1, 3) 0.24, 4) 0.5, 5) 0.8, 6) 1.1, 7) 1.45, 8) 2.1, and 9) 3.19. λ_{ex} = 490 nm. Inset of (B) shows the binding isotherm fl. intensity v/s concentration of β -CD, $K = (K_1.K_2) = 3.3 \times 10^6 M^{-2}$

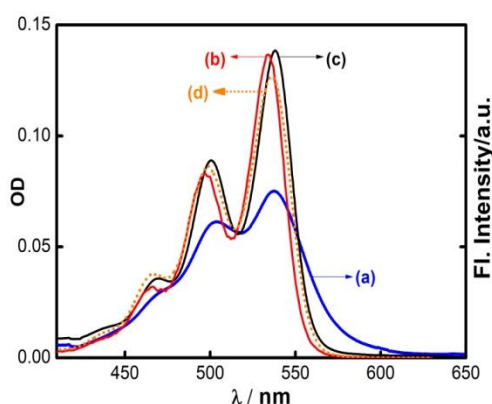


Figure 4.15: Absorption spectra (a) and excitation spectra (b) of L-Phe-PDI. Spectrum (c) is the absorption and excitation spectra (d) obtained for the β -CD/L-Phe-PDI complex.

Similar changes in the absorption and fluorescence measurements were also observed for the D-isomer, D-Phe-PDI, with β -CD and the detailed titration data are provided in Fig. 4.14. The emission quantum yield of β -CD/L-Phe-PDI complex estimated by comparing the area under the curve with that of diglycyl imide derivative of PDI (PDG) in ethanol:water (1:1) mixture ($\Phi_f=0.96$)²⁰¹ rendered significant enhancement in the quantum yield from 0.28 to 0.9 in presence of adequate concentration of β -CD.

4.2.3.2 Circular Dichroism (CD) Measurements

Aggregation of chiral PDI-derivatives is very sensitive to CD measurements that displays strong exciton coupled bisignate CD bands originating from the interaction of π -stacked PDI cores.²⁰⁴ L-Phe-PDI is also intrinsically chiral and its CD spectrum in aqueous medium shows strong exciton coupled bisignate signals with negative Cotton band at 509 nm and positive band at 575 nm, which are clear indications of strong aggregation of L-Phe-PDI derivative. Further, as shown in the Fig. 4.16A, gradual addition of β -CD host (up to ~ 15 mM), the CD profile shows well resolved negative bands with maxima at 470 nm, 501 nm and 537 nm, and all correspond to the spectral signature of monomeric L-Phe-PDI with their respective chirality. Similar CD spectral changes attributable to the aggregation/de-aggregation of D-Phe-PDI, with β -CD were also observed and are provided in Figure 4.16B.

Steady-state absorption, emission and CD measurements clearly displayed distinct spectral changes confirming the interaction of L/D-Phe-PDI with β -CD. Considering the cavity size/shape of the β -CD host and the PDI guest it may be inferred that unlike the reported inclusion of planar and bulky PDI core by the β -CD host having larger cavity,¹⁹⁵ inclusion of the central PDI core by the smaller β -CD host is quite

improbable. Instead, the inclusion of the two peripheral hydrophobic phenyl substituent by the β -CD host cavity is a more likely mechanism, which would give rise to a 2:1 [β -CD:L-Phe-PDI] host-guest stoichiometry.

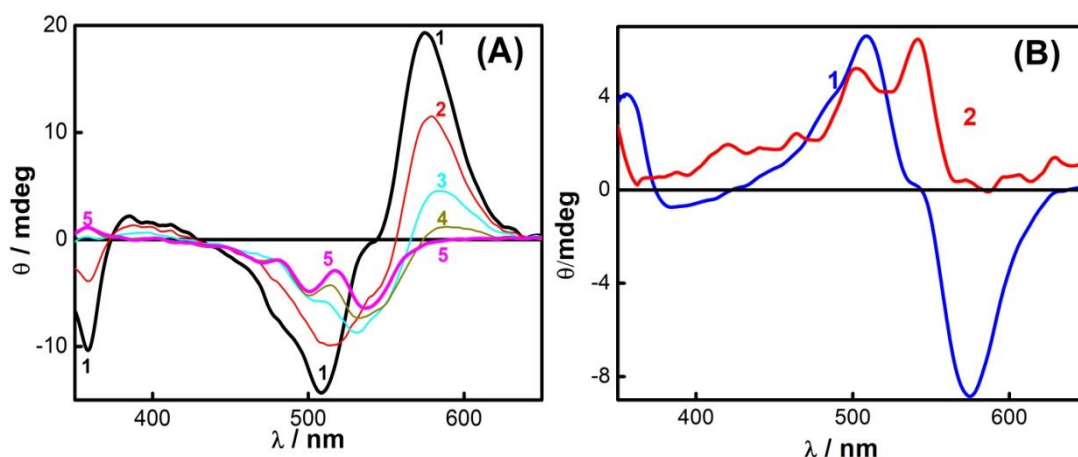


Figure 4.16: (A) CD spectra of L-Phe-PDI (30 μ M, pH 7.5, tris buffer) recorded in presence of [β -CD]/mM: 0.0 (1); 1.16 (2); 3.1 (3); 6.3 (4); 15.0 (5). (B) CD spectra of D-Phe-PDI (20 μ M) dye (1) and in presence of β -CD (10 mM, 2) in Tris-HCl buffer, pH 7.5

The complex stoichiometry is verified from the absorbance changes by the Jobs continuous variation method which displayed maximum at ~ 0.33 mole fraction of L-Phe-PDI (Inset, Fig. 4.13A), in good accordance to a 2:1 host-guest stoichiometry. Further, the changes in the emission intensities have also been plotted against the β -CD concentration (inset, Fig.4.13B). The binding isotherm is fitted with a modified Benesi-Hildebrand equation for a 2:1 complexation. An apparent overall binding constant $K = (K_1 \times K_2)$ value obtained is about $2.8 \times 10^6 \text{ M}^{-2}$.

In addition, isothermal titration calorimetric (ITC) measurements have been carried out to determine the binding constants, stoichiometry and other thermodynamic parameters of the complex formation. As presented in Fig. 4.17, the preliminary data agreed to a 2:1 composition with a binding constant of $\sim 10^3 \text{ M}^{-1}$, typical of β -CD host with such aromatic moiety.

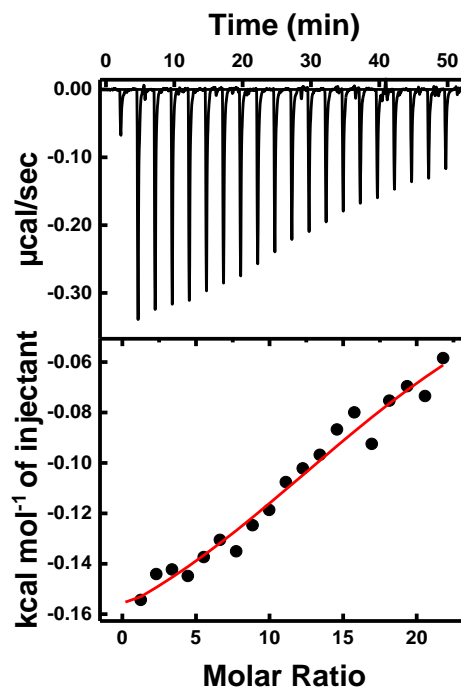


Figure 4.17: ITC isotherm for titration of L-Phe-PDI with β -CD host in Tris-HCl buffer pH 7.5 at 25 °C.

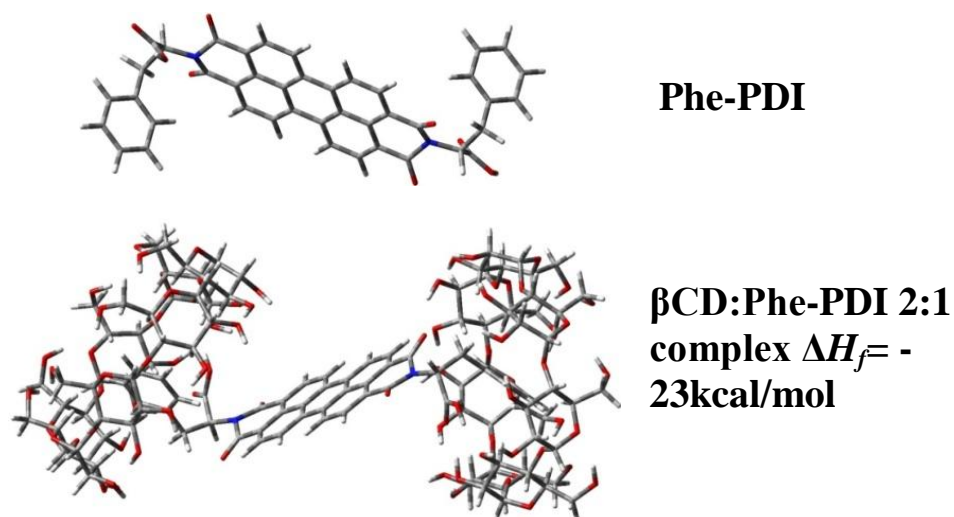


Figure 4.18: Geometry optimized structures of free Phe-PDI and 1:1 and 2:1 host-guest complexes with β -CD host.

From the Jobs plot and presuming a 2:1 stoichiometry, geometry optimization calculations (without solvent consideration) were carried out which conformed to a

2:1 β -CD:(L/D)-Phe-PDI arrangement (Fig. 4.18) with $\Delta H \sim -23$ kcal/mol. In this geometry, the wider rims of two β -CD hosts encapsulate the aromatic part of the phenylalanyl groups at both ends, rendering them as bulky (L/D)-Phe-PDI monomers.

4.2.3.3 Fluorescence Lifetime and Anisotropy Measurements

Evidence for the β -CD interaction also emerged from the excited state lifetime of L-Phe-PDI obtained from the fluorescence decay trace recorded in a time correlated single photon counting (TCSPC) setup. As presented in Fig. 4.19B, while the fluorescence decay of free L-Phe-PDI displayed single exponential lifetime of 4.52 ± 0.12 ns at pH 7.5, the decay at lower pH (<4) displayed multiexponential kinetics (see in Fig. 4.19B). The observation of single exponential decay from a solution where considerable aggregation is expected (~ 4.5 ns above pH 4.5) suggests that the emitting species is the molecularly dissolved L-Phe-PDI monomer only whereas the dimer and higher aggregates are non emissive.

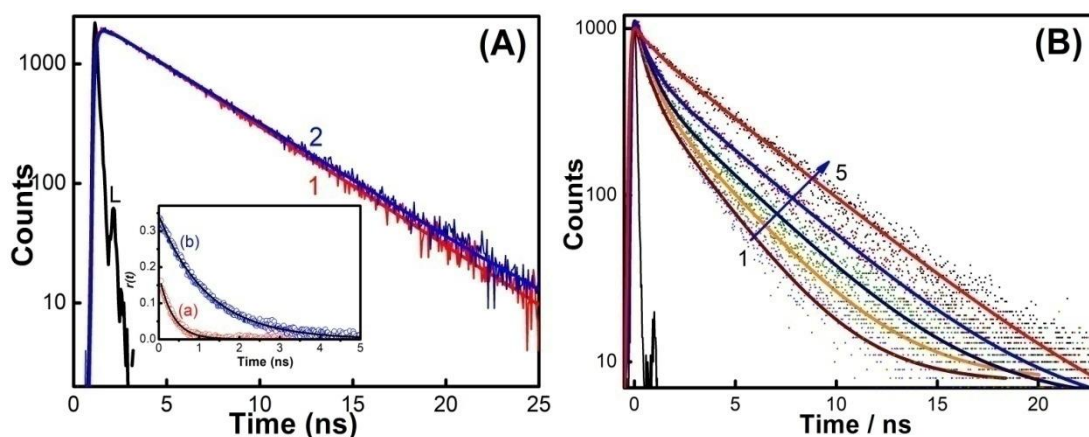


Figure 4.19: (A) Decay traces of L-Phe-PDI ($2.4 \mu\text{M}$ in tris buffer, pH 7.5) in absence (1) and in presence (2) of 5.0 mM β -CD host and IRF (L). Inset: Anisotropy decay of free L-Phe-PDI (a) and in presence of β -CD host (b). $\lambda_{\text{ex}} = 445 \text{ nm}$, $\lambda_{\text{em}} = 580 \text{ nm}$. (B) Fluorescence decay traces of L-Phe-PDI ($1.85 \mu\text{M}$) dye at different concentration of β -CD in water at pH-2.5. β -CD / mM: 1) 0.0, 2) 1.4, 3) 2.4, 4) 4.3, 5) 13.26, 'L' represents the lamp profile. $\lambda_{\text{ex}} = 490 \text{ nm}$

This was also revealed in the excitation spectra recorded, which corresponds to the absorption spectrum of the monomeric dye (*vide supra*). Further, the addition of β -CD to L-Phe-PDI did not result any change in the decay profile of L-Phe-PDI dye as such. This indicates that the central PDI fluorophore is unaffected and not encapsulated by the β -CD host. Instead, the interaction is apparently through the encapsulation of the peripheral phenyl groups in to the β -CD cavity, bringing out de-aggregation of the L-Phe-PDI. At less than pH 4.5, the propensity for aggregation due to the undissociated carboxylate groups leads to emissive higher aggregates having broad low energy emission band centered at 685 nm (Fig.4.20A). Accordingly, the fluorescence decay displayed a multiexponential decay showing faster decay profile as shown in Fig.4.20B.

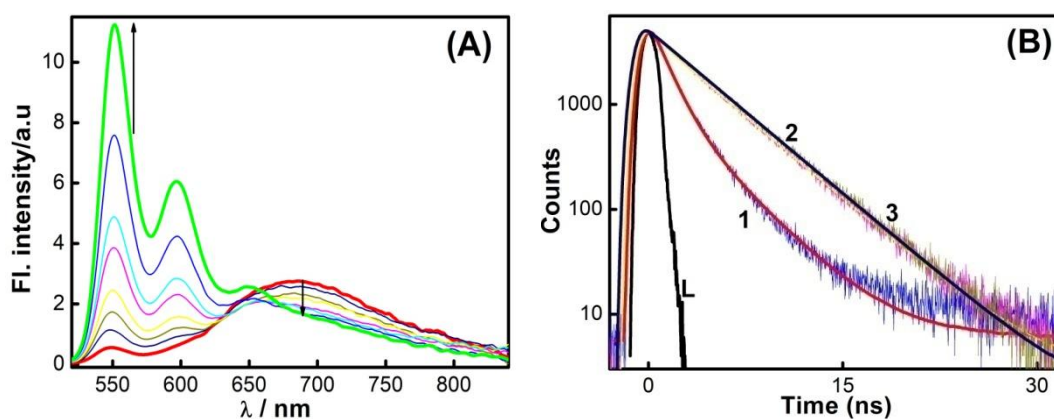


Figure 4.20: (A) Fluorescence spectra of L-Phe-PDI (1.85 μ M) dye at different concentration of β -CD in water pH-2.5 β -CD / mM: 1) 0.0, 2) 0.15, 3) 0.5, 4) 0.9, 5) 1.4, 6) 2.42, 7) 4.35, 8) 7.56, λ_{ex} = 490 nm. (B) Decay trace of L-Phe-PDI (35 μ M) in water with different pH: 1) 2.5, 2) 4.0, 3) 7.5, 'L' represents the lamp profile. λ_{ex} = 490 nm.

Measurement of fluorescence anisotropy decay is often used to examine the changes in the size of the emitting fluorophore which is expected on its complex formation with a macrocyclic host. The time resolved fluorescence anisotropy decays, $r(t)$, clearly documented large differences in the decay profiles of free L-Phe-PDI and

β -CD/L-Phe-PDI complex, pointing to an increase in the hydrodynamic molecular volume due to complex formation. For the dye alone at pH 7.5, the anisotropy decay (Inset Fig. 4.19A, trace (a)) fits to a single-exponential kinetics with a time constant (τ_r) of 0.43 ± 0.02 ns, which in the presence of β -CD, gets significantly increased to 1.21 ± 0.05 ns (Inset Figure 4.19A, trace (b)), conceding an increase in molecular diameter from ~ 7.8 Å to ~ 11.2 Å due to the complexation of β -CD at both the ends.

4.2.3.4 ^1H -NMR Measurements

An interaction site of L-Phe-PDI with β -CD host is further verified by ^1H -NMR spectroscopy. As shown in Fig. 4.21, due to the strong aggregation of L-Phe-PDI (c. 100 μM , pH 8) in aqueous medium the aromatic protons appeared as broad and weak signals at δ 7.51 along with the aliphatic methane and the benzylic protons at δ 6.0 and δ 3.74 respectively.

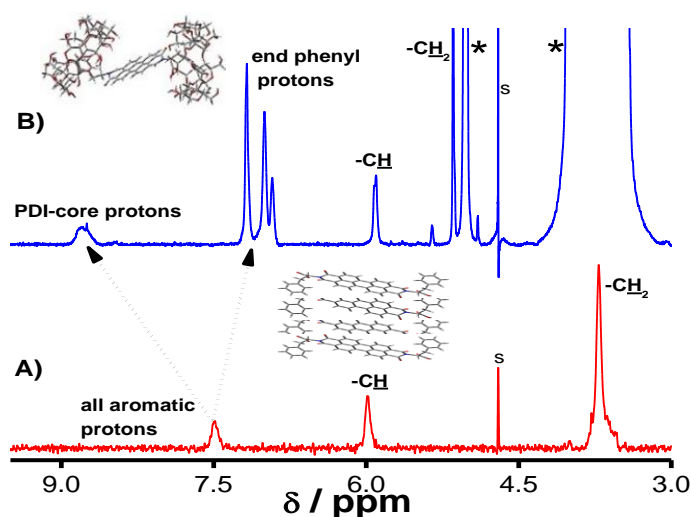


Figure 4.21 ^1H -NMR spectra recorded for uncomplexed L-Phe-PDI (A); and in presence of β -CD host (B); s, solvent, asterisks indicate β -CD protons.

In presence of β -CD host, although not very clearly resolved, the PDI core protons and the phenyl protons appeared separately at δ 8.55 and δ 6.9-7.4 respectively. On the other hand, while the methine protons as expected, did not show

any shift from its parent positions, the benzylic $-\text{CH}_2$ proton signals displayed downfield shift of 1.7 ppm to δ 5.44 in presence of β -CD host, indicating that they reside closer to the hydroxyl groups of β -CD host experiencing the electron withdrawing effect of the oxygen atoms. Such spatial arrangement is certainly achievable through the encapsulation of the phenyl group by the hydrophobic cavity of β -CD host in 1:2 L-Phe-PDI: β -CD host-guest complex stoichiometry, and is also inferred from the geometry optimization studies. Similar changes were observed in the ^1H NMR signals of D-Phe-PDI in the absence and presence of β -CD.

4.2.3.5 SEM, AFM and FM Measurements

To explore the advantages of the strong deaggregation of L-Phe-PDI achieved here, we attempted to study the morphological changes introduced in (L/D)-Phe-PDI due to β -CD complexation. The morphological analyses were carried out on the β -CD/(L/D)-Phe-PDI samples deposited on respective substrate surface by SEM, AFM and FM methods and the comparative images are arranged in Fig. 4.22. As mentioned in the experimental section in chapter 2, images were accepted only after verifying its reproducibility from several regions of the sample film. As shown in the Fig. 4.22 (a-c) the SEM images of L-Phe-PDI dye alone displayed randomly distributed globule type structures, due to the self-aggregation of PDI units. However, the SEM image (Fig. 4.22, d-f) obtained for L-Phe-PDI in presence of β -CD presented solid strips of about 5-6 μm width having well connected sheet like morphology. We believe that the encapsulation of the peripheral phenyl groups of L-Phe-PDI by β -CDs prevents the otherwise potent π -stacking of PDI units, allowing the assembly of monomeric β -CD/L-Phe-PDI complex units to form the sheet like morphology.

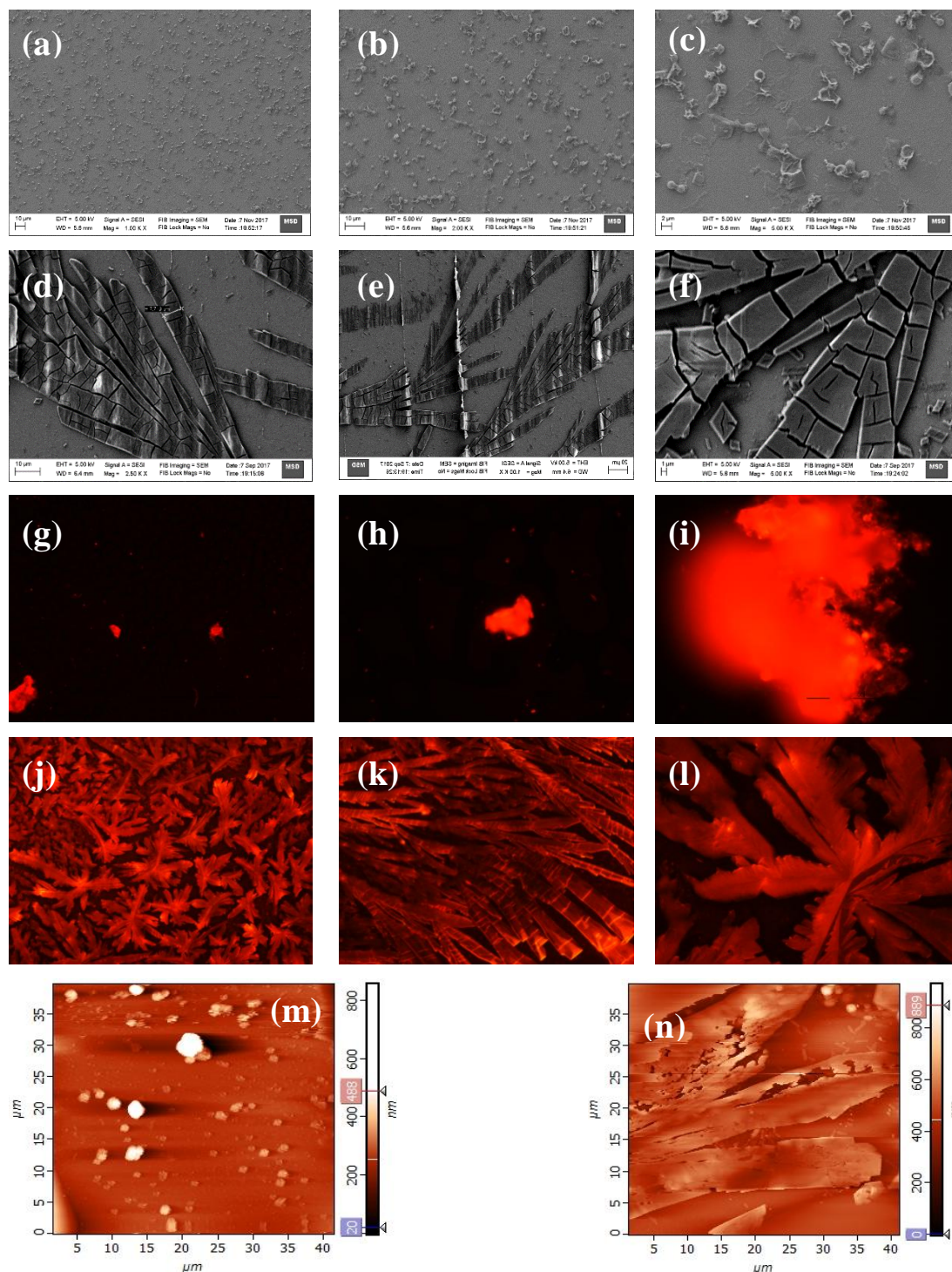


Figure 4.22: SEM (a-c, d-f); FM (g-i, j-l); and AFM (m, n) images obtained from samples deposited on respective substrate surface; L-Phe-PDI (a-c, g-i, m) and β -CD/L-Phe-PDI complex (d-f, j-l, n).

The association among the complex may be facilitated through hydrogen bonding between the β -CD units in the complex with the carboxylate group of an

adjacent complex. Conforming observations were also made from the AFM images (Fig.4.22, m, n) where the images revealed $\sim 5\text{-}6\text{ }\mu\text{m}$ wide long structures only in the $\beta\text{-CD/L-Phe-PDI}$ complex (Fig.4.22, m) whereas aggregated lumps were seen in bare L-Phe-PDI sample (Fig.4.22, n). More convincingly, fluorescence microscopy images captured by using the green excitation ($\lambda_{\text{ex}}=500\text{ nm}$) (Fig.4.22, g-l) displayed bright red lumps for the free dye (Fig.4.22, g-i), whereas the $\beta\text{-CD/L-Phe-PDI}$ complex (Fig. 4.22, j-l) confirmed the presence of fluorescing L-Phe-PDI dyes in the highly ordered stripe type pattern. Equivalent observations were made with the D-Phe-PDI derivative as well.

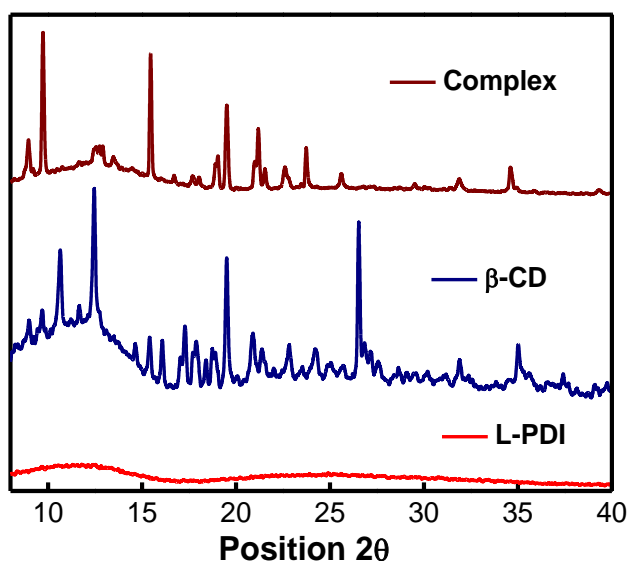


Figure 4.23: The powder XRD patterns recorded for L-Phe-PDI, $\beta\text{-CD}$ and the $\beta\text{-CD/L-Phe-PDI}$ complex.

Moreover, as presented in Fig. 4.23, the powder XRD pattern obtained for the drop-casted thin film of $\beta\text{-CD/L-Phe-PDI}$ complex displayed well resolved sharp and intense XRD peaks representing the crystalline nature of the complex, whereas the L-Phe-PDI dye showed very broad XRD peaks due to the amorphous behavior. In short,

the above patterns reaffirm the deaggregated orderly state of β -CD/(L/D)-Phe-PDI complex against its free form.

4.2.3.6 *I-V Characteristics and Negative Differential Resistance (NDR) Behavior*

In the past, improved semiconductor materials have been created from various organic molecules including self-assembled materials with much importance on the substitution, redox properties, molecular length and conjugation.¹³ Considering the immense potential of PDI derivatives as the n-type semiconducting materials and in organic electronics/optoelectronics, we deployed a thin film of above demonstrated β -CD/L-Phe-PDI complex to evaluate its NDR behavior in a current-voltage measurement (I-V curve).

The typical schematic (Fig. 4.30) for the *I-V* measurement device and its constituent assembly is shown in Fig. 4.30(e) and its construction details are provided in the experimental section in chapter 2, 2.14.5. Fig.4.24A presents the *I-V* characteristics recorded at ambient conditions from the device made with β -CD/L-Phe-PDI complex. As seen in trace (a), during the positive voltage sweep from 0 V to +15 V and to 0 V, the current displayed a steep rise to reach its maximum at voltage ~ 4.64 V. Thereafter with further increase in the voltage, the current decreased sharply, bringing it down to the base value at +15 V and the current steadily decreased to zero in its path from +15 V to 0V. During the voltage sweep carried out in the negative direction from 0 V to -15 V and to 0 V, current once again displayed steep increase reaching its maximum at ~ -4.67 V and dropped back to the base value at -15 V and reached to the minimum at 0 V. Thus, the voltage sweep in the positive and negative direction displayed bistability in the *I-V* curve for the β -CD/L-Phe-PDI complex (Fig.4.24A). The observed *I-V* pattern clearly shows the characteristics of an

NDR curve such as peak point, valley point, and negative differential resistance (NDR) with a peak to valley ratio (PVR) of ~ 2 . The peaks maintained its reproducibility even after several subsequent to and fro voltage sweeps (Fig.4.24B). Similar *I-V* scans were repeated with L-Phe-PDI dye or β -CD alone in the device as a control system. Interestingly, in both the control devices the complete voltage sweep from 0 to +15V and 0 to -15 V did not display any noticeable changes in the current with the voltage sweep (Fig.4.24A, trace b, trace c respectively) and it became evident that the NDR effect originated only from the β -CD/L-Phe-PDI complex and not from its individual components. In addition, the *I-V* characteristics were recorded multiple times with voltage sweep only in one direction, either in the +ve or -ve direction. It may be noted that these traces displayed the NDR peak only in the first scan (Fig.4.27) in either cases and in the subsequent scans in the same direction, the NDR peak did not appear. However, when the device was subjected to a complete cycle of +ve and -ve voltage sweep, the device generated the contended NDR peaks as in Fig. 4.24. Moreover, several such to and fro voltage sweeps with varying concentrations of L-Phe-PDI reproduced the bistable NDR characteristics as displayed in Fig. 4.25. Moreover, changes in the PVR were also observed when complexes containing different concentrations of the dye or host were used in the film (Fig. 4.25). It is quite possible that moisture content, if remaining in the β -CD/L-Phe-PDI film at the ambient conditions, can also produce charge carriers during the voltage sweep in the form of hydronium and hydroxyl ions by dissociation and may give rise to such increase in the current.^{205, 206} To rule out the possibility from such a mechanism, *I-V* measurements were carried out in a setup maintained under vacuum.

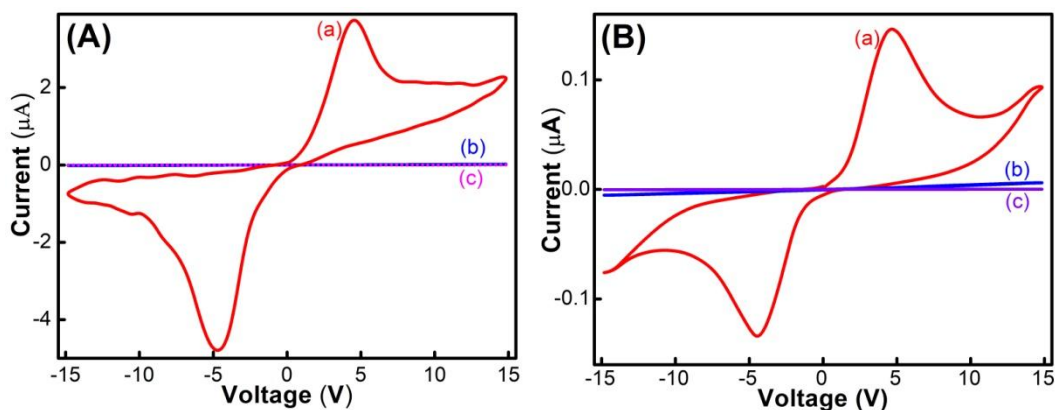


Figure 4.24: *I-V characteristics recorded for the film of β -CD/L-Phe-PDI complex (a), for the control L-Phe-PDI dye (b) and the β -CD (c) under ambient condition (A) and under Vacuum (B).*

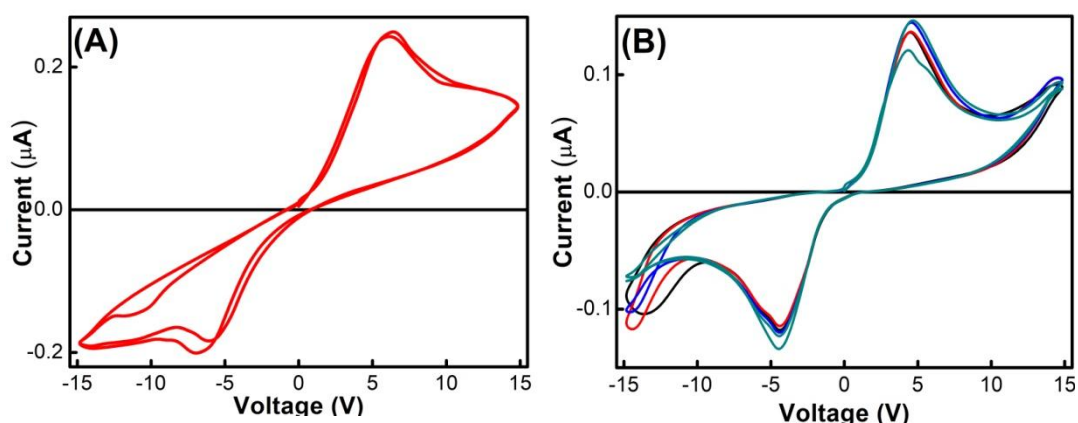


Figure 4.25: (A) *I-V characteristics recorded for the film of β -CD/L-Phe-PDI complex at ambient conditions and at different concentrations than the traces presented in Fig. 4.24A and (B) Several scans of the I-V characteristics recorded for the film of β -CD/L-Phe-PDI complex under vacuum.*

As displayed in Fig. 4.24B, the *I-V* characteristics recorded under vacuum condition also presented neat bistable NDR peaks at 4.62 V and -4.56 V and are in good agreement to the NDR peaks obtained from the devices maintained at ambient conditions (Fig. 4.24A), upholding genuineness of the NDR behavior of the complex. Generally, the NDR behavior in molecular systems have been described in terms of transformation of molecule into its insulating state that prevents further conduction,

availability of redox species, or diffusion-limited redox reaction.²⁰⁷⁻²¹⁰ In the present case, the Phe-PDI dye consists of redox active π rich perylene core. Supporting this, the cyclic voltammetry measurements carried out with the L-Phe-PDI dye solutions in the absence and presence of β -CD provided oxidation and reduction peaks, corresponding to their reversible redox behavior at the electrode (Fig. 4.28).

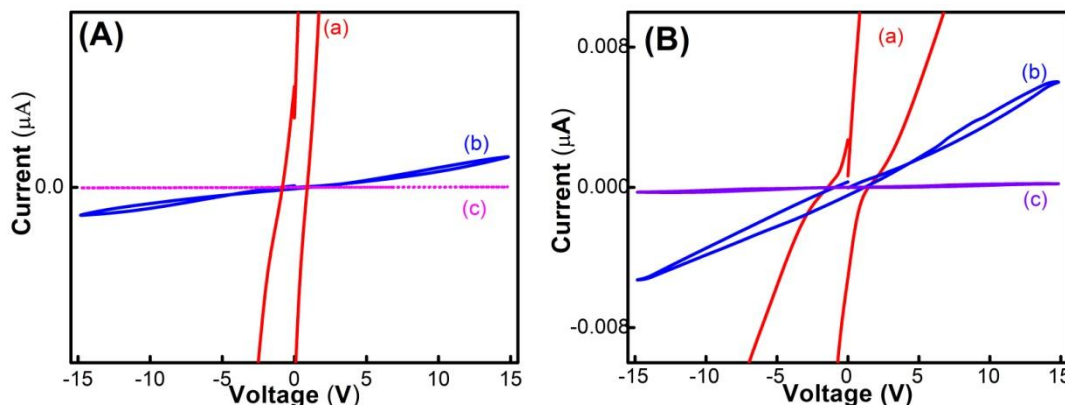


Figure 4.26: Enlarged scale display of Fig. 4.2.12 showing the I-V characteristics recorded for the film of β -CD/L-Phe-PDI complex (a), for the control L-Phe-PDI dye (b) and the β -CD (c) under ambient condition (A) and under Vacuum (B)

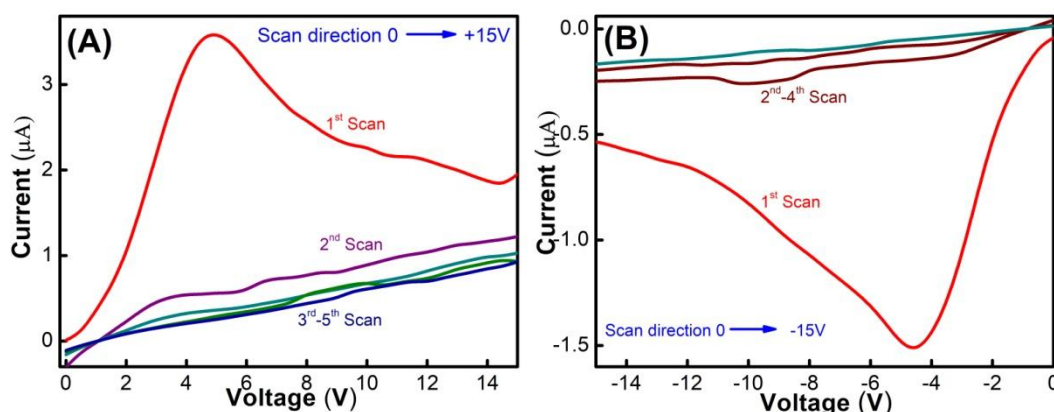


Figure 4.27: I-V curve recorded with multiple scans only in one direction; only in the positive (0 to +15V) (A) and only in the negative (0 to -15V) (B) directions.

Hence, the origin of NDR behavior strongly points to the reversible electrochemical redox chemistry operating only in the complex film and not from the L-Phe-PDI dye alone deposited in the electrode nano gap. On the mechanistic aspect of the observed NDR behavior, as established *vide supra*, the β -CD/L-Phe-PDI

complex conserve the L-Phe-PDI dyes in its monomeric state even in the solid phase (Fig.4.29), whereas due to the strong π - π stacking interaction of the π rich perylene cores, the dye alone exists as non-fluorescent aggregates, both in aqueous medium as well as in its film form. The emission spectra recorded from the thin films of β -CD/L-Phe-PDI complex and L-Phe-PDI dye alone distinctly differentiate them as monomeric emission and aggregate emission in their spectral profile presented in Fig.4.29. Therefore, the NDR behavior observed in the β -CD/L-Phe-PDI complex could be attributed to the oxidation/reduction processes involving the π rich monomeric PDI core during the I - V scan. This is further supported by the I - V characteristics presented in Fig. 4.27, which displayed the NDR peak only in the first scan in one direction and was reproducible only in a complete redox cycle.¹⁹⁷

This, on the other hand, brings out the disparity with the conventional cyclic voltammetry (CV) experiments where the species/ions in solution diffuse to the respective electrodes and gets oxidized/reduced. The current will increase as the potential reaches the reduction potential of the analyte, then falls off as the concentration of the analyte is depleted close to the electrode surface, a mechanism which does not comply with the diffusional tail of NDR process. In the NDR process the system reach a state that prevents further movement of the charge carriers and conduction, leading to the NDR behavior and is seen only when the molecules are in their non-aggregated state. In the case where β -CD is absent, the L-Phe-PDI dyes in the film exists as aggregates and apparently the redox properties are lost in its aggregated state and hence L-Phe-PDI dyes alone does not display any NDR behavior. This striking difference in the I - V characteristics of β -CD/L-Phe-PDI complex vs the L-Phe-PDI is very promising for its application in organic electronic devices.

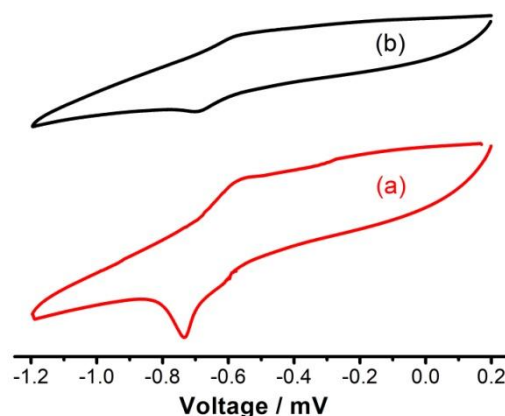


Figure 4.28: Cyclic Voltammetry traces (scan rate 100mV/sec, Ag/AgCl reference) obtained from PDI (100 μ M) in the presence (a) and absence (b) of β -CD (16mM).

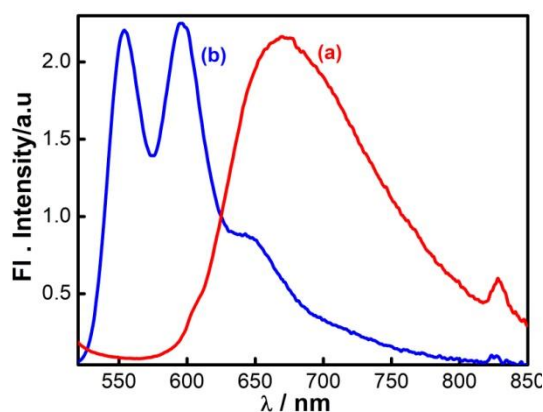


Figure 4.29: Solid state fluorescence spectra of L-Phe-PDI (10 μ M) dye (a) and that of β -CD/L-Phe-PDI complex (b) deposited as thin films.

The NDR behavior of the β -CD/L-Phe-PDI film stored/operated under ambient conditions were reliably stable as its I-V characteristics recorded after six months displayed reasonably good reproducibility with similar peak ratios and reversibility (Fig.4.25). Such stable redox behavior also suggests that these films can not only be employed as active layer in electrical bistable devices but also, they are well suited as pseudo-capacitors. Moreover, it is commonly known that n-type organic semiconductors are not very stable in air, for example, C60, C70 based materials^{211, 212} degrade rapidly within a few hours in air. The excellent air stability exhibited by these n-type semiconductors for at least 6 months, even stored in air, identify them to be best

suitable candidates for photovoltaics applications as they also strongly absorb in visible region.

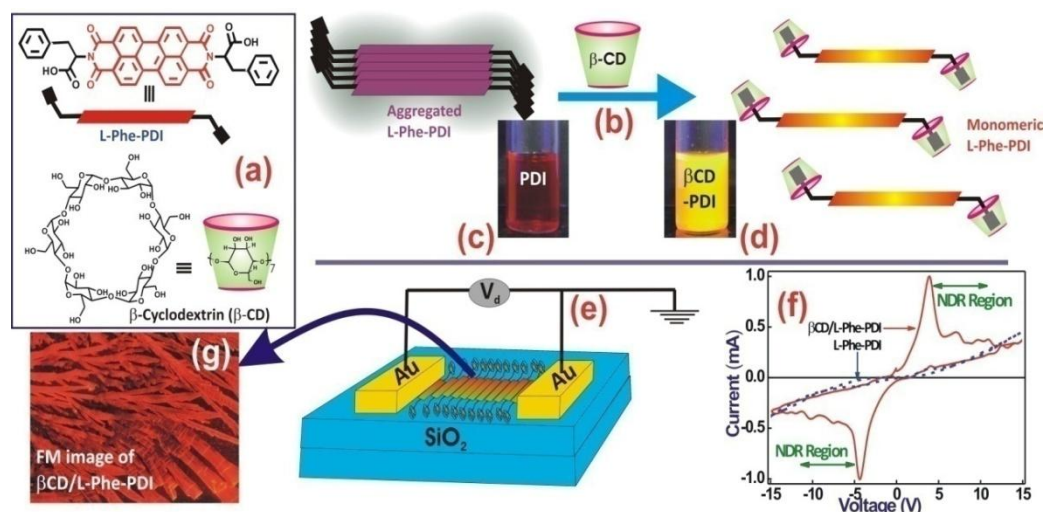


Figure 4.30: Chemical structure of L-Phe-PDI and β -CD host (a); schematic representation of host induced deaggregation process (b); photograph of solution of L-Phe-PDI (c) and β -CD/L-Phe-PDI complex under UV light (d); I-V scan setup (e), I-V curve (f) and the FM images of β -CD/L-Phe-PDI complex (g).

4.2.4 Conclusions

In conclusion, for the first time we demonstrate a metal-dye-metal constructed intense and stable negative differential resistance (NDR) behavior at ambient conditions using a supramolecularly deaggregated (L/D)-Phe-PDI derivative and gold electrodes. Through detailed spectroscopic and imaging analysis, we validate the proposal that the encapsulation of bay-substituted phenyl groups of aggregated (L/D)-Phe-PDI by the β -CD macrocyclic host bring them in their monomeric state through a 2:1 host-guest complex. The deaggregated PDI dyes displayed remarkable fluorescence enhancement and is responsive to external stimuli, such as temperature or additives like adamantanol suitable for stimuli responsive self-assembled systems. In the thin film deposits, the monomeric β -CD/(L/D)-Phe-PDI complex displayed sheet like

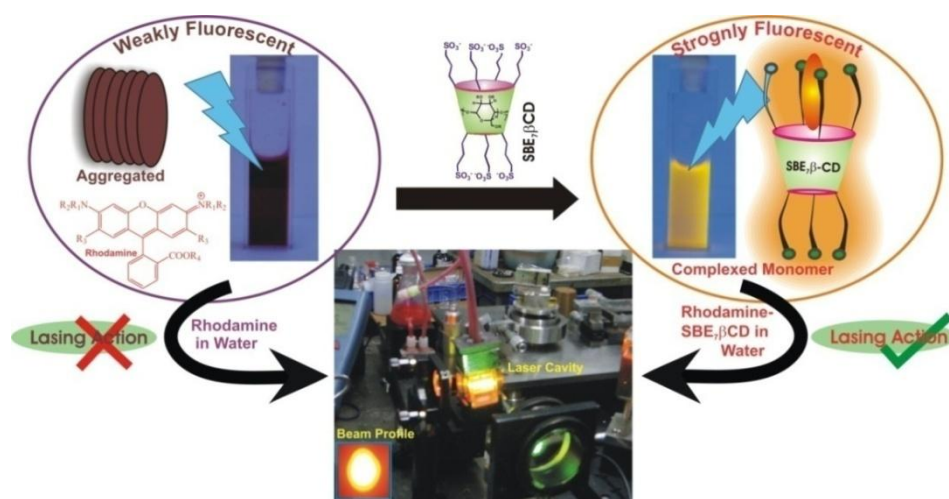
morphology, and is ascertained from the SEM, AFM and FM images. However, the uncomplexed (L/D)-Phe-PDI dye remained as scattered lumps, reiterating their strong aggregation tendency. The contended negative differential resistance behavior of the complex was seen as intense and reversible peak in the I-V scan and is attributed to the oxidation/reduction processes involving the rigid π rich monomeric PDI core, retained through macrocyclic complexation. The clear reproducibility of the I-V characteristics from the device stored at ambient conditions even after six months recommend them for organic electronics application. On the other hand, the strong absorption of the complex in the visible region also projects them as best suited for photovoltaics applications as well.

Chapter 5

Supramolecular Interaction of Rhodamines and Thiazole Orange with Sulfobutylether- β - cyclodextrin: Applications in Aqueous Dye Laser and Fluorescence Sensor

Part-1

Host–Guest Interaction of Rhodamine Dyes with Sulfobutylether- β -cyclodextrin: A Viable Approach for Supramolecular Aqueous Dye Laser



ChemPhysChem. 19, 2018, 2349-2356.

5.1.1 Introduction

One of the key goals of supramolecular chemistry is to assemble structural building blocks into regular arrays with new properties and emergent phenomena.²¹³ Host–guest chemistry has tremendous potential to provide us with strategies to design and build these structures.^{23, 214} A host-guest system with well-defined stoichiometry allows one to study the interplay of various noncovalent interactions in the recognition event, structure-property relations etc., and more importantly, the unique physicochemical outcome characteristic to such supramolecular systems.^{213, 214} Presently, this approach has proved its utility in wide range of applications like, in chemosensing,¹¹³ optoelectronics like optical sensor,¹¹⁵ on-off switches^{53, 69} and logic gates,²¹⁵ photostabilization,^{22, 216} supramolecular catalysis,⁷² drug delivery vehicles,^{38, 73} enzymatic assay,¹¹⁶ nanocapsules,²¹⁷ supramolecular architectures^{23, 114} and other stimulus responsive functional devices.¹¹⁷ Especially, encapsulation of fluorophores by macrocyclic hosts often leads to dramatic modulation of photophysical aspects of guest dyes.⁹⁴ One such phenomenon is the deaggregation of fluorophores in aqueous medium by supramolecular encapsulation. Organic fluorophores often tend to form aggregates with diminishing optical output in aqueous medium.^{218, 219} The hydrophobic aggregation of organic fluorophores in aqueous medium can be avoided by their supramolecular host-guest complex formation with appropriate water soluble macrocyclic hosts.²¹⁸ Such supramolecular deaggregation yields dramatic enhancement of fluorophore emission as well as photostability in aqueous medium.²²⁰ Specifically, this approach has tremendous potential when applied to the organic laser dyes towards the development of aqueous dye laser systems. Among various laser dyes, rhodamine dyes are the most important class of fluorescent dyes as shown by

their applications in dye lasers, as quantum counters, photosensitizers, for spectral calibration in fluorometers, in single-molecule detection, in bioimaging, for scanning confocal microscopy, in fluorescence correlation spectroscopy (FCS), and in high-throughput screening assays.^{219, 221-224} The various applications are made possible through the combination of their water solubility, high quantum yields, high extinction coefficients, and very high photostability.²¹⁶ Despite of all these positive notes, application of rhodamine dyes for lasing purpose in aqueous medium is still limited because of its low quantum yield in water as a consequence of its highly favorable aggregation and adsorption in aqueous medium.^{93, 219, 225} On the other hand, the known solid-state (mainly polymer based) dye lasers as well as organic solvent-based dye lasers need recurrent replacement of dye media due to its rapid degradation.²²⁶ Additionally, the major concerns in the use of organic solvents mainly involve the disposal of dye solutions and safety hazards due to the flammable nature of these solvents, which are generally used in bulk amounts in dye lasers.⁹³ To address these issues, it is worth to explore the options for laser dyes with high quantum yield with sufficient photostability in aqueous medium. Earlier, Mohanty et al. have established an efficient and stable “supramolecular dye laser” using Rh6G and RhB dye solutions in the presence of cucurbit[7]uril (CB7) macrocyclic host. However, the limited water solubility, tedious separation procedure to get pure synthesized CB7 or the high cost of commercially available CB7 restricts to establish a cost effective supramolecular dye laser system for routine use.

Sulfobutylether- β -cyclodextrin (SBE β CD) (see in Fig. 5.1.1), commercially known as captisol, is a β -cyclodextrin (β CD) derivative, in which four secondary alcoholic groups in the wider rim and three alternate primary alcoholic groups in the

narrow rim have been replaced by sulfobutylether chains.^{227, 228} Since, SBE₇βCD contains the same βCD core with sulfobutylether chains at both the portals, it carries the extended hydrophobic nature along with the stretched cavity of SBE₇βCD (already explained in chapter-1, 1.4.2). Whereas, the hydrophilic portals containing SO₃⁻ bearing sulfobutyl ether chains show strong interaction towards cationic guests.²²⁹ The solubility is much higher than the parent βCD and other cationic receptors with similar cavity dimension such as cucurbit[7]uril (CB7).⁹⁴ In an earlier work, Shinde et al. have established stimuli-responsive assembly of DAPI with SBE₇β-CD for *on-off* fluorescent switch and controlled drug delivery applications.²²⁹ Of late, utilising the recognition behaviour of SBE₇βCD towards insulin and lysozyme proteins, the efficient inhibition and disintegration of amyloid fibrils from these proteins have been demonstrated and shows promising for the treatment of amyloid related diseases.²⁷ However, the host-guest interaction studies of SBE₇βCD with practical laser dyes and their technological applications are hardly explored. In this study, the molecular details of the host-guest interaction of two technologically important rhodamine dyes, namely, rhodamineB (RhB) and rhodamine6G (Rh6G) with SBE₇βCD enhanced fluorescence to establish an efficient laser operation in aqueous solution. Practically, these vital parameters are utilized to optimize and demonstrate a working cost-effective supramolecular broad-band as well as narrow-band aqueous dye laser systems with improved lasing efficiencies, better beam profile and enhanced durability, as compared to that in organic medium. The chemical structures of both RhB, Rh6G and SBE₇βCD are given in Fig.5.1.1

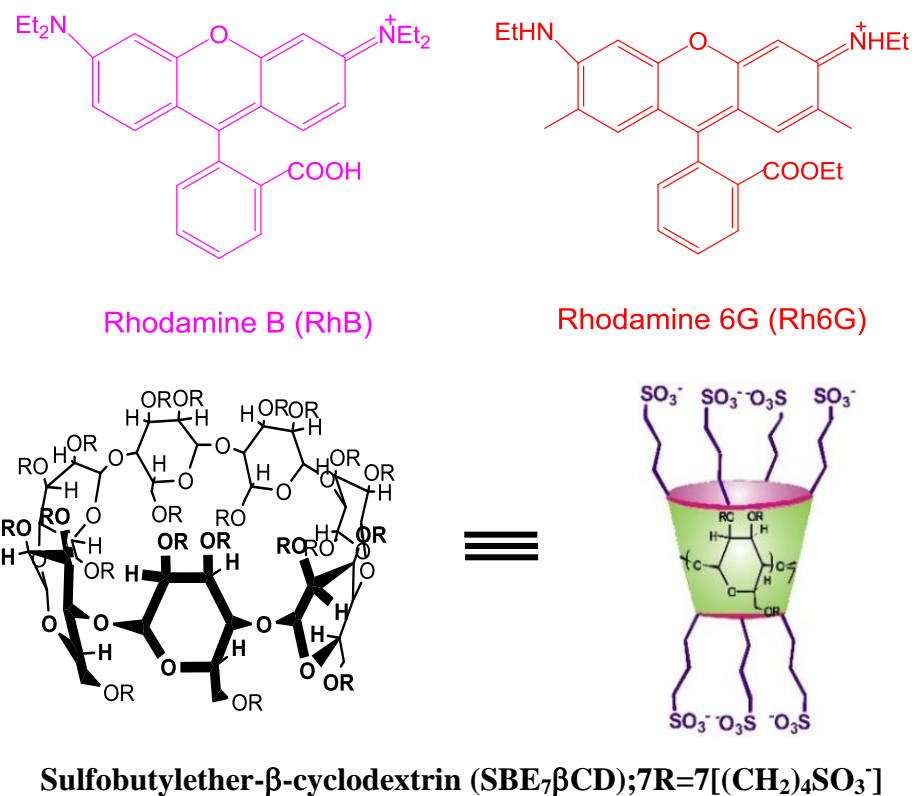


Figure 5.1.1: Chemical structures of Rhodamine B, Rhodamine 6G and Sulfobutylether-β-cyclodextrin (SBE₇βCD)

5.1.2 Materials and Methods

Rhodamine B and Rhodamine 6G laser dyes were obtained from Lambda Physik and used as received. SBE₇βCD were obtained from Advent ChemBioPvt. Ltd., India. Spectroscopic grade ethanol was procured from s.d. Fine-Chem Ltd., India. Nanopure water (conductivity of 0.06 μS cm⁻¹) obtained from Millipore Gradient A10 system, was used to prepare the dye solutions. The methods absorption, fluorescence, (steady state and time resolved) measurements, Broad-band Dye Laser Experiments and Narrow-band Dye Laser Experiments were used in this study have already been described in Chapter 2.

5.1.3. Results and Discussion

5.1.3.1 Absorption and Fluorescence Properties of Rhodamine dyes with SBE₇βCD

RhB and Rh6G display absorption band from 450 nm to 620 nm region with maxima at 553 nm and 525 nm, respectively. Upon increasing addition of SBE₇βCD to the dye solutions, the peak maxima of the dye displayed ~11 nm bathochromic shift for RhB and ~7 nm for Rh6G, along with hypochromic spectral changes with an apparent isosbestic point at 561 nm for RhB and 531 nm for Rh6G (see in Fig. 5.1.2) and attained saturation at ~400 μM of SBE₇βCD. These distinct changes in the absorption spectra clearly indicated strong interaction between RhB/Rh6G and SBE₇βCD.

To evaluate their stoichiometric composition, Job plots were constructed at a particular wavelength where the maximum changes in the absorbance were observed in the absorption spectra (i.e., 570 nm for RhB and 540 nm for Rh6G). The results are presented in Fig 5.1.3. In both the cases the maxima appear at ~0.5 mole fraction of the dye which points to a 1:1 stoichiometry of the RhB/Rh6G:SBE₇βCD complexes.

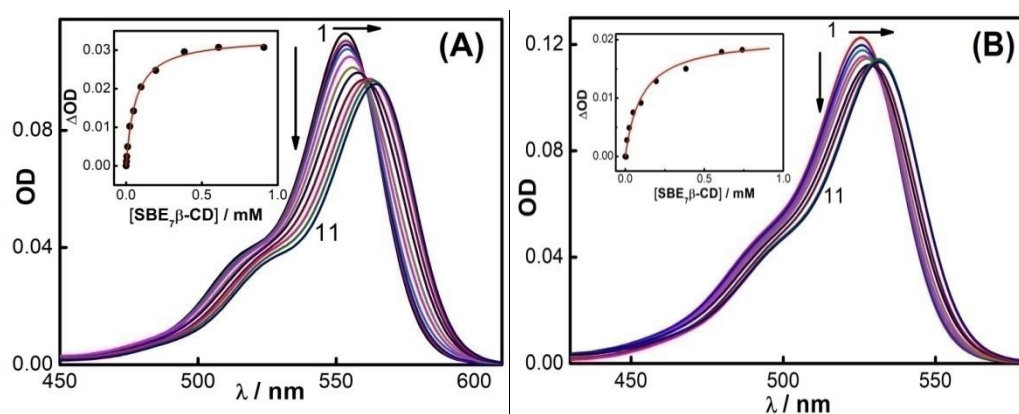


Figure 5.1.2: Absorption spectra of (A) RhB (~1.4 μM) and (B) Rh6G (~1.5 μM) at different concentrations of SBE₇β-CD. (A) [SBE₇βCD] / μM: (1) 0.0, (2) 2.5, (3) 5.0, (4) 10.0, (5) 25.0, (6) 49.7, (7) 99.0, (8) 196.0, (9) 384.0, (10) 610.0 and (11) 909. (B) [SBE₇βCD] / μM: (1) 0.0, (2) 5.0, (3) 10.0, (4) 25.0, (5) 49.7, (6) 99.0, (7) 196.0, (8) 384.0, (9) 610.0, (10) 740.7 and (11) 909. Insets show the binding isotherms. λ_{mon} = 567 nm for RhB and 525 nm for Rh6G.

The binding isotherms were constructed by plotting the optical density versus SBE₇β-CD concentration (insets of Fig. 5.1.2) and is fitted with a non-linear quadratic equation for 1:1 complex model (see in Chapter 2, 2.14.1).^{115, 229-231} The binding constant (K) value is estimated as $(1.6 \pm 0.1) \times 10^4 \text{ M}^{-1}$ for SBE₇β-CD:RhB complex and $(9.5 \pm 1.3) \times 10^3 \text{ M}^{-1}$ for SBE₇β-CD:Rh6G complex. The moderate binding constant values indicate the involvement of both ion-dipole and hydrophobic interactions between SBE₇βCD and RhB/Rh6G.

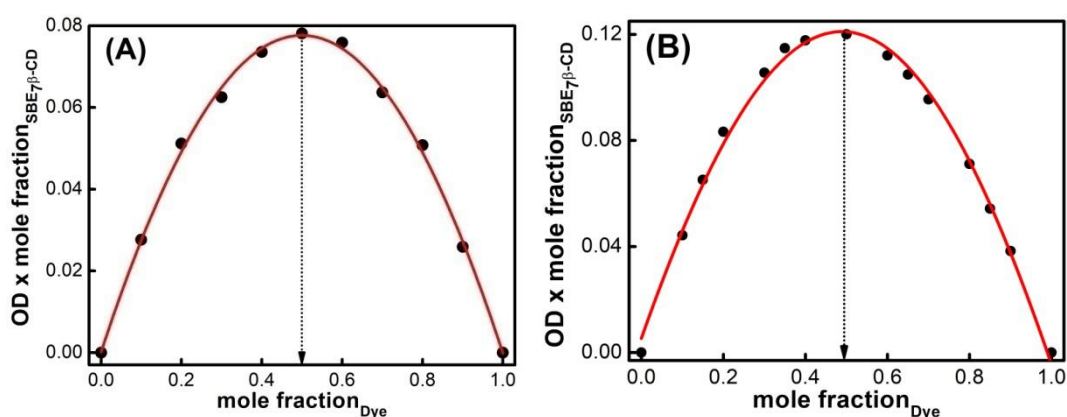


Figure 5.1.3: Job plots for the SBE₇βCD:RhB (A) and SBE₇βCD:Rh6G (B) complexes. Total concentration of the two components was 10 μM. $\lambda_{mon} = 570 \text{ nm}$ (A) and $\lambda_{mon} = 540 \text{ nm}$ (B).

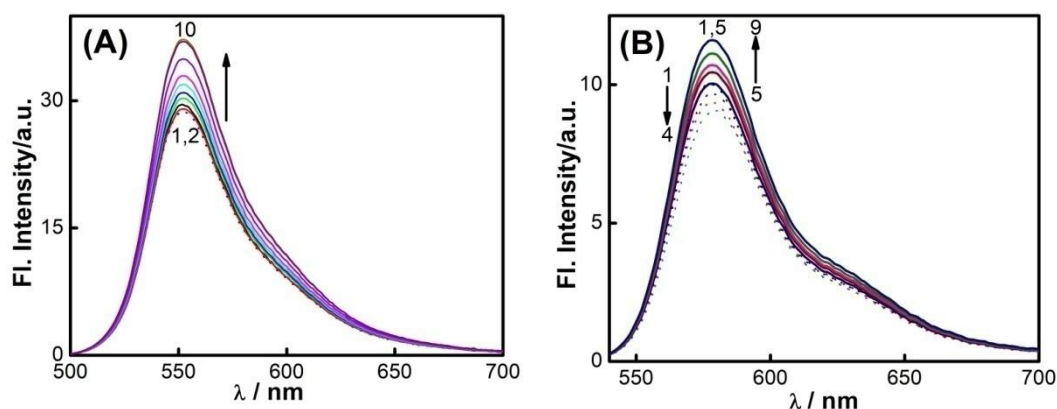
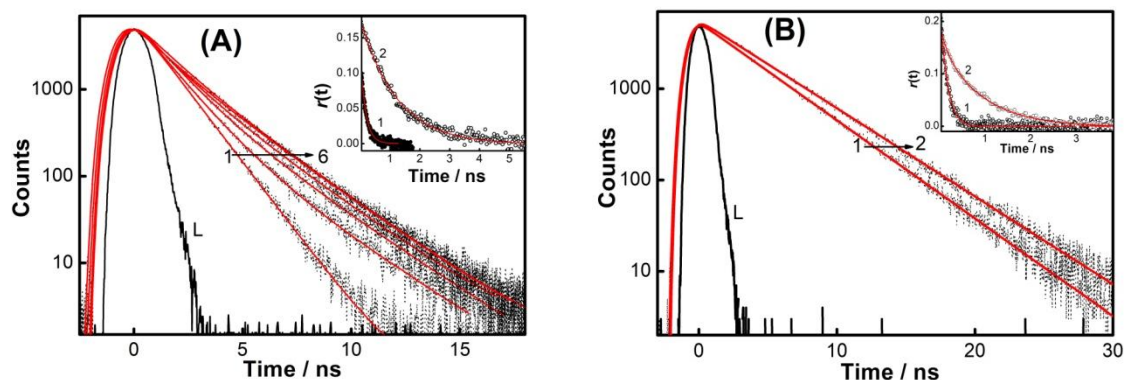


Figure 5.1.4: Fluorescence spectra of (A) RhB ($\sim 1.4 \text{ } \mu\text{M}$) and (B) Rh6G ($\sim 1.5 \text{ } \mu\text{M}$) at different concentrations of SBE₇β-CD. (A) [SBE₇βCD] / μM: (1) 0.0, (2) 5.0, (3) 10.0, (4) 25.0, (5) 49.7, (6) 99.0, (7) 196.0, (8) 384.0, (9) 610.0 and (10) 909. (B) [SBE₇βCD] / μM: (1) 0.0, (2) 2.5, (3) 5.0, (4) 10.0, (5) 99.0, (6) 196.0, (7) 384, (8) 610.0 and (9) 909. $\lambda_{ex} = 520 \text{ nm}$ for RhB and 490 nm for Rh6G.

On the other hand, fluorescence measurements show that initially there is decrease in the fluorescence intensity upto the addition of $\sim 10 \mu\text{M}$ of $\text{SBE}_7\beta\text{CD}$ and beyond this fluorescence intensity increases with increase in the $\text{SBE}_7\beta\text{CD}$ concentration and attains saturation at $\sim 385 \mu\text{M}$ of $\text{SBE}_7\beta\text{CD}$ for RhB and $\sim 600 \mu\text{M}$ of $\text{SBE}_7\beta\text{CD}$ for Rh6G (see in Fig. 5.1.4). The initial decrease in the fluorescence intensity could be attributed to the formation of rhodamine aggregates facilitated by the sulfonated groups at the portals, whereas at higher concentration the fluorescence intensity increases due to deaggregation of dye through 1:1 complex formation. Though the changes in the fluorescence intensity due to the deaggregating effect of $\text{SBE}_7\beta\text{CD}$ is expected to be only nominal in these concentration ranges, the signatures of the host-guest interactions were clearly visible in the fluorescence lifetime and anisotropy measurements. The fluorescence lifetime of free RhB in water is $\sim 1.3 \text{ ns}$.²²⁰ It is seen that upon gradual addition of $\text{SBE}_7\beta\text{CD}$ to RhB solution, the decay trace of RhB became biexponential (see in Fig. 5.1.5A) and the lifetime values are estimated as 1.3 ns and 2.6 ns . The contribution of 1.3 ns component corresponding to the free dye decreases from 100% to 37% and the contribution of 2.6 ns component corresponding to the complexed dye increases to 63% at the saturation host concentration (0.9 mM). Whereas the fluorescence lifetime of Rh6G in the presence of 0.9 mM of $\text{SBE}_7\beta\text{CD}$ also increases from 4.0 ns to 4.5 ns (see in Fig. 5.1.5B). Similarly, the rotational correlation time (τ_r) obtained from the fluorescence anisotropy decay traces (insets of Fig. 5.1.5), which is correlated with the hydrodynamic volume/effective size of the dye,²³² also increases significantly from 0.15 ns to 1.2 ns for RhB and 0.14 ns to 0.99 ns for Rh6G in the presence of

SBE₇βCD. These results clearly support the formation of complex formation between the rhodamine dye and SBE₇βCD.



Figures 5.1.5: (A) Fluorescence decay traces of RhB ($\sim 1.4 \mu\text{M}$) at different concentrations of SBE₇βCD. (A) [SBE₇βCD] / μM : (1) 0, (2) 64, (3) 160, (4) 302, (5) 484 and (6) 909. (B) Fluorescence decay traces of Rh6G ($\sim 1.4 \mu\text{M}$) in the absence and presence of 909 μM of SBE₇βCD. $\lambda_{\text{ex}} = 490 \text{ nm}$, $\lambda_{\text{mon}} = 580 \text{ nm}$ and L represents the lamp profile. Insets show the anisotropy decay traces of the corresponding dyes in the absence (1) and presence of 0.9 mM of SBE₇βCD (2). $\lambda_{\text{ex}} = 445 \text{ nm}$ and $\lambda_{\text{mon}} = 580 \text{ nm}$.

5.1.3.2 Isothermal Titration Calorimetric (ITC) Study

Isothermal titration calorimetric measurements have also been carried out to determine the binding constants and the thermodynamic parameters of the complex formation. From the ITC data (Fig. 5.1.6) a sequential 1:2 binding model gave a satisfactory fit rather than one-set-of-sites model, in contrast to 1:1 model fitting for the absorption titration data (Fig. 5.1.1). This could be due to the aggregation behaviour of the rhodamine dyes at higher concentration used in the ITC measurements. During addition of SBE₇βCD, first there is a change in the aggregation to deaggregation of dye (K_1) followed by complex formation (K_2).

Hence, two binding constant values are obtained for each complex system ($K_1 = 155 \text{ M}^{-1}$ and $K_2 = 1.7 \times 10^4 \text{ M}^{-1}$ for SBE₇βCD:RhB system and $K_1 = 206 \text{ M}^{-1}$ and $K_2 = 3.1 \times 10^4 \text{ M}^{-1}$ for SBE₇βCD:Rh6G system). The second binding constant value for

each complex matches well with the binding constant values obtained from the absorption titration data and corresponds to the association constant for the rhodamines with the SBE₇βCD host. The enthalpy, entropy and free energy changes for these processes for both the systems were evaluated (given below) and are found to be energetically favourable.

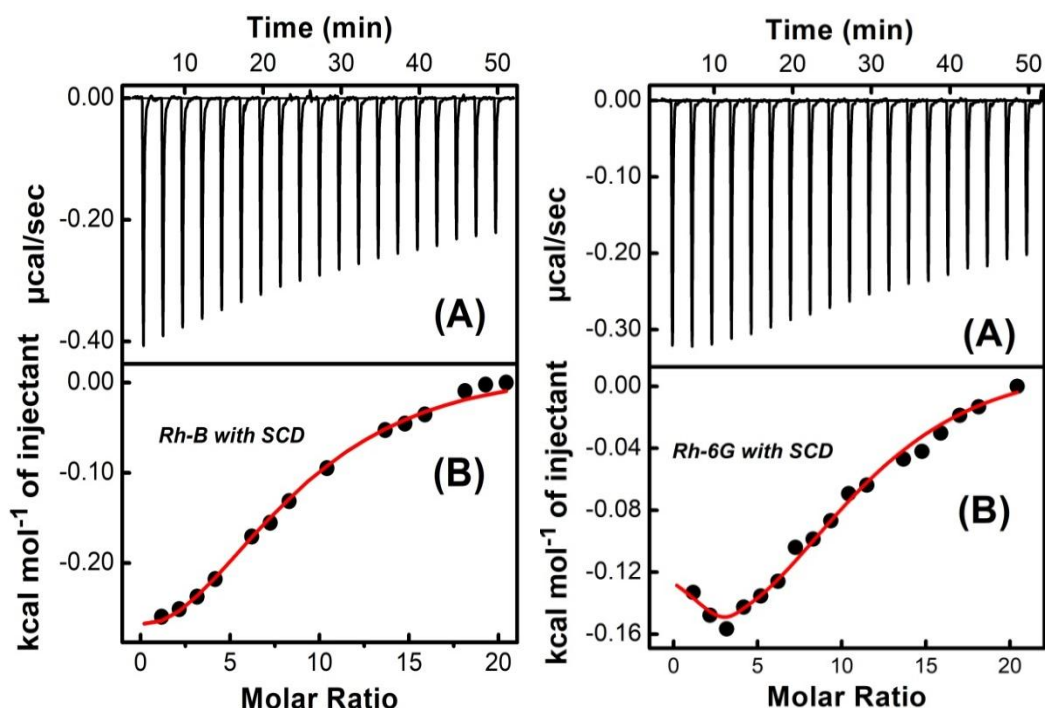


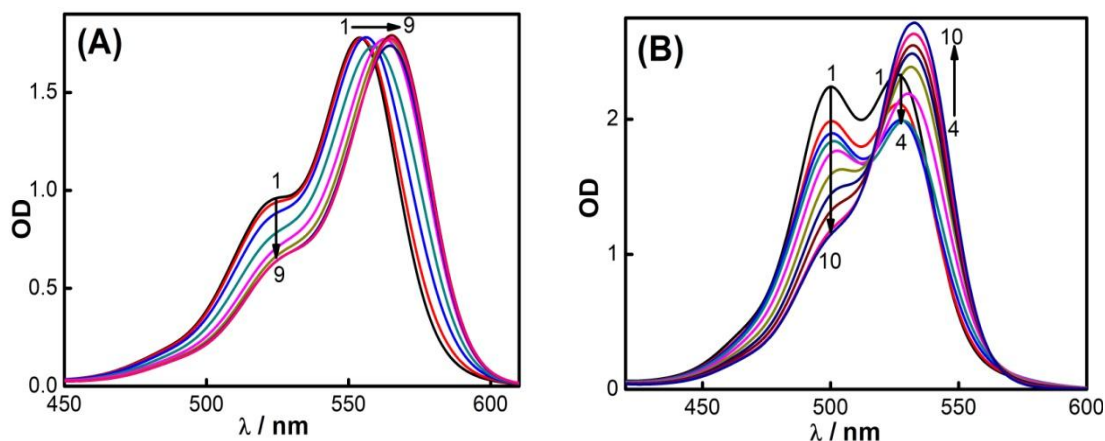
Figure 5.1.6: (A) Raw data for the titration of 50 μM Rhodamine B and Rhodamine 6G with 5 mM SBE₇βCD at pH 7.4 in tris-buffer (10 mM) and 25 °C, showing the calorimetric response as successive injections of the host are added to the sample cell. (B) Integrated heat profile of the calorimetric titration shown in panel A. The solid line represents the best nonlinear least-squares fit to a sequential binding- site model.

(1) $\Delta H_1 = -34.8 \text{ kcal mol}^{-1}$, $-T\Delta S_1 = 31.9 \text{ kcal mol}^{-1}$, $\Delta G_1 = -2.9 \text{ kcal mol}^{-1}$ and $\Delta H_2 = 33.6 \text{ kcal mol}^{-1}$, $-T\Delta S_2 = -39.3 \text{ kcal mol}^{-1}$, $\Delta G_2 = -5.7 \text{ kcal mol}^{-1}$ for SBE₇βCD:RhB

(2) $\Delta H_1 = -11.1 \text{ kcal mol}^{-1}$, $-T\Delta S_1 = 7.9 \text{ kcal mol}^{-1}$, $\Delta G_1 = -3.2 \text{ kcal mol}^{-1}$ and $\Delta H_2 = 9.5 \text{ kcal mol}^{-1}$, $-T\Delta S_2 = -15.6 \text{ kcal mol}^{-1}$, $\Delta G_2 = -6.1 \text{ kcal mol}^{-1}$ for SBE₇βCD:Rh6G complexes.

5.1.3.3 Deaggregation of Rhodamine Dyes with SBE₇βCD

To study the effect of SBE₇βCD on the aggregation behaviour of both these dyes we have used higher concentration (OD_{553nm}~1.8 for RhB (220 μM) and OD_{525nm} ~2.3 for Rh6G (285 μM) in a 1 mm path length cuvette) of RhB and Rh6G where most of the dyes is in the aggregated form²²⁵ and recorded their absorption spectra with the addition of SBE₇βCD. It is seen that the shoulder band at around 524 nm for RhB and 499 nm for Rh6G corresponding to the respective aggregated forms²⁷ reduces largely in the presence of SBE₇βCD and the main band at 532 nm, corresponding to the monomeric form of Rh6G, showed bathochromic shift along with increased absorbance (see in Fig. 5.1.7). In case of RhB, the absorption band displayed bathochromic shift with slight change in absorbance at the peak position and the ratio between main band to shoulder band increases. Beside the absorbance changes, the dye solutions in the presence of SBE₇βCD becomes highly fluorescent (respective insets of Fig. 5.1.8) and the enhanced brightness of the solution can also be visualized with the naked eye (inset of Fig. 5.1.8). This result strongly indicates that the encapsulation of the dyes by SBE₇βCD leads to the deaggregation of the dyes in aqueous medium. For the fluorescence measurements, we adopted front-face geometry for recording the fluorescence spectra and lifetime decay traces of these dye solutions in the absence and presence of SBE₇βCD. Qualitatively, the fluorescence intensity (Fig. 5.1.8) and lifetime of RhB/Rh6G increased (see in Fig. 5.1.9) substantially in the presence of SBE₇βCD.



Figures 5.1.7: Absorption spectra (in 1 mm cuvette) of (A) RhB (~220 μM) and (B) Rh6G (~285 μM) at different concentrations of SBE₇βCD. (A) [SBE₇βCD] / mM: (1) 0.0, (2) 0.03, (3) 0.1, (4) 0.2, (5) 0.38, (6) 0.65, (7) 0.91, (8) 1.75 and (9) 3.85. (B) [SBE₇βCD] / mM: (1) 0.0, (2) 0.03, (3) 0.08, (4) 0.15, (5) 0.29, (6) 0.48, (7) 0.65, (8) 0.91, (9) 1.75 and (10) 3.00.

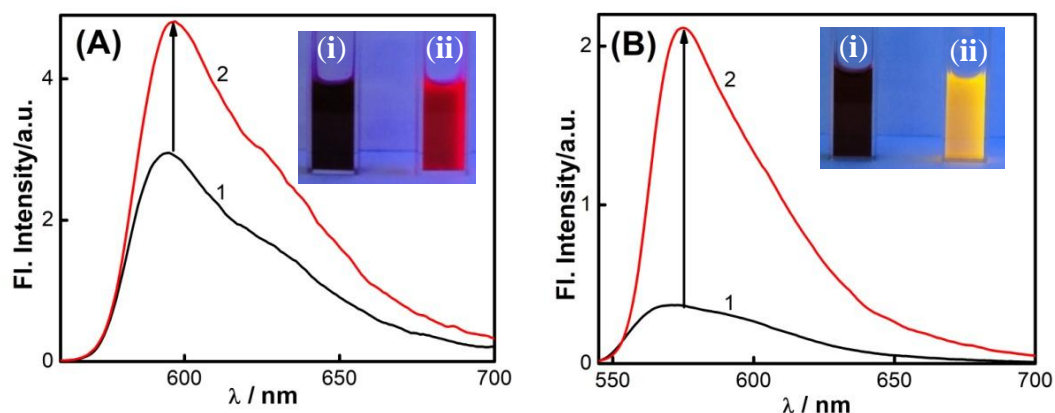


Figure 5.1.8: Fluorescence spectra (in 1 mm cuvette, front face geometry) of (A) RhB (~220 μM) and (B) Rh6G (~285 μM) in the absence (1) and presence (2) of SBE₇βCD (3.85 mM for RhB and 3 mM for Rh6G) in water. Insets in (A) & (B) show the photographs of the respective dyes in water in the absence (i) and presence (ii) SBE₇βCD under UV-light.

The fluorescence decay trace of RhB showed almost single exponential fitting with lifetime of ~3.0 ns and the fluorescence lifetime of Rh6G increased to 6.3 ns (Fig. 5.1.9). These lifetime values of the dyes in the presence of SBE₇βCD are almost comparable to the values obtained for these dyes in EtOH.

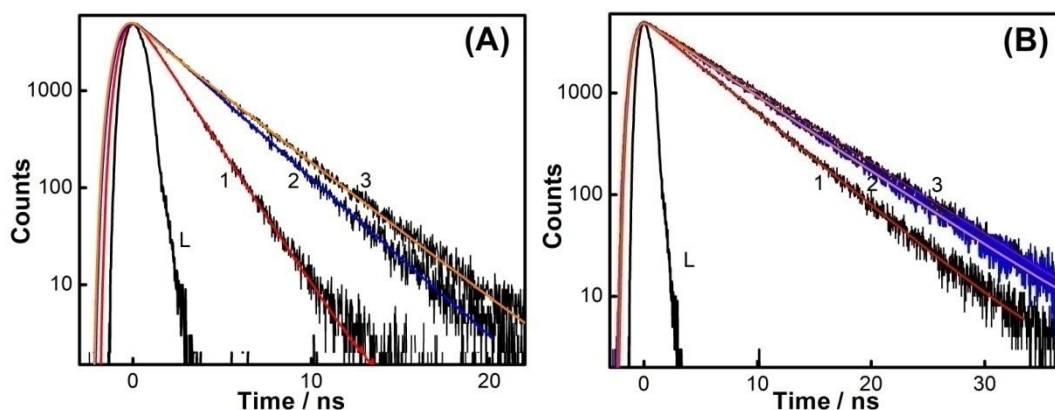


Figure 5.1.9: Fluorescence decay traces (in 1 mm cuvette, front face geometry) of (A) RhB ($\sim 220 \mu\text{M}$) and (B) Rh6G ($\sim 285 \mu\text{M}$) in the absence (1) and presence (3) of SBE₇βCD (3.85 mM for RhB and 3 mM for Rh6G) in water and in EtOH (2). L represents the lamp profile. $\lambda_{\text{ex}} = 490 \text{ nm}$.

5.1.3.4. Broad-band and Narrow-band Lasing Behaviour of Rhodamine Dyes in presence of SBE₇βCD

As discussed before, the aggregation of rhodamine dyes in water leads to the formation of weakly fluorescent aggregates which restricts the operation of aqueous dye laser systems. The lasing behaviour of RhB and Rh6G in aqueous solution in the presence of increasing concentration of SBE₇βCD was tested in a broad-band dye laser setup using 532 nm excitation from a pulsed Q-switched Nd-YAG laser (10 Hz, $\sim 5 \text{ mJ}$ pulse energy). The optical density of the dye solutions was kept ~ 1.6 at the excitation wavelength in 1 mm path length cuvettes. The respective dyes in ethanol solution were used as the references. Fig. 5.1.10 shows the typical changes in lasing efficiency of Rh6G and RhB dyes with increasing concentration of SBE₇βCD. It is seen that the lasing efficiency increases and attains saturation with 1.5-2.0 mM of SBE₇βCD. Lasing efficiency achieved for these systems is about 61% and is attributed to the deaggregating effect by SBE₇βCD by its complex formation with the RhB/Rh6G dyes. Note that the lasing efficiency recorded here is $\sim 25\%$ higher for the

SBE₇βCD:RhB system and ~10% higher for SBE₇βCD:Rh6G system than the respective dyes in optically matched ethanol solutions (dashed lines in Fig. 5.1.10).

The sharp increase in lasing efficiency in SBE₇βCD:RhB system as compared to SBE₇βCD:Rh6G is exactly reflected in the difference in the binding constant values of these two systems, where the host-guest complexation goes concomitantly with deaggregation. In short, these measurements establish the translation of low-efficiency aqueous dye laser into high-efficiency dye laser system in the presence of SBE₇βCD macrocyclic host.

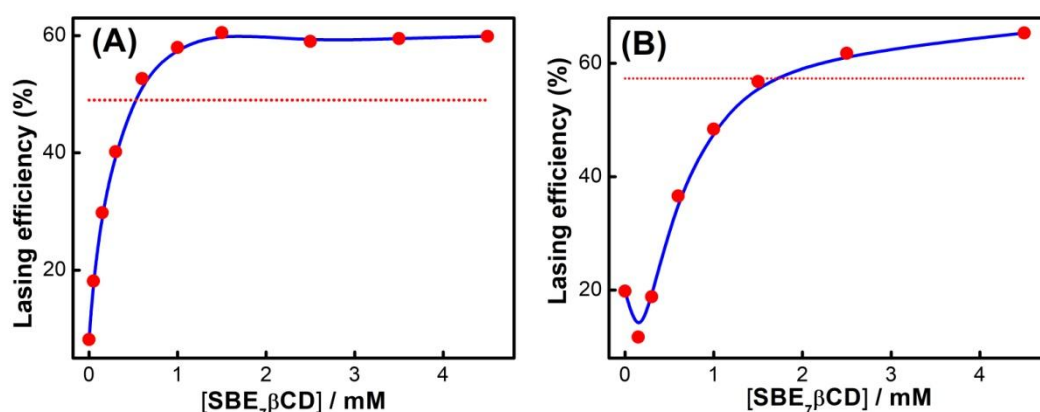


Figure 5.1.10: Lasing efficiency of plot of (A) RhB (~300 μM) and (B) Rh6G (~300 μM) in aqueous solution at different concentrations of SBE₇βCD using a broad-band dye laser setup. The dotted line represents the lasing efficiency of (A) RhB and (B) Rh6G in optically matched ethanol solutions.

Following the demonstration of efficient lasing features for the SBE₇βCD complexed RhB/Rh6G dyes in water, the tuning curves for these lasing systems have been generated using a narrow-band dye laser setup (see in Fig. 5.1.11; for details see in chapter 2, 2.14.7). Figure 5.1.12 presents the tuning curves generated from the lasing efficiencies for RhB and Rh6G dyes in water in the presence of about 4 mM SBE₇βCD. The graphs also display the control tuning curves generated for the respective dyes in ethanol solutions. Evidently, while the peak lasing efficiency

(~20%) for the aqueous SBE₇βCD:RhB system is found to be comparable with the ethanolic RhB solution, the aqueous SBE₇βCD:Rh6G solution displayed higher peak lasing efficiency (~24%) than that of its ethanolic Rh6G solution (~20%).²²⁰ It is advantageous that both the SBE₇βCD complexed rhodamines in aqueous solutions show distinctly different tuning ranges compared to their ethanolic solutions (see in Fig. 5.1.12 A and B) and support much broader tuning ranges, which in turn can be modulated judiciously by varying the solvent medium for wavelength specific applications.

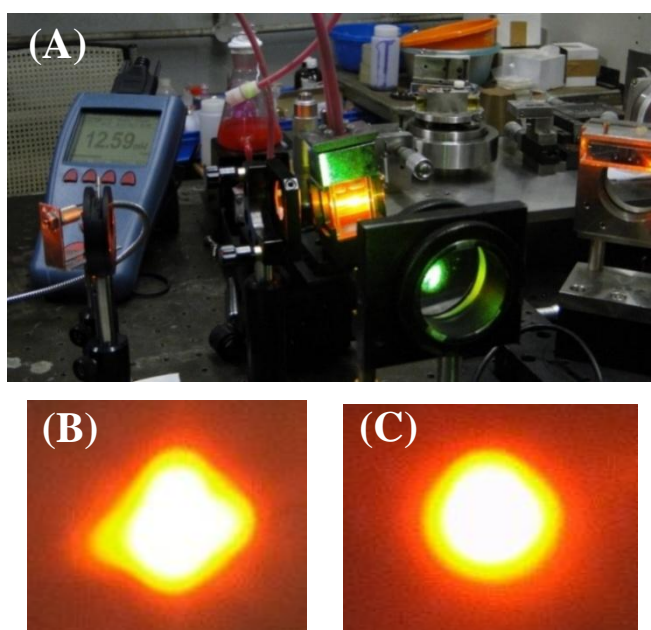


Figure 5.1.11: (A) Narrow band dye laser setup. The laser beam profiles for RhB in water with 4mM SBE₇βCD (B) and in ethanol (C), obtained at identical gain depth (similar OD at pump wavelength i.e. 532 nm) using a digital camera.

We have further measured the laser output as a function of pump power to elucidate various lasing parameters. Fig 5.1.12 (C&D) shows the measurements carried out at their respective peak wavelengths (λ_L) of the tuning curves and the slope efficiencies (η_s), pump threshold energies (E_T) and other parameters estimated from

Fig 5.1.12 are tabulated in Table 5.1.1. It is observed that the slope efficiencies (η_s) for the ethanolic solutions of RhB/Rh6 G are higher than their laser peak efficiencies (η), whereas for their aqueous SBE₇ β CD complex solution, while RhB maintained the same relation, the Rh6G:SBE₇ β CD complex is played slightly higher laser peak efficiency than its slope efficiency.

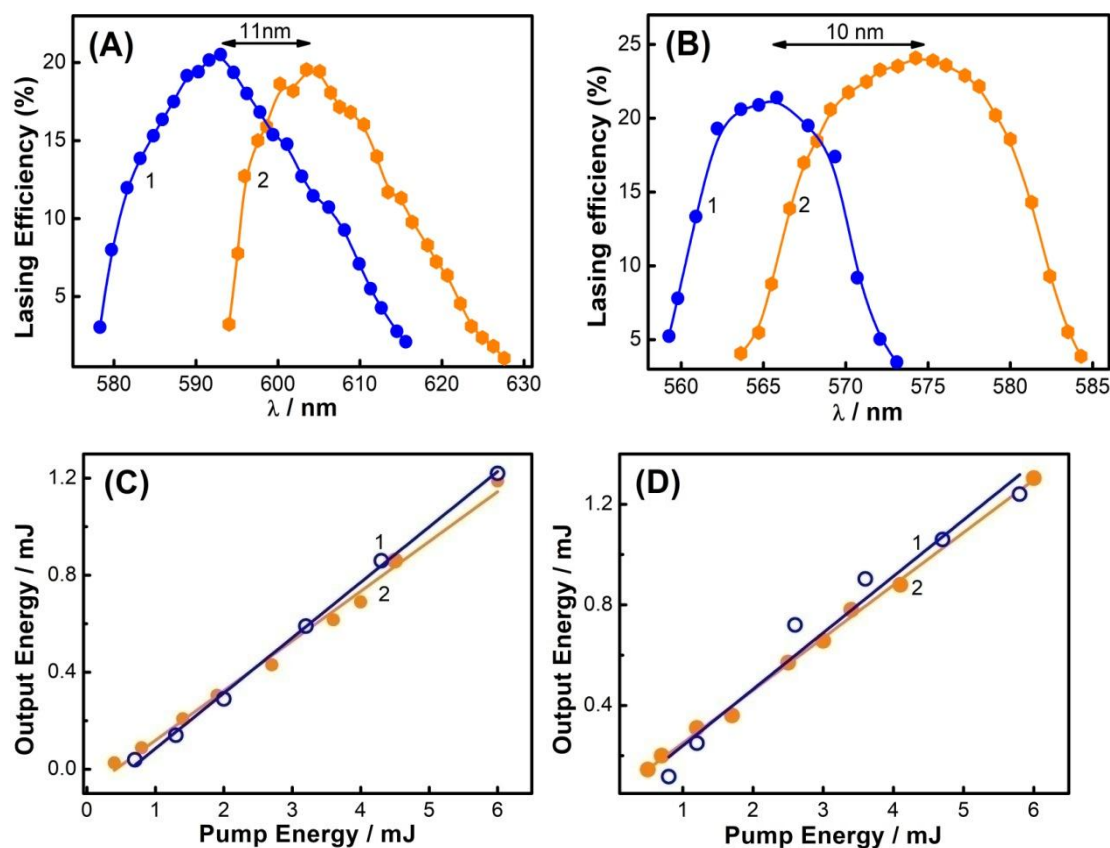


Figure 5.1.12: Tuning curves of RhB (A) and Rh6G (B) in EtOH (1) and in the presence of 4 mM SBE₇ β CD (2) at a pump energy of ~5 mJ. Variation of output energy of RhB (C) and Rh6G (D) in EtOH (1) and in the presence of ~4 mM SBE₇ β CD (2).

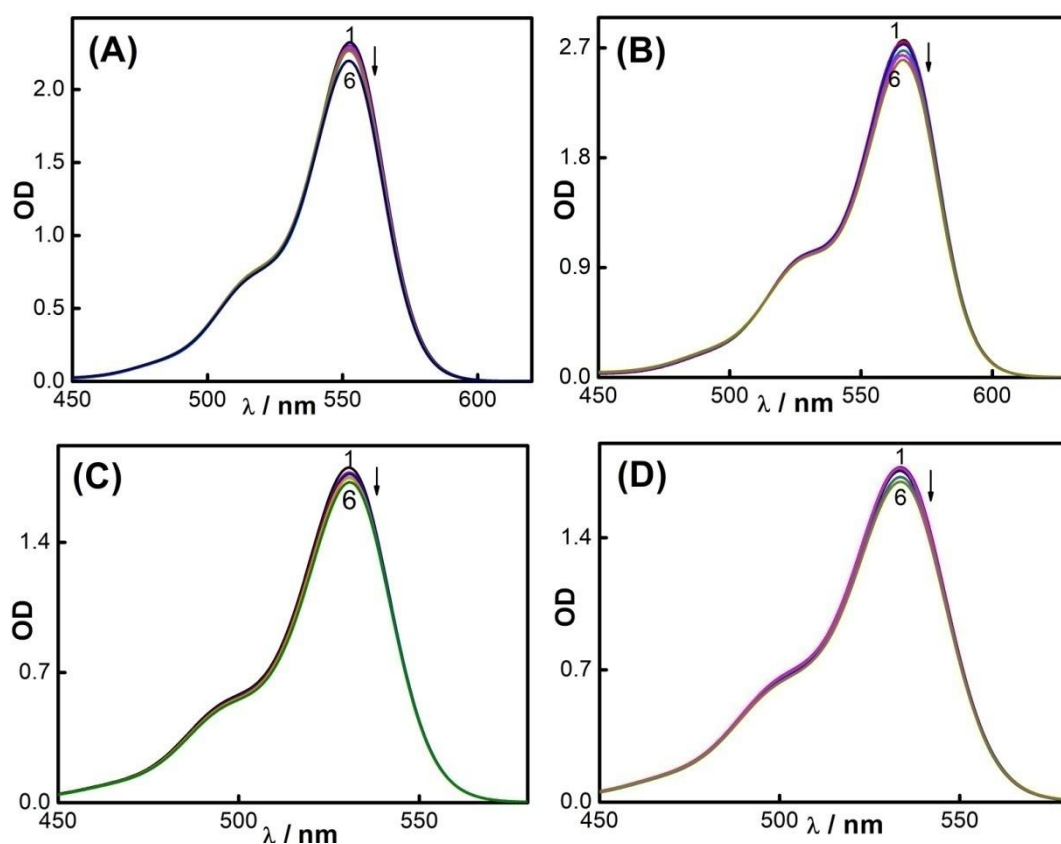
In addition, the laser peak efficiency for Rh6G with SBE₇ β CD in water is considerably higher than that of Rh6G in EtOH (Table 5.1.1). Beside these promising enhanced lasing behaviour of rhodamine dyes with SBE₇ β CD in aqueous medium, the

beam profile of RhB and Rh6G dyes has been seen quite improved to a better spherical profile in the presence of SBE₇βCD (see for RhB in Fig.5.1.11 (B & C)).

Table 5.1: Lasing parameters of RhB and Rh6G dyes in EtOH and SBE₇βCD/water systems using 532 nm laser irradiation (10 Hz, 5 mJ).

System	Tuning range (nm)	λ_L (nm)	η (%)	η_s (%)	E_T (mJ)
RhB-EtOH	578-616	593	20.6	22.8	---
RhB-SBE ₇ βCD/Water	594-628	604	19.6	20.5	---
Rh6G/Ethanol	559-573	565	20.2	22.4	0.15
Rh6G-SBE ₇ βCD/Water	564-584	575	24.0	21.0	0.41

5.1.3.5 Photostability of Rhodamine Dyes with SBE₇βCD



Figures 5.1.13. Absorption spectra of RhB in EtOH (A) and in the presence of SBE₇β-CD in water (B) and Rh6G in EtOH (C) and in the presence of SBE₇β-CD in water (D) at different times of laser irradiation. $\lambda_{irrdn} = 532$ nm. Time of irrdn/min: 1) 0, 2) 15, 3) 45, 4) 105, 5) 180 and 240.

Proposing the supramolecular strategy for the rhodamine dyes to attain lasing in water, we have also carried out the photostability measurements of RhB and Rh6G dyes ($\sim 300 \mu\text{M}$) in the presence of SBE₇ β CD in aqueous medium as well as in ethanol solutions using 532 nm laser irradiation from a Nd:YAG laser (10 Hz, 5 mJ, 4 hrs). As presented in Fig. 5.1.13, the optical density at the peak position in all these systems with laser irradiation indicated similar nominal decrease and document comparable photostability of dye in ethanol as well as in the presence of SBE₇ β CD in aqueous medium.

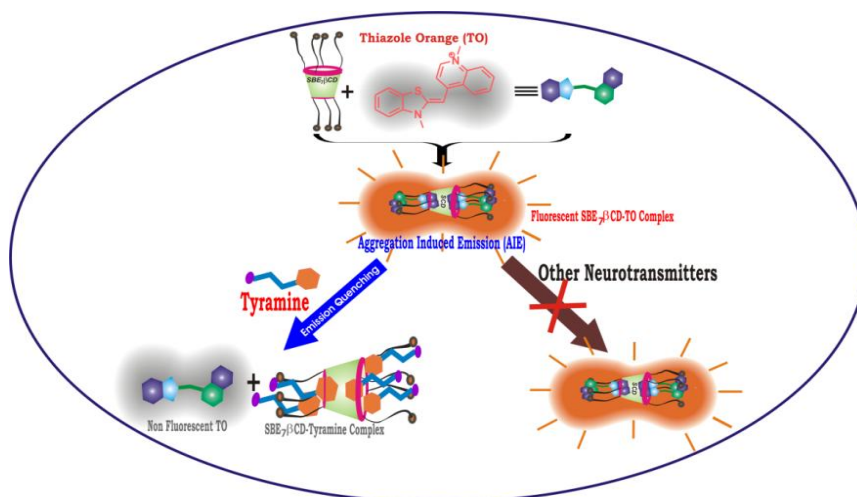
5.1.4. Conclusions

In summary, this article presents a methodology for achieving ultra-bright Rhodamines in water and its applicability has been proven in a practical laser system. In the first part of this study we evaluated the host-guest interaction of two prominent laser dyes, namely, RhB and Rh6G with sulfobutylether- β -cyclodextrin (SBE₇ β CD) in aqueous medium and demonstrate its complex formation having association constant $K \sim 10^4 \text{ M}^{-1}$, by different photophysical and thermodynamic measurements. The host-guest complex formation, in turn, resulted in the deaggregation and stabilization of these dyes in water having emission features at par with that in organic solvents. Taking advantage of these promising emission features, we introduced the aqueous rhodamine solutions containing SBE₇ β CD as the active medium in a broad-band as well as narrow-band dye laser setup and established its efficient operation in comparison with their respective ethanol solutions. The aqueous rhodamine dye laser system demonstrated here rendered superior beam profile as compared to that in ethanol solution. In addition to the impressively advantageous green features of the water medium, the higher solubility and lower cost of the SBE₇ β CD host (compared

to the CB7 macrocycle) highlight the acceptability of this cost-effective supramolecular aqueous dye laser strategy. This strategy is being further worked out in other dye laser systems, especially that works in the IR regions for supporting biological and medical applications.

Part-2

Supramolecularly Enhanced Emission of Thiazole Orange with Sulfobutylether- β - cyclodextrin: On/Off fluorescence Sensor for Tyramine neurotransmitter



ChemPhysChem., 2019
(DOI: 10.1002/cphc.201900656).

5.2.1 Introduction

The term aggregation induced fluorescence generally describes the phenomenon of molecular probe with low fluorescence quantum yield of the monomeric form in dilute solution “lighting up” with enhanced fluorescence emission upon aggregation.^{233, 234} Luminogens exhibiting such behaviour, first reported by Tang’s group in 2001,²³⁵ are finding enormous research interests owing to their potential applications in optoelectronic devices,²³⁶⁻²³⁸ chemo/ biosensing,²³⁹ bioimaging,²⁴⁰ stimulus responsive materials and functionalized self-assembly systems.^{233, 241} Upon absorption of UV-Vis light, the excited molecule in the condensed state transfers its excitational energy to the surrounding through different radiative and nonradiative processes. The involvement of more number of nonradiative processes including intramolecular vibrational and rotational motions makes the molecule weakly fluorescent or nonfluorescent. Restricting these nonradiative processes through aggregation is one of the key features for the aggregation induced emission effect.²³³ Among several factors such as concentration, temperature, solvents, pH of the solution responsible for the aggregation of the molecules,²³³ noncovalently linked host-guest interactions are one of the facile supramolecular approach to bring the guest monomers together to form dimers/ aggregates, particularly in dilute solutions. Furthermore, tuning the aggregated moieties/assemblies by triggering with external stimuli has been effectively utilized for various applications, especially as fluorescence on-off sensor etc.²³⁴

Thiazole orange (TO), one of the asymmetric cyanine dyes, exists as monomer, dimer or aggregates depending upon its concentration in aqueous

solution and each form displays characteristic absorption and fluorescence features.²⁴² TO is very weakly fluorescent ($\Phi_f \sim 0.0002$) due to the E-Z photoisomerization combined with the intramolecular torsional motion between the benzothiazole and the quinolone heterocycles.^{243, 244} It is extensively used as fluorogenic dye as the fluorescence intensity increases significantly with increasing viscosity of the medium or in the presence of biomolecules such as DNAs/ RNAs, which occurs mainly due to the restriction in the intramolecular torsional motion caused by the local (microscopic) rigidity or aggregation.^{245, 246} In this direction, several attempts to achieve modulation/control of such tunable emission features has been made in the studies carried out in organized assemblies like micelles, reverse micelles, or cavitand macrocycles such as calixarenes, cucurbit[7]uril and cucurbit[8]urils.^{242, 247-249}

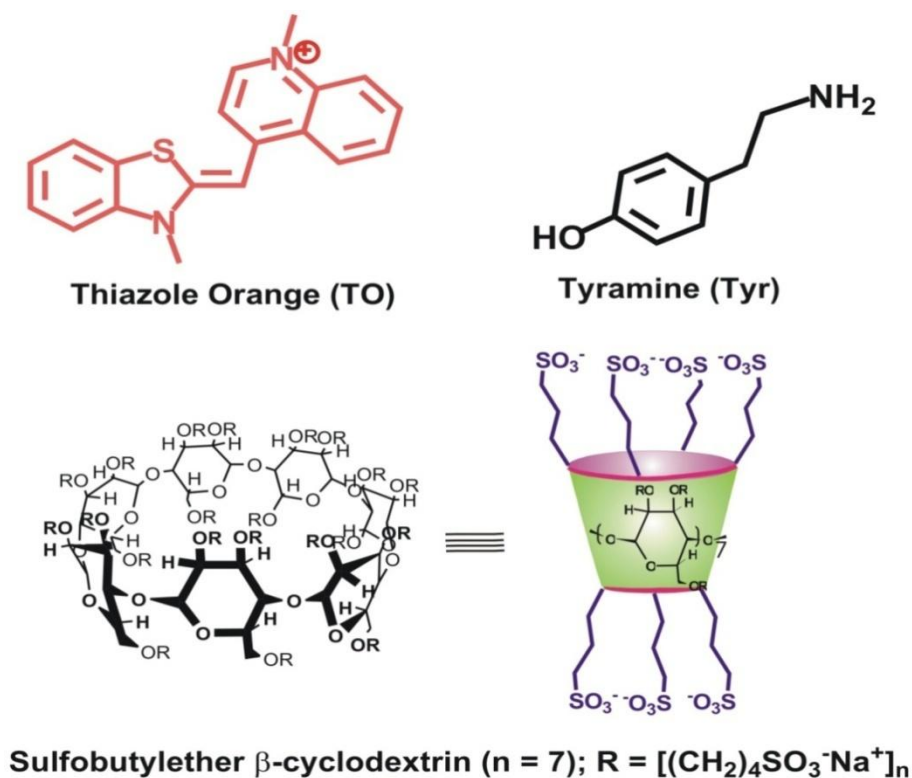


Figure 5.2.1: Chemical structures of thiazole orange (TO) Tyramine (Tyr) and the macrocyclic host, sulfobutyl ether β -cyclodextrin sodium salt.

On the other hand, host-guest interaction of sulfobutylether derivative of β -cyclodextrin macrocycle (SBE₇ β CD; or Captisol) with organic guests (fluorescent dyes/drugs) has received immense research interest in recent years due to their several applications such as excipients in drug formulation,²²⁸ for making stimuli-responsive on-off fluorescence sensor,²²⁹ aqueous dye laser systems,³² supramolecular photosensitizer and as amyloid fibril inhibitor.²⁷ Having 7 extended negatively charged sulfobutyl ether arms available at both the portals, SBE₇ β CD is found to be very effective in modulating the molecular properties of cationic dyes/drugs through efficient host-guest interaction. In this work, we report a remarkable display of enhanced emission from the SBE₇ β CD-assisted self-assembly of TO molecules positioned at the SBE₇ β CD portals. Advantageously, the quenching response of the emission was found to be highly efficient and selective towards Tyramine, a biogenic amine/neurotransmitter, among several other aliphatic/ aromatic-based neurotransmitters attempted, proclaiming the emissive SBE₇ β CD-TO assembly established here as a Tyramine sensor with limit of detection ~575 nM (79 ppb).²⁹ Since the biogenic amines/neurotransmitters such as amino acids (e.g., glutamate), monoamines (e.g., dopamine, tyramine etc), peptides and others which are associated with many physiological processes in the body, the fluorescence-based selective detection of them in trace amount has received significant importance in recent years for their facile detection/diagnosis for treatment and medication.²⁵⁰⁻²⁵³

5.2.2 Materials and Methods

Thiazole orange and sulfobutylether β -cyclodextrin (SBE₇ β CD) sodium salt with a degree of substitution of 6.4 were procured from Sigma-Aldrich and

Advent ChemBio Pvt. Ltd., India, respectively and used as received. Nanopure water (Millipore Gradient A10 System; conductivity of $0.06 \mu\text{S cm}^{-1}$) was used to prepare the sample solutions. Neurotransmitters (tyramine, glycine, D-serine, acetylcholine, aspartate, dopamine, glutamate, melatonin, arginine), choline and guanidiniumchloride were obtained from Sigma-Aldrich/SRL and used as received without further purification. The methods absorption and fluorescence, (steady state and time resolved) measurements, were used in this study have already been described in Chapter 2.

5.2.3 Results and Discussion

5.2.3.1 Absorption Spectral Characteristics of Thiazole Orange with SBE₇βCD

Three different forms of TO (monomer, dimer and aggregates) show discrete absorption band/spectra with peak around 500, 470 nm and a weaker band at 430 nm, respectively, depending upon the concentration of dye in aqueous solution.^{249, 254} Upon gradual addition of SBE₇βCD to the dilute solution of TO (3 μM), the absorbance at ~500 nm corresponding to monomer absorption decreased and concomitantly, the shoulder band at ~470 nm, corresponding to dimer absorption, remained unchanged and became more prominent with an isosbestic point at 466 nm (see in Fig. 5.2.2, spectra 1-5). These changes were seen upto ~3 μM of SBE₇βCD and is an indication that at lower concentrations of SBE₇βCD stabilizes the TO dyes preferably in its dimeric form. Further addition of SBE₇βCD (beyond 1:1 concentration ratio), the absorbance at both 500 and 470 nm decreased upto 20 μM SBE₇βCD without any isosbestic point and beyond 20 μM of SBE₇βCD, the absorbance at 500 nm increased along with

the decrease in the shoulder band at ~ 470 nm, in all, indicating the revival of the spectral signatures of the monomeric dye (Fig.5.2.2, spectra 6-10).

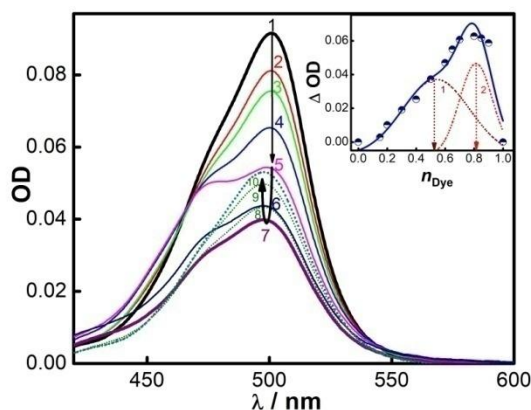


Figure 5.2.2: Absorption spectra of TO ($3 \mu\text{M}$) in aqueous solution at different concentrations of $\text{SBE}_7\beta\text{CD}$. $[\text{SBE}_7\beta\text{CD}] / \mu\text{M}$: (1) 0.0, (2) 0.25, (3) 0.5, (4) 1.5, (5) 3.0, (6) 6.0, (7) 20.0, (8) 40.0, (9) 80 and (10) 130.0. Inset shows the Job plot evaluated by the absorbance changes at 500 nm for the $\text{SBE}_7\beta\text{CD}$:TO complex. n_{Dye} represents the mole fraction of TO. The trace has been analysed for multiple distribution; 1 and 2.

To explore this intriguing multiple step complexation interactions of TO with $\text{SBE}_7\beta\text{CD}$, Job continuous variation method was adopted to determine the stoichiometry of the $\text{SBE}_7\beta\text{CD}$:TO system. The Job plot, evaluated from the absorbance changes at 500 nm with mole fraction of TO (inset of Fig. 5.2.2), showed a broad profile with an inflection at ~ 0.8 and a shoulder at ~ 0.5 mole fraction of the dye. This profile has been further analyzed for the distribution of multiple components and the deconvoluted profiles showed a distribution with a maximum at around 0.81 and another at ~ 0.52 mole fraction of TO. The inflection point at 0.81 mole fraction of TO and the appearance of dimer absorbance in the spectral features indicates that at lower concentration of $\text{SBE}_7\beta\text{CD}$, four TO dye molecules are bound to one $\text{SBE}_7\beta\text{CD}$ host (apparently, two dyes per each portal of $\text{SBE}_7\beta\text{CD}$). At the same time, the inflection point at 0.52 and the reappearance of the TO monomer band at ~ 498 nm support that

at higher concentration of SBE₇βCD, the aggregated TO dyes gets destabilized to form predominantly the 1:1 stoichiometric complex. It is quite likely that the initial crowding of cationic TO takes place at the strongly negatively charged SBE₇βCD portal sulfonate groups which move on to a 1:1 inclusion complex.

5.2.3.2 Fluorescence Spectral Characteristics of Thiazole Orange with SBE₇βCD

Corresponding to the absorption bands, the monomer, dimer and higher aggregates of TO in aqueous solution also display distinct fluorescence spectra with peak positions at around 525, 600 and 650 nm, respectively.^{249, 254} In aqueous solution, TO is very weakly fluorescent ($\phi_f \sim 0.0002$) which is due to the nonradiative torsional motion between the benzothiazole and quinolone moieties along with the photo-isomerization. As presented in Fig. 5.2.3, fluorescence spectra of TO monomer (λ_{em} 525 nm) showed intriguing changes in its spectral characteristics in the presence of different concentrations of SBE₇βCD. At lower concentration of SBE₇βCD (upto 3 μM), the fluorescence intensity increased significantly and the emission spectra became broad with maximum at ~660 nm, which is indicative of the formation of TO dimers/aggregates.²⁵⁴ On further addition of SBE₇βCD (beyond 3 μM), this broad fluorescence band diminished considerably and alongside a gradual increase in a fluorescence band centered at ~525 nm corresponding to the monomer emission was observed. These intensity changes monitored at 660 nm and 525 nm (inset of Fig.5.2.3) clearly indicate the dynamic changes in the complexation with the composition of the host and the guest. In line with the interpretation arrived from the absorption measurements, these fluorescence intensity changes also corroborate that the initial addition of SBE₇βCD brings out aggregation/clustering of TO molecules at the SBE₇βCD portals. This aggregation-induced emission (AIE) enhancement

disappears when the availability of SBE₇βCD host is increased, where TO molecules move to a 1:1 inclusion complex formation and display its characteristics of weak monomeric emission.

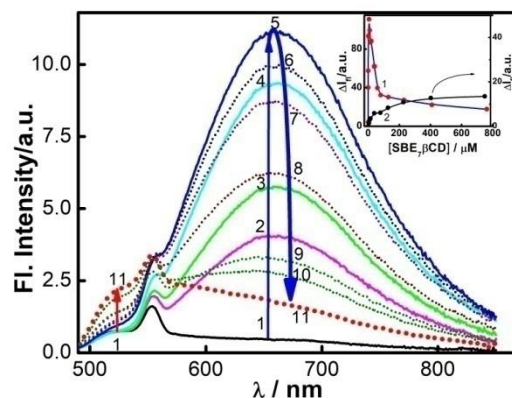


Figure 5.2.3: Fluorescence spectra of TO (3 μM) in aqueous solution at different concentrations of SBE₇βCD. [SBE₇βCD] / μM : (1) 0.0, (2) 0.25, (3) 0.5, (4) 1.5, (5) 3.0, (6) 6.0, (7) 20.0, (8) 40.0, (9) 80, (10) 230 and (11) 760. Inset shows the variation in the fluorescence intensity at 660 nm (1) and 520 nm (2) with increase in the concentration of SBE₇βCD.

5.2.3.3 Time-Resolved Fluorescence and Anisotropy studies of Thiazole Orange with SBE₇βCD

Fluorescence lifetime measurements of TO has been carried out on excitation at 445 nm to explore the individuality of the excited states of the SBE₇βCD:TO complexes at lower and higher concentrations of SBE₇βCD. The excited-state lifetime of TO in aqueous solution is very short (in the order of few picoseconds)²⁴⁴ and is within the time-resolution of the time-correlated single-photon counting (TCSPC) instrument used here. However, the lifetime became longer and measurable on their interaction with the SBE₇βCD. As presented in Fig. 5.2.4, the decay traces recorded at 640nm were fairly distinct at both the concentrations of SBE₇βCD. At lower concentration of SBE₇βCD (6 μM), the

fluorescence decay trace of TO (3 μ M) could be fitted to a triexponential function with lifetime components of 40 ps, 955 ps and 3.87 ns with their relative contributions of 12%, 32% and 56%, respectively, having average lifetime of 2.48 ns (Table 5.2.1). The shortest lifetime component is kept fixed (time resolution of TCSPC setup) and is attributed to free TO dye, the intermediate and long lifetime components are ascribed to the overlapping emissions from the dimers/aggregates (1:4 SBE₇ β CD:TO assemblies). Further increasing the concentration of SBE₇ β CD upto 400 μ M, the contribution of the shortest component increases from 12 to 56%, the intermediate lifetime decreases nominally from 955 to 912 ps without any significant variation in the relative distribution (\sim 32%) and the longest lifetime component decreases from 3.87 ns to 3.15 ns along with the reduction in its contribution from 56% to 14%. The average lifetime decreases significantly from 2.48 ns to 0.74 ns with increase in SBE₇ β CD (see in Table 5.2.1). Since the fluorescence spectral feature of TO at higher SBE₇ β CD corresponds to weak monomer emission from a 1:1 complex, the decay trace recorded at 520 nm (see in Fig. 5.2.4, trace 3), however, could not be fitted properly. Anisotropy measurements were performed to distinguish these two complexes by their sizes as the rotational correlation time is directly related to the hydrodynamic volume of the emitting system.^{232, 255} The anisotropy decay traces recorded at 640 nm are also quite different for both the complexes (inset of Fig.5.2.4).

The anisotropy decay traces are fitted with monoexponential function and the rotational correlation time (τ_r) values were estimated to be 0.81 ns and 0.41 ns for SBE₇ β CD (6 μ M):TO (3 μ M) and SBE₇ β CD(400 μ M):TO (3 μ M)

compositions, respectively. The average radii evaluated from the τ_r values (see in chapter 2, 2.14.3) are ~ 9.7 Å and ~ 7.7 Å, respectively, for the above complexes. In other words, the size of the molecular complex decreases from its initial dimension on higher dilution with the host. This is suggestive of a change over from a bulky 1:4 portal complex to a 1:1 inclusion complex and is quite justified as the number of host molecules increases in the solution.

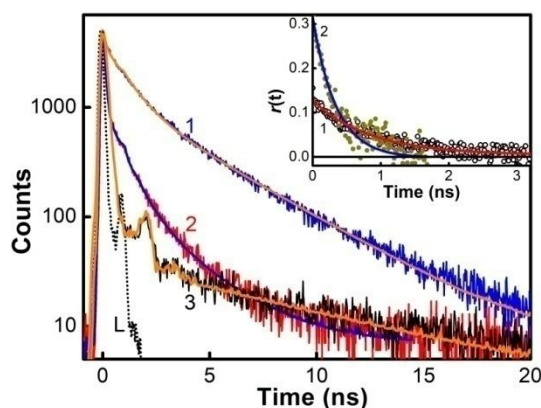


Figure 5.2.4: Fluorescence decay traces of SBE₇βCD (6 μM):TO (3 μM) (trace 1) and SBE₇βCD (400 μM):TO (3 μM) at 640 nm (trace 2) and 520 nm (trace 3). L is the lamp profile. Inset shows the anisotropy decay traces of the respective complexes. $\lambda_{ex} = 445$ nm, $\lambda_{mon} = 640$ nm.

Table-5.2.1: Fluorescence decay parameters for TO (~ 3 μM) at different concentrations of SBE₇βCD.

[SBE ₇ βCD]	τ_1 (ps) ^a	τ_2 (ps)	τ_3 (ns)	$\langle \tau \rangle$ (ns)
6 μM	40 (12 %)	955 (32%)	3.87 (56%)	2.48
400 μM	40 (56%)	912 (30%)	3.15 (14%)	0.74

5.2.3.4 ¹H NMR Studies of Thiazole Orange with SBE₇βCD

¹H NMR measurements were carried out to investigate the two types of binding interactions between TO and SBE₇βCD and the positioning of TO in the complexes by observing the changes in the chemical shift. In the presence of

low (1:1 equivalent) concentration of SBE₇βCD with respect to TO, the signal of some of the aromatic protons became broad or disappeared completely and -H_c proton showed considerable downfield shift (see in Fig. 5.2.5) which clearly supports the formation of TO aggregates through binding of multiple TO molecules at the portals of SBE₇βCD.

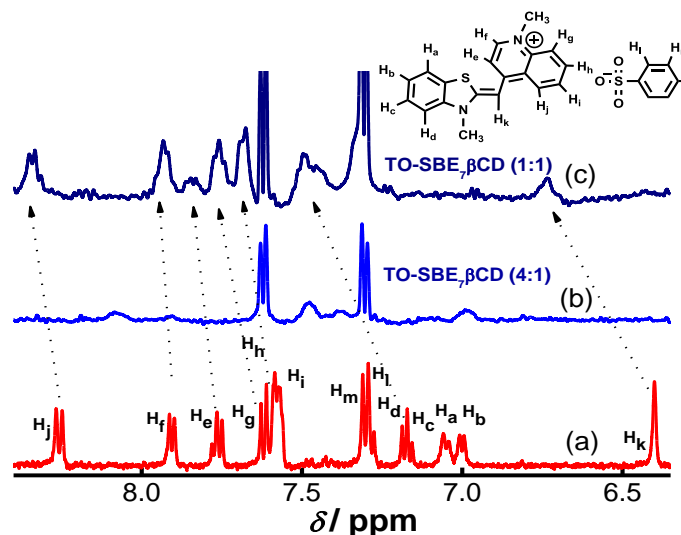


Figure 5.2.5: Upper layer shows the chemical structure of TO. (B) ¹H NMR signals of the aromatic rings of TO (100 μM) in the absence (a) and presence of 200 μM (b) and 4 mM (c) of SBE₇βCD in D₂O.

However, at higher concentration of SBE₇βCD (>1:1 equivalent), the broad and structureless bands became significantly narrow and structured and the missing signals (at lower concentration of SBE₇βCD) reappeared along with significant downfield shift. These signals at higher concentration of SBE₇βCD:TO matched well with the free TO indicating the deaggregation leading to a 1:1 SBE₇βCD:TO inclusion complex. The methine proton (H_k) experiences deshielding effect in the presence of SBE₇βCD host displaying considerable downfield shift from its original position at δ6.48. However, the

signals from -CH₃/benzothiazole and -CH₃/quinolone overlap with the proton signals from SBE₇βCD and could not be analysed properly.

5.2.3.5 Isothermal Titration Calorimetric (ITC) Measurements of Thiazole Orange with SBE₇βCD

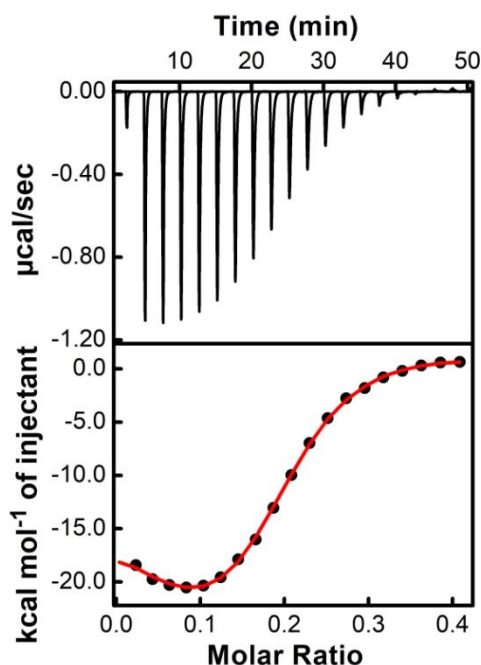


Figure 5.2.6: ITC isotherms for titration of TO (200 μM) with SBE₇βCD (400 μM) at 25 °C in aqueous solution. The upper panel shows the instrumental power function versus time (injected aliquots) plot. The lower panel shows the plot for heat of reaction obtained from the integration of the calorimetric traces, plotted against the host/guest molar ratio. The solid line represents the best nonlinear least-squares fit to a sequential binding-site model.

To document the SBE₇βCD and TO interaction thermodynamically and to estimate the binding constants for the multiple interactions of TO with SBE₇βCD indicated from the spectroscopic data, ITC measurements have been performed. From the plot of heat of reaction obtained from the integration of the calorimetric traces against the host/guest molar ratio (see in Fig. 5.2.6), a sequential 1:4 binding model is found to be best suited to fit the data and is in good support to the TO aggregation at the SBE₇βCD portals. Four binding constants in the range of $((0.8\text{--}7.9) \times 10^4 \text{ M}^{-1})$

were obtained indicating moderate interactions between TO and SBE₇βCD. The thermodynamic parameters for this interaction were evaluated and are provided in Table 5.2.2.

Table 5.2.2: Thermodynamic parameters of SBE₇βCD:TO system obtained from the ITC data

Binding constant		Enthalpy		Entropy factor		Gibb's free energy	
K ₁	(7.9±2.0) × 10 ⁴ M ⁻¹	ΔH ₁	-4.65 kcal mol ⁻¹	TΔS ₁	2.03 kcal mol ⁻¹	ΔG ₁	-6.68 kcal mol ⁻¹
K ₂	(3.1±0.9) × 10 ⁴ M ⁻¹	ΔH ₂	-1.37 kcal mol ⁻¹	TΔS ₂	4.74 kcal mol ⁻¹	ΔG ₂	-6.11 kcal mol ⁻¹
K ₃	(5.2±2.0) × 10 ⁴ M ⁻¹	ΔH ₃	-4.42 kcal mol ⁻¹	TΔS ₃	2.01 kcal mol ⁻¹	ΔG ₃	-6.43 kcal mol ⁻¹
K ₄	(8.0±3.0) × 10 ³ M ⁻¹	ΔH ₄	31.25 kcal mol ⁻¹	TΔS ₄	36.65 kcal mol ⁻¹	ΔG ₄	-5.40 kcal mol ⁻¹

5.2.3.6 Circular Dichroism (CD) Studies of Thiazole Orange with SBE₇βCD

It is not unusual that certain achiral molecules display chirality due to their organized association/aggregation. We have carried out circular dichroism measurements to get more information about the proposed host-assisted TO aggregate formation. Fig. 5.2.7 shows the CD spectra in the absence and presence of SBE₇βCD at different concentrations. In the absence of SBE₇βCD, TO (~30 μM) displays a broad negative CD band in the 430-550 nm region having a peak around 475 nm, in the region of the absorption band. This verifies the presence of fairly aggregated TO dyes at this concentration. Upon addition of SBE₇βCD to TO solution, CD band of TO changed significantly and splits into a bisignet spectrum having a strong negative band at ~475 nm and an equally intense positive band at ~533 nm (see in Fig. 5.2.7, spectrum 2). This SBE₇βCD-induced bisignet spectrum could be attributed to the strong exciton coupling among the organized TO chromophores as aggregate at the portals of SBE₇βCD.²⁵⁶ Such bisignet CD bands are quite prevalent in strongly aggregating dyes such as, perylenediimide derivatives.^{185, 256}

However, further addition of SBE₇βCD leads to the decrease in the peak intensities of the bisignet spectrum as presented in Fig. 5.2.7 (spectra 3-5) and is in good support to the conversion of SBE₇βCD-induced organized TO portal assembly to a 1:1 SBE₇βCD:TO inclusion complex as adjudged from the absorption and fluorescence studies discussed above.

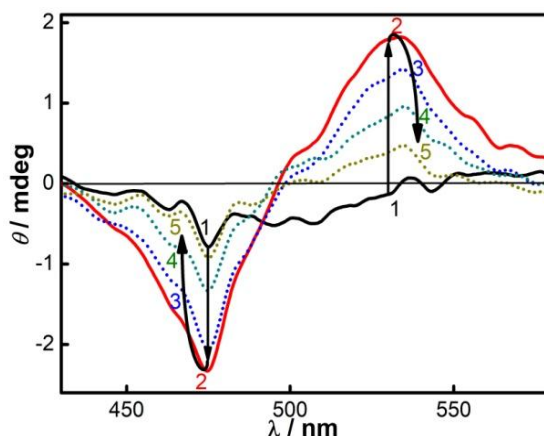


Figure 5.2.7: Circular dichroism spectra of TO (30 μ M) at different concentrations of SBE₇βCD. [SBE₇βCD] / mM: (1) 0.0, (2) 0.06, (3) 1.06, (4) 2.7 and (5) 7.7.

5.2.3.7 Stimuli-Responsive Fluorescence on-off Mechanism of SBE₇βCD:TO Assembly

Having established the AIE from the organized assembly of TO at the SBE₇βCD portals, we have advanced to investigate the effect of external stimuli such as temperature and chemical stimuli on the photophysical behaviour of SBE₇βCD:TO assembly, which would allow for several applications. Herein, we discuss the competence of the 1:4 SBE₇βCD:TO assembly to perform as a fluorescent sensor through competitive binding interaction using chemical stimuli or as an optical thermometer by introducing temperature variation.

Since, aggregation and deaggregation behaviour is largely dependent on the temperature of the system, we have studied the AIE behaviour of the 1:4

SBE₇βCD:TO at different temperatures of the solution between 10-90°C. As shown in Fig. 5.2.8A, the strong emission at 10°C (emission *on*) decreased with increase in the temperature and made the emission *turn off* at 90°C (by more than 95%).

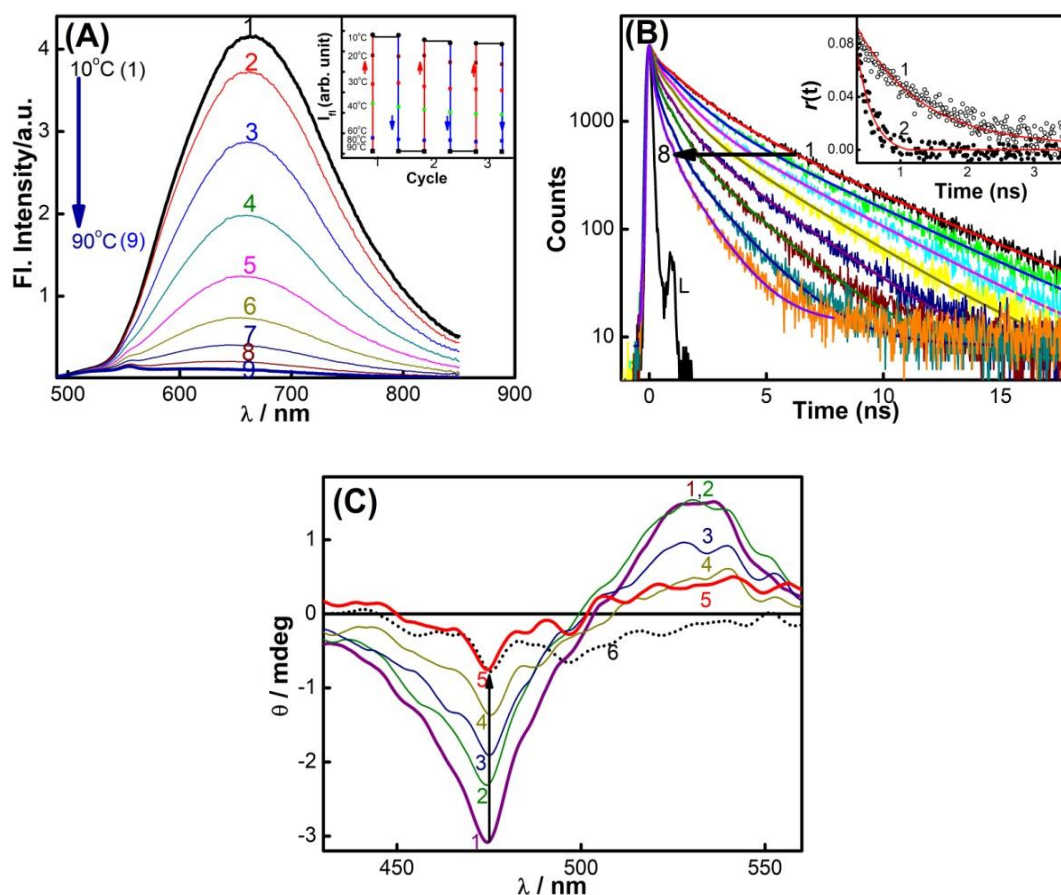


Figure 5.2.8: (A) Fluorescence spectra of 1:4 (SBE₇βCD:TO) assembly at different temperatures, Temp (°C): 10 (1), 20 (2), 30 (3), 40 (4), 50 (5), 60 (6), 70 (7), 80 (8) and 90 (9). Inset shows the emission intensities at 660 nm monitored at different temperatures with heating and cooling cycles in the range 10 °C to 90 °C. (B) Lifetime decay traces of (1:4) SBE₇βCD:TO assembly at different temperatures. Temp/°C: 20 (1), 30 (2), 40 (3), 50 (4), 60 (5), 70 (6), 80 (7) and 90 (8). Inset of Fig.5.2.7B shows the anisotropy decay traces at 20 °C (1) and 90 °C (2). λ_{ex} = 465 nm (for fluorescence spectra measurements), λ_{ex} = 445 nm and λ_{mon} = 650 nm. (C) CD spectrum recorded for SBE₇βCD:TO assembly at different temperatures. Temp/°C: 10 (1), 30 (2), 50 (3), 70 (4) and 90 (5). Dotted line in Fig. C indicates the CD spectrum of TO free dye at higher concentration (30 μM).

To validate the reproducibility and the stability of the *on-off* response of the assembly, temperature dependent emission intensity studies has been carried out in 3-4 cycles on the same sample, with steady increase and decrease of temperature. As displayed in the inset of Fig. 5.2.8A, for about 3 heating and cooling cycles, the responsive emission intensities at various temperatures remained the same, within the experimental errors. Here we propose that this stable *on-off* behaviour of AIE of the SBE₇βCD:TO (1:4) assembly with temperature can be utilized to fabricate an optical thermometer in the temperature region studied. Consequent to the changes in the fluorescence intensity, the respective average fluorescence lifetime has been decreased significantly from 3.42 ns (at 20 °C) to 0.54 ns (at 90 °C) (Fig. 5.2.8B, Table 5.2.3) and the fluorescence anisotropy value has been decreased from 0.96 ns (at 20 °C) to 0.23 ns (at 90 °C) as displayed in Fig. 5.2.8B, inset. As discussed before, decreased anisotropy value at higher temperature clearly indicates deaggregation of TO assembly at SBE₇βCD portals.

This is further confirmed from the temperature dependent circular dichroism spectra as shown in Fig. 5.2.8C. The intensity of the negative band at 475 nm and the positive band at 533 nm of the bisignet CD spectrum of SBE₇βCD:TO assembly decreases with increasing temperature. This is attributed to the weakening of the intermolecular interactions between TO molecules which subsequently reduces the extent of exciton coupling between them. As a result, the intensity of the bisignet ICD band, which originates due to the exciton coupling, reduces significantly. Therefore, the CD result confirms

the dissociation of 1:4 SBE₇βCD:TO assembly into 1:1 SBE₇βCD:TO complex with temperature.

Table 5.2.3: Fluorescence decay parameters for TO (~8.8 μM):SBE₇βCD (~15 μM) systems at different temperatures

Temp/ °C	τ ₁ (ps) ^a	τ ₂ (ns)	τ ₃ (ns)	<τ> (ns)
20	40 (4 %)	1.37 (31%)	4.61 (65%)	3.42
30	40 (4 %)	1.18 (33%)	4.26 (61%)	2.99
40	40 (4 %)	0.96 (32%)	3.76 (60%)	2.57
50	40 (4 %)	0.77 (33%)	3.19 (59%)	2.14
60	40 (4 %)	0.64 (35%)	2.86 (53%)	1.75
70	40 (4 %)	0.54 (35%)	2.22 (48%)	1.26
80	40 (4 %)	0.45 (35%)	1.78 (40%)	0.88
90	40 (4 %)	0.43 (34%)	1.59 (30%)	0.54

Of late, stimuli responsive supramolecular assemblies have found wide utility in developing sensors for trace molecules/ metal ions.²⁵⁷ In this context, we have made an attempt to explore the above established SBE₇βCD:TO (1:4) emissive molecular assembly of TO for its dissociative and optical response towards small molecules of diagnostic importance. Detection of neurotransmitters/biogenic amines in traces is an important area of research for the diagnosis and treatment/medication.²⁵⁸ We have screened a set of small aliphatic- and aromatic-based neurotransmitters/biogenic amines and interfering analytes such as choline, guanidinium hydrochloride etc., for their ability to replace the TO assembly from the -SO₃⁻ portals of SBE₇βCD through competitive binding. In the initial screening, we found that Tyramine (Tyr) facilitates a substantial quenching in the fluorescence intensity of 1:4 SBE₇βCD:TO assembly compared to other biogenic amines. Tyramine (4-hydroxyphenethylamine) is a monoamine that works by releasing other neurotransmitters like adrenaline, noradrenaline and dopamine into the body and

helps to regulate blood pressure^{259, 260} and occurs naturally in the body and it is found in certain foods. It's extremely significant to establish a sensitive and rapid detection technology for the determination of tyramine or other biogenic amines (BAs), which will play an important role in promoting the quality of food safety and safeguarding the health of people.²⁶¹ Several analytical techniques were used for the determination of Tyr such as capillary electrophoresis,²⁶² quantitative polymerase chain reaction (PCR)²⁶³ and HPLC etc.,^{264, 265} however, these methods often require time consuming complex pretreatment steps and are too expensive for routine analysis. In this regard we have explored the utility of the above established AIE assembly to respond exclusively to the presence of Tyr in the system against other biogenic amines.

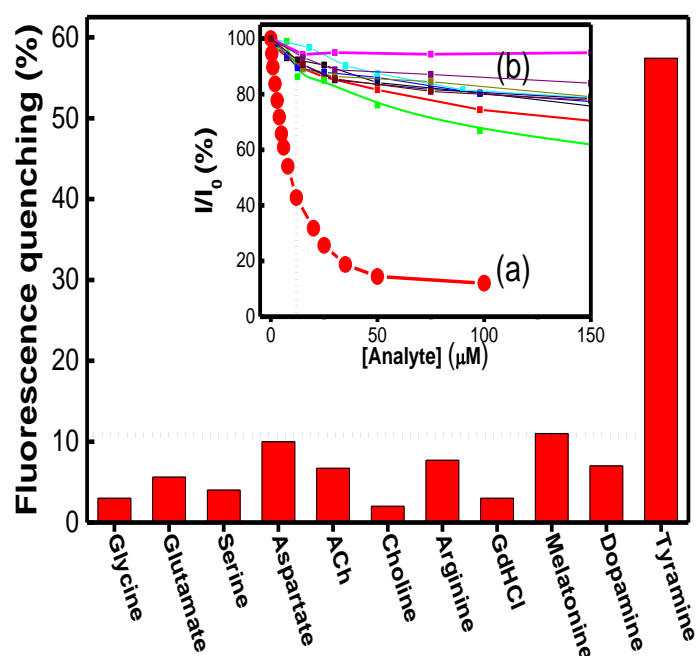


Figure 5.2.9: The percentage of fluorescence quenching of $SBE_7\beta CD:TO$ (1:4) assembly in the presence of 12 μM concentration of neurotransmitters. **Inset:** Fluorescence quenching at 660 nm for the $SBE_7\beta CD:TO$ (1:4) assembly for (a) Tyramine and (b) other neurotransmitter amines.

The response in the emission intensity of the SBE₇βCD:TO (1:4) assembly at 660 nm has been systematically followed with incremental addition of different biological amines, including Tyr, upto ~100 μM or more and changes are presented in the inset of Fig. 5.2.9. From this, it is clear that while more than 88% quenching is observed with Tyr, other biogenic amines were successful only by ~25-28%. The concentration of these analytes can be further reduced to ~12 μM amine concentration, where the addition of 12 μM of tyramine to the SBE₇βCD:TO assembly solution results in >58% reduction and the rest of the analytes presents only ~11% quenching at the same concentration. This comparison is plotted as bar charts in Fig. 5.2.9. Strikingly, majority of aliphatic neurotransmitters such as glycine, glutamate, serine, aspartate, acetylcholine and its precursor choline, does not show any creditable interaction with the sulfonate portals of SBE₇βCD so as to replace the TO dyes. As a result, only nominal changes in the AIE behaviour are observed. It is probable that due to the presence of nearby carboxylate groups or tertiary amine groups, the -NH₂ groups become not available for interaction with the SBE₇βCD portals. On the other hand, arginine, guanidinium chloride and aromatic neurotransmitters such as melatonine and dopamine, show AIE quenching ~3-11% and are believed to exert weak interactions with the sulfonate portals and are able to replace some of the TO molecules from the portals. However, the > 58% AIE quenching witnessed in the case of tyramine with SBE₇βCD:TO (1:4) assembly is very much promising for a sensing application and is quite likely that the amine group interacts strongly with the sulfonate portals while the phenol group is better stabilized by the hydrophobic cavity of SBE₇βCD. This facilitates the

replenishment of TO from the portals of SBE₇βCD resulting in a strong quenching in the AIE from TO. It is intriguing that though dopamine and tyramine have common structural features, except the additional -OH substitution in dopamine, the response in the fluorescence quenching is distinctly significant and acknowledge the selectivity of the system for tyramine detection against the other biogenic amines. The two -OH groups in dopamine are in the ortho positions and due to the presence of intramolecular hydrogen bonding between these two OH groups,²⁶⁶ the monoanionic form of dopamine is stable at neutral pH region and therefore, shows negligible interaction with SBE₇βCD.

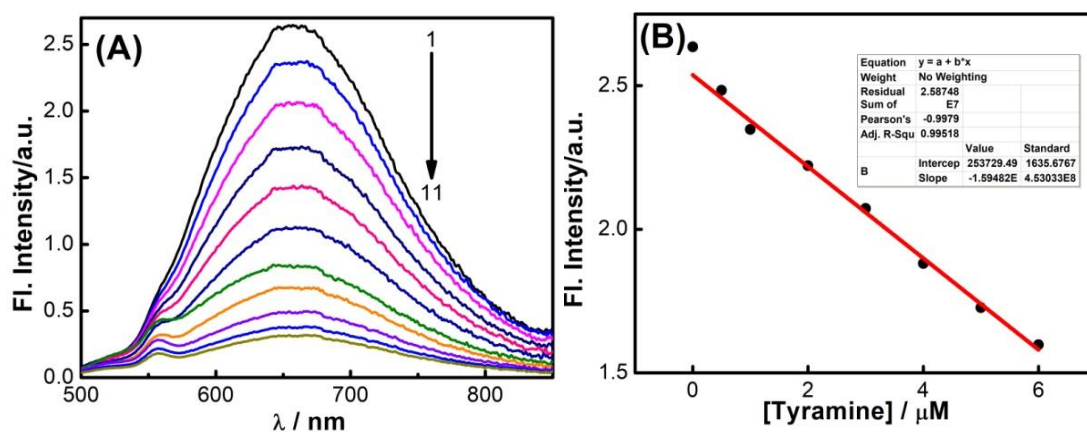


Figure 5.2.10: (A) The fluorescence titration of 1:4 SBE₇βCD:TO assembly with tyramine. [Tyramine]/μM: 0 (1), 1 (2), 3 (3), 5 (4), 8 (5), 12 (6), 20 (7), 25 (8), 35 (9), 50 (10) and 100 (11). (B) Fluorescence quenching of 1:4 SBE₇βCD:TO assembly at different concentrations of tyramine. λ_{ex} = 465 nm and λ_{mon} = 660 nm.

On the application of this stimuli-responsive assembly as a fluorescent sensor for the selective detection of Tyr, we have determined the limit of detection (LOD) by following the 3σ approach.²⁶⁷ From the tyramine titration spectra presented in Fig. 5.2.10A, the fluorescence quenching changes were

seen significant in the initial additions and a linear correlation was observed in the concentration range (0.5-6 μM) of tyramine (Fig. 5.2.10B). From the fitted linear data (expressed as $F = -1.59482C + 253729$ ($R^2 = 0.99518$), where F is represented by the fluorescence intensity and C is the concentration of tyramine), we have determined the LOD as 575 nM (~ 79 ppb), which is very close to the LOD of tyramine reported by electrochemical/electroanalytical methods (voltametric sensor and amperometric biosensor).^{265, 268, 269}

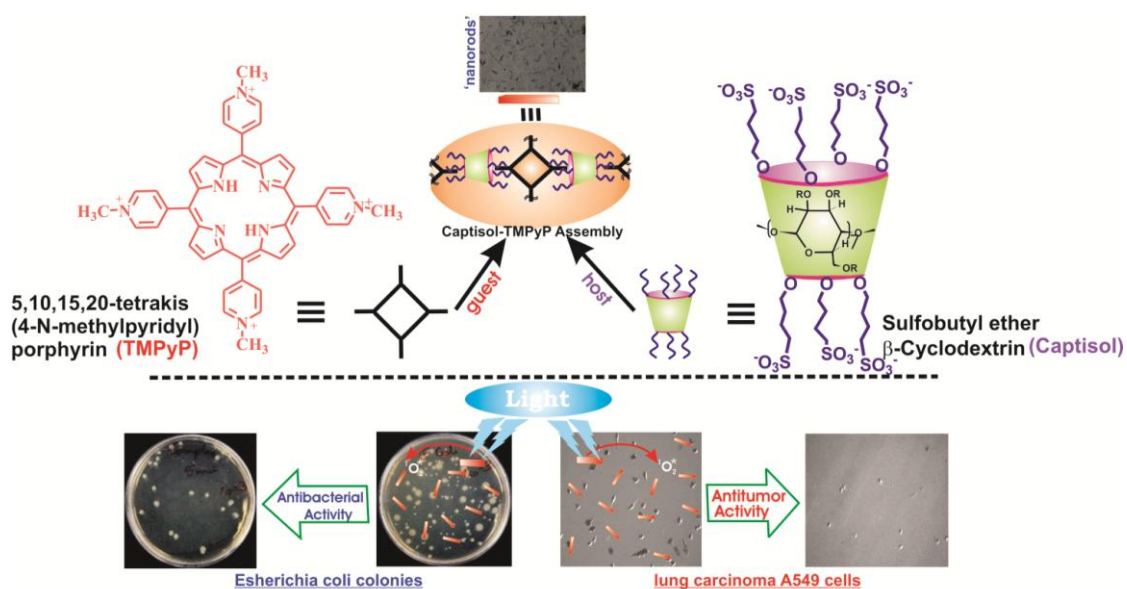
5.2.4 Conclusions

In summary, for the first time, we have established the formation of distinct 1:4 and 1:1 host-guest complexes of SBE₇ β CD and TO and explored their remarkable differences in the emissive characteristics. This has been achieved by different photophysical measurements such as absorption, steady-state and time-resolved fluorescence/anisotropy and circular dichroism studies along with ¹H NMR and ITC measurements. The enhanced fluorescence emission (fluorescence *on*) upon aggregation of the chromophore, in other words the Aggregation Induced Emission (AIE) behavior, has been demonstrated due to the uptake of about four TO dyes at the SBE₇ β CD portals when the SBE₇ β CD concentration is fairly low, but gets the emission quenched (fluorescence *off*) with the deaggregation facilitated due to the increased presence of SBE₇ β CD, or with an increase in temperature or an extrinsic competitive binder for the SBE₇ β CD. This stimuli-responsive tuning in the AIE behavior of SBE₇ β CD:TO has been translated to achieve a selective *on-off* fluorescence sensor for the detection of tyramine against other neurotransmitters with LOD ~ 575 nM (79 ppb). The AIE assembly was also shown to provide quantifiable and

reproducible emission intensities with changes in temperature, mimicking an optical thermometer responsive in the temperature region of 10-90°C.

Chapter 6

Supramolecular Photosensitizer of (N-methyl pyridyl) Porphyrin with Captisol: Enhanced Antibacterial and Antitumor Activities



Front Chem. 7, 2019, 452.

6.1. Introduction

Photosensitizers play an important role in photodynamic therapy (PDT) where the photosensitizers have the ability of absorbing light energy and transfer that to surrounding oxygen to generate highly reactive singlet oxygen and thereby destroy the cancerous or diseased tissues or inhibit the microorganism growth.²⁷⁰⁻²⁷² Generally, the specific criteria for a good photosensitizer is that it should show strong absorption with a high extinction coefficient in the red/near infrared region of the electromagnetic spectrum (600–850 nm) and should have good fluorescence yield, high photostability, high singlet oxygen quantum yield and low dark toxicity.²⁷² Porphyrins and their derivatives comprise of several properties such as absorption in the wavelength range 350-800 nm, phototoxic upon light irradiation and singlet oxygen generation, low dark toxicity which render them preferential candidates as photosensitizers.²⁷³ However, the inherent self-assembling behavior of porphyrins in aqueous medium due to strong hydrophobic or π - π stacking interactions greatly affects/reduces the ability to generate singlet oxygen as the stacked molecules release the absorbed energy mainly as heat and thereby quench the fluorescence emission.²⁷³⁻²⁷⁵ Covalent modification of porphyrins, involving time consuming tedious chemical synthesis and purification processes, is one of the ways to overcome this practical difficulty.²⁷¹ Nevertheless, the noncovalent modification of porphyrins through macrocyclic hosts without affecting their chemical composition is another way to achieve the desired property of porphyrin for singlet oxygen generation supramolecular photosensitizing behavior.²⁷¹ Among the huge collection of porphyrins, 5,10,15,20-tetrakis(4-*N*-methylpyridyl) porphyrin (TMPyP) has attracted a great deal of attention due to its efficient photosensitizing action in photodynamic therapy²⁷⁶ and molecular assembly formation

with macrocyclic receptors like cyclodextrins,²⁷⁷ cucurbiturils,¹¹⁴ and calixarenes.^{278,}
²⁷⁹ In few recent studies, Zhang et al. have established the enhanced antibacterial activity of naphthalene/phenyl derivatives of methylpyridinium moiety of TMPyP in the presence of cucurbit[7]uril against *E. coli*.^{271, 280} In an earlier study, Mohanty et al. have shown the formation of stable and extendable supramolecular architecture of TMPyP with cucurbit[7]uril (CB7) having 1:4 stoichiometry.¹¹⁴ Furthermore, this group also demonstrated the uptake and stimulus-responsive release of TMPyP from the cucurbituril-functionalized silver nanoparticle conjugates for the drug delivery application.⁷⁹ In another study, they have shown efficient interaction of TMPyP with single-strand DNA homopolymers, whereas, (dG)₄₀ DNA significantly quenches the fluorescence intensity of porphyrin through photo-induced electron transfer from dG to TMPyP.²⁸¹

In the recent past, several attempts have been made to functionalize the host and/or the guest molecules to control and tune the host-guest interactions for targeted applications. In this context, captisol (SBE₇βCD), a chemically modified cyclodextrin moiety with a structure designed to optimize the solubility and stability of drugs, has received much attention. Structurally, captisol is a modified β-CD macrocycle, details are already discussed in chapter-1. The solubility of captisol in water is much higher than the native β-CD, has an advantageously low degree of toxicity and it does not show nephrotoxicity connected with β-CD.^{227,23} In our recent study on its biological/medicinal application, we have established that the benign captisol macrocycle can be effectively used to inhibit and disintegrate amyloid fibrils/plaques, signifying its role as therapeutic agent towards neurodegenerative diseases such as Alzheimer's and Parkinson's diseases.²⁷

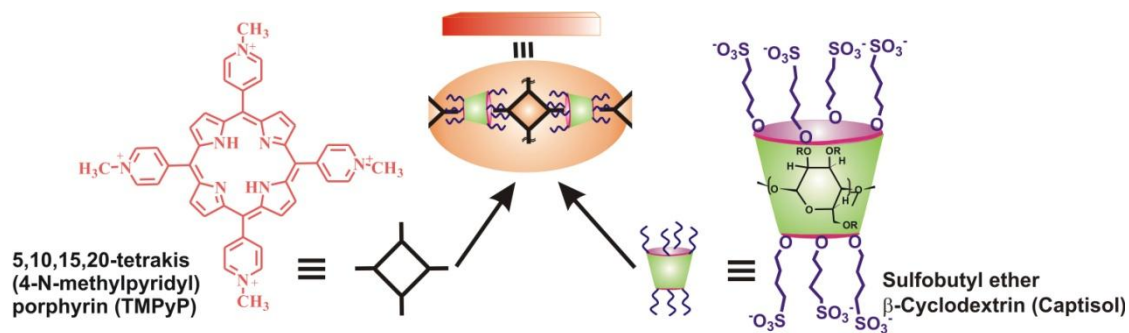


Figure 6.1: Chemical structures of TMPyP, captisol and the representation of the Captisol:TMPyP complex.

In the present study, we anticipate that the interaction of negatively charged captisol portals with the four N-methylpyridyl ends of TMPyP will prevent the inherent self-assembling behavior of TMPyP and will deaggregate the π -stacked porphyrins, which will improve its photophysical properties and enhance their active singlet oxygen yield. In this study, we have discussed the construction of supramolecular nanorods of 5,10,15,20-tetrakis(4-N-methylpyridyl)porphyrin dye/drug with captisol through host-guest interaction and demonstrated its phototherapeutic application as effective photosensitizer and a superior antibacterial and antitumor agent.

6.2 Material and Methods

1 Sulfobutylether- β -cyclodextrin sodium salt, commercially known as captisol, with a degree of substitution of 6.4 were obtained from Advent ChemBio Pvt. Ltd., India and used without further purification. The tosylate form of TMPyP obtained from Aldrich was converted to its chloride form by using an anion exchange resin.¹¹⁴ In the present study, the experimental solutions were prepared by using nanopure water obtained from a Millipore Elix 3/A10 water purification system (conductivity less than $0.1 \mu\text{S cm}^{-1}$). The methods like

absorption, fluorescence, Photostability Measurements, Singlet Oxygen ($^1\text{O}_2$) Generation Measurements, Antibacterial Activity Measurements and Photosensitization activity in tumor cells used in this study have already been described in Chapter 2.

6.3 Results and Discussion

6.3.1 Absorption and Emission Behavior of TMPyP with Captisol

TMPyP shows absorption in the wavelength range 350-700 nm including the *soret* and *Q*-bands.¹¹⁴ Initial addition of captisol up to $\sim 1.5 \mu\text{M}$ to the aqueous solution of TMPyP results a decrease in the absorbance, further addition of captisol leads to increase in the absorbance along with small bathochromic shift $\sim 4 \text{ nm}$ in the *soret* band (Fig. 6.2A). The strong interaction between TMPyP and captisol is clearly visualized by the drastic change in the broad fluorescence band (due to intramolecular charge transfer between the *N*-methylpyridinium ring and the central porphyrin moiety of TMPyP)¹¹⁴ and a reasonable enhancement in the fluorescence yield from 0.047 to 0.08.¹¹⁴ The aggregation-induced/intramolecular charge transfer fluorescence self-quenching of TMPyP is largely suppressed in their aggregates by the bulky captisol host that are noncovalently attached on the porphyrin aromatic rings. The fluorescence band resolves into two narrow bands with maximum at 653 nm and 717 nm and a trough at 683 nm along with the variation in the fluorescence intensity ratio of 653 nm to 717 nm (I_{653}/I_{717}) with the increasing concentration of captisol (Fig. 6.2B). Very low concentration ($3.5 \mu\text{M}$) of captisol is sufficient to attain saturation, indicating strong binding interaction between captisol and TMPyP. In view of the modulations in the absorption and emission spectra and the high affinity of captisol toward $\text{N}^+\text{-CH}_3$,

an inclusion of the pyridinium arm of TMPyP into captisol would be the most probable interaction mode.

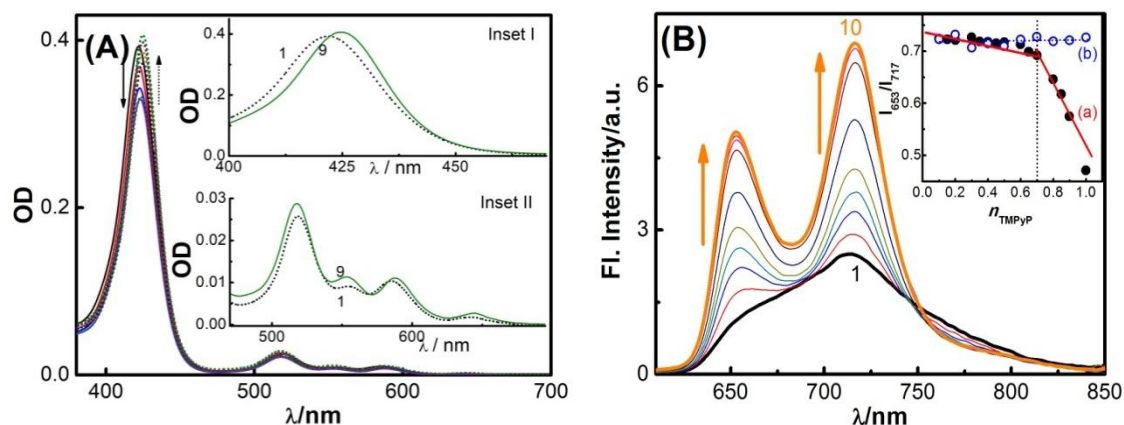


Figure 6.2: Absorption (A) and fluorescence (B) spectra of TMPyP (2.1 μM) in aqueous solution at different concentrations of captisol. [Captisol]/μM: (1) 0, (2) 0.25, (3) 0.5, (4) 0.75, (5) 1.0, (6) 3.5, (8) 7.0, (8) 14.8 and (9) 22 at pH ~7.4. In (A), Inset I and Inset II show the changes in the soret band and Q band (500-700 nm) region, respectively, in the presence of 22 μM captisol. In (B), Inset shows Jobs plot using the fluorescence intensity ratio (I_{717}/I_{653}) with mole fraction of TMPyP, n_{TMPyP} , for the Captisol:TMPyP complex (a) and only TMPyP solution (b) under identical concentration conditions.

This type of encapsulation will interrupt the intramolecular charge transfer between the central porphyrin moiety and the *N*-methylpyridinium ring, which in turn disturbs the electronic distribution, bringing about two discrete emission bands centered at 653 and 717 nm, consistent with the Q(0,0) and Q(0,1) transitions.²⁸² These variations are markedly different from those observed on interaction of TMPyP with parent β-cyclodextrin (β-CD), where the I_{653}/I_{717} ratio remains almost constant with observable variations in the trough region.²⁷⁷ The influence of captisol binding on the excited state properties of TMPyP was clearly observable in the changes of its excited state lifetime as well. The fluorescence decay traces recorded in a TCSPC setup at 650/710 nm displayed significant increase in the singlet state lifetime of

TMPyP from 5.2 ns to ~11 ns with increasing concentrations of captisol (see in Fig.6.3). As claimed above, the strong complexation at the *N*-methyl pyridinium rings of TMPyP arrest the otherwise active intramolecular charge transfer pathways, thereby allowing extended lifetime for the excited singlet state, which may become advantageous for its photosensitizing and other photochemical features. Considering the availability of four such pyridinium moieties, TMPyP is expected to undergo multiple interactions with captisol, as observed with other hosts like calixarenes,^{278, 279} cucurbiturils¹¹⁴ and cyclodextrins.^{8,10} In other words, the feasibility for such multiple binding would support for an extended/networked arrays of Captisol:TMPyP complex, realizing the formation of a new supramolecular assembly with altered photophysical properties of the TMPyP dye/drug.

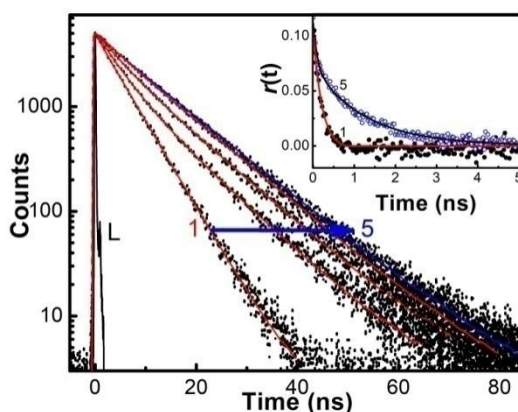


Figure 6.2: Fluorescence decay traces ($\lambda_{ex} = 445$ nm, $\lambda_{mon} = 650$ nm) of ~ 2 μ M TMPyP solution at different concentration of captisol. [Captisol] / μ M: 0.0 (1), 0.25 (2), 0.5 (3), 1.0 (4) and 22.0 (5). L represents the instrument response function. The inset displays the fluorescence anisotropy traces under the conditions for the fluorescence decay traces 1 and 5.

To determine the binding stoichiometry, we monitored the ratio of the fluorescence intensities at 653 nm and 713 nm with varying mole fractions of TMPyP and captisol and the plots are shown in the inset of Fig. 6.2B. A distinct inflection in the slope close to 0.66 mole fraction of TMPyP (Fig.6.2B, inset trace (a)), as

compared to that obtained for the TMPyP alone in a similar experiment (Fig.6.2, inset trace (b)), proposes a 1:2 stoichiometry for the Captisol:TMPyP complex. The formation of a 1:2 complex is further recognized by the values obtained from time-resolved fluorescence anisotropy measurements. Due to complex formation there will be increase in the molecular hydrodynamic volume of the fluorophore, which will reflect in its rotational correlation time constant (τ_r) evaluated from the anisotropy decay and the details are provided in the Chapter 2, (2.14.3). The inset of Fig. 6.3 displays the fluorescence anisotropy decay traces of TMPyP measured at 650 nm in the presence (trace 5) and absence (trace 1) of captisol. A single exponential decay analysis provided τ_r as 1.28 ns for the Captisol:TMPyP complex, against the 0.21 ns estimated for the free TMPyP. Since the radius of free TMPyP is ~ 9.7 Å,¹¹⁴ the above significant change in the τ_r value specifies that the radius of the emitting Captisol:TMPyP complex increases by about 8.0 Å as compared to TMPyP,^{23,86} suggestive of a complete inclusion of the pyridyl arm into the extended cavity of captisol with the positively charged nitrogen closer to the sulfonate groups. Such an arrangement is in good support for the assertion of 1:2 (Captisol:TMPyP) complex formation.

6.3.2 ¹H NMR Measurements

The formation of host-guest complexation is further supported by the changes in the chemical shift observed on the α - and β -pyridyl protons as well as the $>\text{NCH}_3^+$ protons of TMPyP in the presence of captisol (Fig. 6.4). These three different protons of TMPyP show large downfield shift in the ¹H NMR signal ranging from 0.027 to 0.171 in the presence of 1 equivalent of captisol with respect to TMPyP. These positions were further shifted slightly by increasing the host concentration to 2 equivalents of

captisol. This result points to the deshielding of the electron distribution in the N-methylpyridyl rings reside near to the sulfonate groups of captisol through strong electrostatic interactions. It may be noted that in the present case, separate signals for bound and unbound N-methylpyridyl protons were not observed which may be due to a probable faster host-guest exchange process in the NMR time scale that leads to the observation of N-methylpyridyl proton resonance at an average position.

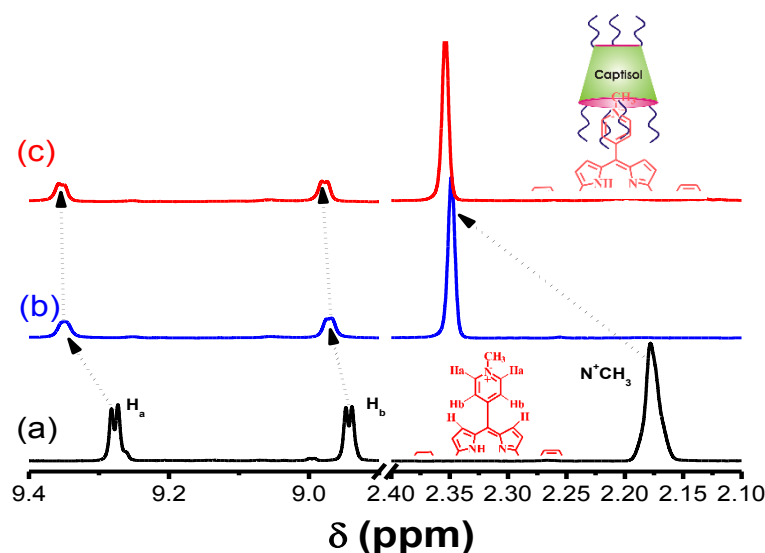


Figure 6.4: ^1H NMR spectra of (a) TMPyP, (b) TMPyP and captisol (1.0 equiv.) and (c) TMPyP and captisol (2.0 equiv.) in D_2O . Inset: N-methyl pyridyl moiety with a part of the central porphyrin moiety and the pictorial representation of the host interaction.

6.3.3 Isothermal Titration Calorimetric Measurement

To confirm the proposed 1:2 stoichiometry of the host-guest complex, isothermal titration calorimetric (ITC) measurements have been carried out considering captisol as host and TMPyP as guest/ligand. The integrated heat profile *versus* the mole ratio has been generated from the heat evolved during the titration and is presented in Fig. 6.5, which gave a satisfactory fit for a sequential 1:2 binding model. The overall binding constant value ($K = K_1 \times K_2$) was estimated as $9.3 \times 10^8 \text{ M}^{-2}$. The individual

binding constants along with thermodynamic parameters obtained from the ITC plots are provided below.

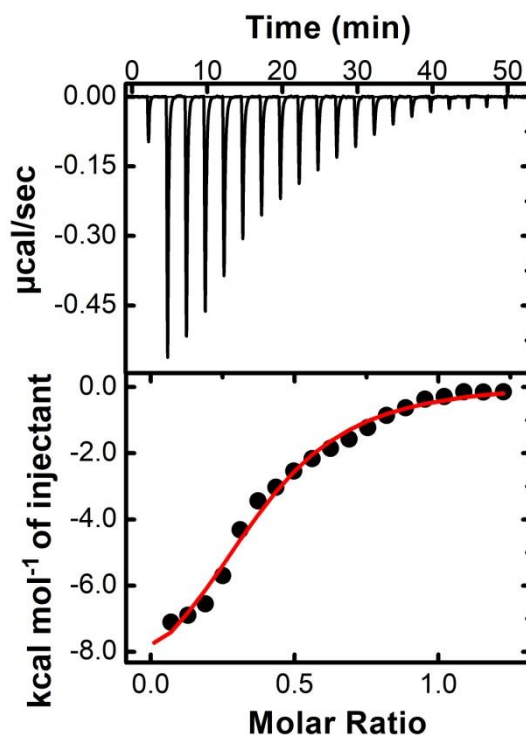


Figure 6.5: Upper panel shows the raw data for the titration of 100 μM TMPyP with 600 μM captisol at pH 7.4 in phosphate buffer (10 mM) and 25 $^{\circ}\text{C}$, showing the calorimetric response as successive injections of the host are added to the sample cell. Lower panel shows the integrated heat profile of the calorimetric titration given in the upper panel. The solid line represents the best nonlinear least-squares fit to a sequential binding- site model.

6.3.4 Dynamic Light Scattering (DLS) Measurements

To explore the formation of extended assembly from Captisol:TMPyP complex leading to larger assembly/particles, we carried out DLS measurement of TMPyP (500 μM) at different concentrations of captisol (0.25 mM to 2 mM). As shown in Fig. 6.6 and Table 6.1, the particle size increased gradually on increased addition of captisol host, confirming the formation of extended assembly/large moieties by virtue of its multiple binding sites available on both the host and the guest.

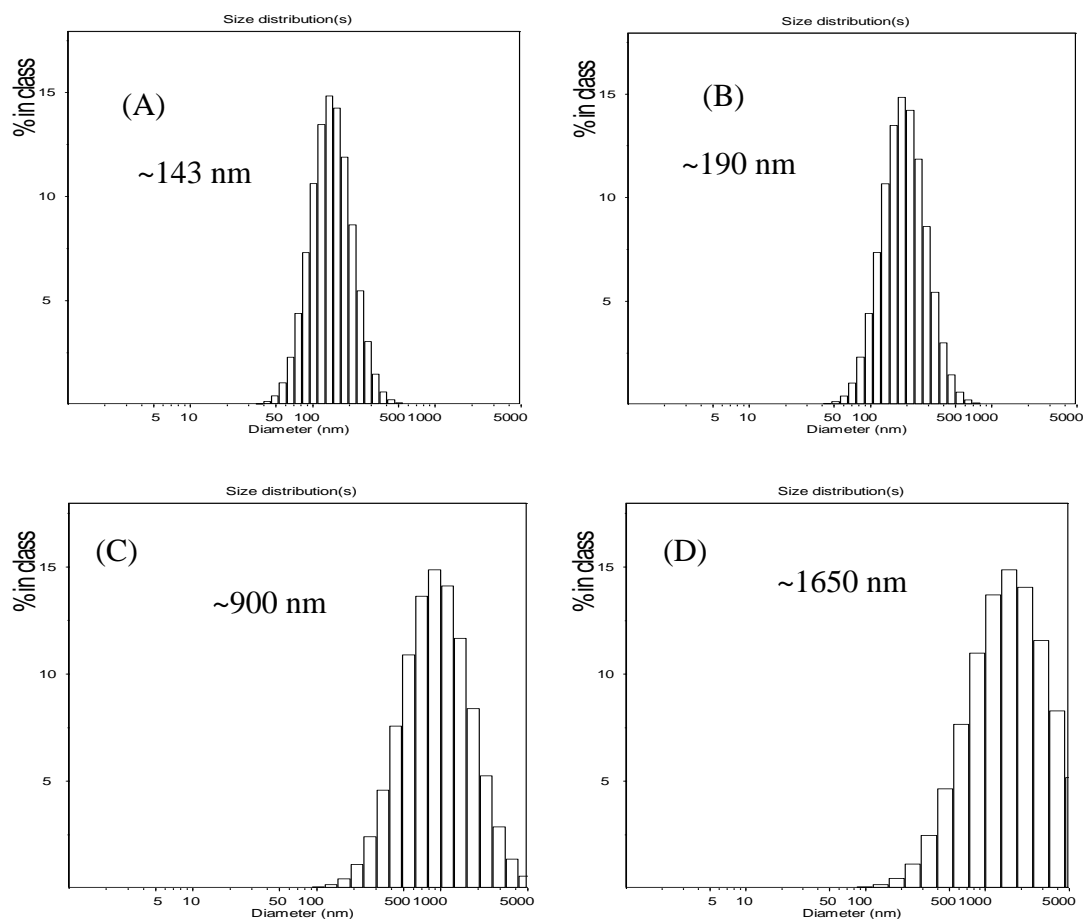


Figure 6.6: Size distribution curve obtained during addition of captisol to TMPyP(500 μ M) solution with Captisol (A) 0.25 mM, (B) 0.5 mM, (C) 1mM, (D) 2 mM indicating the formation of extended assemblies/moieties.

Table 6.1: DLS measurements carried out in solutions of 500 μ M TMPyP with the addition of varying concentrations of Captisol

	[Captisol](μ M)	Particle Size (nm)
A	250	143
B	500	190
C	1000	900
D	2000	1650

6.3.5 SEM and FM Measurements

As envisaged, the strong and multiple binding would eventually lead to extended/self-assembled supramolecular structures. In these experiments we have employed SEM

and FM method to look into the formation of such probable nanostructures in the samples drop casted on silica wafer/cover slip, by monitoring the surface morphology of TMPyP in the absence and presence of captisol (Fig. 6.7 (a-c, g, h) and (d-f, i, j)).

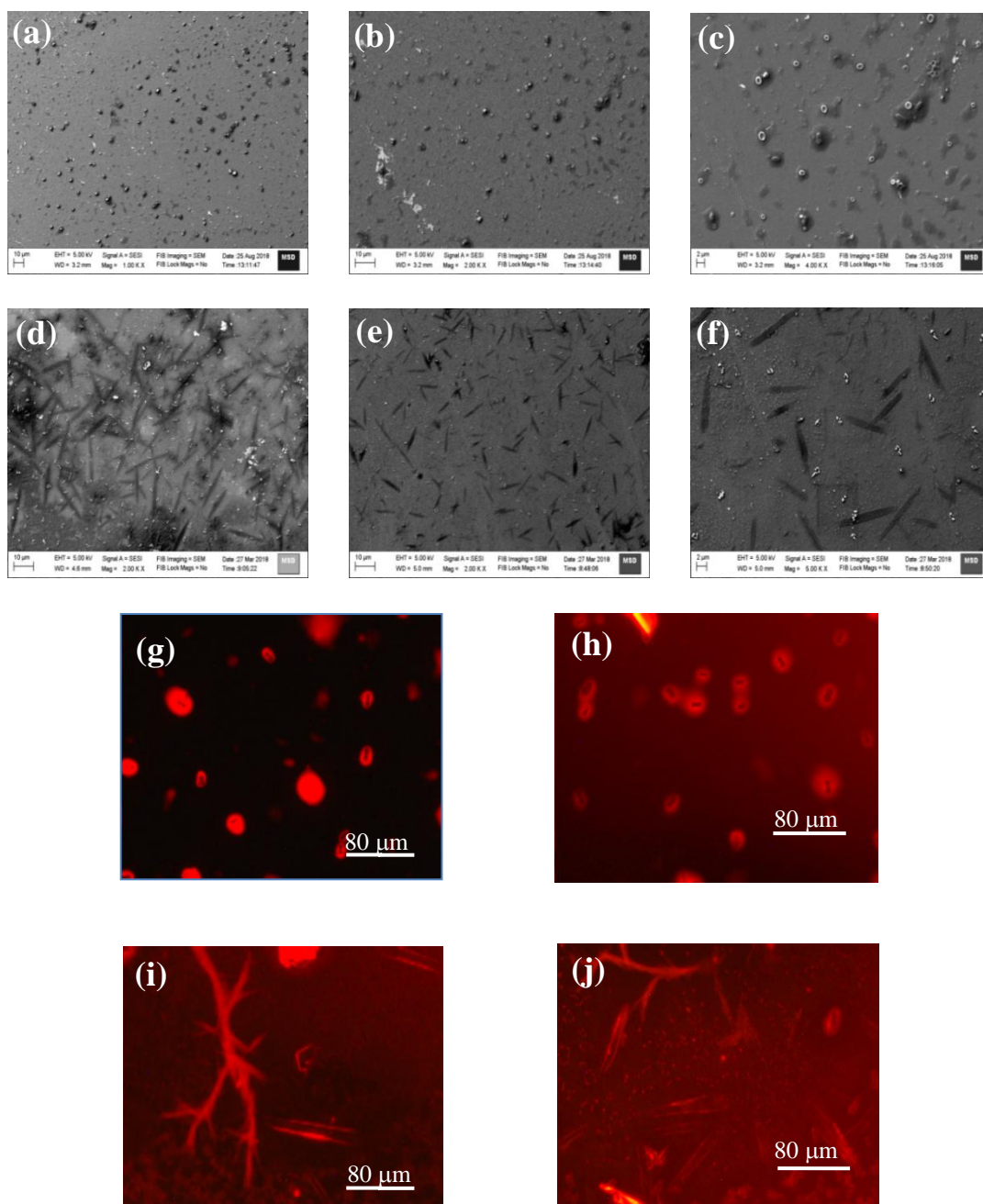


Figure 6.7: SEM (a-f) and FM (g-j) images of TMPyP alone (a-c, g, h) and TMPyP (2 μ M) with captisol (25 μ M) (d-f, i, j) using green light excitation.

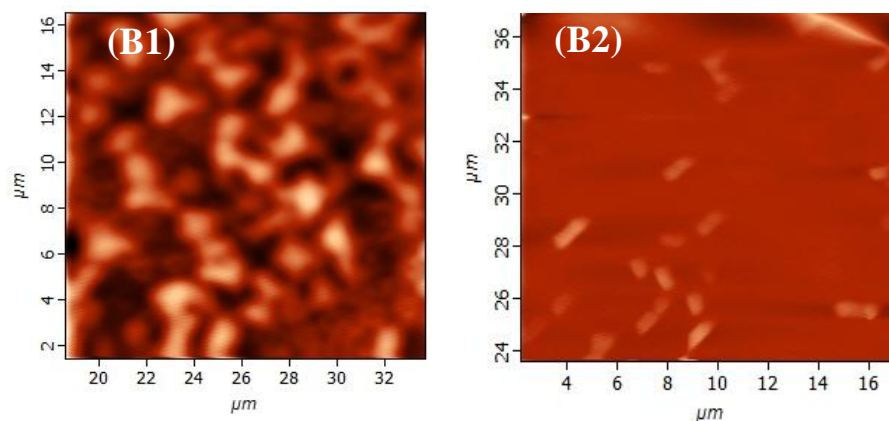


Figure 6.8: AFM images of (B1) TMPyP and (B2) TMPyP (2 μM) with captisol (25 μM).

We have added excess concentration of captisol to the TMPyP solution to have >95% complex formation in the solution. SEM images recorded from the sample of Captisol:TMPyP complex displayed distinctive nanorods of $\sim 10\ \mu\text{m}$ length, whereas free TMPyP under similar conditions displayed only lumps of aggregated dyes without any discrete morphology. The confirmation that these nanorods do incorporate the TMPyP chromophore came from the fluorescence microscopy (FM) images (Fig.6.7 (i & j)) obtained from the free and captisol complexed TMPyP samples casted on pre-cleaned glass surface. Bright orange fluorescent streaks of micron length structures seen from images asserts that the captisol complexed TMPyP do grow in extended supramolecular structures, whereas the TMPyP alone remains as aggregated lumps of no specific morphology. The smaller nanorods ($\sim 2\ \mu\text{m}$) of Captisol:TMPyP complex are also seen in the AFM images (Fig. 6.8 (B1 and B2)).

6.3.6 Photostability and Singlet Oxygen Generation Measurements

After establishing the formation of captisol assisted supramolecular nanorod assembly of TMPyP with improved excited state features, we were inquisitive to investigate its photostability and the ability to generate singlet oxygen ($^1\text{O}_2^*$) which are essential to

assess their practical use, particularly as photosensitizer in photodynamic therapy. In most of the dye based PDT systems, the unspecific surface adsorption, aggregation propensity and photo bleaching of the chromophore reduce their photosensitizing efficacy. However, such unspecific aggregation interactions and nonradiative pathways are largely prevented on macrocyclic encapsulation of the dye/drug. Apparently, in the host confined environment, the excited singlet state of the dye/drug find relatively longer lifetime favoring more triplet yield.⁹⁴ To take advantage of the improved photophysical features of Captisol:TMPyP complex and to attest its improved photostability, we have irradiated the aqueous solution of TMPyP in the absence and presence of captisol host using low irradiance light from a 150W Xenon lamp (fluence rate $\sim 80 \mu\text{W cm}^{-2}$ for 1 hr at $422 \pm 2.5 \text{ nm}$). From the corresponding absorption spectra (Fig. 6.9) and the plot of the changes in the absorbance at the Soret band position (422 nm) with irradiation time monitored both in the presence and absence of captisol (Fig. 6.9C), displayed remarkable improvement in the photostability of TMPyP when it is complexed with captisol.

On the other hand, generation of reactive singlet oxygen is considered to be the central issue of PDT procedure. In this regard, porphyrins and expanded porphyrins are under intense investigation due to their photosensitizing ability for PDT application. These photosensitizers are activated on exposure to light and become photosensitizers triplet, which react with dissolved molecular oxygen to produce the reactive singlet oxygen ($^1\text{O}_2^*$), which are responsible for therapeutic action.

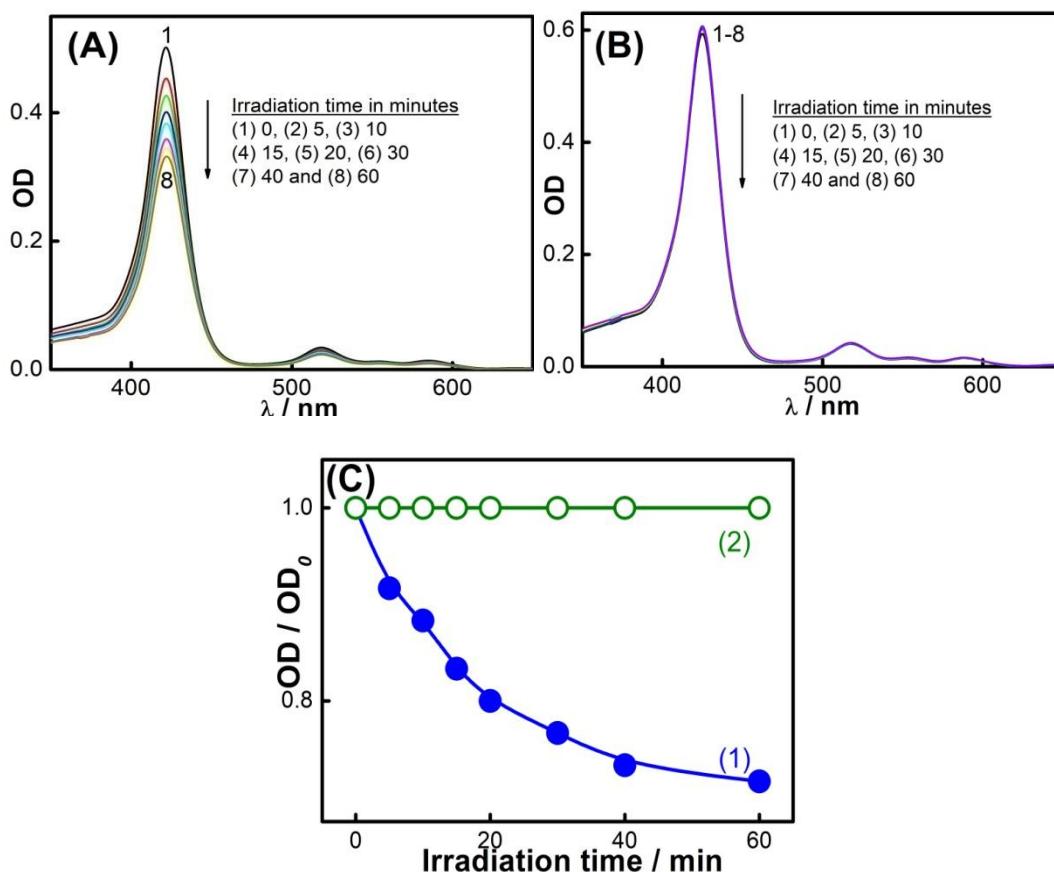


Figure 6.9: Photodegradation of TMPyP (2 μ m) in aerated water in the absence (A) and presence (B) of 25 μ m of captisol followed through the decrease of the visible absorption with increasing time of irradiation at 422 nm using a 150 W xenon lamp from a steady state fluorimeter. (C) Changes in the absorbance of TMPyP monitored at 422 nm on irradiation at 422 \pm 2.5 nm using 150W Xenon lamp from the steady state fluorimeter; TMPyP alone (1) and Captisol:TMPyP complex (2).

On the basis of our present finding that the Captisol:TMPyP complex displayed enhanced excited singlet state lifetime and photostability, we foresee that this supramolecular assembly of TMPyP can largely enhance the singlet oxygen generation favoring PDT. Following the established method of measurement, we have adopted the reaction of singlet oxygen with 1,3-diphenylisobenzofuran (DPBF) and the consumption of DPBF as a measure of the yield of singlet oxygen generation in the system.²⁸³ Due to poor solubility of DPBF in water, these measurements were

carried out in DMF solvent. We have verified that the complexation interaction of TMPyP with captisol follows comparable binding behavior in DMF and gets saturated at slightly higher concentration of captisol as compared to the captisol concentration in H₂O medium (see in Fig. 6.10). Fig. 6.11 shows the changes in the absorbance of DPBF monitored at 417 nm upon photoirradiation of air-saturated DMF solution at 510 nm (which is selected to avoid the direct excitation of DPBF) containing DPBF and TMPyP in the presence/absence of captisol. Similar irradiation studies were also carried out with [Ru(bpy)₃]²⁺ system as control to correlate with the change in the singlet oxygen generation with time. As displayed in trace 1 and 2 (Fig. 6.11), the yield of singlet oxygen increases linearly with irradiation time and the photogenerated singlet oxygen quantum yields from TMPyP and its captisol complex were estimated to be 0.73 and 0.91, respectively, in comparison with that of standard ([Ru(bpy)₃]²⁺, $\Phi(^1\text{O}_2^*) = 0.81$ in air-saturated methanol (trace 3)).¹¹² The significant enhancement (0.73 to 0.91) in the efficiency to generate singlet oxygen and the photostability of TMPyP in the presence of captisol is attributed to the enhancement of excited state lifetime and the concurrent improvement in the triplet yield. Due to the overlapping absorption spectra of DPBF and TMPyP, the control experiments have been performed in the absence of DPBF to take care of the absorption loss due to TMPyP and the complex during photoirradiation. To document the constructive role of the captisol host, it may be stated here that similar studies on TMPyP in presence of parent β -CD host, having no extended sulfobutyl arms, provided singlet oxygen yield of 0.4, which is much less than that observed for free TMPyP itself.

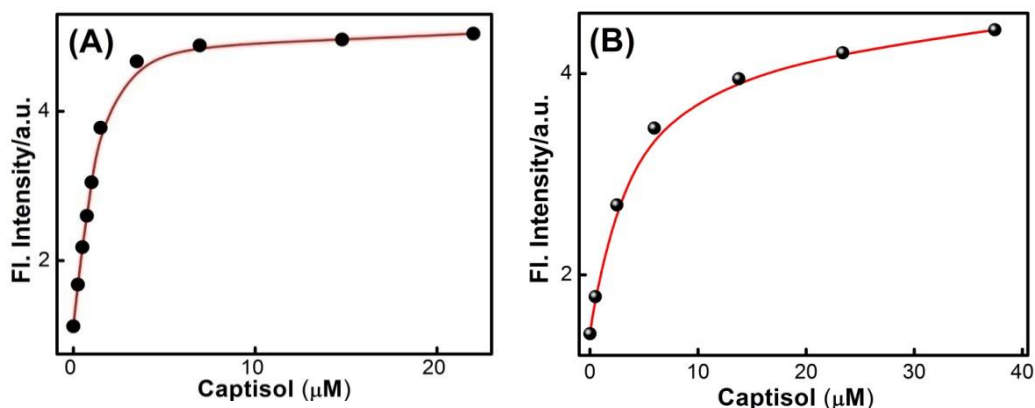


Figure 6.10: Plot of the changes in the fluorescence intensity (I_{fl}) with increasing concentration of Captisol at 660 nm in aqueous solution (A) and in DMF (B).

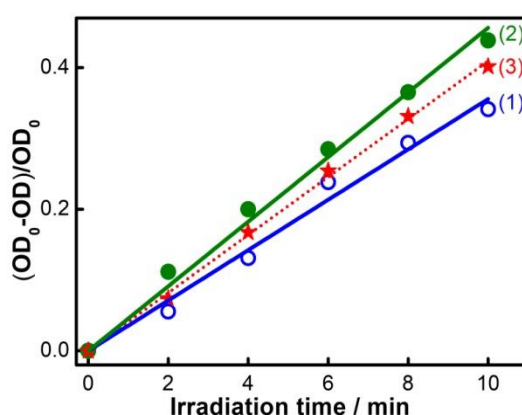


Figure 6.11: The consumption of DPBF as a function of irradiation time in the air-equilibrated DMF solution of DPBF and TMPyP ($\sim 2\mu\text{M}$) in the absence (1), presence of 20 μM captisol (2). Trace (3) represent the singlet oxygen yield evaluated for $[\text{Ru}(\text{bpy})_3]^{2+}$ as standard ($\Phi(^1\text{O}_2^*) = 0.81$) in air equilibrated CH_3OH) under similar irradiation conditions.

6.3.7 Photosensitized Antibacterial and Antitumor Activities

Quaternary ammonium compounds are broadly used as antibacterial agents to kill various types of bacteria.^{280, 284} Since methylpyridinium moiety in TMPyP contains quaternary ammonium group, we were interested to investigate whether the enhanced singlet oxygen yield of TMPyP in the presence of captisol will have any effect on the antibacterial activity. In this perspective, we have investigated the antibacterial

activity of TMPyP and the Captisol:TMPyP complex with and without light irradiation against a pathogenic Gram-negative micro-organism i.e. *Escherichia coli* (*E. coli*) and Gram-positive micro-organism *Staphylococcus aureus*, by well-known spread plating method (Fig. 6.12(a-c) and 6.13(a,b)). In this method *Escherichia coli* culture was diluted to obtain 10^7 cfu/ml using 0.85% saline. The cells were incubated in dark with TMPyP or Captisol:TMPyP systems for 15 min. (15.0 ml culture containing 100 μ l of dye or complexed dye) and then exposed to white light (LED, fluence rate ~ 50 mW cm $^{-2}$) at different time durations for irradiate condition. Appropriate dilutions (10^4 , 10^3) were spread plated (100 μ l) on Luria agar plates. The plates were incubated at 35 ± 2 °C for 18-20 hrs and the colonies were counted (details are given in chapter-2, 2.14.11). It is observed that in the unirradiated condition (Fig. 6.12d, (i)) there is a nominal inhibition ($\sim 18\%$) in the bacterial growth in the presence of TMPyP and the inhibition is reduced to $\sim 5\%$ in presence of Captisol:TMPyP complex, indicating that the Captisol:TMPyP complex is less toxic under dark conditions. However, assessment of the bacterial growth from the plates containing TMPyP or Captisol:TMPyP complex and irradiated with white light (LED, fluence rate ~ 50 mW cm $^{-2}$) showed notable inhibition in the growth of colonies of *E. coli* as compared to their respective blanks having no TMPyP or the complex (Fig. 6.12a-c).

More importantly, the extent of inhibition (or the antibacterial activity) is found to be significantly higher in the irradiated plates containing the Captisol:TMPyP complex and are found to be effective in killing $\sim 81\%$ of the bacteria on ~ 5 min white light irradiation, as compared to $\sim 49\%$ by TMPyP alone under similar conditions (Fig.6.12d, (iii)).

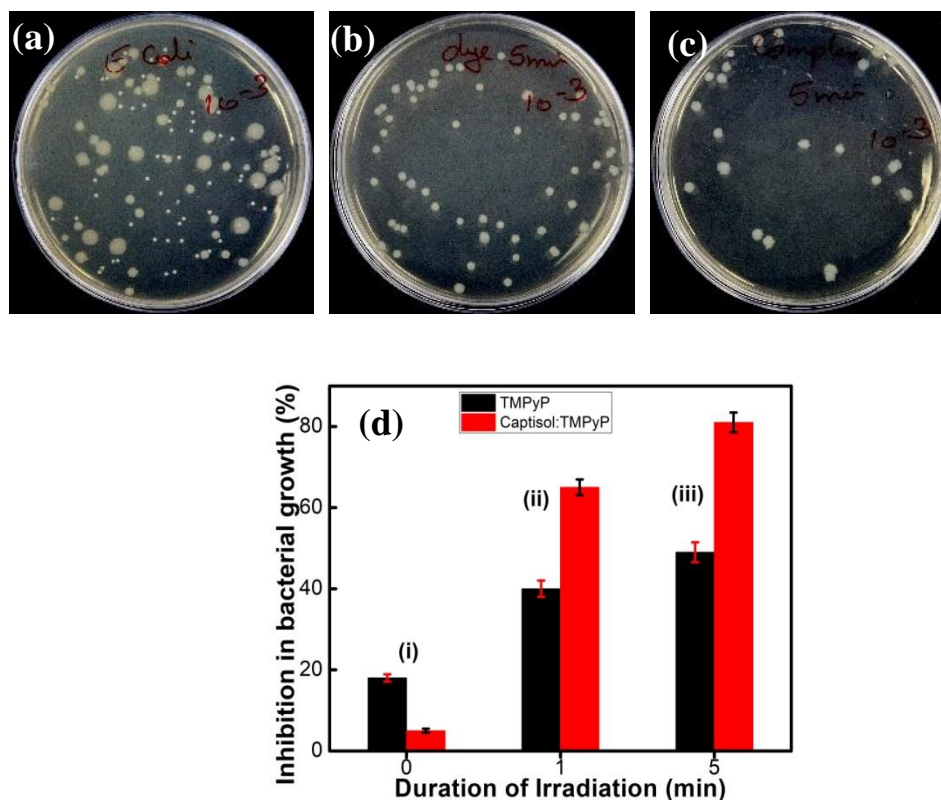


Figure 6.12: Images of plates showing bacterial growth of *E. coli* in terms of colonies in the absence of any additive (a) and presence of TMPyP (5 μ M) (b) and with TMPyP (5 μ M):captisol (20 μ M) (c) at pH 7.5 after white light irradiation for 5 minutes. (d) is the bar chart representation of the percentage of inhibition in bacterial growth by TMPyP (5 μ M) in the absence (black bar) and presence (red bar) of captisol (20 μ M) with irradiation time 0 min (i); 1min (ii); 5 min (iii) against *E. Coli* (Gram -ve) bacteria.

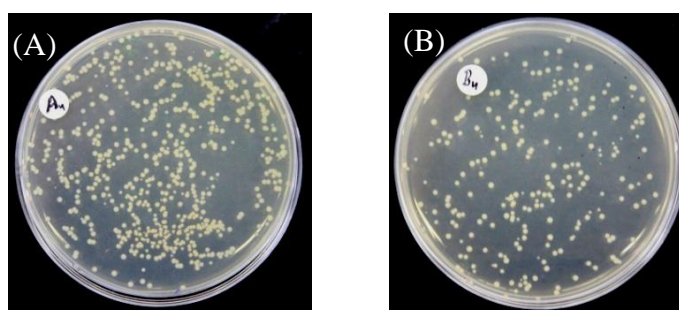


Figure 6.13: Plates showing growth of Gram positive *Staphylococcus aureus* in colonies with TMPyP (A) and Captisol:TMPyP complex (B) on light irradiation.

Comparable killing effect was also observed with Gram positive *Staphylococcus aureus* bacteria in a similar experimental follow up (Fig.6.13). This

enhanced antibacterial activity in the Captisol:TMPyP complex is in good agreement to the contention of captisol assisted enhancement in the generation of reactive singlet oxygen by TMPyP dye/drug, mainly due to its modulation in the excited state dynamics.

Studies have been further extended to explore the photosensitizing effect of the Captisol:TMPyP complex towards cancer cells on white light irradiation (LED, fluence rate $\sim 50 \text{ mW cm}^{-2}$) using MTT assay. Though the imaged assemblies/nanorods are of micron size, quite large for cellular uptake, it may be noted here that the basic unit of the assembly is of only few nanometer size and beside the micron size extended assemblies, there are smaller assemblies/particles of ~ 100 to 150 nm of size in solution, which can contribute to the cellular effect. Figure 6.14A shows the percent viability of A549 cells (human lung carcinoma) under different treatment conditions. It clearly indicated that treatment with TMPyP alone without white light irradiation (Fig.6.14A, (b)) led to significant decrease ($P < 0.05$) in viability of A549 cells suggesting its cytotoxic effect. As expected the exposure to white light further enhanced the cytotoxic effect of TMPyP (Fig.6.14A, (a)). Notably the cytotoxic effect of Captisol:TMPyP system on white light irradiation (Fig.6.14A, c) was significantly ($P < 0.05$) higher as compared to that of TMPyP (Fig.6.14A, (a)).

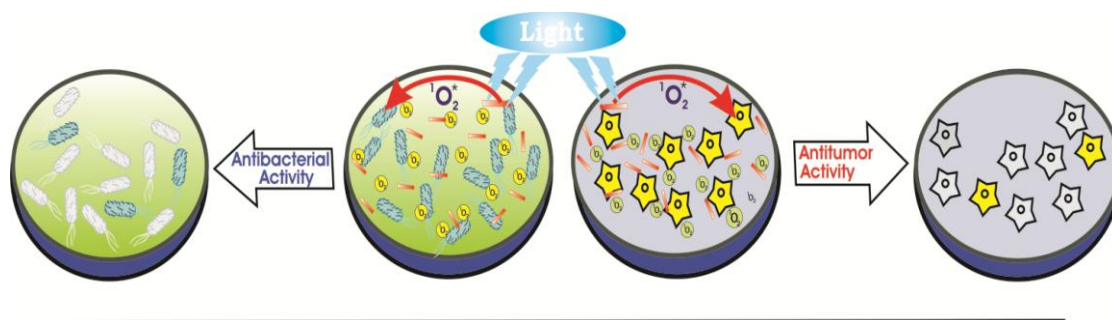


Figure 6.14: Pictorial representation of the singlet oxygen generation from the TMPyP complex and killing of *E. coli* bacteria and A549 cancerous cell lines.

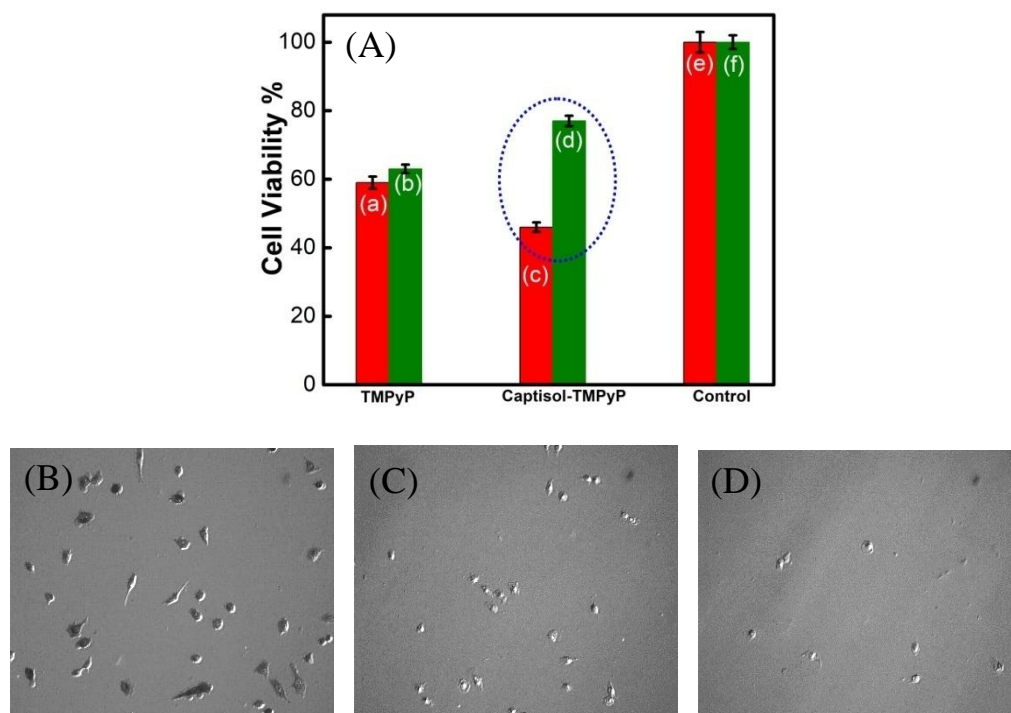


Figure 6.15: (A) Cell viability studies carried out in lung carcinoma A549 cell lines using MTT assay with the addition of respective TMPyP, Captisol:TMPyP and Control systems under white light irradiation (red bars, a, c, e) and in dark conditions (green bars b, d, f). The circled portion indicates the enhanced toxicity of Captisol:TMPyP complex in the A549 cancer cell lines under white light irradiation. (B-D) The phase contrast images of living lung carcinoma A549 cells in DMEM medium in the absence of any additive treated as control (B), in the presence of TMPyP (5 μ M) (C) and in the presence of Captisol (75 μ M):TMPyP (5 μ M) complex (D), after 30 minutes white light irradiation during MTT assay.

This confirmed the improvement in photosensitizing effect of TMPyP upon complexation with Captisol. These results were also supported by the bright field images showing reduction in the number as well as change in morphology of A549 cells treated with TMPyP or Captisol:TMPyP under white light irradiation as compared to control cells (see in Fig 6.14, B-D). Interestingly, as indicated in Fig.6.14A (c, d), it was seen that under the dark condition the cytotoxic effect of Captisol:TMPyP was significantly ($P < 0.05$) lower as compared to that of TMPyP alone in A549 cells. To further validate this result, the dark toxicity of TMPyP and

Captisol:TMPyP systems was also evaluated in normal epithelial (CHO) cells and the results were found to be in similar lines (Fig.6.15). Moreover, the cell viability data obtained with the captisol alone revealed no cytotoxicity with $\sim 75 \mu\text{M}$ of captisol, which is used in these studies. Similar non-toxic data were observed in our earlier study using insulin fibrils,²⁷ where we did not observe any cytotoxicity effect of captisol up to $\sim 250 \mu\text{M}$ using CHO cell lines.

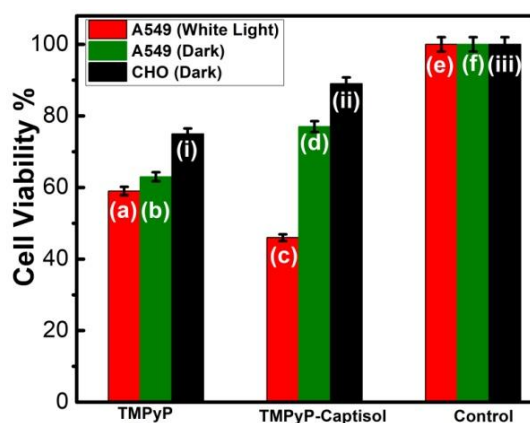


Figure 6.16: Cell viability studies carried out in lung carcinoma A549 cell lines (red and green bars) using MTT assay with the addition of respective TMPyP, Captisol:TMPyP and Control systems under white light irradiation (red bars, a, c, e) and in dark conditions (green bars b, d, f). The black bars (i, ii, iii) represent similar studies carried out in normal CHO cells under dark condition.

6.4 Conclusions

In summary, we have demonstrated the construction of a supramolecular assembly of TMPyP dye/drug with captisol macrocycle through host-guest interaction. The presence of several binding sites both on TMPyP as well as on captisol allows strong multiple host-guest interactions, building an extended supramolecular assembly containing TMPyP and is imaged as nanorods of $\sim 10 \mu\text{m}$ in length or more. Detailed spectroscopic and imaging measurements revealed that the Captisol:TMPyP assembly exhibits a number of advantageous features over the uncomplexed TMPyP dye,

namely, increased singlet state yield and lifetime, enhanced singlet oxygen yield, improved photostability and overall, much better photosensitizing effect. Utilizing these features in its biological stride, enhanced antibacterial activity towards *E. coli* and increased cytotoxicity towards lung carcinoma A549 cells on light illumination and reduced dark toxicity towards normal cells have been demonstrated. All these synergistic effects of supramolecular nanorod formation of Captisol:TMPyP complex are beneficial for improving the efficacy of photodynamic therapy for the treatment of cancer as well as proves it to be a good antibacterial agent.

Chapter 7

Conclusions and Future Perspectives

7.1 Summary

The main endeavor of this thesis is the demonstration of the construction of supramolecular assemblies by host-guest approach and to utilize them in wide range of practical applications. In this research work we constructed few such novel supramolecular assemblies of selective chromophoric dyes as guest molecules with specific macrocyclic hosts, which have been characterized by different spectroscopic and imaging methods such as UV-visible and fluorescence spectroscopy, circular dichroism (CD), atomic force microscopy (AFM), scanning electron microscopy (SEM), ^1H NMR spectroscopy and isothermal titration calorimetry (ITC). Structurally and functionally different types of chromophoric guest molecules such as acridine, rhodamines, thiazole orange, porphyrin and aromatic diimides have been employed against suitable macrocyclic hosts of distinct interaction sites in realizing their tunable/stimuli responsive applications. The thesis also presents their promising applications in drug delivery, photodynamic therapy, organic electronics, aqueous dye laser and fluorescence sensor, etc.^{31, 32} Two classes of macrocyclic hosts have been used, one, the Cucurbit[*n*]uril (CBn), which comprises of glycoluril units and the other one is β -cyclodextrin (βCD) and its derivative sulfobutylether- β -cyclodextrin ($\text{SBE}_7\beta\text{CD}$, commercially known as captisol).

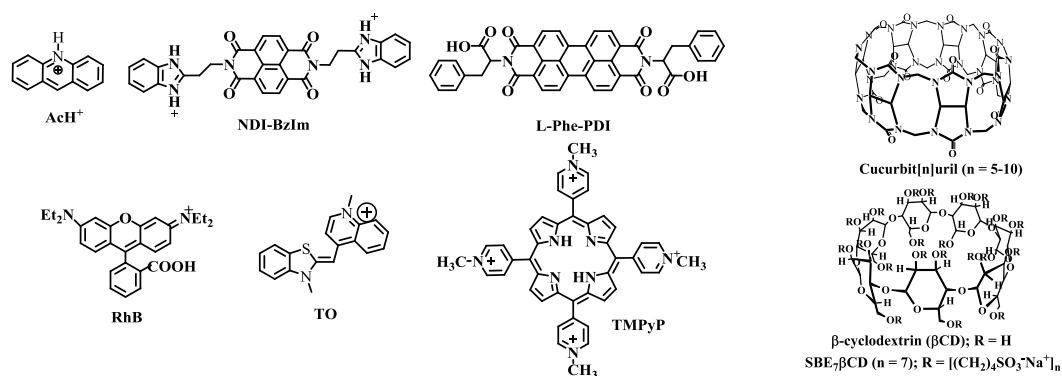


Figure 7.1: Chemical structures of guest dyes and macrocyclic hosts

After discussion the fundamentals of supramolecular chemistry of host-guest interactions, the types of noncovalent interactions, binding mechanism between the host and guest to form supramolecular assemblies, stoichiometry and their applications in different areas in chapter 1, we elaborated on the details of various experimental techniques and methods, used in the studies in chapter 2.

Chapter 3 discuss the noncovalent host-guest interactions of cationic (AcH^+) and neutral (Ac) forms of the acridine dye with the macrocyclic hosts such as cucurbit[7]uril (CB7) and cucurbit[8]uril (CB8) and explored the effect of cavity size on the photophysical properties and the protolytic equilibrium of acridine dye.³¹ The cationic form of acridine undergoes significant complexation with CB7 ($K_{\text{eq}} = 10^6 \text{ M}^{-1}$), causing a sharp decrease in the fluorescence intensity, whereas, the neutral Ac form of the dye undergoes weak complexation with CB7 ($K_{\text{eq}} = 10^3 \text{ M}^{-1}$) displaying significant distinction of order in binding affinity of the two forms with CB7. On the other hand, AcH^+ form shows strong emission quenching on interaction with CB8 by virtue of a 1:2 CB8: AcH^+ complex formation. The strong affinity of CB7 and CB8 to the protonated (AcH^+) form resulted in a large upward pK_{a} shift ($\Delta\text{pK}_{\text{a}} \sim 3.6$ units for CB7 and ~ 1.3 units for CB8) in the dye. Taking advantage of the above modulations in the fluorescence, pK_{a} and adamantylamine-induced fluorescence regeneration, controlled pK_{a} tuning and dye relocation from the CB7 cavity to cell lines have been established which find potential applications in drug delivery.

In chapter 4, in the first part we synthesized the N, N'-bis-2-(2-aminoethyl) benzimidazolyl naphthalenediimide (NDI-BzIm) derivative and investigated the host-guest interaction between NDI derivative and two cucurbituril hosts (CB7/CB8) by ground-state optical absorption and steady-state and isothermal titration calorimetric

studies. The studies demonstrated the formation of stable and emissive NDI radical anion of ethyl benzimidazole appended NDI derivative (NDI-BzIm) through contrasting encapsulation behavior of CB7 and CB8 under light irradiation in aqueous environment at ambient condition. The generation of emissive radical anion will broaden the scope of NDI radical anion chemistry for potential application in fluorescence spectroscopy and optoelectronic applications. In another study we synthesized N, N'-bis-(L/D)-phenylalanyl-PDI derivatives and demonstrated a metal-dye-metal constructed large and stable negative differential resistance (NDR) behavior at ambient conditions using a facile supramolecular strategy.³⁰ This is achieved through the encapsulation of the bay-substituted phenyl groups of aggregated (L/D)-Phe-PDI dyes by the β -CD macrocyclic host and the mechanistic aspects have been validated through detailed spectroscopic and imaging techniques. The large and reversible *I-V* characteristics displaying strong NDR behavior is attributed to the oxidation/reduction processes involving the rigid π rich monomeric PDI core and the system promising for organic electronics application.

In Chapter 5, the noncovalent chemistry involving aggregations/deaggregations of two fluorogenic dyes rhodamine (Rh) and thiazole orange (TO) by SBE₇ β CD has been discussed. In the first section, the results present the noncovalent interactions of two prominent laser dyes, namely, rhodamine 6G (Rh6G) and rhodamine B (RhB) with sulfobutylether- β -cyclodextrin (SBE₇ β CD).³² A combination of various photophysical parameters from Job plot, fluorescence lifetime/anisotropy measurements and the thermodynamic parameters from ITC measurements adjudicated a 1:1 stoichiometric complex formation between dyes and SBE₇ β CD host resulting enhanced fluorescence yield and brightness. These vital

parameters are utilized to demonstrate a cost-effective supramolecular broad-band as well as narrow-band aqueous dye laser systems with improved lasing efficiencies, better beam profile and enhanced durability as compared to the presently available non-aqueous dye lasers. On the other hand, in part-2 discuss the formation of a discrete molecular assembly of thiazole orange (TO) dyes at the portals of SBE7 β CD macrocycle leading to the evolution of a strong and distinct emission band from an aggregation of TO. The supramolecularly promoted emission enhancements of TO in its 1:4 (SBE7 β CD:TO) composition, characterized by absorption, fluorescence, circular dichroism, ITC and ^1H NMR measurements, was established to be selectively responsive to Tyramine as fluorescence on-off sensor among other biogenic amines/neurotransmitters with LOD as low as ~ 575 nM (79 ppb).²⁹ Further the emission features of the assembly with changes in temperature is found to be highly reproducible even after several temperature cycles and is promising to design optical supramolecular thermometer in the ambient temperature range.

Chapter 6 presents the studies on Porphyrins, especially the 5,10,15,20-tetrakis(4-*N*-methylpyridyl) porphyrin (TMPyP) as the availability of four cationic *N*-methylpyridyl groups favors multiple binding interactions with the captisol (sulfobutylether- β -cyclodextrin) host, building an extended supramolecular assembly of captisol and TMPyP. In addition to the spectroscopic characterizations for the assembly formation, the same has been pictured in SEM and FM images as nanorods of ~ 10 μm in length or more. Complexation of TMPyP has brought out beneficial features over the uncomplexed TMPyP dye; enhanced singlet oxygen yield, improved photostability and better photosensitizing effect, all supportive of efficient photodynamic therapy activity. The Captisol:TMPyP complex displayed enhanced

antibacterial activity towards *E. coli* under white light irradiation as compared to TMPyP alone. Cell viability studies performed in lung carcinoma A549 cells with light irradiation documented increased cytotoxicity of the complex towards the cancer cells whereas reduced dark toxicity is observed towards normal CHO cells.²⁸ All these synergistic effects of supramolecular nanorods of Captisol-TMPyP complex make the system an effective photosensitizer and a superior antibacterial and antitumor agent.

7.2 Future perspective

The essence of this thesis work evidently established various tunable/technological applications of noncovalent host-guest interactions and its control. Supramolecular tuning in the pK_a value using macrocyclic hosts and our studies with CHO cell lines rightly established a controlled relocation of acridine (the neutral form) into the cell lines by adamantylamine as the stimulant. In future, it would be appropriate to work on the complexes of active drug molecules of similar structural features incorporated in relevant cell lines to enhance the desired effect. The generation and stabilization of emissive NDI radical anion in presence of CB7 and CB8 hosts in aqueous medium may be useful in lifetime imaging studies which employ NDI based compounds for photodynamic therapy. The *metal-dye-metal* constructed intense and stable negative differential resistance (NDR) behavior at ambient conditions may fetch utility in developing controlled NDR effect in organic electronics and hence more studies on varied derivatization in improving the NDR feature may be taken up and the same may be studied for their photovoltaic activity as well. We also presented a methodology for achieving ultra-bright Rhodamines in water and its applicability has been proven in a practical laser system and several such laser dyes of different tuning region need to be examined in future, with different hosts as well. The claim of

selective *on-off* fluorescence sensor for the detection of tyramine is quite promising and expect its continued study for improving the LOD in a varied mixture of other amines and real biological samples. On the other hand, supramolecular assembly of TMPyP dye/drug with captisol macrocycle enhanced singlet oxygen yield, much better photosensitizing effect. Utilizing the improved features of TMPyP-captisol complex in its biological stride of A549 cells and *E. coli*, more studies are pending to ascertain its utility in a selective manner towards other pathogens and selective malignant cells.

REFERENCES:

- 1 J.-M. Lehn, 'Supramolecular Chemistry: Concepts and Perspectives', VCH Verlagsgesellschaft mbH D-69451, 1995.
- 2 J. W. Steed and J. L. Atwood, 'Supramolecular Chemistry', Wiley, 2009.
- 3 J. W. Steed and P. A. Gale, in 'Supramolecular Chemistry: From Molecules to Nanomaterials ', Chichester, UK, 2012.
- 4 K. Ariga and T. Kunitake, 'Supramolecular Chemistry - Fundamentals and Applications', Springer, 2006.
- 5 J. Mohanty, S. D. Choudhury, N. Barooah, H. Pal, and A. C. Bhasikuttan, *Reference Module in Chemistry, Molecular Sciences and Chemical Engineering*, 2014, 01.
- 6 A. K. Manna, *IJSR*, 2015, **4**, 892.
- 7 X. Ma and Y. Zhao, *Chem. Rev.*, 2015, **115**, 7794.
- 8 J.-M. Lehn, *Science*, 1985, **227**, 849.
- 9 J.-M. Lehn, *Science*, 1993, **260**, 1762.
- 10 J. W. Lee, S. Samal, N. Selvapalam, H.-J. Kim, and K. Kim, *Acc. Chem. Res.*, 2003, **36**, 621.
- 11 T. Loftsson, P. Jarho, M. Masson, and T. Jarvinen, *Expert Opin. Drug Deliv.*, 2005, **2**, 335.
- 12 M. J. Webber and R. Langer, *Chem. Soc. Rev.*, 2017, **46**, 6600.
- 13 X. Xiao, L. A. Nagahara, A. M. Rawlett, and N. Tao, *J. Am. Chem. Soc.*, 2005, **127**, 9235.
- 14 H.-J. Schneider, 'Applications of Supramolecular Chemistry for 21st Century Technology', Taylor & Francis, Boca Raton, FL, 2012.
- 15 A. J. Blacker, J. Jazwinski, J.-M. Lehn, M. Cesario, J. Guilhem, and C. Pascard, *Tetrahedron Lett.*, 1987, **28**, 6057.
- 16 J. W. Steed and J. L. Atwood, Wiley, 2009.
- 17 R. A. Bissell, E. Córdova, A. E. Kaifer, and J. F. Stoddart, *Nature*, 1994, **369**, 133.
- 18 S. P. Fletcher, F. Dumur, M. M. Pollard, and B. L. Feringa, *Science*, 2005, **310**, 80.
- 19 J. M. Lehn, in 'Supramolecular chemistry - scope and perspective Molecule - supramolecule - Molecular devices', ed. N. lecture, 1987.
- 20 A. C. Bhasikuttan, J. Mohanty, W. M. Nau, and H. Pal, *Angew. Chem. Int. Ed.*, 2007, **46**, 4120.
- 21 R. Wang, Y. L., and D. H. Macartney, *Chem. Commun.*, 2005, 5867.
- 22 W. M. Nau and J. Mohanty, *Int. J. Photoenergy*, 2005, **7**, 133.
- 23 M. J. Frampton and H. L. Anderson, *Angew. Chem. Int. Ed.*, 2007, **46**, 1028.
- 24 Y. H. Ko, E. Kim, I. Hwang, and K. Kim, *Chem. Commun.*, 2007, 1305.
- 25 J. Zhang, Q. Tang, Z.-Z. Gao, S.-C. Qiu, Y. Huang, and Z. Tao, *Chem. Eur.J.*, 2017, 10092.
- 26 N. Barooah, R. Khurana, A. C. Bhasikuttan, and J. Mohanty, *Isr. J. Chem.*, 2018, **58**, 276.
- 27 M. N. Shinde, R. Khurana, N. Barooah, A. C. Bhasikuttan, and J. Mohanty, *J. Phys. Chem. C.*, 2017, **121**, 20057.
- 28 R. Khurana, A. S. Kakatkar, S. Chatterjee, N. Barooah, A. Kunwar, A. C. Bhasikuttan, and J. Mohanty, *Front. Chem.*, 2019, **7**, 452.

- 29 R. Khurana, N. Barooah, A. C. Bhasikuttan, and J. Mohanty, *ChemPhysChem.*,
2019, DOI: **10.1002/cphc.201900656**.
- 30 R. Khurana, J. Mohanty, N. Padma, A. C. Bhasikuttan, and N. Barooah, *Chem.*
Eur. J., 2019 DOI: **10.1002/chem.201902641**.
- 31 R. Khurana, N. Barooah, A. C. Bhasikuttan, and J. Mohanty, *Org. Biomol.*
Chem., 2017, **15**, 8448.
- 32 R. Khurana, S. Agarwalla, G. Sridhar, N. Barooah, A. C. Bhasikuttan, and J.
Mohanty, *ChemPhysChem*, 2018, **19**, 2349.
- 33 M. Wiemann and P. Jonkheijm, *Isr. J. Chem.*, 2018, **58**, 314.
- 34 L. Shao, B. Hua, J. Sun, Q. Li, J. Yang, and G. Yu, *Tetrahedron Letts.*, 2017,
58, 1863.
- 35 I. Ghosh and W. M. Nau, *Adv. Drug Deliv. Rev.*, 2012, **64**, 764.
- 36 A. A. Karim, Q. Dou, Z. Li, and X. J. Loh., *Chem. Asian J.*, 2016, **11**, 1300.
- 37 X. Wu, Y.-M. Zhang, and Y. Liu., *RSC Adv.*, 2016, **6**, 99729.
- 38 N. Barooah, A. Kunwar, R. Khurana, A. C. Bhasikuttan, and J. Mohanty,
Chem. Asian J., 2017, **12**, 122.
- 39 E. Masson, X. Ling, R. Joseph, L. Kyeremeh-Mensah, and X. Lu, *RSC Adv.*,
2012, **2**, 1213.
- 40 R. N. Dsouza, U. Pischel, and W. M. Nau, *Chem. Rev.*, 2011, **111**, 7941.
- 41 J. W. Lee, S. Samal, N. Salvapalam, H.-J. Kim, and K. Kim, *Acc. Chem. Res.* ,
2003, **36**, 621.
- 42 A. C. Bhasikuttan, H. Pal, and J. Mohanty, *Chem. Commun.*, 2011, **47**, 9959.
- 43 J. Lagona, P. Mukhopadhyay, S. Chakrabarti, and L. Isaacs, *Angew. Chem. Int.*
Ed., 2005, **44**, 4844
- 44 C. Marquez, F. Huang, and W. M. Nau, *IEEE Trans. NanoBiosci.*, 2004, **3**, 39.
- 45 L. Isaacs, S-K. Park, S. Liu, Y. H. Ko, N. Selvapalam, Y. Kim, H. Kim, P. Y.
Zavalij, G-H. Kim, H-S. Lee and K. Kim, *J. Am. Chem. Soc.*, 2005, **127**,
18000.
- 46 J. Kim, I. S. Jung, S. Y. Kim, E. Lee, J. K. Kang, S. Sakamoto, K. Yamaguchi,
and K. Kim, *J. Am. Chem. Soc.*, 2000, **122**, 540.
- 47 K. I. Assaf and W. M. Nau, *Chem. Soc. Rev.*, 2015, **44**, 394.
- 48 X.-L. Ni, S. Chen, Y. Yang, and Z. Tao, *J. Am. Chem. Soc.*, 2016, **138**, 6177.
- 49 S. K. Samanta, J. Quigley, B. Vinciguerra, V. Briken, and L. Isaacs, *J. Am.*
Chem. Soc., 2017, **139**, 9066.
- 50 X.-J. Cheng, L.-L. Liang, K. Chen, N.-N. Ji, X. Xiao, J.-X. Zhang, Y.-Q.
Zhang, S.-F. Xue, Q.-J. Zhu, X.-L. Ni, and Z. Tao, *Angew. Chem., Int. Ed.*,
2013, **52**, 7252.
- 51 X. Fang, P. Kogerler, L. Isaacs, S. Uchida, and N. Mizuno, *J. Am. Chem. Soc.*,
2009, **131**, 432.
- 52 T. Goel, N. Barooah, M. B. Mallia, A. C. Bhasikuttan, and J. Mohanty, *Chem.*
Commun., 2016, **52**, 7306.
- 53 J. Mohanty, S. Dutta-Choudhury, H. P. Upadhyaya, A. C. Bhasikuttan, and H.
Pal, *Chem. Eur. J.*, 2009, **15**, 5215.
- 54 M. Sayed, F. Biedermann, V. D. Uzunova, K. I. Assaf, A. C. Bhasikuttan, H.
Pal, W. M. Nau, and J. Mohanty, *Chem. Eur. J.*, 2015, **21**, 691
- 55 M. Shaikh, S. Dutta-Choudhury, J. Mohanty, A. C. Bhasikuttan, and H. Pal,
Phys. Chem. Chem. Phys., 2010, **12**, 7050.

- 56 M. Shaikh, S. D. Choudhury, J. Mohanty, A. C. Bhasikuttan, and H. Pal, *Phys. Chem. Chem. Phys.*, 2010, **12**, 7050.
- 57 G. Hettiarachchi, D. Nguyen, J. Wu, D. Lucas, D. Ma, L. Isaacs, V. Briken, and P. One, *PLoS One*, 2010, **5**, e10514.
- 58 V. D. Uzunova, C. Cullinane, K. Brix, W. M. Nau, and A. I. Day, *Org. Biomol. Chem.*, 2010, **8**, 2037.
- 59 A. Villiers, *Comptes Rendus. Chimie*, 1891, **112**, 536.
- 60 D. Prochowicz, A. Kornowicz, J. L. ski, A. Kornowicz, and J. Lewiński, *Chem. Rev.*, 2017, **117**, 13461.
- 61 M. V. Rekharsky and Y. Inoue, *Chem. Rev.*, 1998, **98**, 1875.
- 62 M. K. Singh, H. Pal, A. S. R. Koti, and A. V. Sapre, *J. Phys. Chem. A*, 2004, **108**, 1465.
- 63 J. Mohanty, A. C. Bhasikuttan, W. M. Nau, and H. Pal, *J. Phys. Chem. B*, 2006, **110**, 5132.
- 64 N. Kandoth, S. D. Choudhury, J. Mohanty, and A. C. Bhasikuttan, *J. Phys. Chem. B* 2010, **114**, 2617.
- 65 B. V. K. J. Schmidt and C. Barner-Kowollik, *Angew. Chem. Int. Ed.*, 2017, **56**, 8350.
- 66 K. A. Connors, *Chem. Rev.*, 1997, **97**, 1325.
- 67 A. S. Jain, A. A. Date, R. R. S. Pissurlenkar, E. C. Coutinho, and M. S. Nagarsenker, *AAPS PharmSciTech*, 2011, **12**, 1163.
- 68 M. Kumar, V. Bhalla, A. Dhir, and J. N. Babu, *Dalton Trans.*, 2010, **39**, 10116.
- 69 J. Mohanty, N. Thakur, S. Dutta-Choudhury, N. Barooah, H. Pal, and A. C. Bhasikuttan, *J. Phys. Chem. B*, 2012, **116**, 130.
- 70 U. Pischel, V. D. Uzunova, P. Remóna, and W. M. Nau, *Chem. Commun.*, 2010, **46**, 2635.
- 71 J. Mohanty and W. M. Nau, *Angew. Chem. Int. Ed.*, 2005, **44**, 3750.
- 72 N. Barooah, B. C. Pemberton, and J. Sivaguru, *Org. Lett.*, 2008, **10**, 3339.
- 73 J. Zhou, G. Yu, and F. Huang, *Chem. Soc. Rev.*, 2017, **46**, 7021.
- 74 W. M. Nau, G. Ghale, A. Hennig, H. Bakirci, and D. M. Bailey, *J. Am. Chem. Soc.*, 2009, **131**, 11558.
- 75 S. Dutta-Choudhury, J. Mohanty, H. Pal, and A. C. Bhasikuttan, *J. Am. Chem. Soc.*, 2010, **132**, 1395.
- 76 M. R. Dreher, A. J. Simnick, K. Fischer, R. J. Smith, A. Patel, M. Schmidt, and A. Chilkoti, *J. Am. Chem. Soc.*, 2008, **130**, 2687.
- 77 J. Mohanty and W. M. Nau, *Angew. Chem. Int. Ed.*, 2005, **44**, 3750.
- 78 S. Liu, C. Ruspice, P. Mukhopadhyay, S. Chakrabarti, P. Y. Zavalij, and L. Isaacs, *J. Am. Chem. Soc.*, 2005, **127**, 15959.
- 79 N. Barooah, A. C. Bhasikuttan, V. Sudarsan, S. Dutta-Choudhury, H. Pal, and J. Mohanty, *Chem. Commun.*, 2011, **47**, 9182.
- 80 A. C. Bhasikuttan, S. Dutta-Choudhury, H. Pal, and J. Mohanty, *Isr. J. Chem.*, 2011, **51**, 634.
- 81 W. M. Nau and X. Zhang, *J. Am. Chem. Soc.*, 1999, **121**, 8022.
- 82 J. Mohanty, R. Khurana, N. Barooah, and A. C. Bhasikuttan, *J. Indian Chem. Soc.*, 2018, **95**, 533.
- 83 H.-J. Schneider, F. Hackett, and V. Rüdiger, *Chem. Rev.*, 1998, **98**, 1755.
- 84 N. Barooah, R. Khurana, A. C. Bhasikuttan, and J. Mohanty, *Chem. Select.*, 2017, **2**, 7387.

- 85 A. Gilbert, J. Baggott, and P. J. Wagner, 'Essential of Molecular
Photochemistry', Blackwell science Inc., 1991.
- 86 J. R. Lakowicz, 'Principles of Fluorescence Spectroscopy', Springer, 2006.
- 87 Rohatgi-Mukherjee, 'K. K. Fundamentals of Photochemistry', Wiley Eastern
Ltd: India, 1986.
- 88 N. J. Turro, V. Ramamurthy, and J. C. Scaiano, 'Principles of molecular
photochemistry', University Science Books, 2015.
- 89 C. Schalley, 'Analytical Methods in Supramolecular Chemistry', Wiley-VCH
Verlag GmbH & Co 2007.
- 90 J. N. Demas, 'Excited state lifetime measurement', Academic press, 1983.
- 91 T. S. Wiseman, S. Williston, J. F. Brandts, and L. N. Lin, *Anal. Biochem.*,
1989, **179**, 131.
- 92 J. Mohanty, K. Jagtap, A. K. Ray, W. M. Nau, and H. Pal, *ChemPhysChem*,
2010, **11**, 3333
- 93 J. Mohanty, H. Pal, A. K. Ray, S. Kumar, and W. M. Nau, *ChemPhysChem*,
2007, **8**, 54.
- 94 A. C. Bhasikuttan, H. Pal, and J. Mohanty, *Chem. Commun.*, 2011, **47**, 9959.
- 95 L. Chen, H. Bai, J.-F. Xu, S. Wang, and X. Zhang, *ACS Appl. Mater.
Interfaces* 2017, **9**, 13950.
- 96 H. S. El-Sheshtawy, S. Chatterjee, K. I. Assaf, M. N. Shinde, W. M. Nau, and
J. Mohanty, *Scientific Reports*, 2018, **8**, 13925.
- 97 J. B. Birks, 'Photo Physics of Aromatic Molecules', Wiley-Interscience: New
York, 1970.
- 98 R. N. Dsouza, U. Pischel, and W. M. Nau, *Chem. Rev.*, 2011, **111**, 7941
- 99 P. R. Bevington, 'Data Reduction and Error Analysis for the Physical Sciences',
McGraw-Hill, 1969.
- 100 D. V. O'Connor and D. Phillips, 'Time Correlated Single Photon Counting',
Academic Press, 1984.
- 101 W. R. Ware, 'Creation and detection of the Excited State', Lamola, A. A.,
Marcel Dekker, 1971.
- 102 M. Ito, H. Kume, and K. Oba, *IEEE Trans. Nucl. Sci.*, 1984, **NS-31**, 408.
- 103 W. Becker, 'Advanced Time Correlated Single Photon Counting Technique',
Springer, 2005.
- 104 W. R. Ware, in 'Creation and detection of the Excited State', ed. A. A. Lamola,
New York, 1971.
- 105 N. Berova, K. Nakanishi, and R. W. Woody, 'Circular Dichroism. Principles
and Applications', John Wiley & Sons, Inc., 2000.
- 106 I. Wadso, *Chem. Soc. Rev.*, 1997, 79.
- 107 J. Gershberg, M. R. Stojkovic', M. S. kugor, S. Tomic', T. H. Rehm, S. Rehm,
C. R. Saha-McJler, I. Piantanida, and F. Wurthner, *Chem. Eur. J.*, 2015, **21**,
7886
- 108 J. Mohanty, A. C. Bhasikuttan, W. M. Nau, and H. Pal, *J. Phys. Chem. B*, 2006,
110, 5132.
- 109 M. Shaikh, J. Mohanty, P. K. Singh, W. M. Nau, and H. Pal, *Photochem.
Photobiol. Sci.*, 2008, **7**, 408.
- 110 A. Jadhav, V. S. Kalyani, N. Barooah, D. D. Malkhede, and J. Mohanty,
ChemPhysChem, 2015, **16**, 420.

- 111 S. M. Pradeepa, H. S. B. Naik, B. V. Kumar, K. I. Priyadarsini, A. Barik, and
 112 T. R. R. Naik, *Spectrochim. Acta, Part A*, 2013, **101**, 132.
- 113 A. A. Abdel-Shafi, P. D. Beer, R. J. Mortimer, and F. Wilkinson, *J. Phys.*
 114 *Chem. A*, 2000, **104**, 192.
- 115 M. Kumar, V. Bhalla, A. Dhir, and J. N. Babu, *Dalton Trans.*, 2010, **39**, 10116.
- 116 J. Mohanty, A. C. Bhasikuttan, S. Dutta Choudhury, and H. Pal, *J. Phys. Chem.*
 117 *B (Letts.)*, 2008, **112**, 10782.
- 118 M. Sayed, F. Biedermann, V. D. Uzunova, K. I. Assaf, A. C. Bhasikuttan, H.
 119 Pal, W. M. Nau, and J. Mohanty, *Chem. Eur. J.*, 2015, **21**, 691.
- 120 W. M. Nau, G. Ghale, A. Hennig, H. Bakirci, and D. M. Bailey, *J. Am. Chem.*
 121 *Soc.*, 2009, **131**, 11558.
- 122 M. R. Dreher, A. J. Simnich, K. Fisher, R. J. Smith, A. Patel, M. Schmidt, and
 123 A. Chilkoti, *J. Am. Chem. Soc.*, 2008, **130**, 687.
- 124 M. N. Shinde, N. Barooah, A. C. Bhasikuttan, and J. Mohanty, *Chem.*
 125 *Commun.*, 2016, **52**, 2992.
- 126 A. C. Bhasikuttan and J. Mohanty, *Chem. Commun.*, 2017, **53**, 2789.
- 127 M. J. Webber and R. Langer, *Chem. Soc. Rev.*, 2017, **46**, 6600.
- 128 M.-J. Ji, J.-G. Kim, and U. S. Shin, *Bull. Korean Chem. Soc.*, 2012, **33**, 2489.
- 129 P. Belmont, J. Bosson, T. Godet, and M. Tiano, *Anticancer Agents Med.*
 130 *Chem.*, 2007, **7**, 139.
- 131 O. Sedláček, M. Hruby, M. Studenovsky, D. Vetvicka, J. Svoboda, D.
 132 Kanková, J. Kovár, and K. Ulbrich, *Bioorg. Med. Chem.*, 2012, **20**, 4056.
- 133 P. Proks, T. Hianik, and P. Kvasnicka, *Gen. Physiol. Biophys.*, 1992, **11**, 441.
- 134 R. Woods and L. J. C. Love, *Spectrochim. Acta*, 1984, **40A**, 643.
- 135 J. M. Schuette, T. Ndou, A. M. Pena, K. L. Greene, C. K. Williamson, and I.
 136 M. Warner, *J. Phys. Chem.*, 1991, **95**, 4897.
- 137 T. Pedzinski, B. Marciniak, and G. L. Hugb, *J. Photochem. Photobiol. A*, 2002,
150, 21.
- 138 M. Shaikh, Y. M. Swamy, and H. Pal, *J. Photochem. Photobiol. A*, 2013, **258**,
 139 41.
- 140 N. Barooah, J. Mohanty, H. Pal, and A. C. Bhasikuttan, *J. Phys. Chem. B*,
 141 2012, **116**, 3683–3689.
- 142 B. D. Wagner, in 'Fluorescence Studies of Supramolecular Host-Guest
 143 Inclusion Complexes', ed. H. S. Nalwa, Stevenson Ranch, CA, 2003.
- 144 S. Dutta Choudhury, J. Mohanty, H. P. Upadhyaya, A. C. Bhasikuttan, and H.
 145 Pal, *J. Phys. Chem. B*, 2009, **113**, 1891.
- 146 K. Kasama, K. Klkuchl, S. Yamamoto, K. UjI-le, Y. Nlshlda, and H. Kokubun,
 147 *J. Phys. Chem.*, 1981, **85**, 1291.
- 148 N. Barooah, J. Mohanty, and A. C. Bhasikuttan, *Chem. Commun.*, 2015, **51**,
 149 13225.
- 150 M. Shaikh, S. Dutta-Choudhury, J. Mohanty, A. C. Bhasikuttan, W. M. Nau,
 151 and H. Pal, *Chem. Eur. J.*, 2009, **15**, 12362
- 152 N. Barooah, J. Mohanty, and A. C. Bhasikuttan, *J. Phys. Chem. B*, 2013, **117**
 153 13595–13603.
- 154 N. Barooah, M. Sundararajan, J. Mohanty, and A. C. Bhasikuttan, *J. Phys.*
 155 *Chem. B*, 2014, **118**, 7136.
- 156 M. J. Frisch, 'GAUSSIAN 92, Revision E.1, Gaussian Inc.' 1992.

- 138 S. Gadde, E. K. Batchelor, J. P. Weiss, Y. Ling, and A. E. Kaifer, *J. Am. Chem.*
Soc., 2008, **130**, 17114.
- 139 M. Shaikh, J. Mohanty, A. C. Bhasikuttan, V. D. Uzunova, W. M. Nau, and H.
 Pal, *Chem. Commun.*, 2008, 3681.
- 140 W. Herbst and K. Hunger, 'Industrial Organic Pigments: Production, Properties,
 Applications', WILEY-VCH, Weinheim, 1997.
- 141 F. Wurthmer, in 'Top. Curr. Chem.' 2005.
- 142 F. Würthner and M. Stolte, *Chem. Commun.*, 2011, **47**, 5109–5115.
- 143 Z. Liu, G. Zhang, Z. Cai, X. Chen, H. Luo, Y. Li, J. Wang, and D. Zhang, *Adv.*
Mater., 2014, **26**, 6965–697.
- 144 T. Weil, T. Vosch, J. Hofkens, K. Peneva, and K. Müllen, *Angew. Chem. Int.*
Ed., 2010, **49**, 9068–9093.
- 145 C.-C. You and F. Würthner, *J. Am. Chem. Soc.*, 2003, **125**, 9716.
- 146 F. N. Castellano, *Dalton Trans.*, 2012, **41**, 8493–8501.
- 147 V. Kunz, V. Stepanenko, and F. Würthner, *Chem. Commun.*, 2015, **51**, 290.
- 148 D. Gohl, X. Zhang, and F. Würthner, *Angew. Chem. Int. Ed.*, 2012, **51**, 6328.
- 149 X. Ai, Y. Chen, Y. Feng, and F. Li, *Angew. Chem. Int. Ed.*, 2018, **130**, 2319.
- 150 Y. Gao, A. Obolda, M. Zhang, and F. Li, *Dyes and Pigments*, 2017, **139**, 644.
- 151 Q. Peng, A. Obolda, M. Zhang, and F. Li, *Angew. Chem. Int. Ed.*, 2015, **54**,
 7091.
- 152 A. Obolda, X. Ai, M. Zhang, and F. Li, *ACS Appl. Mater. Interfaces* 2016, **8**,
 35472.
- 153 M. A. Kobaisi, S. V. Bhosale, K. Latham, A. M. Raynor, and S. V. Bhosale,
Chem. Rev., 2016, **116**, 11685.
- 154 Y. Jiao, K. Liu, G. Wang, Y. Wang, and X. Zhang, *Chem. Sci.*, 2015, **6**, 3975.
- 155 G. Belanger-Chabot, A. Ali, and F. P. Gabbaï, *Angew. Chem. Int. Ed.*, 2017,
56.
- 156 V. V. Roznyatovskiy, D. M. Gardner, S. W. Eaton, and M. R. Wasielewski,
Org. Lett., 2014, **16**, 696.
- 157 S. V. Bhosale, C. H. Janiab, and S. J. Langford, *Chem. Soc. Rev.*, 2008, **37**,
 331.
- 158 S. Guha, F. S. Goodson, L. J. Corson, and S. Saha, *J. Am. Chem. Soc.*, 2012,
134, 13679.
- 159 A. M. Sanders, T. J. Magnanelli, A. E. Bragg, and J. D. Tovar, *J. Am. Chem.*
Soc., 2015.
- 160 Y. Matsunaga, K. Goto, K. Kubono, K. Sako, and T. Shinmyozu, *Chem. Eur.*
J., 2014, **20**, 1.
- 161 M. R. Molla and S. Ghosh, *Chem. Eur. J.*, 2012.
- 162 A. Lorente, M. Fernández-Saiza, J.-M. Lehn, and J.-P. Vigneron, *Tetrahedron Lett.*, 1995, 8279.
- 163 H. Shao, T. Nguyen, N. C. Romano, D. A. Modarelli, and J. R. Parquette, *J.*
Am. Chem. Soc., 2009, **131**, 16374.
- 164 M. Tomasulo, D. M. Naistat, A. J. P. White, D. J. Williams, and F. M.
 Raymo, *Tetrahedron Letters*, 2005, **46**, 5695.
- 165 Q. Song, F. Li, Z. Wang, and X. Zhang, *Chem. Sci.*, 2015, **6**, 3342.
- 166 X. Zhao, F. Liu, Z. Zhao, H. Karoui, D. Bardelang, O. Ouari, and S. Liu, *Org.*
Biomol. Chem., 2018, **16**, 3809.

- 167 S. Guha, F. S. Goodson, S. Roy, L. J. Corson, C. A. Gravenmier, and S. Saha,
168 *J. Am. Chem. Soc.*, 2011, **133**, 15256.
- 169 I. M. F. Doria, V. Grande, S. Monti, M. Freccero, *J. Org. Chem.*, 2013, **78**,
8265.
- 170 H. E. Katz, A. J. Lovinger, J. Johnson, C. Kloc, T. Siegrist, W. Li, Y.-Y. Lin,
and A. Dodabalapur, *NATURE*, 2000, **404**.
- 171 S. A. Boera, R. P. Cox, M. J. Beards, H. Wang, W. A. Donald, T. D. M. Bell,
and D. R. Turner, *Chem. Commun.*, 2019, **55**, 663.
- 172 P. Ganesan, J. Baggerman, H. Zhang, E. J. R. Sudholter, and H. Zuilhof, *J.*
Phys. Chem. A, 2007, **111**, 6154.
- 173 S. Kimura, T. Kusamoto, S. Kimura, K. Kato, Y. Teki, and H. Nishihara,
Angew. Chem. Int. Ed., 2018, **130**, 12893.
- 174 J. E. Rogers, S. J. Weiss, and L. A. Kelly, *J. Am. Chem. Soc.*, 2000, **122**, 427.
- 175 C. Huang, S. Barlow, and S. R. Marder, *J. Org. Chem.*, 2011, **76**, 2386.
- 176 E. R. Draper, L. J. Archibald, M. C. Nolan, R. Schweins, M. A. Zwijnenburg,
S. Sproules, and D. J. Adams, *Chem. Eur. J.*, 2018, **24**, 4006
- 177 J. M. Lim, P. Kim, M.-C. Yoon, J. Sung, V. Dehm, Z. Chen, F. Wurthner, and
D. Kim, *Chem. Sci.*, 2013, **4**, 388.
- 178 M. C. Nolan, J. J. Walsh, L. L. E. Mears, E. R. Draper, M. Wallace, M.
Barrow, B. Dietrich, S. M. King, A. J. Cowan, and D. J. Adams, *J. Mater.*
Chem. A, 2017, **5**, 7555.
- 179 P. Chal, A. Shit, and A. K. Nandi, *J. Mater. Chem. A*, 2016, **4**, 16108.
- 180 E. R. Draper, J. J. Walsh, T. O. McDonald, M. A. Zwijnenburg, P. J. Cameron,
A. J. Cowan, and D. J. Adams, *J. Mater. Chem. C*, 2014, **2**, 5570.
- 181 W. Jiang, Y. Li, and Z. Wang, *Acc. Chem. Res.*, 2014, **47**, 3135–3147.
- 182 S. Tatemichi, M. Ichikawa, T. Koyama, and Y. Taniguchi, *Appl.*
Phys. Lett., 2006, **89**, 112108.
- 183 M. G. Debije and P. P. C. Verbunt, *Adv. Energy Mater.*, 2012, **2**, 12–35.
- 184 K. Y. Law, *Chem. Rev.*, 1993, **93**, 449–486.
- 185 B. Pramanik, J. H. Mondal, N. Singha, S. Ahmed, J. Mohanty, and D. Das,
ChemPhysChem, 2017, **18**, 245.
- 186 J. H. Mondal, B. Pramanik, M. N. Shinde, R. Khurana, N. Barooah, A. C.
Bhasikuttan, D. Das, and J. Mohanty, *J. Phys. Chem. C* 2018, **122**,
18061–18069.
- 187 R. Gvishi and R. Reisfeld, *Chem. Phys. Lett.*, 1993, **213**, 338
- 188 Y. Zang, C.-Z. Li, C.-C. Chueh, S. T. Williams, W. Jiang, Z.-H. Wang, J.-S.
Yu, and A. K. Y. Jen, *Adv. Mater.*, 2014, **26**, 5708–5714.
- 189 Y. Zhong, M. T. Trinh, R. Chen, W. Wang, P. P. Khlyabich, B. Kumar, Q. Xu,
C.-Y. Nam, M. Y. Sfeir, C. Black, M. L. Steigerwald, Y.-L. Loo, S. Xiao, F.
Ng, X. Y. Zhu, and C. Nuckolls, *J. Am. Chem. Soc.*, 2014, **136**, 15215–15221.
- 190 A. Sharenko, C. M. Proctor, T. S. v. d. Poll, Z. B. Henson, T.-Q. Nguyen, and
G. C. Bazan, *Adv. Mater.*, 2013, **25**, 4403–4406.
- 191 K. D. Belfield, M. V. Bondar, F. E. Hernandez, and O. V. Przhonska, *J. Phys.*
Chem. C, 2008, **112**, 5618–5622.
- 192 J. Gao, C. Xiao, W. Jiang, and Z. Wang, *Org. Lett.*, 2014, **16**, 394–397.
- S. Rehm, V. Stepanenko, X. Zhang, T. H. Rehm, and F. Wurthner, *Chem. Eur.*
J., 2010, **16**, 3372.

- 193 T. Heek, C. Fasting, C. Rest, X. Zhang, F. Wurthner, and R. Haag, *Chem*
 194 *Commun.*, 2010, **46**, 1884.
- 195 B. Gao, H. Li, H. Liu, L. Zhang, Q. Bai, and X. Ba, *Chem. Commun.*, 2011, **47**,
 3894.
- 196 F. Biedermann, E. Elmalem, I. Ghosh, W. M. Nau, and O. A. Scherman,
Angew. Chem. Int. Ed., 2012, **51**, 7739
- 197 I. Kratochvilova, M. Kocirik, A. Zambova, J. Mbindyo, T. E. Mallouk, and T.
 S. Mayer, *J. Mater. Chem.*, 2002, **12**, 2927.
- 198 Q. Tang, H. K. Moon, Y. Lee, S. M. Yoon, H. J. Song, H. Lim, and H. C. Choi,
J. Am. Chem. Soc., 2007, **129**, 11018.
- 199 R. A. Wassel, G. M. Credo, R. R. Fuierer, D. L. Feldheim, and C. B. Gorman,
J. Am. Chem. Soc., 2004, **126**, 295.
- 200 R. A. Kiehl, J. D. Le, P. Candra, R. C. Hoye, and T. R. Hoye, *Appl. Phys. Lett.*,
 2006, **88**, 172102.
- 201 B. V. K. J. Schmidt and C. Barner-Kowollik, *Angew. Chem. Int. Ed.*, 2017, **56**,
 8350.
- 202 W. E. Ford, *J. Photochem.*, 1987, **37**, 189
- 203 Z. Chen, B. Fimmel, and F. Wurthner, *Org. Biomol. Chem.*, 2012, **10**, 5845.
- 204 C. D. Schmidt, C. Böttcher, and A. Hirsch, *Eur. J. Org. Chem.*, 2007, 5497.
- 205 J. Seibt, V. Dehm, F. Würthner, and V. Engel, *J. Chem. Phys.*, 2008, **128**,
 204303.
- 206 M. Ghosh, S. C. Gadkari, and S. K. Gupta, *J. Appl. Phys.*, 2012, **112**, 024314.
- 207 M. Ghosh, R. S. Ningthoujam, R. K. Vatsa, D. Das, V. Nataraju, S. C. Gadkari,
 S. K. Gupta, and D. Bahadur, *J. Appl. Phys.*, 2011, **110**, 054309.
- 208 J. Chen, W. Wang, M. A. Reed, A. M. Rawlett, D. W. Price, and J. M. Tour,
Appl. Phys. Lett., 2000, **77**, 1224.
- 209 Q. Tang, H. K. Moon, Y. Lee, S. M. Yoon, H. J. Song, H. Lim, and H. C. Choi,
J. Am. Chem. Soc., 2007, **129**, 11018.
- 210 R. Waser, R. Dittmann, G. Staikov, and K. Szot, *Adv. Mater.*, 2009, **21**, 2632.
- 211 H.-K. Lee and M. H.-C. Jin, *Appl. Phys. Lett.*, 2010, **97**, 013306.
- 212 J. Paloheimo, H. Isotalo, J. Kastner, and H. Kuzmany, *Synth. Met.*, 1993, **55-57**,
 3185.
- 213 R. C. Haddon, A. S. Perel, R. C. Morris, T. T. M. Palstra, A. F. Hebard, and R.
 M. Fleming, *Appl. Phys. Lett.*, 1995, **67**, 121.
- 214 J.-M. Lehn, *Science*, 1985, **227**, 849.
- 215 K. Kim, N. Selvapalam, Y. H. Ko, K. M. Park, D. Kim, and J. Kim, *Chem. Soc.*
Rev., 2007, **36**, 267.
- 216 U. Pischel, V. D. Uzunova, P. Remon, and W. M. Nau, *Chem. Commun.*, 2010,
46 2635.
- 217 J. Mohanty and W. M. Nau, *Angew. Chem. Int. Ed.*, 2005, **44**, 3750.
- 218 S. Dutta-Choudhury, J. Mohanty, H. Pal, and A. C. Bhasikuttan, *J. Am. Chem.*
Soc., 2010, **132**, 1395.
- 219 S. Gadde, E. K. Batchelor, J. P. Weiss, Y. Ling, and A. E. Kaifer, *J. Am. Chem.*
Soc., 2008, **130**, 17114.
- 220 O. Valdes-Aguilera and D. C. Neckers, *Acc. Chem. Res.*, 1989, **22**, 171.
- J. Mohanty, K. Jagtap, A. K. Ray, W. M. Nau, and H. Pal, *ChemPhysChem*,
 2010, **11**, 3333.

- 221 K. H. Drexhage, T. W. Hansch, E. P. Ippen, F. P. Schafer, C. V. Shank, and B.
 222 B. Snively, 'Dye Lasers', ed. F. P. Schafer, Springer-Verlag, 1973.
- 223 C. Eggeling, J. Widengren, R. Rigler, and C. A. M. Seidel, *Anal. Chem.*, 1998,
 224 **70**, 2651.
- 225 P. S. Dittrich and P. Schwille, *Appl. Phys. B*, 2001, **73**, 829.
- 226 J. Slavik, 'Fluorescent probes in cellular and molecular biology', CRC Press,
 1994.
- 227 M. K. Gofar, K. Moradi, and N. M. Kor, *Euro. J. Exp. Bio.*, 2014, **4**, 72.
- 228 I. Garcia-Moreno, A. Costela, M. Pintado-Sierra, V. Martin, and R. Sastre, *J.*
 229 *Phys. Chem. B* 2009, **113**, 10611.
- 230 A. S. Jain, A. A. Date, R. R. S. Pissurlenkar, E. C. Coutinho, and M. S.
 231 Nagarsenker, *AAPS PharmSciTech*, 2011, **12**, 1163.
- 232 T. Loftsson and M. E. Brewster, *J. Pharm. Sci.*, 1996, **85**, 1017.
- 233 M. N. Shinde, A. C. Bhasikuttan, and J. Mohanty, *ChemPhysChem*, 2015, **16**,
 234 3425
- 235 M. N. Shinde, A. C. Bhasikuttana, and J. Mohanty, *Supramol. Chem.*, 2016, **28**,
 236 517.
- 237 M. N. Shinde, R. Khurana, N. Barooah, A. C. Bhasikuttan, and J. Mohanty,
 238 *Org. Biomol. Chem.*, 2017, **15** 3975.
- 239 B. Valeur, in 'Molecular Fluorescence Principles and Applications', 2002.
- 240 J. Mei, N. L. C. Leung, R. T. K. Kwok, J. W. Y. Lam, and B. Z. Tang, *Chem.*
 241 *Rev.*, 2015, **115**, 11718–11940
- 242 Z. He, C. Ke, and B. Z. Tang, *ACS Omega*, 2018, **3**, 3267.
- 243 J. Luo, Z. Xie, J. W. Y. Lam, L. Cheng, B. Z. Tang, H. Chen, C. Qiu, H. S.
 244 Kwok, X. Zhan, and Y. Liu, *Chem. Commun.*, 2001, 1740–1741.
- 245 M.-T. Lee, C.-H. Liao, C.-H. Tsai, and C. H. Chen, *Adv. Mater.*, 2005, **17**,
 246 2493–2497.
- 247 J. Huang, N. Sun, Y. Dong, R. Tang, P. Lu, P. Cai, Q. Li, D. Ma, J. Qin, and Z.
 248 Li, *Adv. Funct. Mater.*, 2013, **23**, 2329–2337.
- 249 J. Huang, N. Sun, P. Chen, R. Tang, Q. Li, D. Ma, and Z. Li, *Chem. Commun.*,
 250 2014, **50**, 2136–2138.
- 251 F. Hu, Y. Huang, G. Zhang, R. Zhao, and D. Zhang, *Tetrahedron Lett.*, 2014,
 252 **55**, 1471–1474.
- 253 Y. Yuan, R. T. K. Kwok, G. Feng, J. Liang, J. Geng, B. Z. Tang, and B. Liu,
 254 *Chem. Commun.*, 2014, **50**, 295–297.
- 255 L. Hu, Y. Duan, Z. Xu, J. Yuan, Y. Dong, and T. Han, *J.Mater.Chem.C* 2016,
 256 **4**, 5334.
- 257 S. Dutta-Choudhury, A. C. Bhasikuttan, H. Pal, and J. Mohanty, *Langmuir*,
 258 2011, **27**, 12312.
- 259 G. L. Silva, V. Ediz, D. Yaron, and B. A. Armitage, *J. Am. Chem. Soc.*, 2007,
 260 **129**, 5710.
- 261 V. Karunakaran, J. L. P. Lustres, L. Zhao, N. P. Ernsting, and O. Seitz, *J. Am.*
 262 *Chem. Soc.*, 2006, **128**, 2954.
- 263 I. Lubitz, D. Zikich, and A. Kotlyar, *Biochemistry* 2010, **49**, 3567.
- 264 J. Nygren, N. Svanvik, and M. Kubista, *Biopolymers*, 1998, **46**, 39.
- 265 V. Lau and B. Heyne, *Chem Commun.*, 2010, **46**, 3595.
- 266 M. N. Shinde, S. Dutta-Choudhury, N. Barooah, H. Pal, A. C. Bhasikuttan, and
 267 J. Mohanty, *J. Phys. Chem. B*, 2015, **119**, 3815.

- 249 J. Mohanty, N. Thakur, S. Dutta Choudhury, N. Barooah, H. Pal, and A. C.
Bhasikuttan, *J. Phys. Chem. B*, 2012, **116**, 130.
- 250 M. J. Alkema, M. Hunter-Ensor, N. Ringstad, and H. R. Horvitz, *Neuron* 2005,
251 **46**, 247.
- 252 M. Jing, P. Zhang, G. Wang, J. Feng, L. Mesik, J. Zeng, H. Jiang, S. Wang, J.
C. Looby, N. A. Guagliardo, L. W. Langma, J. Lu, Y. Zuo, D. A. Talmage, L.
W. Role, P. Q. Barrett, L. I. Zhang, M. Luo, Y. Song, J. J. Zhu, and Y. Li, *Nat*
Biotechnol., 2018, **36**, 726.
- 253 F. Sun, J. Zeng, M. Jing, J. Zhou, J. Feng, S. F. Owen, Y. Luo, F. Li, H. Wang,
T. Yamaguchi, Z. Yong, Y. Gao, W. Peng, L. Wang, S. Zhang, J. Du, D. Lin,
M. Xu, A. C. Kreitzer, G. Cui, and Y. Li, *Cell*, 2018, **174**, 481.
- 254 J. S. Marvin, B. G. Borghuis, L. Tian, J. Cichon, M. T. Harnett, J. Akerboom,
A. Gordus, S. L. Renninger, T. W. Chen, C. I. Bargmann, M. B. Orger, E. R.
Schreiter, J. B. Demb, W. B. Gan, S. A. Hires, and L. L. Looger, *Nat. Methods*,
2013, **10**, 162.
- 255 J. Nygren, J. M. Andrade, and M. Kubista, *Anal. Chem.*, 1996, **68**, 1706.
- 256 J. Mohanty, A. C. Bhasikuttan, W. M. Nau, and H. Pal, *J. Phys. Chem. B*, 2006,
257 **110**, 5132.
- 258 J. Seibt, V. Dehm, F. Würthner, and V. Engel, *J. Chem. Phys.*, 2008, **128**,
204303.
- 259 Y. Guo, Y. Gong, Y. Gao, J. Xiao, T. Wang, and L. Yu, *Langmuir*, 2016, **32**,
9293.
- 260 P. Pearl, T. Hartka, and J. Taylor, *Current Treatment Options in Neurology*,
2006, **8**, 441.
- 261 S. Bodmer, C. Imark, and M. Kneubühl, *Inflamm. Res.*, 1999, **48**, 296.
- 262 B. J. McCabe-Sellers, C. G. Staggs, and M. L. Bogle, *J. Food Compos. Anal.*,
2006, **19**, S58.
- 263 X. Zhao, L. Yi, C. Wang, Y. Xian, X. Zeng, and W. Bai, *Int. J. Electrochem.*
Sci., 2018, **13**, 10289.
- 264 T. Lapainis, C. Scanlan, S. S. Rubakhin, and J. V. Sweedler, *Anal. Bioanal.*
Chem., 2007, **387**, 97.
- 265 V. Ladero, N. Martinez, M. C. Martin, M. Fernandez, and M. A. Alvarez,
Food Res. Int., 2010, **43**, 289.
- 266 V. Gianotti, U. Chiuminatto, E. Mazzucco, F. Gosetti, M. Bottaro, and P.
Frascarolo, *J. Chromatogr. A*, 2008, **1185**, 296.
- 267 J. B. Raoof, R. Ojani, M. Baghayeri, and M. Amiri-Aref, *Anal. Methods* 2012,
268 **4**, 1579.
- 269 J. Mohanty, H. Pal, and A. V. Sapre, *Bull. Chem. Soc. Jpn.*, 1999, **72**, 2193.
- 270 P. J. Ogren, A. Meetze, and W. C. Duer, *J. Anal. Toxicol.*, 2009, **33**, 129.
- 271 I. M. Apetrei and C. Apetrei, *Sens. Actuators B*, 2013, **178**, 40.
- 272 J. B. Raoof, R. Ojani, M. Amiri-Aref, and M. Baghayeri, *Sens. Actuators B*,
273 2012, **166-167**, 508.
- 274 A. B. Ormond and H. S. Freeman, *Materials*, 2013, **6**, 817.
- 275 K. Liu, Y. Liu, Y. Yao, H. Yuan, S. Wang, Z. Wang, and X. Zhang, *Angew.*
Chem. Int. Ed., 2013, **52** 8285
- 276 J. F. Lovell, T. W. B. Liu, J. Chen, and G. Zheng, *Chem. Rev.*, 2010, **110**, 2839.
- 277 M. Vermathen, M. Marzorati, and P. Bigler, *J. Phys. Chem. B*, 2013, **117**,
6990–7001.

- 274 J. Voskuhl, U. Kauscher, M. Gruener, H. Frisch, B. Wibbeling, C. A. Strassert,
and B. J. Ravoo, *Soft Matter*, 2013, **9**, 2453.
- 275 D. A. Fernandez, J. Awruch, and L. E. Dixelio, *Photochem. Photobiol.*, 1996,
63, 784.
- 276 L. Kaestner, M. Cesson, K. Kassab, T. Christensen, P. D. Edminson, M. J.
Cook, I. Chambrier, and G. Jori, *Photochem. Photobiol. Sci.*, 2003, **2**, 660.
- 277 P. Cosma, L. Catucci, P. Fini, P. L. Dentuto, A. Agostiano, N. Angelini, and L.
M. Scolaro, *Photochem. Photobiol.*, 2006, **82**, 563.
- 278 G. Moschetto, R. Lauceri, F. G. Gulino, D. Sciotto, and R. Purrello, *J. Am.*
Chem. Soc., 2002, **124**, 14536.
- 279 K. Lang, P. Kubat, P. Lhotak, J. Mosinger, and D. M. Wagnerova, *Photochem.*
Photobiol., 2001, **74**, 558.
- 280 L. Chen, H. Bai, J.-F. Xu, S. Wang, and X. Zhang, *ACS Appl. Mater.*
Interfaces, 2017, **9**, 13950–13957.
- 281 S. Dutta-Choudhury, J. Mohanty, H. Pal, and A. C. Bhasikuttan, *J. Chem. Sci.*,
2014 **126**, 911.
- 282 F. J. Vergeldt, R. B. M. Koehorst, A. van-Hoek, and T. J. Schaafsma, *J. Phys.*
Chem., 1995, **99**, 4397.
- 283 S. M. Pradeepa, H. S. B. Naik, B. V. Kumar, K. I. Priyadarsini, A. Barik, and
T. R. R. Naik, *Spectrochim. Acta, Part A*, 2013, **101**, 132.
- 284 C. Zhu, Q. Yang, L. Liu, F. Lv, S. Li, G. Yang, and S. Wang, *Adv. Mater.*,
2011, **23**, 4805–4810.